University of Copenhagen

Faculty of Science

PhD thesis in Physics

Emergent disorder phenomena in correlated Fe-based superconductors

by

Maria Navarro Gastiasoro

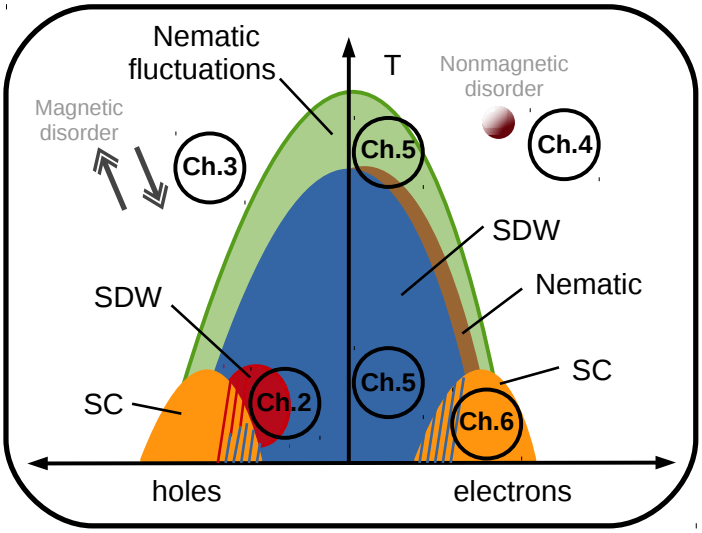

Supervisor:

Brian M. Andersen

Abstract

The fundamental pairing mechanism causing high-T superconductivity in Fe-based superconductors remains controversial. Superconductivity is only one of several phases exhibited by these materials, and it is widely believed that the mechanism responsible for pairing may be closely linked to the existence of other proximate ordered phases. Most of these materials are obtained by chemical doping, which besides extra carriers, introduces *disorder* in the system. Therefore, understanding the role of these impurities is crucial, and is a main focus of our work.

In this thesis, we start with the assumption that the observed electronic phases are captured within the itinerant electron scenario. We investigate competing spin density wave phases in homogeneous systems, but also in disordered systems where the interaction between impurity moments becomes relevant. The theory of emergent states around potentials in multi-band systems is introduced, and we propose strongly anisotropic defect states as a source of the reported transport anisotropy. Finally, we discuss unconventional correlation-driven disorder phenomena in the superconducting state, revealing a highly unusual impurity response.

Acknowledgements

First of all I would like to thank Brian for his patience and guidance, especially in those times when nothing makes sense, and I go into stubborn mode. Also for always finding the way of making the projects exciting. Milesker.

In am grateful for stimulating and helpful discussions with Morten, Astrid, Andreas, Shantanu, Beñat and Daniel. You are some of the few people around that care about details of orbitals, factors of two, and minus signs.

Thank you Astrid, for being the best office mate anyone could have. For great conversations, most of the times non-physics related, and usually full of humor. Gracias.

I have very much benefited from long conversations with Peter (a.k.a. pjh). Thank you for sharing with me your ideas and opinions about the 'big questions' in the field.

Finally, I thank my 'sestras', for invaluable pedagogical input in the late stages of the thesis, and for being around after a long day.

Maria Navarro Gastiasoro
Copenhagen, March 2016.

Contents

1 Introduction to Fe-based superconductors **5**

2 Competing magnetic phases **9**
2.1 Introduction 9
2.2 Itinerant magnetism in FeSC 13
2.3 Single-Q and double-Q phases 15
2.3.1 Mean-field model 16
2.3.2 Stability and spectral properties 17
2.3.3 Competition with superconductivity 21
2.3.4 Conclusions 25
2.4 Spectroscopy as a probe of magnetic ground state 25
2.4.1 Homogeneous case 26
2.4.2 Impurity potential 28
2.4.3 Impurity moment 31
2.4.4 Conclusions 36

3 Enhancement of magnetic stripe order from the interaction between conduction electrons and magnetic impurities **37**
3.1 Introduction 37
3.2 Magnetic impurities in a paramagnetic host 40
3.3 Single-impurity 41
3.4 Multiple impurities: order-from-disorder 42
3.5 Conclusions 47

4 Local magnetization nucleated by non-magnetic impurities **48**
4.1 Introduction 48
4.2 Model 49
4.3 Local magnetic order and impurity states 50
4.4 The "gapped" e_g orbitals 53
4.5 Strong potentials 56
4.6 Conclusions 57

5 Emergent defect states as a source of resistivity anisotropy 59
5.1 Introduction . . . 59
5.2 Transport in the nematic phase . . . 63
5.2.1 Model . . . 65
5.2.2 Nematogens and anisotropic elastic scattering rate . . . 66
5.2.3 Discussion . . . 70
5.3 New developments and outlook . . . 71
5.3.1 Elastoresistivity measurements . . . 71
5.3.2 Disorder independent transport anisotropy . . . 75
5.3.3 Nematogens in FeSe . . . 77
5.4 Impurities in the spin-density wave phase . . . 79
5.4.1 Electronic dimers . . . 81
5.5 Conclusions . . . 86

6 Unconventional disorder effects in correlated multi-band superconductors 87
6.1 Introduction . . . 87
6.1.1 Gap symmetry and structure . . . 88
6.1.2 Impurity bound states . . . 90
6.1.3 T_c suppression . . . 92
6.2 Spectroscopic signatures of a single-impurity . . . 94
6.2.1 Homogeneous superconducting state . . . 94
6.2.2 Single-impurity in the SC state . . . 96
6.2.3 Conclusions . . . 101
6.3 Correlation-driven disorder effects . . . 101
6.3.1 Model . . . 102
6.3.2 Magnetic disorder . . . 103
6.3.3 Non-magnetic disorder . . . 107
6.3.4 Conclusion . . . 113
6.4 Outlook . . . 114

A Mean-field model for competing magnetic phases 115
A.1 Real space . . . 115
A.2 Momentum space . . . 116
A.3 Orbitally resolved order parameters . . . 119

B Elastic scattering rate 120

C Band structure for LiFeAs 122

D Self-consistent BdG equations with superconductivity **125**
D.1 BdG equations 125
D.2 Self-consistent fields 128
D.3 Local density of states 129

E Ru substitution **131**
E.1 Bandwidth increase 131
E.2 Comparison with μSR 133

Chapter 1

Introduction to Fe-based superconductors

The discovery of superconductivity at 26 K in LaFeAsO by Kamihara *et al.* [1] in 2008 opened a new route to high-temperature superconductivity. In the past few years the family of Fe-based superconductors (FeSC) has grown to be large. Despite the enormous effort to understand the physical properties of these materials, however, the fundamental pairing mechanism causing high-T superconductivity remains controversial.

The key ingredient of these compounds is a common chemical building block: the quasi-two-dimensional FeX layer. The X = As, P, S, Se or Te element, exists in nearly tetrahedral positions above and below a square array of Fe ions as shown in figure 1.1(a), where FeX is highlighted in yellow. It is widely believed that the interaction leading to superconductivity originates within these common FeX layers. In some of the compounds the FeX layers are separated by other "bridging layers" along the crystallographic c-axis, such as Ba layers in $BaFe_2As_2$, or LaO layers in LaOFeAs.

Most phase diagrams in FeSC are generated by manipulating the chemical properties of the parent compound (using chemical doping), or by applying pressure. Figure 1.2 shows a schematic phase diagram of FeSC, which we will describe in detail below. As seen, the superconducting phase (orange in Fig. 1.2) usually emerges upon hole or electron doping. However, superconductivity is only one of several fascinating phases exhibited by these materials, and it is widely believed that the mechanism responsible for the emergence of superconductivity may be closely linked to the existence of neighboring phases.

The parent compounds of FeSC are metals with well defined Fermi surfaces. At low temperatures, they usually appear antiferromagnetically ordered (blue in Fig. 1.2). Notable exceptions to antiferromagnetic order in parent compounds are FeSe and LiFeAs, where for low enough temperatures superconductivity emerges

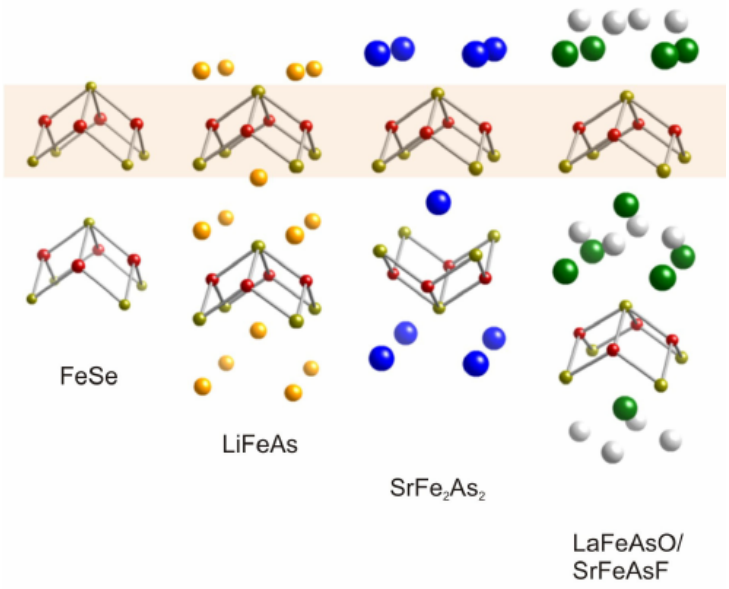

Figure 1.1: Crystallographic structures of various FeSC subfamilies. From left to right 11, 111, 122, 1111. From [2]

instead. The long-range spin ordered phase is weakened upon doping the system, and eventually disappears in a region that coincides with the emergence of superconductivity. A co-existence of both phases can take place on both electron and hole doped sides (blue and red stripes in Fig. 1.2). An important recent development is the discovery of a new type of spin order in several hole doped compounds (red in Fig. 1.2), close to the appearance of superconductivity. One of the big questions in the community is the nature of the spin ordered states. It has been mainly described in terms of *localized* spins, *itinerant* spins, or a combination of both. The first scenario involves Heisenberg-type antiferromagnetism, where the spins are essentially bound to the sites of the lattice. Some of the orbitals of the Fe atoms undergo a spontaneous symmetry breaking of their occupancy, which renormalizes the magnetic exchange parameters and triggers magnetic order. In this sense, antiferromagnetism is a secondary effect of *orbital* order. In the itinerant approach on the contrary, electrons are relatively free to travel through the lattice, and the spin order is a consequence of a Stoner-type magnetic instability. The *spins* of the itinerant electrons spontaneously develop a polarization, or in other words, the system develops a spin density wave. Finally, the combination of both localized and itinerant spins has been also discussed, with some orbitals exhibiting local moment behavior while others remain itinerant. A detailed introduction to the antiferromagnetic phase in these materials can be found in chapter 2.

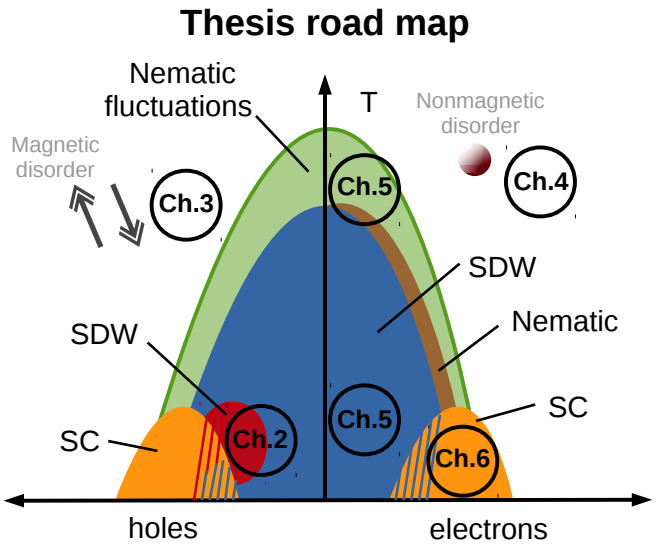

Figure 1.2: Schematic temperature versus chemical doping phase diagram of FeSC, which includes a 'road map' of this thesis. Ch.*i* refers to the chapter and magnetic (nonmagnetic) to that type of disorder.

At higher temperatures, preceding the antiferromagnetic phase, one finds the electronic nematic phase (brown in Fig. 1.2), also known as 'enigmatic-nematic'. In this state, the tetragonal symmetry of the lattice is broken, but translational and spin rotational symmetries are preserved. One of the manifestations of this type of electronic behavior is the orthorhombic transition. The distance between Fe atoms in one of the directions shortens by approximately 1% as compared to the perpendicular direction. Other perhaps more subtle expressions of nematic order are strong in-plane *anisotropy* in local density of states [78], transport [66], occupation of orbitals [69], spin excitations [70], Young's modulus [74] and charge fluctuations [75]. Some of these works have shown that nematic fluctuations (green in Fig. 1.2) persist far above the ordering temperatures of the nematic, antiferromagnetic and superconducting phases. The origin of electronic nematic behavior in FeCS is currently one of the most debated topics, involving the interplay of magnetic, orbital, and ionic fluctuations. Theoretically, both spin and orbital scenarios have been proposed[11].

The BCS-like electron-phonon mechanism, which has been successful in explaining superconductivity in a lot of materials, does not work for FeSC. Then what can cause superconductivity? This leaves us with the challenge of getting Cooper pairing instability from the repulsive electron-electron interaction. In the early days after the discovery of superconductivity in FeSC, the proximity to a

magnetic phase led to propose pairing from spin fluctuations, which combined with the Fermi surface topology, predicted the so-called $s_{\pm}$ state. On the other hand, the importance of orbital fluctuations has been also pointed out, and is currently one of the debated topics in the field. The superconducting state arising from these type of fluctuations is the s_{++} state. Recently, a great deal of attention has been focused on the simplest crystallographic compound, FeSe. This material undergoes nematic and superconducting transitions, but does not develop long-range magnetic order down to the lowest temperatures. In principle, this makes FeSe a perfect candidate to disentangle contributions from spin and orbital degrees of freedom.

As mentioned earlier, most of these materials are obtained by chemical doping, i.e. some of the elements in the parent compounds are substituted for different impurity atoms. For example, a way of moving along the electron doping axis of figure 1.2, is by substituting some of the Fe atoms for Co. In this process, besides extra carriers, one introduces *disorder* in the system. Understanding the role of these impurities is important, and becomes necessary when interpreting experimental data, and contrasting it with the available theories. We argue that, in many cases, disorder plays a crucial role, with a surprisingly rich behavior generated by the multi-orbital nature of these correlated systems.

A 'road map' of this thesis is illustrated in figure 1.2. We start with the assumption that the observed electronic phases are captured within the itinerant electron scenario. The spin degrees of freedom drives the system to nematic, SDW and superconducting instabilities, and the orbitals (and lattice) simply follow. In chapter 2, we investigate the competing SDW phases relevant for FeSC, also in the presence of superconductivity (Ch.2). We extend the study of magnetism by exploring the interaction between impurity moments and itinerant electrons in chapter 3, which constitutes an unusual example of order-from-disorder (Ch.3). The local changes and emergent defect states around potentials in the paramagnetic normal state are introduced in chapter 4 (Ch.4). Specifically, we present the concept of freezing of spin fluctuations around inhomogeneities. These ideas are extended in the subsequent chapter, where we propose strongly anisotropic defect states as a source of the reported transport anisotropy (Ch.5). Finally, we discuss unconventional correlation-driven disorder phenomena in the superconducting state in chapter 6 (Ch.6). Each chapter starts with a motivating introductory section.

The overall agreement between our results and the experimental data, both in the clean and disordered systems, provide evidence that itineracy is a good starting point that captures the essential low-energy physical aspects of FeSC. Spin fluctuations are a key ingredient in our model, and the orbital degrees of freedom, while present, play only a passive role.

Chapter 2

Competing magnetic phases

Most of the material in this chapter has been published in
Phys. Rev. B 92, 140506(R) (2015). Part of it is in preparation to be submitted

2.1 Introduction

In correlated materials in general, and unconventional superconductors in particular, a microscopic understanding of the magnetism is of paramount importance. Generally, this is because a proper description of the relevant exchange mechanism in these materials is intimately tied to their basic electronic properties. More specifically, it is additionally shown within a wide class of models that the nature of the magnetic fluctuations may be closely linked to the emergence of the superconducting condensate.[3, 4, 5]

Focussing on the iron-based superconductors, the prevalent magnetic structure consists of collinear magnetic stripe (MS) order with in-plane moments oriented antiferromagnetically (ferromagnetically) along the a (b) axis of the orthorhombic Fe lattice as shown in Fig. 2.1(a). This state has been described mainly in terms of two electronic mechanisms: *localized* spins where the orbital degree of freedom becomes relevant and *itinerant* spins with a modulation of their polarization, i.e. a spin density wave. The first scenario involves orbital ordering of the $3d$-electrons which renormalizes the magnetic exchange parameters and triggers magnetic order. [6] The spin-stripe state can be accompanied by different types of orbital orders, some of which do not require atomic displacements relative to the parent tetragonal symmetry. The favorite candidate, ferro-orbital order ($d_{xz} \neq d_{yz}$), breaks the in-plane symmetry and leads to an orthorhombic distorsion of the lattice. In the itinerant scenario, on the other hand, the metallic character and quasi-nesting features of the electronic dispersion has motivated the study of spin density wave order in these materials. The magnetic stripes state, with a

single ordering vector (1Q) modulation of the spin polarization of the electrons, induces a structural distorsion $a \neq b$, and gives rise to ferro-orbital order. No matter what drives the magnetic stripes transition, both spin and orbital order parameters, as well as a structural distorsion, are present once the transition takes place. Besides the 1Q state, additional double-Q (2Q) magnetic phases consisting of superpositions of two ordering vectors, or bidirectional SDW, were predicted in the early itinerant models. [7, 8, 9, 10] These works have identified two competing magnetic structures of the 2Q type: 1) a collinear non-uniform charge-and-spin density wave (CSDW) phase as shown in Fig. 2.1(b), and 2) a spin-vortex crystal (SVC) non-collinear phase with nearest neighbor moments at right angles as shown in Fig. 2.1(c). In contrast to the 1Q stripes state, the 2Q phases do not require a structural distorsion, i.e. tetragonal symmetry is preserved.

Whether the electronic fluctuations in these materials are predominantly of magnetic or orbital nature remains controversial.[11] The orbital and spin order parameters are intimately linked by symmetry and cannot exist on their own in the nematic of magnetic magnetic stripes state, making it hard to determine experimentally which order exhibits the dominant susceptibility in the high-T normal phase and hence drive e.g. the structural and magnetic transition. A resolution to this question is of great interest since the dominant fluctuations are likely to also mediate the pairing required for superconductivity. Therefore, the presence of a magnetic *tetragonal* phase has attracted a lot of attention[12, 13]; this phase exhibits magnetic order at the same ordering vectors $(\pi, 0), (0, \pi) \equiv \mathbf{Q}_{1,2}$ as the standard stripe magnetic order, but without breaking the tetragonal symmetry.

Experimentally, the dominating magnetic order in the iron pnictides is the MS state. This phase lowers the C_4 symmetry of the high-T tetragonal phase to orthorhombic C_2, and causes an associated splitting of the crystal Bragg peaks due to magneto-elastic coupling. Recently, several experiments have, however, reported the discovery of magnetic order without an associated structural splitting, i.e. in the tetragonal phase,[12, 13] which has been taken as indirect evidence for a magnetic driven structural transition in the case of 1Q MS order.[14] In the case of $Ba(Fe_{1-x}Mn_x)_2As_2$,[12] however, additional experiments have shown that Mn induce local regions of magnetic (π, π) order and a crystal structure consistent with intertwined short-range clusters of both tetragonal and orthorhombic structure.[15, 16, 17, 18] The collective outcomes of these experiments are explained in the next chapter within a microscopic *disorder* scenario, where the correlations among the spins of the in-plane Mn atoms result in a long-range magnetic order.

The study of 2Q order in $Ba(Fe_{1-x}Mn_x)_2As_2$ should be contrasted to other pnictides with out-of-plane dopants where a disorder scenario seems less relevant. This includes for example Ba-122 doped with Na or K or Sr-122 doped with Na, where experiments have found evidence for a phase transition into a long-range

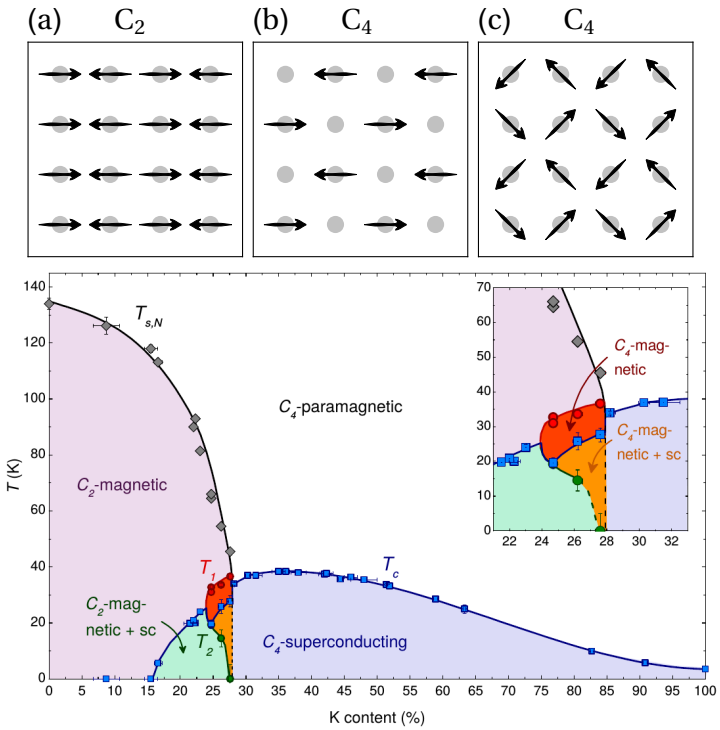

Figure 2.1: Competing magnetic phases from the itinerant picture: (a) orthorhombic MS, and tetragonal 2Q phases (b) CSDW and (c) SVC. Bottom: Novel tetragonal magnetic phase (red) in $Ba_{1-x}K_xFe_2As_2$, occurring within the C_2 stripes phase (purple). The coexistence with superconductivity (orange) displays a reduced T_c. SC-induced re-entrance of the C_2 magnetic phase (green) occurs at T_2. The inset shows an enlarged view of the region containing the C_4 magnetic phase. From [21].

ordered magnetic phase with tetragonal crystal structure.[13, 19, 21, 22, 23, 24, 25, 27, 26, 28] For the case of hole doped $Ba_{1-x}Na_xFe_2As_2$, the first reported tetragonal magnetic phase case by neutron and x-ray scattering techniques, this novel phase exists at the foot of the magnetic dome in the phase diagram.[13] More recently, Böhmer *et al.*, used thermal expansion measurements to find a tetragonal low-T phase consistent with a magnetic 2Q phase, and additionally revealed a superconductivity-induced re-entrant orthorhombic phase at even lower temperatures.[21] The resulting phase diagram, shown in figure 2.1(d), exhibits the novel tetragonal magnetic phase at compositions close to the onset of superconductivity. Subsequent experiments have corroborated the stronger competition of the new magnetic phase with superconductivity. [23, 26, 28] Mössbauer spectroscopy studies of $Sr_{1-x}Na_xFe_2As_2$ reported data consistent with non-uniform spin amplitudes at the Fe sites, vanishing on half of the sites and doubling on the

others, which seems incompatible with the localized spin picture. [24] In addition, moun spin rotation measurements on $Ba_{1-x}K_xFe_2As_2$ found a collinear spin re-orientation of the moments along the c-axis. [25] These two experiments provide strong indications that the tetragonal phase of the hole-doped systems seems to be the double-Q CSDW phase with out of plane moments [figure 2.4(c)]. The spin re-orientation has been recently explained in terms of an interplay between spin-orbit coupling and Hund's interaction. [29]

The universality of this novel magnetic phase in the pnictides is quite established by now, with three series of hole-doped compounds having reported to show its existence. Collectively, these experimental findings define the following main challenges for a theoretical description:

1. The existence of 2Q phases in restricted (intermediate) doping regimes limited by MS order and superconductivity (SC).

2. The 2Q phases exist in a limited (intermediate) temperature range.

3. SC competes with magnetic order causing a lowering of T_c upon entering the magnetic 2Q phase from the paramagnet.

4. SC competes more strongly with 2Q phases than the C_2 MS as seen by an upward T_c jump when transitioning from the coexistence phase of SC and 2Q magnetism to a coexistence phase of MS order and SC.[21]

Within the mechanism of localized spins, it is possible to construct models of orbital order that are consistent with a tetragonal crystal structure [31], but still the spin structure consists of orthorhombic single-Q stripes. This magnetic symmetry permits a coupling to the symmetry-breaking strain component e_{12} that was not detected in any of the experiments, with the corresponding need for a somehow extremely weakened magneto-elastic coupling in this state. It would also be hard to reconcile the non-magnetic sites found in [24] with the localized spin models, in which the Fe spins live on the sites of the lattice with fixed amplitude M. On the other hand, tetragonal magnetic phases arise naturally in itinerant models and a double-Q spin density wave seems to be the best candidate for these experiments. In this chapter we study the competing magnetic phases obtained from a five-orbital Hamiltonian relevant to the iron pnictides within the *itinerant* scenario. The Coulomb interaction is treated within unrestricted self-consistent Hartree-Fock, which allows one to access the entire temperature regime also in the presence of superconductivity, contrary to previous theoretical studies. The model provides an explanation of all four challenges outlined above.

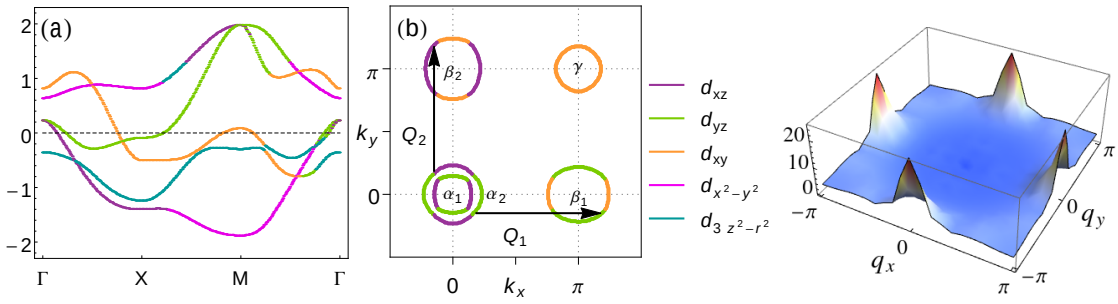

Figure 2.2: (a) Band structure along the high symmetry directions ($\Gamma = (0,0)$, $X = (\pi, 0)$, and $M = (\pi, \pi)$), and (b) Fermi surface with main orbital character for the undoped system. (c) The RPA spin susceptibility $\chi_s(\mathbf{q}, \omega = 0)$ of the system.

2.2 Itinerant magnetism in FeSC

The starting point of the theoretical analysis for the itinerant scenario is the following Hamiltonian

$$\mathcal{H} = \mathcal{H}_0 + \mathcal{H}_{int} \tag{2.1}$$

which consists of a kinetic part and the Coulomb interaction term. The former is described by a five-orbital tight-binding band relevant to the pnictides [32]

$$\mathcal{H}_0 = \sum_{ij,\mu\nu,\sigma} t_{ij}^{\mu\nu} \hat{c}_{i\mu\sigma}^{\dagger} \hat{c}_{j\nu\sigma} - \mu_0 \sum_{i\mu\sigma} \hat{c}_{i\mu\sigma}^{\dagger} \hat{c}_{i\mu\sigma}. \tag{2.2}$$

where the operators $c_{\mathbf{i}\mu\sigma}^{\dagger}$ ($c_{\mathbf{i}\mu\sigma}$) create (annihilate) an electron at site i in orbital state μ with spin σ, and μ_0 is the chemical potential which adjusts the filling. The indices μ and ν denote the five iron orbitals d_{xz}, d_{yz}, d_{xy}, $d_{x^2-y^2}$, and $d_{3z^2-r^2}$. The band structure and Fermi surface (FS) for a $n \sim 6.0$ filling is shown in Fig. 2.2. The different colors represent the *main* orbital content of the dispersion $E_0(\mathbf{k})$, described by the orbital to band unitary transformation $c_{\mathbf{k}\mu} = \sum_n u_{\mathbf{k}\mu}^n \gamma_{\mathbf{k}n}$ that diagonalizes $\mathcal{H}_0$. Despite the large variety of crystal structures, all FeSC exhibit very similar electronic structures consisting of two or more hole bands at the Γ point, and two electron bands at the X and Y points. As a result, at least two hole-like pockets and two electron-like pockets with centers shifted by $\mathbf{Q}_1 = (\pi, 0)$ and $\mathbf{Q}_2 = (0, \pi)$ is a general feature in these materials. This topology of the low-energy states is an essential ingredient of microscopic models trying to explain the phase diagram of these materials, including the magnetic, nematic and superconducting states.

The band structure near the Fermi level consist mainly of t_{2g} orbitals: xz, yz and xy dominate the orbital character of all the FS pockets, clearly seen in

figures 2.2(a) and (b). The remaining two e_g orbitals are essentially 'gapped' at this filling, and it is the t_{2g} that typically dominate the density of states around the Fermi energy. This has been used as an argument to restrict the number of orbitals included in theoretical models to two or three. In the following chapters we will argue that the e_g orbitals are essential when one considers disordered systems, and interesting multi-orbital local physics will be discussed.

A very relevant concept in the discussion of itinerant magnetism is *nesting*, which happens when different sections of the non-interacting electronic dispersion coincide when shifted by a certain wavevector $\mathbf{q}$ around the Fermi level: $E_0(\mathbf{k}+\mathbf{q}) = -E_0(\mathbf{k})$. The hole and electron bands of the iron pnictides are partly nested at the wavevectors $\mathbf{Q_1} = (\pi, 0)$ and $\mathbf{Q_2} = (0, \pi)$, as explicitly shown in figure 2.2(b). These kind of electronic structures have strong features at the nesting wavevector in the non-interacting response function $\chi_0(\mathbf{q})$, and are ideal candidates for the emergence of *spin density wave* order. A representative example of itinerant magnetism arising from a nested band dispersion is found in Cr. [33]

The interactions in the system, included in the second term of the Hamiltonian (2.1), are described by the multi-orbital on-site Hubbard model

$$\begin{aligned}\mathcal{H}_{int} = U\sum_{i\mu}\hat{n}_{i\mu\uparrow}\hat{n}_{i\mu\downarrow} + U'\sum_{i,\mu<\nu,\sigma}\hat{n}_{i\mu\sigma}\hat{n}_{i\nu\bar{\sigma}} + (U'-J)\sum_{i,\mu<\nu,\sigma}\hat{n}_{i\mu\sigma}\hat{n}_{i\nu\sigma} \\ + J\sum_{i,\mu<\nu,\sigma}\hat{c}^{\dagger}_{i\mu\sigma}\hat{c}^{\dagger}_{i\nu\bar{\sigma}}\hat{c}_{i\mu\bar{\sigma}}\hat{c}_{i\nu\sigma} + J'\sum_{i,\mu<\nu,\sigma}\hat{c}^{\dagger}_{i\mu\sigma}\hat{c}^{\dagger}_{i\mu\bar{\sigma}}\hat{c}_{i\nu\bar{\sigma}}\hat{c}_{i\nu\sigma},\end{aligned} \tag{2.3}$$

with intra-(inter-)orbital Coulomb repulsion U (U'), the Hund's coupling J, and pair-hopping energy J'. Spin rotational invariance is assumed throughout our work and we set $U' = U - 2J$ and $J' = J$. Including these interactions in the response function through standard random phase approximation (RPA) we get the spin susceptibility of the system, shown in figure 2.4(c). The magnetic response is clearly peaked at the nesting wavevectors $\mathbf{Q_1}$ and $\mathbf{Q_2}$, and within the itinerant scenario, the spin ordered state will be in general a combination of both ordering vectors, $\mathbf{M}(\mathbf{r}) = \sum_{l=1,2}\mathbf{M}_l \exp(i\mathbf{Q}_l\cdot\mathbf{r})$. Figure 2.1 shows examples of the possible SDW states that were introduced in the previous section as relevant candidates for the magnetic ground state of iron pnictides. Details of the band structure, filling and interacting parameters will determine the prefered ordering vector combination $\mathbf{M}_l$ and is the subject of study in the next section.

Once the modulation of the spin polarization of the itinerant electrons has taken place, i.e. the magnetic order parameters $\mathbf{M}_l = \sum_{\mathbf{k}\sigma}\sigma\langle\hat{c}^{\dagger}_{\sigma}(\mathbf{k})\hat{c}_{\sigma}(\mathbf{k}+\mathbf{Q}_l)\rangle$ are non-zero, a reconstruction of the electronic dispersion occurs and the SDW-mixed bands form new Fermi surfaces. An important feature of this reconstruction is the opening of SDW *gaps* at the ordering wavevectors $\mathbf{Q}_l$ which results in partial gapping of the Fermi surface and will have crucial consequences in the presence of

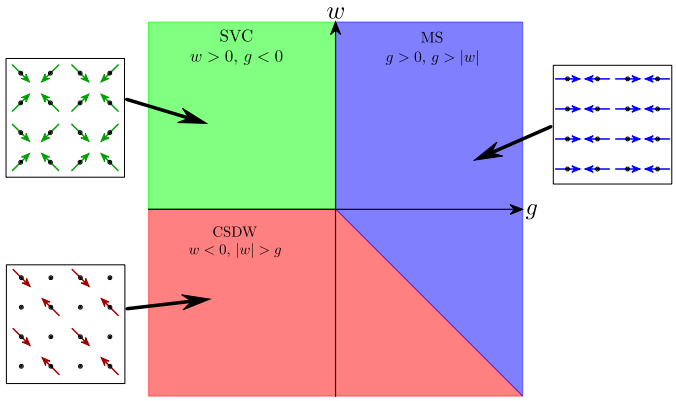

Figure 2.3: Phase diagram of the phenomenological GL model (2.5), as a function of the fourth order terms g and ω, with the three competing states: single-Q MS, and double-Q CSDW and SVC.

superconductivity. The band reconstructions taking place in the different magnetic phases and their repercussions in the coexistence phase with superconductivity are presented in the next section.

2.3 Single-Q and double-Q phases

The generic spin configuration of the system has the form

$$\mathbf{M}(\mathbf{r}) = \mathbf{M}_1 \exp(i\mathbf{Q}_1 \cdot \mathbf{r}) + \mathbf{M}_2 \exp(i\mathbf{Q}_2 \cdot \mathbf{r}) \tag{2.4}$$

with the order parameters $\mathbf{M}_1$ and $\mathbf{M}_2$ for the ordering vectors $\mathbf{Q}_1 = (\pi, 0)$ and $\mathbf{Q}_2 = (0, \pi)$, respectively. As mentioned before, the prevalent magnetic structure in the pnictides consists of collinear magnetic stripe order, shown in figure 2.4(a). Thus, this configuration of moments singles out the $\mathbf{Q}_1$ ordering vector, i.e. $\mathbf{M}_2 = 0$, and the system ends in a *single-Q* (1Q) magnetic structure. An obvious question, however, is why the system does not take advantage of the enhanced susceptibility at both $\mathbf{Q}_1$ and $\mathbf{Q}_2$ to form other magnetic phases, e.g. *double-Q* (2Q) phases consisting of superpositions of ordering at $\mathbf{Q}_1$ and $\mathbf{Q}_2$. This question has been studied theoretically mainly using various effective field theories restricted to the vicinity of the magnetic transition temperature T_N, and an unrestricted Hartree-Fock approximation in a two-orbital model.[7, 8, 9, 10]

In order to get some insight into the competing magnetic phases in these materials, we present below the results of a Ginzburg-Landau (GL) phenomenological model. [39] Near the magnetic transition, the most general free energy expansion

that respects tetragonal and $O(3)$ symmetries is:

$$\mathcal{F} = \frac{a}{2}(\mathbf{M}_1^2 + \mathbf{M}_2^2) + \frac{u}{4}(\mathbf{M}_1^2 + \mathbf{M}_2^2)^2 - \frac{g}{4}(\mathbf{M}_1^2 - \mathbf{M}_2^2)^2 + \omega(\mathbf{M}_1 \cdot \mathbf{M}_2)^2 \tag{2.5}$$

The first two terms depend only on the combination $\mathbf{M}_1^2 + \mathbf{M}_2^2$, which results in a huge degeneracy of the magnetic ground state. [8] The order parameter manifold can be viewed as a six-component vector (three for each $\mathbf{M}_i$), so the spin ordering is a spontaneous breaking of $O(6)$ symmetry. The last two terms in equation (2.5) lift this degeneracy by selecting the relative amplitudes ($\mathbf{M}_1^2/\mathbf{M}_2^2 = 0$ or $\mathbf{M}_1^2/\mathbf{M}_2^2 = 1$) and relative orientations ($\mathbf{M}_1^2 || \mathbf{M}_2^2$ or $\mathbf{M}_1^2 \perp \mathbf{M}_2^2$) of the two order parameters. A phase diagram of the magnetic ground states as a function the two quartic coefficients g and ω (for $u > 0$) is shown in figure 2.3. In addition to the 1Q MS (blue) there are two competing magnetic structures of the 2Q type: 1) a spin-vortex crystal (SVC) non-collinear phase with nearest neighbor moments at right angles (green), and 2) a collinear non-uniform charge-and-spin density wave (CSDW) phase (red). In order to identify the magnetic ground state of the system one has to evaluate the coefficients in equation (2.5), which depend delicately on the band structure, doping level, and interactions.

In this section we perform a study of the stability of, and phase transitions between, the competing magnetic phases obtained from a five-band Hamiltonian relevant to the iron pnictides. The Coulomb interaction is treated within unrestricted self-consistent Hartree-Fock, i.e. all charge and spin densities are allowed to vary at each separate site. These calculations constitute a comprehensive microscopic study of the 2Q magnetic phases, also in the presence of SC and disorder.

2.3.1 Mean-field model

We start by decoupling the four fermion interaction (2.3) into a sum of all possible bilinear terms by including correlations 'on the average'. This mean-field decoupling of Hamiltonian (2.1) leads to the following model

$$\mathcal{H}^{MF} = \sum_{ij\mu\nu} \begin{pmatrix} \hat{c}^\dagger_{i\mu\uparrow} & \hat{c}^\dagger_{i\mu\downarrow} \end{pmatrix} \begin{pmatrix} \varphi^{\mu\nu}_{ij\uparrow} & \omega^{\mu\nu}_{ii\uparrow} \\ \omega^{\mu\nu}_{ii\downarrow} & \varphi^{\mu\nu}_{ij\downarrow} \end{pmatrix} \begin{pmatrix} \hat{c}_{j\nu\uparrow} \\ \hat{c}_{j\nu\downarrow} \end{pmatrix}, \tag{2.6}$$

where $\varphi^{\mu\nu}_{ij\sigma}$ and $\omega^{\mu\nu}_{ii\sigma}$ are functions of the interaction parameters U, J, U' and J', and the fields $\langle \hat{c}^\dagger_{i\mu\sigma} \hat{c}_{j\nu\sigma'} \rangle$,

$$\begin{aligned} \varphi^{\mu\nu}_{ij\sigma} &= t^{\mu\nu}_{ij} + \delta_{\mu\nu}[-\mu_0 + U\langle \hat{n}_{i\mu\bar{\sigma}} \rangle + U'\langle \hat{n}_{i\nu\bar{\sigma}} \rangle + (U' - J)\langle \hat{n}_{i\nu\sigma} \rangle] \\ &\quad - \bar{\delta}_{\mu\nu}[(U' - J)\langle \hat{c}^\dagger_{i\nu\sigma} \hat{c}_{i\mu\sigma} \rangle + J\langle \hat{c}^\dagger_{i\nu\bar{\sigma}} \hat{c}_{i\mu\bar{\sigma}} \rangle + J'\langle \hat{c}^\dagger_{i\mu\bar{\sigma}} \hat{c}_{i\nu\bar{\sigma}} \rangle], \end{aligned} \tag{2.7}$$

$$\omega^{\mu\nu}_{ii\sigma} = \delta_{\mu\nu}[-U\langle \hat{c}^\dagger_{i\mu\bar{\sigma}} \hat{c}_{i\mu\sigma} \rangle - J\langle \hat{c}^\dagger_{i\nu\bar{\sigma}} \hat{c}_{i\nu\sigma} \rangle] - \bar{\delta}_{\mu\nu}[U'\langle \hat{c}^\dagger_{i\nu\bar{\sigma}} \hat{c}_{i\mu\sigma} \rangle + J'\langle \hat{c}^\dagger_{i\mu\bar{\sigma}} \hat{c}_{i\nu\sigma} \rangle]. \tag{2.8}$$

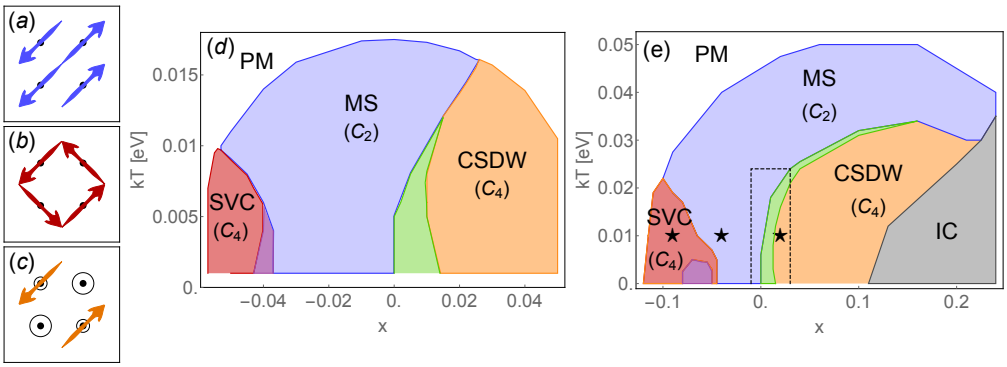

Figure 2.4: Spin and charge order of the (a) 1Q MS ($\mathbf{M_2} = 0$), (b) 2Q SVC ($\mathbf{M_1} \perp \mathbf{M_2}$), and (c) CSDW ($\mathbf{M_1}||\mathbf{M_2}$). The black circles in (c) represent the $\mathbf{Q_1} + \mathbf{Q_2} = (\pi, \pi)$ charge order. (d,e) Magnetic phase diagrams as obtained from Eq. (2.6) as a function of T and filling $n_{opt} - x$ for (d) $U = 0.85$ eV and (e) $U = 0.95$ eV. The green (purple) area indicates regions of coexisting MS and CSDW (SVC).

with $\bar{\delta}_{\mu\nu} = 1 - \delta_{\mu\nu}$. We diagonalize Eq.(2.6) unrestricted on 20×20 lattices, and self-consistently calculate the spin $M^l(\mathbf{r_i}) = \sum_{\mu\sigma\sigma'} \langle \hat{c}^\dagger_{i\mu\sigma} \tau^l_{\sigma\sigma'} \hat{c}_{i\mu\sigma'} \rangle$, and charge density $n(\mathbf{r_i}) = \sum_\mu \left(\langle \hat{c}^\dagger_{i\mu\uparrow} \hat{c}_{i\mu\uparrow} \rangle + \langle \hat{c}^\dagger_{i\mu\downarrow} \hat{c}_{i\mu\downarrow} \rangle \right)$, where $l = x, z$, and extract the ordering components $\mathbf{M_l}$ and n_l of $\mathbf{M}(\mathbf{r}) = \sum_l \mathbf{M}_l \exp(i\mathbf{Q}_l \cdot \mathbf{r})$ and $n(\mathbf{r}) = \sum_l n_l \exp(i\mathbf{Q}_l \cdot \mathbf{r})$. We have compared the free energy of the magnetic states $\mathcal{F} = \langle \mathcal{H}^{MF} \rangle - T\mathcal{S}$ to verify the stability of the results, and checked that 100×100 momentum grids support the same solutions. For more details of real and momentum space equations see Appendix A.

2.3.2 Stability and spectral properties

Figure 2.4(d,e) display two representative phase diagrams as obtained from self-consistently diagonalizing Eq. (2.6) as a function of T and electron filling for $U = 0.85$ eV (d) and $U = 0.95$ eV (e). $n_{opt} = 5.91$ is defined as the electron filling with the highest T_N as deduced by the paramagnetic susceptibility, and the total filling is $n = n_{opt} - x$. The parameter x is directly connected to the electron filling as a deviation from n_{opt} in our model, and not the chemical substitution used in real materials. The fact that the optimal doping level for the magnetic order is offset from $n = 6$ for DFT-generated bands is well known,[34] and not important for the conclusions of this section. As seen from both cases, the 2Q phases, SVC and CSDW, exist at the foot of the MS dome on the electron and hole-doped side respectively, and whereas the transition between the MS and SVC phases is sharp, a more gradual transition takes place between the MS and the CSDW

phases as indicated by the green intermediate regions. Interestingly, both recent Mössbauer spectroscopy studies of $Sr_{1-x}Na_xFe_2As_2$ [24] and moun spin rotation measurements on $Ba_{1-x}K_xFe_2As_2$ [25] found that indeed the 2Q magnetic phase of the hole-doped system seems to be the CSDW phase, in agreement with the phase diagrams in Fig. 2.4(d,e). The colinear spin structure of the CSDW phase was also recently verified by spin polarized neutrons, additionally finding that the moments are oriented along the c-axis. [20] The grey area denoted IC in Fig. 2.4(e) represents an incommensurate magnetic phase where the ordering vectors $\mathbf{Q_1}/\mathbf{Q_2}$ no longer faithfully represent the magnetic ground state of the system. The IC phase is absent in Fig. 2.4(d) because the lower U leads to a vanishing magnetization at significantly lower doping levels compared to Fig. 2.4(e).

In the remainder of this section we focus on the $U = 0.95$ eV case, and use the $x = -0.09$ and $x = 0.02$ electron and hole fillings, respectively, to discuss the transition from the MS state to the SVC and CSDW phases upon lowering T. Figures 2.5(a,b) show the T dependence of the SDW components $M_1 \equiv |\mathbf{M_1}|$ and $M_2 \equiv |\mathbf{M_2}|$ for both fillings. At T_N, M_1 gradually increases while M_2 remains zero, signalling a second order transition into the MS state. In the $x = -0.09$ case, [Fig. 2.5(a)], at $T_1 < T_N$ the 1Q-2Q transition takes place and the moments re-orient to form the SVC state with $\mathbf{M_1} \perp \mathbf{M_2}$ and $M_2 = M_1$. As seen from Fig. 2.5(a), the sudden jump of M_2 at T_1 is compensated by a reduction in M_1, leaving the average magnetization $\bar{M}_r = \frac{1}{2}\sqrt{M_1^2 + M_2^2}$ nearly unchanged. In Fig. 2.5(c) we display the T dependence of the entropy $\mathcal{S}(T)$. The small discontinuity in $\mathcal{S}$ at T_1 [see inset of Fig. 2.5(c)] agrees with a weak first order transition.

The 1Q-2Q transition taking place at $x = 0.02$ is shown in Fig. 2.5(b,d). As seen, in this case the second component M_2 continuously increases below $T_0 < T_N$ in a second order fashion. The increase of M_2 is again compensated by a decrease in M_1. In this case, however, $\mathbf{M_2}$ is aligned with $\mathbf{M_1}$, and the spin order remains collinear. As soon as $M_2 > 0$, a small charge order is induced at $\mathbf{Q_3} \equiv \mathbf{Q_1} + \mathbf{Q_2} = (\pi, \pi)$ which scales with $\mathbf{M_1} \cdot \mathbf{M_2}$ and thus increases gradually (see Appendix A for more details). In the range $T_1 < T < T_0$, where M_2 is increasing, the system is still C_2 symmetric ($0 < M_2 < M_1$) but has developed characteristics of the CSDW state, such as the (π, π) charge order [see Fig. 2.4(c)]. We stress that this new phase, which is a mixture of the MS and CSDW phases, is not spatially segregated, and is the preferred state found from fully unrestricted real-space lattice calculations. This mixed phase has not been previously discussed e.g. within Ginzburg-Landau approaches where it is not allowed, unlike the current approach where we have access to all temperatures including those deep inside the magnetic region. Finally at $T < T_1$ the pristine C_4 symmetric CSDW phase with $M_2 = M_1$ is formed, but we find that at the lowest $T < \tilde{T}_0$ a re-entrance to a weakly C_2 symmetric 2Q phase occurs ($0 < M_2 < M_1$). As can be seen from

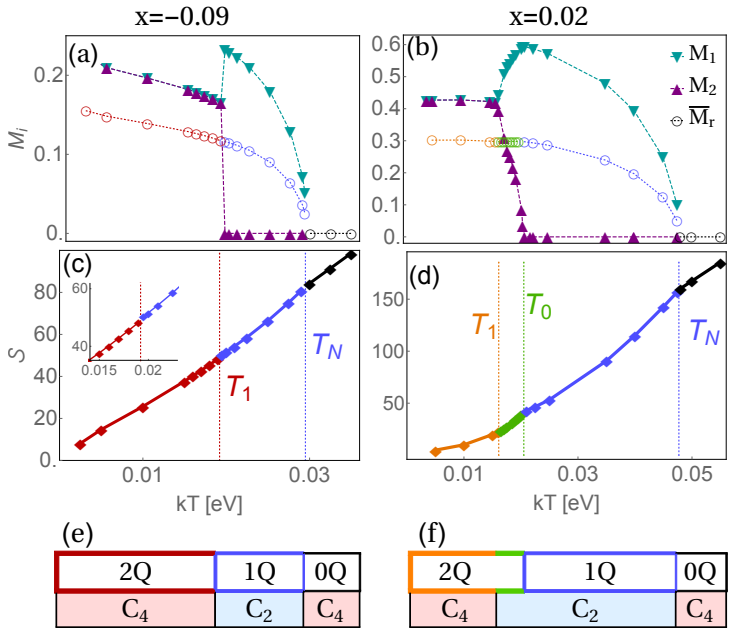

Figure 2.5: (Color online) (a) T evolution at $x = -0.09$ of the magnetic components M_1 (▼), M_2 (▲) and $\bar{M}_r = \frac{1}{2}\sqrt{M_1^2 + M_2^2}$ (○), and (c) the entropy $\mathcal{S}(T)$. A zoom of $\mathcal{S}$ at T_1 is shown in the inset. The color changes in $\bar{M}_r$ and $\mathcal{S}$ represent the magnetic phase transitions shown also in Fig. 2.4(e) with $U = 0.95$ eV. (b,d) The same as (a,c) but for $x = 0.02$ with CSDW order. (e,f) summarize the T-dependence of the magnetic structure and the expected associated lattice symmetry.

$\mathcal{S}(T)$ in Fig. 2.5(d) weak thermodynamic signatures are expected throughout the T range. The T evolution of both transitions and their associated lattice symmetries are summarized in Figs. 2.5(e,f).

Next we compare the electronic properties of the magnetic phases, MS, SVC, and CSDW, by focussing on the three different fillings indicated by the black stars in Fig. 2.4(e). In order to illustrate the different nesting conditions, we first show in Figs. 2.6(a)-(c) the FS in the PM state in the folded Brillouin zone (BZ) where the X and Y centered elliptical electron pockets β_1 and β_2, and the M centered γ hole pocket all fold on top of the Γ point (see section 2.2 for further details). In the ordered state, energy gaps open by the magnetic ordering vector, when their orbital character overlap is non-zero. This is apparent in Fig. 2.6(a,d) where the weakly nested β_i and the outer hole pocket α_2 are gapped around $k_x = \pm k_y$ upon the SVC formation. The rest of the SDW gaps are opened below the Fermi energy ϵ_F, and the reconstructed bands are seen from Fig. 2.6(g) to contain considerable

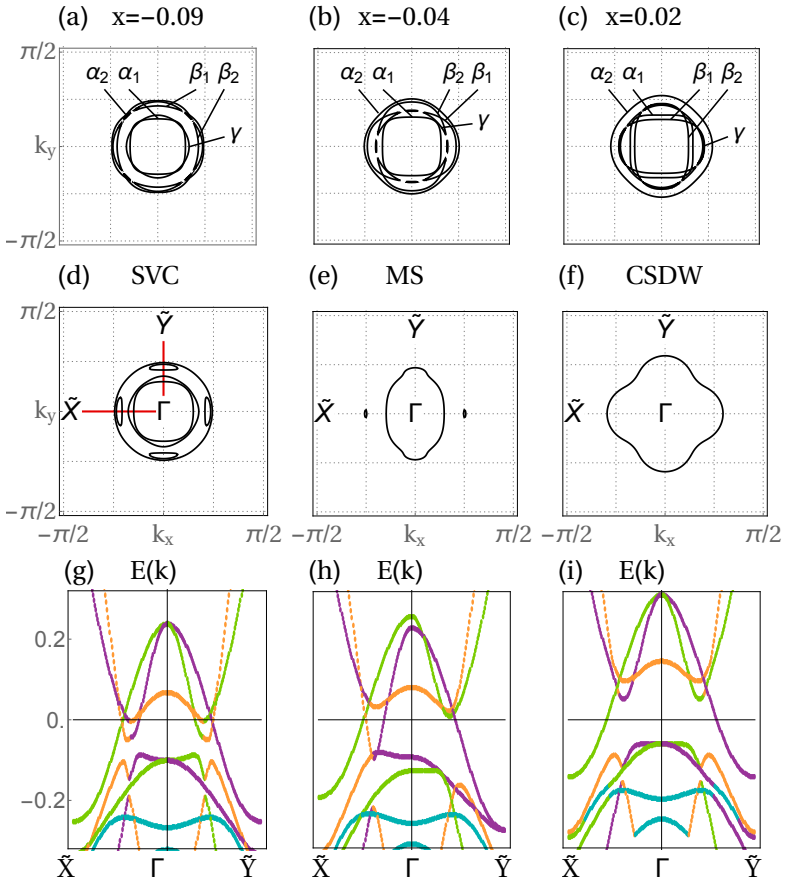

Figure 2.6: Fermi surface in the folded BZ, $-\pi/2 < k_x, k_y < \pi/2$, in the PM state for (a) $x = -0.09$, (b) $x = -0.04$ and (c) $x = 0.02$, and in the magnetic states (d) SVC ($\mathbf{M_1} = 0.2\hat{z}$; $\mathbf{M_2} = 0.2\hat{x}$), (e) MS ($M_1 = 0.52$; $M_2 = 0$), and (f) CSDW ($M_1 = M_2 = 0.43$) for $U = 0.95$ eV. (g-i) Band structure along the momentum path $\tilde{X} - \Gamma - \tilde{Y}$ shown in (d) for the (g) SVC, (h) MS, and (i) CSDW phase. The main orbital contributions are shown by purple: d_{xz}; green: d_{yz}; orange: d_{xy}; cyan: d_{z^2}.

orbital mixture. As the filling is increased in Fig 2.6(b), multiple electron-hole band crossings get closer to the ϵ_F, and additional nested areas appear at the FS, for example the ones connected by the γ and β_i pockets. This enhances the spin susceptibility at $\mathbf{Q_1}/\mathbf{Q_2}$, which naturally leads to larger SDW order and more pronounced energy gaps and FS reconstruction in the MS state. The resulting FS in Fig 2.6(e) exhibits hole-like Dirac cones along the AFM direction and a hole pocket at Γ of mainly d_{xz} character resulting from the mixing of α_1 and α_2. Evidently, since the MS state singles out the $\mathbf{Q_1}$ ordering vector, the spectrum becomes C_2 symmetric as shown in Fig. 2.6(e,h). Because MS breaks the d_{xz}/d_{yz} degeneracy an associated ferro-orbital ordering $n_{xz} > n_{yz}$ results in a splitting of the bands at the Γ point as seen from Fig. 2.6(h). No such splitting takes place in the 2Q states with $M_1 = M_2$ (at least in the absence of spin-orbit coupling). Finally, as the filling is increased further, large nested areas of α_1 and γ with the electron pockets appear at the FS as seen from Fig 2.6(c). For the present band, at this filling the FS-nesting is the strongest of the presented cases, and the resulting SDW order parameter and the gaps are the largest. As seen from Fig 2.6(f), α_1 and β_i become fully gapped, and similarly most of the γ pocket except small pieces around $k_x = \pm k_y$ which hybridize with the outermost α_2 pocket.

The band reconstruction taking place in the spin ordered state obviously depends on the amplitude of the magnetic OPs M_1 and M_2, which in turn depend on the interacting strength U. This is illustrated in Fig. 2.7 where the reconstructed FSs in the (a) SVC, (b) MS and (c) CSDW states are plotted as a function of U. For comparison the paramagnetic FS is shown in the first panel of each case. As seen, the resulting reconstructed Fermi surface depends significantly on the interaction strength.

The dependence of the band structure of the ordered state on U, together with the very similar band reconstructions of the 2Q states suggests that a non-spin-resolved spectroscopy, such as ARPES, will have a hard time identifying signatures of a particular magnetic state. This is further complicated by the presence of orthorhombic domains in these systems, which implies an average measurement on conventional (non-polarized, non detwinned) probes. These issues motivated the study of *local probes* such as scanning tunneling spectroscopy (STM), which can take advantage of the distinct spin arrangements locally. We propose a systematic way of identifying different itinerant spin structures with standard (non-spin-polarized) STM in section 2.4.

2.3.3 Competition with superconductivity

Motivated by the recent experimental discovery of the effects of superconductivity on the magnetic states,[21, 23, 26, 28] we have included SC order to the model by the following BCS term $\mathcal{H}_{BCS} = \sum_{k,\mu\nu} \Delta_{\mu\nu}(k)\hat{c}^\dagger_{k\mu\uparrow}\hat{c}^\dagger_{-k\nu\downarrow}$, where $\Delta_{\mu\nu}(k) =$

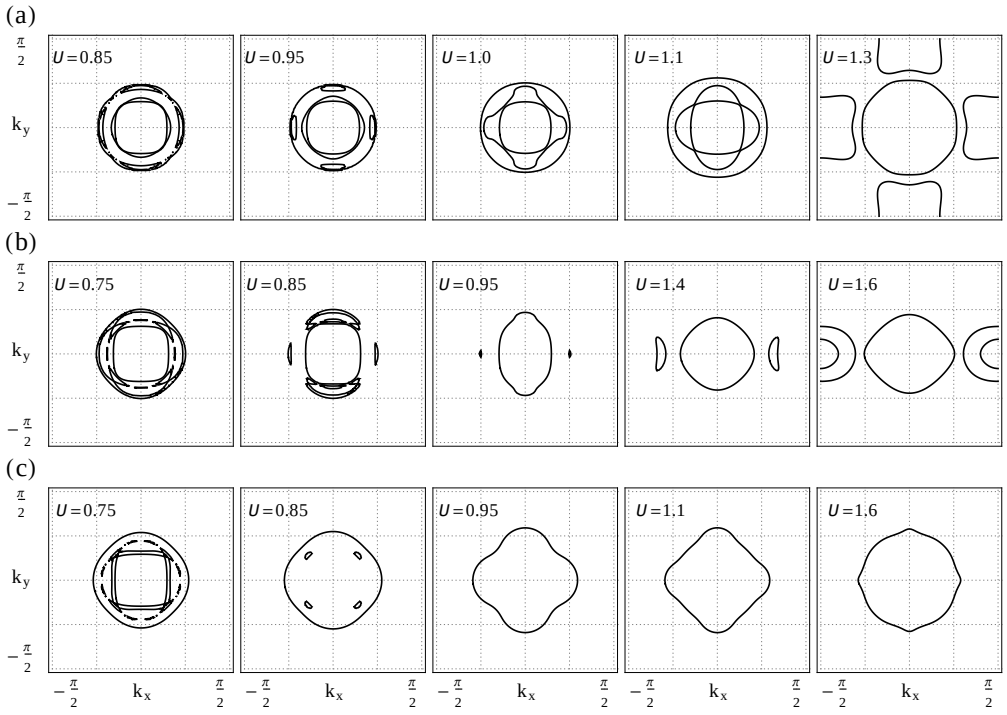

Figure 2.7: Fermi surfaces for different values of the interacting parameter U in the (a) $x = -0.09$ and SVC, (b) $x = -0.04$ and MS, and (c) $x = 0.02$ and CSDW.

$\sum_{k',\alpha\beta} \Gamma^{\beta\nu}_{\mu\alpha}(k-k')\langle \hat{c}_{-k'\beta\downarrow}\hat{c}_{k'\alpha\uparrow}\rangle$. A recent Landau order parameter expansion has also been used to study this problem close to T_N.[30] The effective pairing vertices $\Gamma^{\beta\nu}_{\mu\alpha}(k-k')$ are obtained from the RPA spin and charge susceptibilities in the PM state with leading $s_\pm$ symmetry. A more exhaustive description of spin-fluctuation mediated superconductivity in these materials can be found in chapter 6. The multi-orbital pairing vertex in the singlet channel [35] is calculated from the RPA spin- χ_s^{RPA} and charge-susceptibilities χ_c^{RPA},

$$\Gamma^{st}_{pq}(k-k',0) = \left[\frac{3}{2}U^s\chi_s^{RPA}(k-k',0)U^s + \frac{1}{2}U^s - \frac{1}{2}U^c\chi_c^{RPA}(k-k',0)U^c + \frac{1}{2}U^c\right]^{st}_{pq} \tag{2.9}$$

where U^s and U^c are 5×5 matrices identical to those of Ref. [35]. The real-space pairings are then obtained by Fourier transforming equation (2.9), $\Gamma^{\beta\nu}_{\mu\alpha}(\mathbf{r_{ij}}) = \sum_{\mathbf{q}} \Gamma^{\beta\nu}_{\mu\alpha}(\mathbf{q})\exp(i\mathbf{q}\cdot(\mathbf{r_i}-\mathbf{r_j}))$. We retain all orbital combinations up to next-nearest neighbor sites to calculate the superconducting order parameter $\Delta^{\mu\nu}_{\mathbf{ij}} = \sum_{\alpha\beta}\Gamma^{\beta\nu}_{\mu\alpha}(\mathbf{r_{ij}})\langle\hat{c}_{\mathbf{j}\beta\downarrow}\hat{c}_{\mathbf{i}\alpha\uparrow}\rangle$. The intra-orbital effective pairings, with the largest amplitudes, are shown in Fig. 2.8.

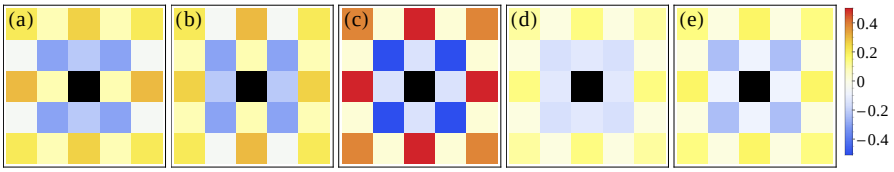

Figure 2.8: Spatial dependence of the intra-orbital effective pairing constants $\Gamma^{\mu\mu}_{\mu\mu}(\mathbf{r_{ij}})$ in eV from the central site. (a) d_{xz} (b) d_{xz}, (c) d_{xy}, (d) $d_{x^2-y^2}$ and (e) d_{z^2}.

In order to study the effects of SC on both the 1Q and 2Q magnetic states, we focus on the region of the phase diagram outlined by the dashed box in Fig. 2.4(e), and self-consistently solve the associated Bogoliubov-de Gennes equations including both magnetic and SC order parameters. The modified phase diagram shown in Fig. 2.9(a) exhibits a noticeable effect of SC on the boundaries between both magnetic states as seen by comparison to the dashed gray lines indicating the transition lines from Fig. 2.4(e) without SC order. (The phase diagram corresponding to Fig. 2.4(d) including superconducting order is supplied in the SI.) Below T_c, where both the magnetic and SC order parameters are non-zero, the MS region expands at the expense of the CSDW phase. This effect is explicitly shown in Fig. 2.9(b) by the evolution of the magnetic anisotropy $\delta_M = (M_1 - M_2)/(M_1 + M_2)$, which is a measure of the C_2 symmetry breaking, i.e. $\delta_M = 0$ ($\delta_M = 1$) for the CSDW (MS) state, and $\delta_M > 0$ for mixed C_2 states with $0 < M_2 < M_1$. As seen from Fig. 2.9(b), without SC δ_M gradually evolves from $\delta_M = 1$ at high T to $\delta_M = 0$ at low T, with a transition that sharpens with increasing x. In the presence of SC order, however, δ_M is pushed up, as indicated by the shaded regions in Fig. 2.9(b), and the magnetic order is driven towards the MS phase. This effect is particularly pronounced in the regions of large $\Delta_{\mu\nu}(k)$ closer to the MS phase, and is consistent with recent experiments.[21]

The T_c line shown by the filled black dots in Fig. 2.9(a) evidently exhibits a clear drop across the MS-CSDW transition. This reduction of T_c is directly caused by the emergence of the CSDW state as verified by the significantly higher T_c (empty circles) found by a separate calculation with the magnetic order forced to the MS type. The stronger competition between SC and magnetic order can be explained by a reduced density of states $N(\epsilon)$ at ϵ_F in the CSDW phase (compared to MS), $N_{2Q}(\epsilon_F) \sim 0.64 N_{1Q}(\epsilon_F)$. In addition, the dominant SC pairing is the intra-orbital d_{xy} element caused by strong γ-β_i FS nesting (see SI). However, as seen explicitly from Figs. 2.9(d) the FS in the CSDW phase (without SC) contains significantly less d_{xy} orbital character (orange points) compared to the corresponding MS FS shown in Fig. 2.9(c). In summary T_c is reduced from the PM state into the magnetic phase ($N_{1Q}(\epsilon_F) \sim 0.42 N_{PM}(\epsilon_F)$ and $N_{2Q}(\epsilon_F) \sim 0.26 N_{PM}(\epsilon_F)$), but

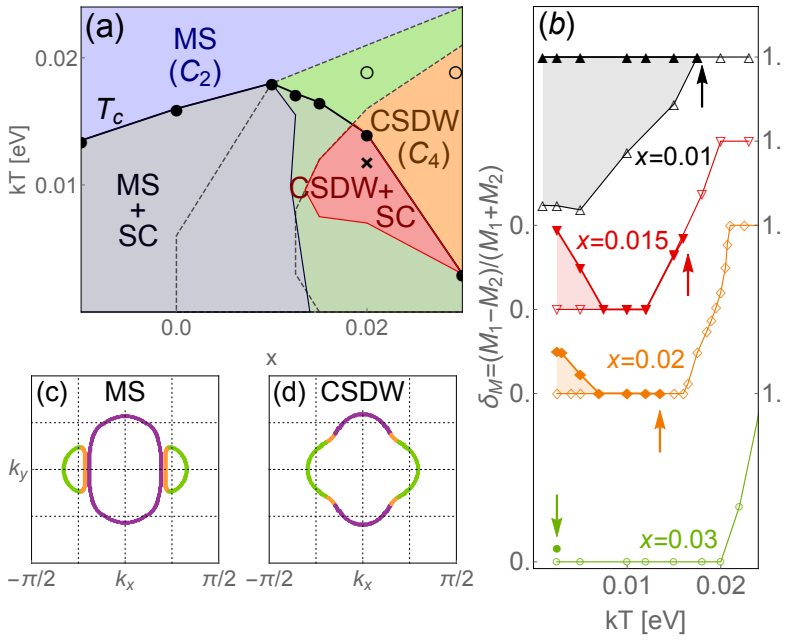

Figure 2.9: (a) Modified phase diagram from the region indicated by the dashed box in Fig. 2.4(e) in the presence of SC order. (b) Magnetic anisotropy $\delta_M = (M_1 - M_2)/(M_1 + M_2)$ versus T for four different x with (without) SC order shown by the solid (open) symbols. The arrows mark T_c. (c,d) Fermi surface at the cross in (a) for MS (c) and CSDW (d) order (without SC) using the same orbital color code as in Fig. 2.6.

enhanced from the CSDW phase into the MS phase at lower T in agreement with the experimental finding of Ref. [21].

We have also calculated the phase diagram in the presence of competing superconductivity at $U = 0.85$ eV shown in Fig. 2.10. The corresponding normal state phase diagram for this case is shown in Fig. 2.4(d). The lower value of U pushes the magnetic structure to lower values of the doping which prevents the occurrence of the IC magnetic phase, and the paramagnetic superconducting phase directly merges with the SCO C_4-magnetic phase in this case. Note that for the particular parameters used to generate Fig. 2.10 there is no superconductivity-induced re-entrance of the C_2 phase, which we attribute to the pairing being too weak to cause a switch of the preferred magnetic structure.

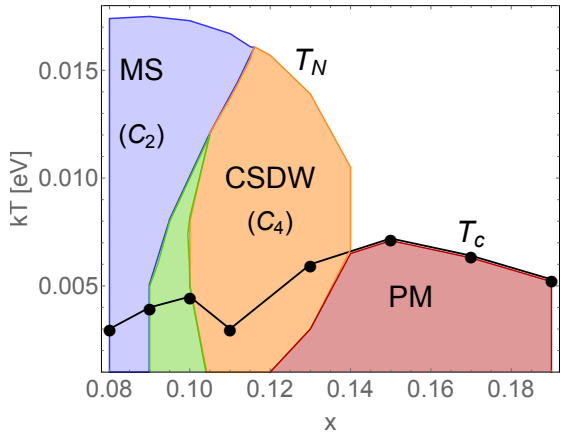

Figure 2.10: Phase diagram showing the magnetic and superconducting phases as a function of T and filling $n_{opt} - x$ for $U = 0.85$ eV.

2.3.4 Conclusions

In summary, we have presented a detailed microscopic study of competing magnetic phases in iron pnictides within the itinerant scenario. As a function of electron filling and temperature, the magnetic stripe (single-Q) order forms a dome, but competing non-collinear and non-uniform double-Q phases exist at the foot of the dome in agreement with recent experiments. We compute and compare the electronic properties of the different magnetic phases and investigate the role of competing superconductivity. Superconductivity is shown to compete more strongly with double-Q magnetic phases, which can lead to re-entrance of the C_2 (single-Q) order in agreement with recent experimental findings.

An open question to this five-orbital study of the magnetic ground state is: what exactly makes the system select one phase over the others? In the beginning of this section we presented the phenomenological GL model, from which we learned that the final magnetic ground state is selected by the quartic coefficients. At the time of writing, we are lacking a simple picture, or indication from the band structure (Fermi surface, orbital characters etc.) that relates, for example, to the sign of the quartic coefficients.

2.4 Spectroscopy as a probe of magnetic ground state

Elucidating the magnetic ground state of metallic magnets with multiple ordering momenta is a challenging task, which requires a combination of various experimen-

tal techniques such as diffraction spectroscopy with the help of neutrons or X-rays, nuclear magnetic resonance (NMR), Mössbauer spectroscopy, and μ-on spin relaxation (μSR). In this section we propose a method, based on the Fourier-transformed scanning tunneling spectroscopy, to reveal the magnetic ground state of quasi-two-dimensional metallic magnets with multiple ordering momenta. We demonstrate the effectiveness of the method by analyzing the impact of the magnetic structures with multiple ordering vectors $\mathbf{Q}$ in the parent materials of the iron-based superconductors on the characteristic features of the Fourier-transformed local electronic density of states (LDOS). Most importantly, we argue that the standard (non-spin-polarized) tunneling conductance in the vicinity of a magnetic impurity moment, whose orientation can be controlled by an external magnetic field, is a powerful tool to determine the structure of the host magnetism.

In order to properly set the stage for the study of the impurity moment further below, we present initially the possible magnetic ground states of the homogeneous itinerant model we will be considering. We proceed with a discussion of the distinct spectral signatures around a single non-magnetic impurity in the different magnetic states, and finally propose a systematic way of identifying the symmetry of the itinerant spin structure by controlling a magnetic impurity with an external magnetic field.

2.4.1 Homogeneous case

As a function of electron filling and temperature three different magnetic ground states were found in the previous section: a single-Q magnetic stripes (MS) state with $\mathbf{M}_2 = 0$ (or the degenerate state $\mathbf{M}_1 = 0$), and the double-Q states charge-spin-density-wave (CSDW) with $\mathbf{M}_1 = \mathbf{M}_2$, and spin-vortex-crystal (SVC) with $\mathbf{M}_1 \perp \mathbf{M}_2$. μSR measurements reported a collinear spin re-orientation of the moments along the c-axis [25] in the region of the tetragonal magnetic phase, and therefore we assume an out-of-plane orientation of the spins in the collinear structures (MS and CSDW) throughout this section. Note however, that none of the results depend on this assumption, since our model does not include spin-orbit coupling; a simple $z \to y$ transformation reproduces the same results with in-plane spins. The spin structures of these three distinct states are shown in Figs. 2.11(c)-(e), respectively. The charge order that develops in the CSDW state exhibits a $\mathbf{Q_1} + \mathbf{Q_2} = (\pi, \pi)$ modulation with larger charge density on the non-magnetic sites (orange circles) than on the magnetic sites (blue circles), as shown in Fig. 2.11(d).

In order to compare the resulting electronic properties of the three SDW states at an equal footing, we fix the temperature to $\kappa_B T = 10$ meV, the electron filling $n = 5.88$, and the interaction parameters $U = 0.95$ eV ($J = U/4$) throughout this section. In this region of parameter space, the CSDW state is the global minimum. The other two magnetic states are local minima, which may be stabilized self-

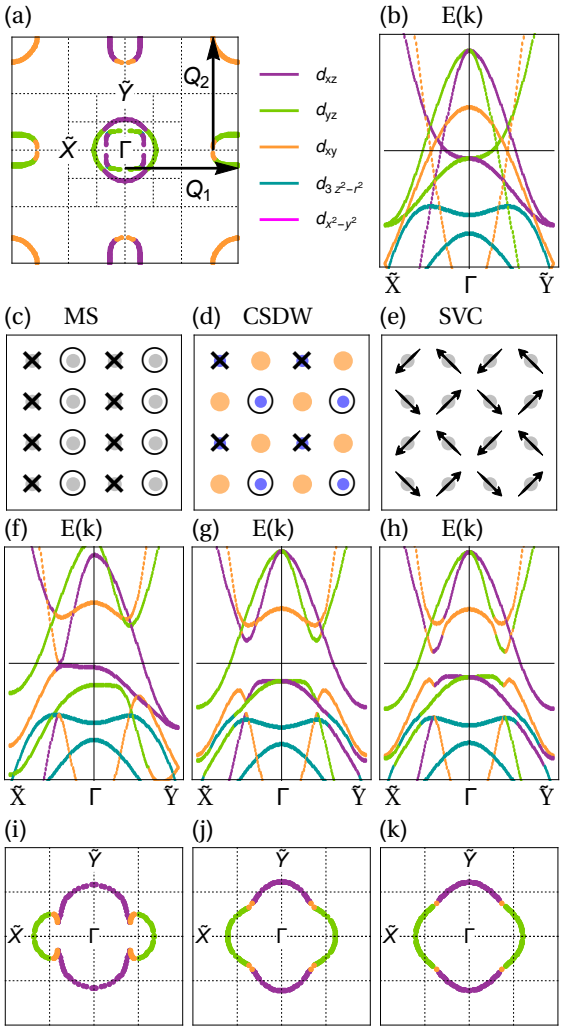

Figure 2.11: (a) Fermi surface of the normal PM state and (b) its band dispersion $E(k)$ along high symmetry lines in the folded BZ (FBZ) obtained by folding the original PM BZ at $\mathbf{Q_1}$ and $\mathbf{Q_2}$. The colors represent the main orbital content, specified in the legend. (c-e) The three SDW states MS with out-of-plane moments (c), CSDW (d) with out-of-plane moments and (π, π) charge order with orange (blue) indicating high (low) electron density n, and SVC (e). The band dispersions (f)-(h) and Fermi surfaces in the FBZ (i)-(k) for the three SDW phases in (c-e).

consistently by applying restrictions to the fields. The point is that, in this section, all three magnetic states are generated from the same paramagnetic (PM) state [Figs. 2.11(a)-(b)]. Figures 2.11(f)-(k) show the reconstructed Fermi surfaces and band structures of the three different SDW states along high symmetry lines in

the folded Brillouin zone (FBZ) ($-\pi/2 < k_x, k_y < \pi/2$). In the single-Q MS state only SDW gaps at momenta connected by the ordering vector $\mathbf{Q_1}$ open, leaving the direction parallel to the stripes metallic, and thus resulting in a C_2 symmetric band dispersion and Fermi surface shown in Figs. 2.11(f) and 2.11(i), respectively. In the double-Q states, the gaps open at momenta connected by either $\mathbf{Q_1}$ or $\mathbf{Q_2}$, which result in two very similar band reconstructions with almost identical Fermi surfaces, as seen by comparison of Figs. 2.11(g)-(h) and Figs. 2.11(j)-(k), despite their very different spin density structures in real space. Below we take advantage of these distinct spin arrangements [Figs. 2.11(c)-(e)], and explore how to use an impurities as a local probe to distinguish between the possible magnetic ground states.

2.4.2 Impurity potential

We start the study of the effects of disorder by the more conventional non-magnetic impurity modelled by the term

$$\mathcal{H}_p = V_p \sum_{\mu\sigma} c^\dagger_{i^*\mu\sigma} c_{i^*\mu\sigma}, \tag{2.10}$$

which adds a local spin-less potential at site i^*. We assume it to be diagonal in orbital space for simplicity. We calculate the projected spin resolved local density of states (LPDOS)

$$N_{\sigma\sigma'}(\mathbf{r},\omega) = -\frac{1}{\pi}\Im(\mathcal{G}_{\sigma\sigma'}(\mathbf{r},\omega)) = \sum_{n,\mu} \frac{u^n_{\mu\sigma}(\mathbf{r}) u^n_{\mu\sigma'}(\mathbf{r})}{\omega - E_n + i\eta}, \tag{2.11}$$

to get the total LDOS $N(\mathbf{r},\omega) = \sum_{\sigma\sigma'} N_{\sigma\sigma'}(\mathbf{r},\omega)$, and the local spin-polarization of the electrons at the Fermi energy ($\omega = 0$), $P^l(\mathbf{r}) = \mathrm{Tr}\left(\tau^l N_{\sigma\sigma'}(\mathbf{r},0)\right)/N(\mathbf{r},0)$. Here, $u^n_{\mu\sigma}(\mathbf{r})$ are the coefficients of the unitary transformation $\hat{c}_{\mu\sigma}(\mathbf{r}) = \sum_n u^n_{\mu\sigma}(\mathbf{r})\hat{\gamma}_n$ that diagonalizes the Hamiltonian $\mathcal{H}^{MF} + \mathcal{H}_p$ describing the magnetic state in the presence of the impurity.

The Figs. 2.12(a)-(c) display the resulting DOS at $\omega = 0$ around a $V_p = 0.5$ eV potential placed in each of the three different magnetic states. In the MS state [Fig. 2.12(a)] the impurity reflects the broken C_4 symmetry of the homogeneous system. Figures 2.12(b) and 2.12(c) show the DOS of the impurity placed in the double-Q collinear and coplanar phases, respectively. In contrast to the single-Q case, tetragonal symmetry is preserved around the potential in both 2Q states as expected. In the CSDW case there is a (π,π) modulation in $N(\mathbf{r})$, arising from the charge order at $\mathbf{q} = \mathbf{Q_1} + \mathbf{Q_2}$ of the homogeneous state. The (π,π) charge

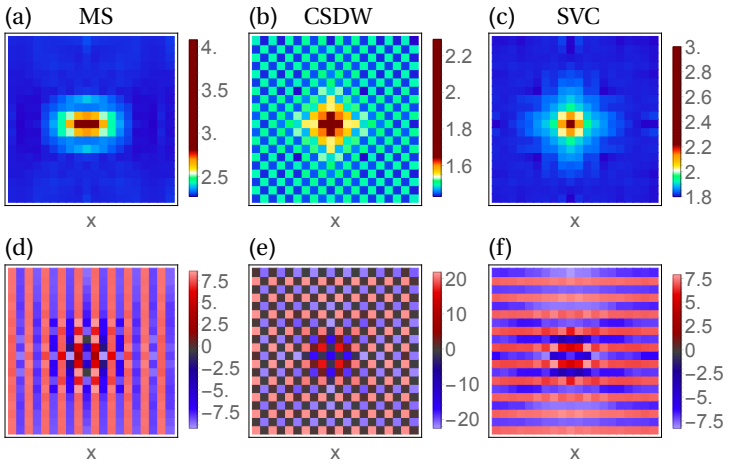

Figure 2.12: (a.c) Total (spin-summed) LDOS $N(r, \omega = 0)$ around a $V_p = 0.5$ eV non-magnetic impurity in the (a) MS, (b) CSDW, and (c) SVC states. (d)-(f) Local spin polarization percent $P^l(\mathbf{r})[\%]$ of the corresponding cases in the upper row with $l = y, z$ and x, respectively.

modulation constitutes a strong STM fingerprint of the CSDW ordered state. The amplitude of this modulation, however, may be too small to be easily detected by tunneling spectroscopy. This implies that there is no simple way to distinguish the SVC and CSDW phases by use of a non-magnetic potential scatterer, since the impurity-induced spectral modulations are qualitatively identical in the two cases as seen by comparison of the central (impurity) regions in Figs. 2.12(b,c).

The local spin polarization $P^l(\mathbf{r})$ gives complementary information that would, in principle, allow one to distinguish between the CSDW and the SVC phases from the spin-polarized tunneling conductance. We show in Figs. 2.12(d)-(f) the polarization at the Fermi level for the relevant spin projection l of the three magnetic states ($P^l(r) \propto M^l(r)$). This property is related to the magnetic contrast measured in a spin-polarized STM (SP-STM) experiment via spin-polarized currents [36]. The polarization of the single-Q state in Fig. 2.12(d) consists of $\mathbf{Q_1}$ modulated stripes for the $l = y$ projection. The $l = x$ and $l = z$ components have no polarization, since $M^l(r) = 0$ in the xz plane. In the case of the collinear CSDW state, the relevant projection is the one parallel to the z axis, where half of the sites appear with alternating polarization and the other half are not polarized, following the spin structure of this state [Fig. 2.11(d)] with an equal superposition of $\mathbf{Q_1}$ and $\mathbf{Q_2}$ parallel spin density waves. As in the MS case, any perpendicular spin projection lacks polarization. Note that the C_4 symmetry is preserved in the polarization pattern around the impurity in this state. The last magnetic state, the SVC, with a coplanar spin structure [Fig. 2.11(e)] has two relevant spin projections,

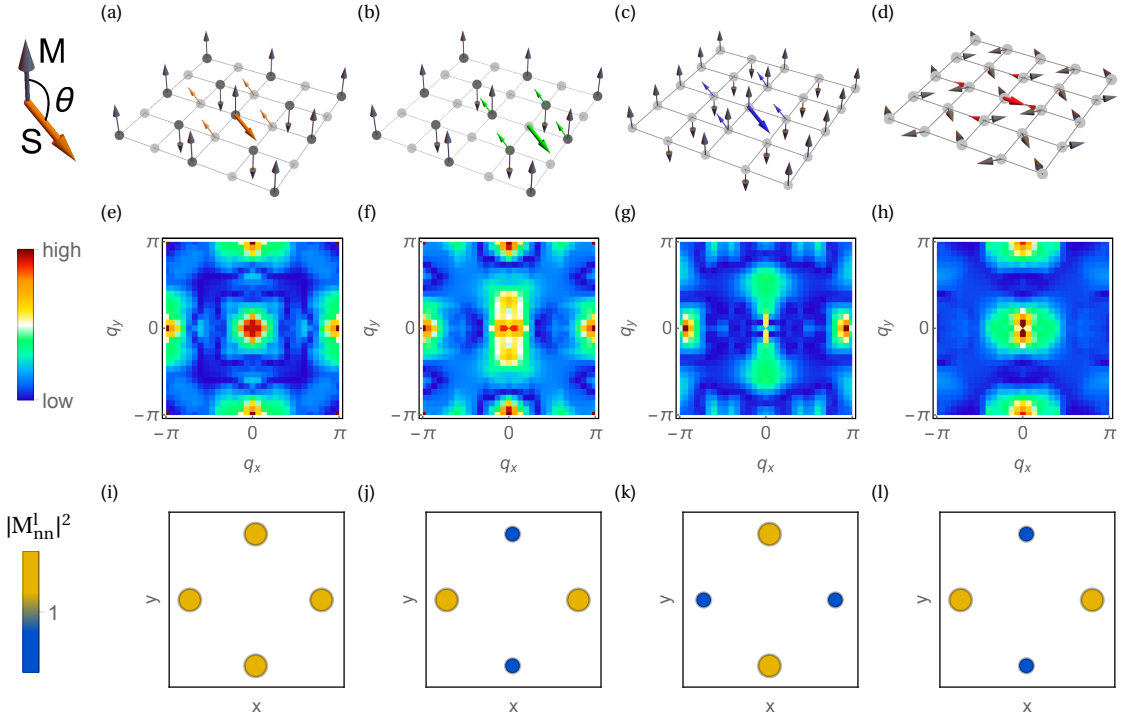

Figure 2.13: Magnetic impurity (colored thick arrow) with $\theta = 3\pi/4$ orientation in a (a) CSDW magnetic site and (b) non-magnetic site, (c) MS site and (d) SVC site. The colored (gray) arrows represent the induced (homogeneous) spin density $\mathbf{M_i^{ind}}$. (e)-(h) The Fourier transformed DOS $N(q, \omega = 0)$ of the previous impurity configurations. The (π, π) peaks of the CSDW state have been removed for clarity. Sketch of the amplitude change in the total moment of the four nearest neighbors $|M^l_{i^*+j}|^2$ in the same four cases for (i) $l = x$ and z, (j) $l = z$ (k) $l = z$ and (l) $l = x$. Yellow (blue) for increased (decreased) spin amplitude compared to the homogeneous case.

the in-plane $l = x$ and $l = y$. $\mathbf{Q_2}$ modulated stripes can be seen in Fig. 2.12(f) for $l = x$, with a local C_2 symmetric polarization pattern around the impurity. The perpendicular $l = y$ polarization (not shown) consists of $\mathbf{Q_1}$ stripes, similar to those in the MS state [Fig. 2.12(d)]. The two 2Q states are now clearly discernible, with distinctive local and global spin-polarization patterns. This should become apparent in, for example, the magnetic contrast measured in a SP-STM experiment.

2.4.3 Impurity moment

We turn now the discussion of how an external impurity moment may be exploited to reveal the ground state magnetic structure, even without the use of spin-polarized STM. A classical magnetic impurity moment is included in the system through the following term in the Hamiltonian

$$\mathcal{H}_j = j \sum_{\mu} \mathbf{S}_{i^*} \cdot \mathbf{M}_{i^*}, \tag{2.12}$$

which adds a spin $\mathbf{S}$ at site i^*, with an angle θ with respect to the spin polarization of the homogeneous state at that site: $\cos\theta \propto \mathbf{S}_{i^*} \cdot \mathbf{M}_{i^*}$, as illustrated in Fig. 2.13(a). The itinerant spins surrounding the impurity interact its moment, resulting in local changes of the spin densities and the DOS. We will focus on the spectral symmetry changes as the impurity rotates, i.e. as a function of the orientation θ, to identify the magnetic structure of the surrounding spins. The orientation of the impurity can be controlled by, for example, an external magnetic field. Mn substituted at the Fe site, for example, was reported to carry a local moment with a Curie-Weiss behavior typical of a paramagnetic moment [16, 17]. We will then assume that the impurity moment orients itself parallel to the applied field, while the itinerant ordered spins are unaffected by it. An appreciable magneto-crystalline anisotropy prevents the spins of the long-range ordered magnetic SDW state from aligning with the external field [37].

In the CSDW state there are four inequivalent sites (quadrupled unit cell) to place an impurity, two magnetic ($\mathbf{M}_{i^*} \neq 0$) and two non-magnetic ($\mathbf{M}_{i^*} = 0$) sites, illustrated in Figs. 2.13(a) and (b), respectively. The gray arrows represent the spin density of the conduction electrons of the homogeneous system (free of impurities), and the thick colored arrow indicates the moment of the impurity $\mathbf{S}_{i^*}$. The induced spin density on the nearest sites is illustrated by the four arrows of the same color (anti-parallel to the impurity spin). In our calculation the induced polarization involves a cluster of sites surrounding the impurity moment, but for the symmetry arguments we will be using below, it is enough to focus on the effect of the nearest neighbors where the effect is largest.

The sum of the induced and the homogeneous spin densities yields the new spin density in the presence of the impurity. We show in Fig. 2.13(e) the Fourier transformed DOS, $N(q, \omega = 0)$, of the case displayed in Fig. 2.13(a). Clearly, the C_4 symmetry of the pristine CSDW state is preserved. If the same impurity moment is placed at a non-magnetic site, however, as illustrated in Fig. 2.13(b) by the green thick arrow, $N(q, \omega)$ becomes C_2 symmetric as seen in Fig. 2.13(f). This symmetry breaking can be understood by considering the total spin density in the presence of the impurity (i.e. adding the green and gray arrows). The z projection amplitude of the total moment on the four neighboring sites is unequal; it has

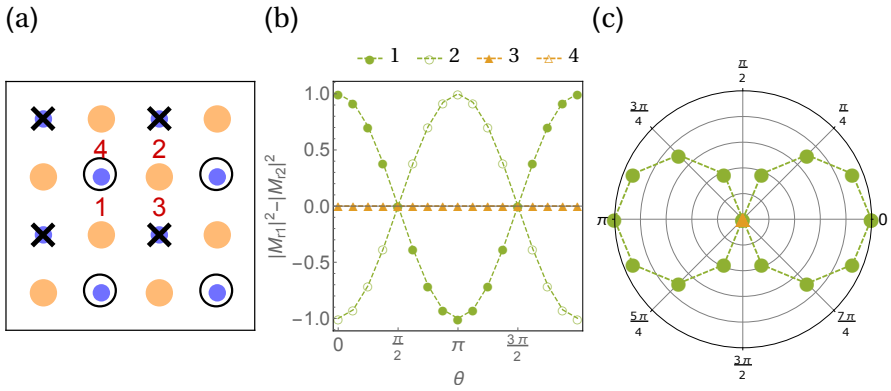

Figure 2.14: Difference between the moment amplitudes at the neighboring sites as a function of θ (equation (2.13)) in the CSDW state. (a) Four inequivalent sites 1,2,3 and 4. (b) $|\mathbf{M}_{r_1}|^2 - |\mathbf{M}_{r_2}|^2$ for the inequivalent sites as specified in (a). (f) Polar plot of the absolute value of the total change $|\mathbf{M}_{r_1}|^2 - |\mathbf{M}_{r_2}|^2$ for sites 1 and 2 (green) and sites 3 and 4 (orange). θ is illustrated in figure 2.13(a).

been reduced on the two sites along the y axis and enhanced on the sites along the x axis. This change of $|m^z_{i^*+j}|$ with $j = \pm\,\hat{\mathrm{x}}, \pm\hat{\mathrm{y}}$ is shown in Fig. 2.13(j). If the impurity is placed at a magnetic site though [Fig. 2.13(a)], the amplitudes of the total spin density on the four neighbors are equal for both the z and x projections, as illustrated in Fig. 2.13(i). The spectral symmetry is in fact tetragonal for all possible orientations of the impurity in the CSDW phase, as long as the impurity moment is placed at a magnetic site. In the case of the non-magnetic site on the other hand, only in the special case of the impurity moment lying in the xy plane, i.e. perpendicular to the ordered moment of the conduction electrons, is the C_4 symmetry preserved. These properties simply reflect the fact that the total DOS measures the spectral composition of the charge density, which is coupled by symmetry only to the magnetization density squared, and therefore only the final amplitude of the spin density at the nearest-neighbor (nn) sites matters.

We can use this result to understand and predict the evolution of the spectral symmetry in all four inequivalent sites as a function of the orientation of the moment θ (set by the external field), without having to calculate the LDOS. The difference between the moment amplitudes at the neighboring sites $r_1 = i^* + \hat{x}$ and $r_2 = i^* + \hat{y}$, which determines the symmetry breaking of the spectral features, is given by

$$|\mathbf{M}_{r_1}|^2 - |\mathbf{M}_{r_2}|^2 = -2|\mathbf{M}^{ind}_{nn}| \left[\left(M^{0x}_{r_1} - M^{0x}_{r_2}\right)\sin\theta + \left(M^{0z}_{r_1} - M^{0z}_{r_2}\right)\cos\theta\right]. \quad (2.13)$$

Here $\mathbf{M}_{r_i} = \mathbf{M}^0_{r_i} + \mathbf{M}^{ind}_{r_i}$ is the total moment at site r_i, $\mathbf{M}^{ind}_{nn}$ is the moment induced

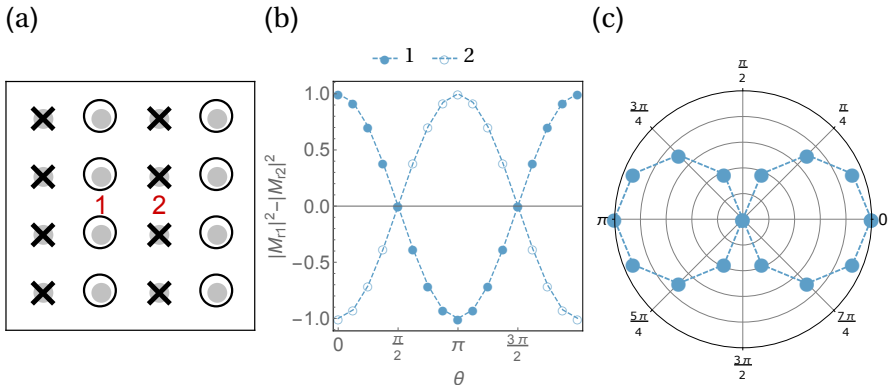

Figure 2.15: Difference between the moment amplitudes at the neighboring sites as a function of θ (equation (2.13)) in the MS state. (a) Two inequivalent sites 1 and 2. (b) $|\mathbf{M}_{r_1}|^2 - |\mathbf{M}_{r_2}|^2$ for the inequivalent sites as specified in (a). (f) Polar plot of the absolute value of the total change $|\mathbf{M}_{r_1}|^2 - |\mathbf{M}_{r_2}|^2$ for sites 1 and 2 (blue).

by the impurity at the nearest neighbors r_1 and r_2, and $M^{0l}_{r_i}$ is the projection along the l axis ($l = x, z$) of the homogeneous moment at r_i (before the impurity is introduced). Because the CSDW state is a collinear structure, i.e. $M^{0x}_r = 0$ for all sites, equation (2.13) reduces to a simple cosine function. Moreover, if the impurity is in a magnetic site (sites 3 and 4 in figure 2.14(a)), one immediately sees that because the spin density is zero at the neighboring sites, $M^{0z}_{r_1} = M^{0z}_{r_2} = 0$, the tetragonal symmetry is preserved for any orientation, i.e. $|\mathbf{M}_{r_1}|^2 = |\mathbf{M}_{r_2}|^2$. If the impurity moment is in a non-magnetic site on the other hand, then $M^{0z}_{r_1} = -M^{0z}_{r_2}$ and the difference between the total amplitudes becomes $|\mathbf{M}_{r_1}|^2 - |\mathbf{M}_{r_2}|^2 = -2|\mathbf{M}^{ind}_{nn}|M^{0z}_{r_1}\cos\theta$. The evolution of this parameter as a function of θ, which reflects the tetragonal symmetry breaking of the spectral signatures, is shown in figure 2.14(b) for the four inequivalent sites, with the particular site specified in figure 2.14(a). When the impurity is placed on the non-magnetic sites 1 and 2 the difference is non-zero for all θ (except when the impurity moment is perpendicular to the itinerant spins at $\theta = \pi/2$), and thus the tetragonal symmetry is broken. The symmetry breaking measured in the LDOS is proportional to the absolute value of equation (2.13) and therefore these two sites have identical contributions as can be seen in the polar plot in figure 2.14(c). This plot emphasizes the directional dependence of the spectral symmetry in the xz plane, with largest radius along the z axis and zero amplitude perpendicular to it.

We turn now to the other collinear state, the single-Q MS, which has two inequivalent sites (doubled unit cell). An example is shown in Fig. 2.13(c) for an

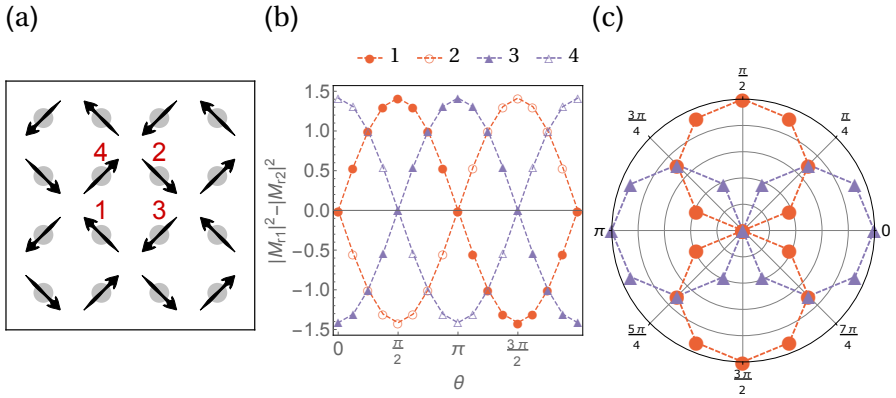

Figure 2.16: Difference between the moment amplitudes at the neighboring sites as a function of θ (equation (2.13)) in the SVC state. (a) Four inequivalent sites 1,2,3 and 4. (b) $|\mathbf{M}_{r_1}|^2 - |\mathbf{M}_{r_2}|^2$ for the inequivalent sites as specified in (a). (f) Polar plot of the absolute value of the total change $|\mathbf{M}_{r_1}|^2 - |\mathbf{M}_{r_2}|^2$ for sites 1 and 2 (red) and sites 3 and 4 (purple).

impurity with $\theta = 3\pi/4$ orientation, and the corresponding C_2 symmetric $N(q, \omega = 0)$ is displayed in Fig. 2.13(g). In this case the inequivalent change takes also place in the spin projection along the z axis $|M^z_{i^*+j}|$ of the four neighboring sites, shown in Fig. 2.13(k). Equation (2.13) reduces to $|\mathbf{M}_{r_1}|^2 - |\mathbf{M}_{r_2}|^2 = -2|\mathbf{M}^{ind}_{nn}|M^{0z}_{r_1}\cos\theta$ in the MS state, where we have used the same $M^{0z}_{r_1} = -M^{0z}_{r_2}$ argument as before. The result for the two inequivalent sites is shown in figure 2.15(b). Taking the absolute value, results in the same symmetry breaking θ dependence for both sites, as can be seen in figure 2.15(c). In the MS state all inequivalent sites give rise to the same symmetry breaking θ dependence. This is in contrast to what was found in the CSDW state, where only half of the sites exhibited this (identical) θ dependence, and the other half were oblivious to the external field. STM measurements of LDOS around several isolated moments can then distinguish between these two states.

Finally we discuss the case of a magnetic impurity in the coplanar SVC phase. One of its four inequivalent sites is shown in figures 2.13(d), with the calculated LDOS in figure 2.13(h). Again, the C_2 symmetric spectral features can be connected to the different moment amplitudes in the nearest-neighbors, as illustrated in figure 2.13(l). Equation (2.13) has now contributions from both x and y projections, in agreement with the coplanar structure of this state: $|\mathbf{M}_{r_1}|^2 - |\mathbf{M}_{r_2}|^2 = -2|\mathbf{M}^{ind}_{nn}|M^{0x}_{r_1}(\sin\theta + \cos\theta)$, which follows from the relations $M^{0l}_{r_1} = -M^{0l}_{r_2}$ for $l =$ x and y. The angular evolution of the four inequivalent sites, in the xy plane for this state, is shown in figure 2.16(b). Contrary to what was found in the other 2Q

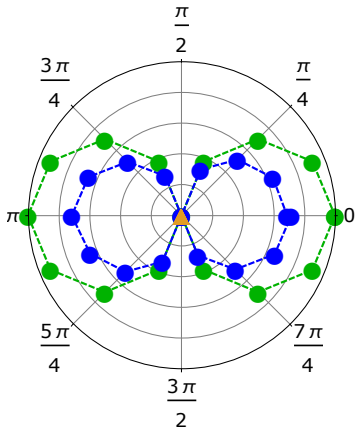

Figure 2.17: Spectral symmetry breaking parameter $\delta_{C_2}(\omega = 0)$ as a function of θ calculated at a magnetic site in the CSDW state (green), a non-magnetic site in the CSDW state (orange) and a site in the MS state (blue).

state, the tetragonal symmetry is broken at all inequivalent sites. The final absolute value of the amplitude, shown in figure 2.16(c), exhibits two perpendicular signals, arising from sites with perpendicular moment orientations (1, 2 and 3, 4).

In order to quantify the evolution of the spectral symmetry as the impurity rotates from the calculated LDOS, we introduce the parameter

$$\delta_{C_2}(\omega) = \sum_r \frac{N(\mathbf{r},\omega) - N(R\mathbf{r},\omega)}{N(\mathbf{r},\omega) + N(R\mathbf{r},\omega)}, \tag{2.14}$$

which measures the breaking of the C_4 symmetry. Here R denotes a $\pi/2$ rotation operation. The evolution of this parameter at $\omega = 0$ for the three states, is in excellent agreement with the simple argument of the change in amplitudes described by of equation (2.13). Figure 2.17 shows the evolution of δ_{C_2} from the calculated LDOS at three different sites in the CSDW and MS as a function of θ. The difference in amplitude is related to the different M^{ind} in the CSDW and MS states, which is related to the eigenvalues and eigenvectors of each state.

We summarize below the main conclusions for STM measurements of LDOS around magnetic impurities in the CSDW, MS and SVC states with an external field:

- In the CSDW state, two distinct signals will be measured [figure 2.14(c)], some single-impurities show C_4 symmetric spectral features for all external field orientations (orange), while the signal will be C_2 symmetric and show a strong field orientation dependence around other single-impurities (green).

- In the MS state, there is only one type of spectral signal around single-impurities [figure 2.15(c)], i.e. LDOS measurements around different impurities exhibit the same C_2 symmetric field evolution.
- In the SVC state, there are two perpendicular field orientation evolutions [figure 2.16(c)].

2.4.4 Conclusions

In summary, we have proposed to use tunneling spectroscopy to directly distinguish between nearly degenerate (in energy) but symmetry-distinct magnetic ground states of itinerant magnetic systems. We have focused on a current case of controversy related to iron-based superconductors but the method should apply generally to other systems as well. Our main results are that while spin-polarized STM can be used to map out the magnetic structure of the long-range ordered phase, one may also apply standard (non-spin-polarized) tunneling conductance in the vicinity of a magnetic impurity moment, whose orientation can be controlled by an external magnetic field, to determine the structure of the host magnetism.

This technique might be helpful when more conventional probes like neutron scattering are not able to distinguish between different magnetic phases. This is the case of the single-Q MS and the double-Q phases in Fe-based superconductors. Because the samples form twin domains, both $\mathbf{Q}_1$ and $\mathbf{Q}_2$ peaks are observed in the magnetic structure factor measured by neutron experiments, and one needs to detwin the sample (a non-trivial technique) or combine it with other probes. One can use the advantage of local probes like STM, which can focus on a particular domain, and make measurements in free standing samples.

Chapter 3

Enhancement of magnetic stripe order from the interaction between conduction electrons and magnetic impurities

Most of the material in this chapter has been published in Phys. Rev. Lett. 113, 067002 (2014).

3.1 Introduction

In this chapter we extend the study of magnetism in Fe-based superconductors by exploring the physics of magnetic disorder. The relevant spin ordered states in these materials were discussed in chapter 2, with particular emphasis on the recently discovered magnetic tetragonal phases. Their existence has been taken as a direct evidence for the itinerant character of the magnetism, and the primary role played by magnetic fluctuations in these materials, and argues against the localized spin scenario with (ferro-)orbital order as the driving instability.

For the pnictides, the above issues have largely focused on hole-doped 122 compounds where particularly $Ba(Fe_{1-x}Mn_x)_2As_2$ constitutes an interesting case in point. The chemical doping takes place *in the plane*, substituting Fe for Mn, as opposed to the 'clean' cases with out-of-plane dopants at the alkaline earth metal sites, e.g substituting Ba for K or Na. For Mn doped Ba-122, Kim *et al.*[12] found that the structural phase transition disappears at a critical amount of Mn ($x_c \sim 0.1$) whereas the $(\pi, 0), (0, \pi) \equiv \mathbf{Q}_{stripe}$ magnetic order remains. X-ray measurements of the structural distortion δ, shown in figure 3.1(a) (red triangles), reveal a collapse of the distortion at $x \sim 0.1$. Remarkably, at higher concentra-

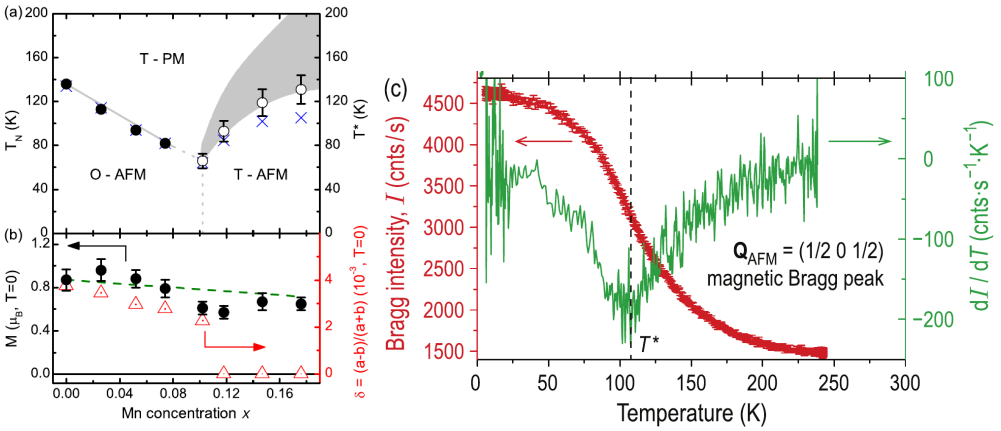

Figure 3.1: Characterization of the $\mathbf{Q}_{stripe}$ magnetic transition on $Ba(Fe_{1-x}Mn_x)_2As_2$. Left: Antiferromagnetic stripe ordering in the absence of structural distortion above a critical concentration, $x_c \sim 0.1$ [12]. Right: Temperature dependence of the elastic neutron scattering intensity at the magnetic Bragg peak. Smeared transition with an onset $\sim$ 100 K above the T_N^0 of the parent compound for $x = 0.12 > x_c$ [18].

tions than x_c the magnetic order exhibits a new high-temperature component as seen by the persistence of a broad $\mathbf{Q}_{stripe}$ magnetic Bragg peak well in excess of the Néel temperature T_N of the lower doped $x < x_c$ samples, represented by the shaded region in figure 3.1(a). In addition, inelastic neutron scattering revealed that Mn ions induce short-range quasi-elastic spin scattering at $(\pi, \pi) \equiv \mathbf{Q}_{Néel}$ [figure 3.2(a)], which persists at all measured T [figure 3.2(c)], and coexists with the long-range ordered $\mathbf{Q}_{stripe}$ phase at low T.[15] The presence of local antiferromagnetic (AF) correlations induced by Mn ions have also been detected by nuclear magnetic resonance (NMR).[16, 17] These studies, which found that Mn does not dope the system, therefore suggest that Mn locally nucleate magnetic moments consistent with $\mathbf{Q}_{Néel}$ structure.

More recently, Inosov *et al.*[18] mapped out a very complete phase diagram of $Ba(Fe_{1-x}Mn_x)_2As_2$ in the range $0 < x < 0.12$. As shown in figure 3.1(b), the existence of the novel high-T stripe magnetic phase at $x > x_c$ was confirmed by these studies. However, by combining neutron data with muon spin relaxation (μSR) and NMR measurements, they proposed an inhomogeneous scenario where Mn ions act as magnetic impurities that induce $(\pi, 0)$ magnetic rare regions already above T_N^0 of the parent compound, with a volume fraction of these rare regions growing continuously with decreasing T. In contrast to Ref. [12], a finite orthorhombic distortion, most likely associated with the stripe-like magnetic rare

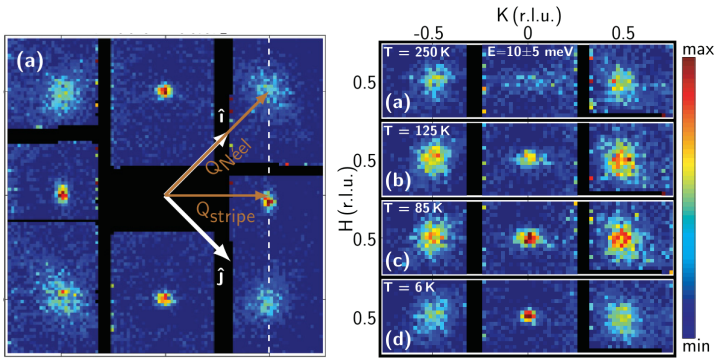

Figure 3.2: Spin fluctuations at two different wavevectors. Right: Quasi-elastic spin scattering at both $\mathbf{Q}_{stripe}$ and $\mathbf{Q}_{N\acute{e}el}$ wavevectors at $x = 0.07 < x_c$ and $T << T_N$. Left: Weakly temperature dependent spin fluctuations at $\mathbf{Q}_{N\acute{e}el}$, persisting at all measured T. From [15].

regions, was shown to coexist with regions of tetragonal lattice symmetry.

To help resolve the controversy of $Ba(Fe_{1-x}Mn_x)_2As_2$, and understand, more generally, the physics of magnetic disorder in iron pnictides, microscopic theoretical model calculations are highly called for. Minimal requirements of such a theoretical description include being able to 1) explain how magnetic impurities can generate long-range magnetic $\mathbf{Q}_{stripe}$ order at high $T > T_N^0$, 2) explain why this happens only above a certain critical concentration of magnetic disorder, 3) explain the presence of diffusive $\mathbf{Q}_{N\acute{e}el}$ magnetic scattering at low concentrations, and 4) explain why the orthorhombicity appears absent at high enough impurity concentrations. In addition, the spatial modulations evidenced by the data of Ref. [18] points to the importance of a real-space approach and a careful study of cooperative impurity effects in these systems.

Here, we provide such a microscopic real-space description of magnetic disorder relevant to iron pnictides. We use a realistic five-band model with standard onsite Coulomb repulsion (described in section 2.2) to study the induced magnetic order nucleated by magnetic impurities. It is found that magnetic impurities exhibit a $\mathbf{Q}_{N\acute{e}el}$ magnetic structure close to its core, as well as longer-ranged magnetic tails of $\mathbf{Q}_{stripe}$ modulations which may overlap with neighboring impurities and induce long-range $\mathbf{Q}_{stripe}$ magnetic order even above T_N^0 of the clean system. This cooperative effect only takes place when the length scale of the magnetic impurity tails is comparable to the average inter-impurity distance, yielding a natural explanation for the detected critical concentration x_c. In fact, as will be shown in detail below, all four criteria above are contained within our model. At higher Mn concentrations we predict that the induced $\mathbf{Q}_{stripe}$ order vanishes because there is

no room to host this order, and only the $\mathbf{Q}_{N\acute{e}el}$ magnetic structure remains. This crossover happens well before reaching the clean system $BaMn_2As_2$ which is known to exhibit $\mathbf{Q}_{N\acute{e}el}$ order.[38]

The study presented here provides an alternative scenario for the magnetism of $Ba(Fe_{1-x}Mn_x)_2As_2$ as compared to previous Landau models assuming homogeneous phases [39, 7, 8, 9, 10, 14] and analysis of magnetism in 'pristine' systems presented in chapter 2. We note that this problem constitutes an interesting example of the general problem of Ruderman-Kittel-Kasuya-Yosida (RKKY) exchange interactions in multi-orbital nested systems at the brink of an instability,[40, 41] and the physics of AF rare regions in itinerant systems.[42] In the standard case of magnetic impurities in metallic hosts, the conduction elections are integrated out, resulting in the RKKY effective exchange interaction between the impurity spins, which may lead to interesting spin-glass behavior.[43, 44] Here, however, we do not integrate out the itinerant electrons since their response to the magnetic impurities is crucial for explaining the measurements discussed above.

3.2 Magnetic impurities in a paramagnetic host

Mn ions in $BaFe_2As_2$ are known to carry a large local magnetic moment[16, 17, 45] $\mathbf{S}$ which interacts with the spin density of the itinerant electrons

$$\mathcal{H}_{imp} = J_0 \sum_{\{\mathbf{i}^*\}\mu\sigma\sigma'} \mathbf{S}_{\mathbf{i}^*} \cdot (c^\dagger_{\mathbf{i}^*\mu\sigma} \boldsymbol{\sigma}_{\sigma\sigma'} c_{\mathbf{i}^*\mu\sigma'}), \tag{3.1}$$

where $\{\mathbf{i}^*\}$ denotes the sub-set of lattice sites containing impurity spins. In the following we treat Eq. (3.1) in the classical limit, and assume the absence of any orbital dependence in Eq. (3.1) for simplicity. In this limit, $\mathcal{H}_{imp}$ reduces to that of a spin dependent potential.[46, 47]

We continue with the *itinerant* approach and use the following five-orbital Hamiltonian to describe magnetic impurities in a metallic host,

$$\mathcal{H} = \mathcal{H}_0 + \mathcal{H}_{int} + \mathcal{H}_{imp}, \tag{3.2}$$

with $\mathcal{H}_0$ the kinetic part and $\mathcal{H}_{int}$ the on-site Coulomb interactions described in chapter 2. The chemical potential is adjusted to yield a fixed doping level of $\delta = \langle n \rangle - 6.0 = 0$ since Mn does not dope the system.[16, 17, 48] In this work we additionally take $U = 1.2$ eV and $J = U/6$, which leads to an ordered moment of the right magnitude relevant for $BaFe_2As_2$. We restrict the study to collinear magnetic order since this is the lowest energy state at the undoped level. After a mean-field decoupling of the interactions $\mathcal{H}_{int}$, we solve the eigenvalue problem $\sum_{\mathbf{j}\nu} H^{\mu\nu}_{\mathbf{ij}\sigma} u^n_{\mathbf{j}\nu} = E_n u^n_{\mathbf{i}\mu}$, where

$$H^{\mu\nu}_{\mathbf{ij}\sigma} = t^{\mu\nu}_{\mathbf{ij}} + \delta_{\mathbf{ij}}\delta_{\mu\nu}[-\mu_0 + \delta_{\mathbf{ii}^*} J_0 S^z_{\mathbf{i}^*\sigma} + U\langle n_{\mathbf{i}\mu\bar{\sigma}}\rangle \tag{3.3}$$

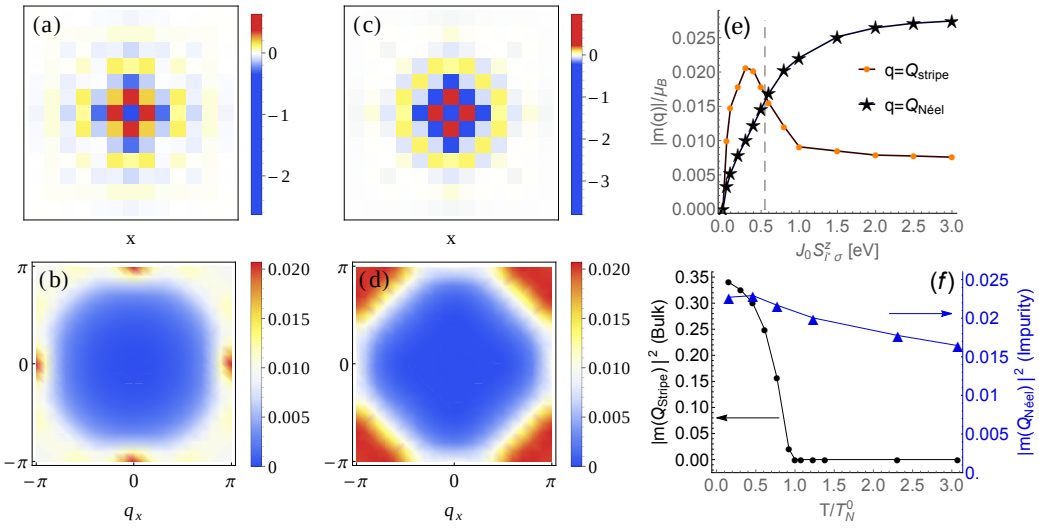

Figure 3.3: Real space magnetization $m(\mathbf{r})$ for (a) $J_0 S^z_{\mathbf{i}^*\sigma} = 0.3$ eV (weak) and (c) $J_0 S^z_{\mathbf{i}^*\sigma} = 0.8$ eV (strong) impurities. (b) and (d) $|m(\mathbf{q})|/\mu_B$ signal for the impurities in (a) and (c), respectively. (e) $|m(\mathbf{q})|/\mu_B$ at $\mathbf{q} = \mathbf{Q}_{stripe}$ (orange dots) and $\mathbf{q} = \mathbf{Q}_{Néel}$ (black stars) as a function of impurity strength. The gray dashed line divides the weak and strong impurity regimes (see text). $T/T_N^0 = 1.2$ for all these panels. (f) Temperature dependence of the intensity $|m(\mathbf{q})|^2/\mu_B^2$ at $\mathbf{Q}_{stripe}$ for the homogeneous system (black dots) and at $\mathbf{Q}_{Néel}$ for the strong impurity (blue triangles).

$$+ \sum_{\mu' \neq \mu} (U' \langle n_{\mathbf{i}\mu'\bar{\sigma}} \rangle + (U' - J) \langle n_{\mathbf{i}\mu'\sigma} \rangle)],$$

on $N_x \times N_y$ lattices with self-consistently obtained densities $\langle n_{\mathbf{i}\mu\sigma} \rangle = \sum_n |u^n_{\mathbf{i}\mu\sigma}|^2 f(E_{n\sigma})$, and $f(E)$ denoting the Fermi function.

When multiple impurities are included at different randomly chosen sites, the relative signs of the individual impurity spins $S^z_{\mathbf{i}^*\sigma}$ become important and are obtained by minimizing the free energy $\mathcal{F} = \mathcal{U} - T\mathcal{S}$. Here the internal energy $\mathcal{U} = \langle \mathcal{H}^{MF} \rangle = \langle \mathcal{H}_0 \rangle + \langle \mathcal{H}^{MF}_{int} \rangle + \langle \mathcal{H}_{imp} \rangle$, and the entropy $\mathcal{S}$ is obtained from the expression

$$\mathcal{S} = -k_B \sum_n [f(E_n) \ln f(E_n) + f(-E_n) \ln f(-E_n)] \,. \tag{3.4}$$

3.3 Single-impurity

We start the discussion with the single-impurity effects above the homogeneous ordering temperature T_N^0. The spin polarization of the surrounding electrons in-

duced by a weak impurity is shown in Fig. 3.3(a). Its structure can be mainly described by $\mathbf{Q}_1 = (\pi, 0)$ and $\mathbf{Q}_2 = (0, \pi)$ stripe-type order along the x and y directions, respectively. The amplitude of the spatial oscillations rapidly weakens and vanishes at a scale of $\sim 5 - 7$ lattice sites. The Fourier transform of the induced magnetization $|m(\mathbf{q})|$ shown in Fig. 3.3(b) exhibits sharp peaks at the $\mathbf{Q}_{stripe}$ wavevectors, arising from the real-space stripes. This local response of weak impurities simply reflects the structure of the spin susceptibility of the clean system, as expected from linear response theory. Large impurity-induced regions of local magnetization have also been recently discussed in the context of excess Fe in $Fe_{1+y}Te_{0.62}Se_{0.38}$.[49] Upon increasing the magnetic impurity potential, however, the local response shown in Fig. 3.3(c,d) exhibits mainly $\mathbf{Q}_{N\acute{e}el}$ structure in the vicinity of the defect, and a weakened stripe order in the farther tails of the induced spin polarization. The broad $\mathbf{Q}_{N\acute{e}el}$ peak indicates shorter-range (π, π) order compared to the $\mathbf{Q}_{stripe}$ peaks characteristic of weak impurities [Fig. 3.3(b)]. The full evolution of the local response is presented in Fig. 3.3(e) showing the intensity of both the $\mathbf{Q}_{stripe}$ and $\mathbf{Q}_{N\acute{e}el}$ wavevectors as a function of impurity strength, revealing the crossover from $\mathbf{Q}_{stripe}$ order to mainly $\mathbf{Q}_{N\acute{e}el}$ order in the strong impurity limit. Note, however, that even the very strong impurities exhibit some weight at $\mathbf{Q}_{stripe}$ from surviving weak stripelike modulations in the tails of the polarization cloud. Finally, Fig. 3.3(f) shows the T dependence of the induced polarization of a strong impurity at $\mathbf{Q}_{N\acute{e}el}$ compared to the $\mathbf{Q}_{stripe}$ amplitude of the homogeneous system. The impurity nucleates a checkerboard polarization which is weakly T-dependent and persists well beyond T_N^0 consistent with μSR,[18] NMR,[16] and neutron scattering[15] [Fig. 3.2(b)].

3.4 Multiple impurities: order-from-disorder

We now turn to the many-impurity case. The presence of both $\mathbf{Q}_{N\acute{e}el}$ and $\mathbf{Q}_{stripe}$ magnetization induced by strong impurities makes them relevant from an experimental point of view [Fig. 3.2]. Below, we focus therefore on the $J_0 S^z_{\mathbf{i}^*\sigma} = \pm 0.8$ eV defects [Fig. 3.3(c,d)]. Consider first the dilute case of 3% disorder. Figs. 3.4(a,c,e) show examples of the resulting real-space magnetization and Figs. 3.4(b,d,f) display the corresponding configuration-averaged $|m(\mathbf{q})|^2$. Above T_N^0 [Fig. 3.4(b)] the total signal in q-space is peaked around $\mathbf{Q}_{N\acute{e}el}$, similar to the single-impurity result for this kind of defect, whereas below T_N^0 [Fig. 3.4(d,f)] the broad $\mathbf{Q}_{N\acute{e}el}$ scattering coexists with the sharp $\mathbf{Q}_{stripe}$ order in agreement with experiments [Fig. 3.2(a)].[15] Now, consider a doubling of the impurity concentration as shown in Fig. 3.4(g-l). Below T_N^0 [Fig. 3.4(j,l)] the same dual nature is evident of sharp $\mathbf{Q}_{stripe}$ and broad $\mathbf{Q}_{N\acute{e}el}$ scattering as in the dilute case. Notably, however, above T_N^0 [Fig. 3.4(h)] the response is now dominated by sharp $\mathbf{Q}_{stripe}$ order as opposed

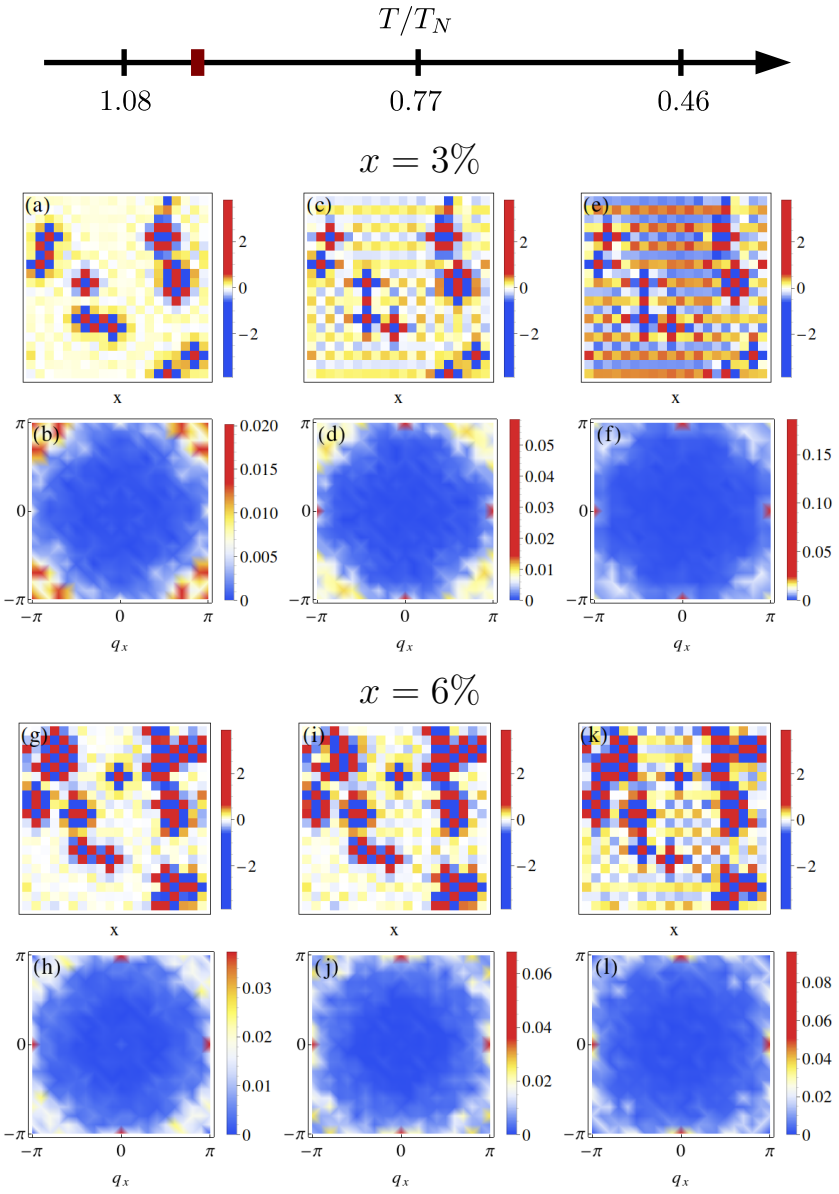

Figure 3.4: (a,c,e) Examples of $m(\mathbf{r})/\mu_B$ for a configuration with $x = 3.0\%$ strong impurities ($J_0 S^z_{\mathbf{i}^*\sigma} = \pm 0.8$ eV) at (a) $T/T_N^0 = 1.08$, (c) 0.77 and (e) 0.46. (b,d,f) Corresponding $|m(\mathbf{q})|^2/\mu_B^2$ after averaging over eight distinct configurations with the same concentration. (g-l) The same as shown in (a-f) for a larger concentration of $x = 6.0\%$.

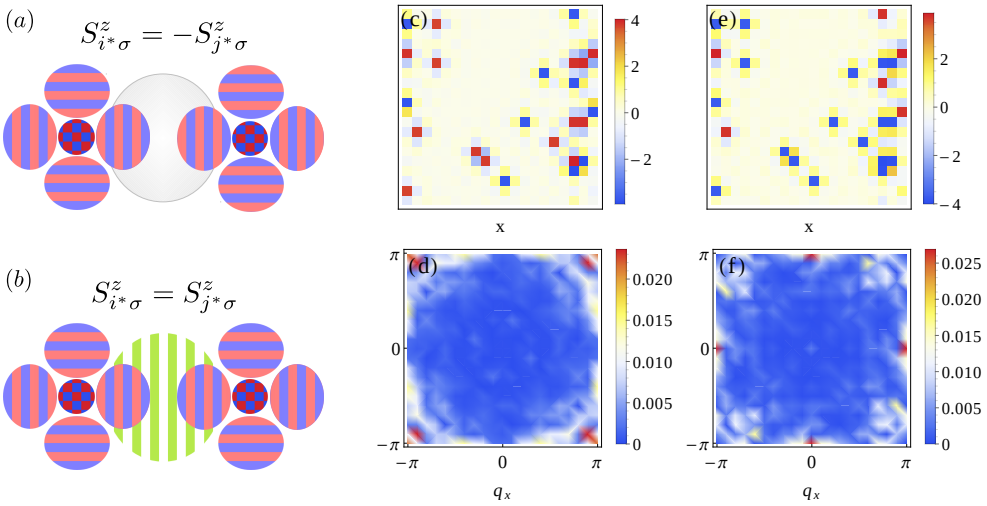

Figure 3.5: (a,b) Illustration of the order-by-disorder caused by constructive interference between two magnetic impurities; (a) destructive and (b) constructive interference. In both cases the impurities are separated by an even number of lattice sites. (c-f) Comparison of the magnetization in the case of "quenched" (a,b) impurity spins versus the "relaxed" case obtained by energy minimisation caused by allowed flipping of the impurity spins (c,d).

to the result shown in Fig. 3.4(b). The cooperative impurity effect yielding this long-range $\mathbf{Q}_{stripe}$ order is remarkable and not obvious from the corresponding real-space magnetization in Fig. 3.4(g). The origin of a critical Mn concentration x_c needed for the emergence of high-T $\mathbf{Q}_{stripe}$ order is evident within the present scenario; for the cooperative impurity effect to be relevant, the inter-impurity distance must be comparable to the size of the induced spin polarization cloud. The critical Mn concentration reported in Refs. [12] and [18] is $x_c \sim 0.1$ implying that the magnetic $\mathbf{Q}_{stripe}$ tails induced by Mn in the real systems is slightly shorter ranged than for the parameters used in Fig. 3.4.

To understand this cooperative behavior let us focus first on the simpler situation of two strong impurities at sites $\mathbf{i}^*$ and $\mathbf{j}^*$. Figure 3.5(a,b) illustrate two cases where the spins are separated by an even number of lattice sites. As seen, the polarization around each impurity spin essentially consists of a strong short range Néel order and four weaker stripe type tails, as explained for Fig. 3.3(c). In Fig. 3.5(b) $S^z_{\mathbf{i}^*\sigma} = S^z_{\mathbf{j}^*\sigma}$, there is constructive interference of their $\mathbf{Q}_{stripe}$ spin polarization, and magnetic stripes are induced in the surrounding conduction electrons. The opposite case of $S^z_{\mathbf{i}^*\sigma} = -S^z_{\mathbf{j}^*\sigma}$ with destructive interference is shown in Fig. 3.5(a). Importantly, the configuration with the lowest free energy $\mathcal{F}$ is

the one with *constructive* interference of the spin-polarized electrons capable of generating inter-impurity regions of $\mathbf{Q}_{stripe}$ order. For impurity spins separated by an odd number of sites the same result applies; the case of constructive magnetization interference is favorable (obtained now by anti-aligning the spins). In the corresponding many-impurity case, the importance of optimizing the impurity spin orientations is shown in Figs. 3.5(c-f). Here we compare the case of randomly chosen spin orientations (quenched case) [Figs. 3.5(c,d)] with the lower energy annealed case where the impurity spins are allowed to orient themselves favorably to the spin polarization of their neighbors [Figs. 3.5(e,f)]. Evidently, the induced $\mathbf{Q}_{stripe}$ order exists only in the latter situation.

The results shown in Figs. 3.4-3.5 constitute an example of order-from-disorder. It is qualitatively similar to the interactions between impurities in quantum spin chains which are non-frustrating because of the freedom of impurity spins to reorient themselves according to the neighboring AF induced impurity clouds and thereby lower the exchange energy.[50] A similar scenario has also been proposed for the spin-glass phase of the cuprates, where non-magnetic dopant-induced AF clouds overlap and form a network of quasi-long-range (π, π) order.[51]

In order to shed light on the constructive polarization, and its connection to the exchange coupling between impurities, we explore the effect of correlations in the cooperative behavior. We focus again on the simpler two-impurity system and map out the difference in the free-energy of the parallel and anti-parallel spin configurations, i.e. the exchange interaction $I(\mathbf{r}) = \mathcal{F}_{\uparrow\downarrow} - \mathcal{F}_{\uparrow\uparrow}$, as a function of the distance between the impurities $\mathbf{r} = (x, y)$. Figure 3.6(a) shows the resulting real space map of $I(\mathbf{r})$ as the second impurity is moved around in the region $(0, 0) < (x, y) \leq (5, 5)$. Whenever both x and y coordinates are even (odd) the preferred configuration is parallel (anti-parallel). The difference $\mathcal{F}_{\uparrow\downarrow} - \mathcal{F}_{\uparrow\uparrow}$ is however not as pronounced at the rest of the sites with mixed even and odd x and y components. This structure of the exchange interaction between the two impurities can be directly linked to the spin polarization of the itinerant electrons at the nesting wavevector $\mathbf{Q}_{stripe}$. This is explicitly shown in figure 3.6(b), where the difference in the $\mathbf{Q}_{stripe}$ component of the total magnetization $M^Q_{\uparrow\uparrow} - M^Q_{\uparrow\downarrow}$ is maximum (minimum) at the even-even (odd-odd) sites and very small in the rest of the sites. The second impurity will then be reoriented according to the maximum $\mathbf{Q}_{stripe}$ spin polarization induced by the two impurities (constructive interference), and thereby lower the free-energy. This effect is very much suppressed when the correlations in the system are turned off as obvious from figure 3.6(c). The effective exchange interaction $I(\mathbf{r})$ is reduced by more than an order of magnitude. The change in both the amplitude and structure of the exchange interaction can be seen very clearly in the $\mathbf{r} = (n, n)$ diagonal cuts of the non-interacting and interacting system shown in figure 3.6(d). A careful study of correlation effects on RKKY

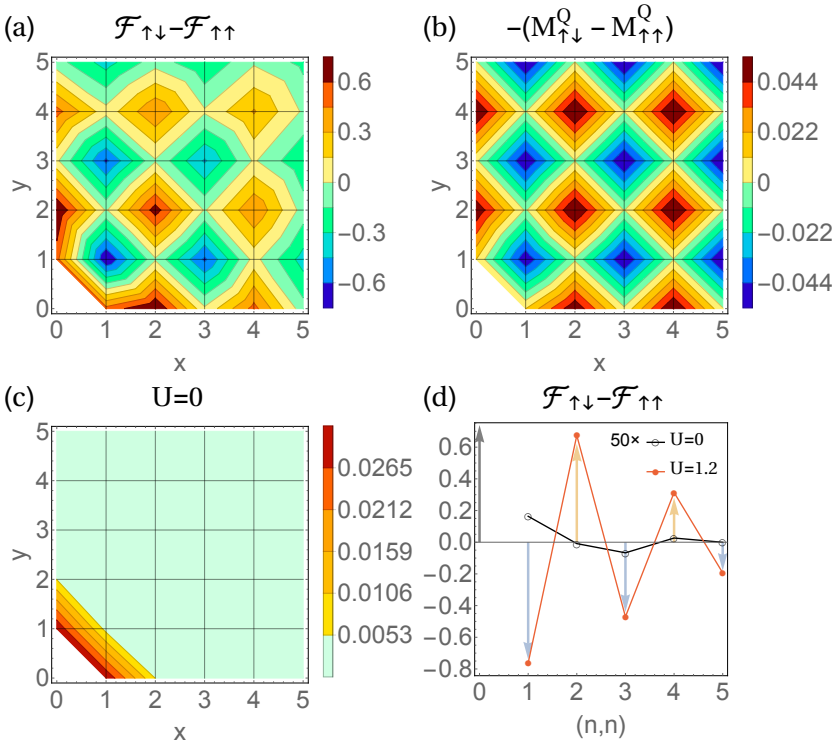

Figure 3.6: Effective exchange interaction $I(\mathbf{r}) = \mathcal{F}_{\uparrow\downarrow} - \mathcal{F}_{\uparrow\uparrow}$ and effect of correlations. Two weak impurities $J_0 S^z_{\mathbf{i}^*\sigma} = \pm 0.1$ eV at coordinates $\mathbf{r}_1 = (0,0)$ and $\mathbf{r}_2 = (x,y)$. (a) $I(\mathbf{r})$ as a function of $\mathbf{r}_2$. (b) Difference of the total polarization at the nesting wavevector $\mathbf{Q}_{stripe}$, $M^Q_{\sigma\sigma'}$, for the configurations in (a). The configuration maximizing M^Q at each $\mathbf{r}_2$ corresponds to the lowest free-energy in (a). (c) Same as (a) without interactions, $U = J = 0$. (d) Diagonal cuts $\mathbf{r}_2 = (n,n)$ in panels (a) with (red) and (c) without (black) interactions. Note the $U = 0$ case has been multiplied by a factor of 50. The arrows illustrate the preferred orientation of the second impurity at $\mathbf{r}_2$ with respect to the first one at $\mathbf{r}_1 = (0,0)$. $T/T^0_N = 1.2$ for all these panels.

physics is beyond the scope of this work, but will be the topic of future studies.

We end the discussion with the T dependence of the $|m(\mathbf{Q}_{stripe})|^2$ magnetic signal. Figure 3.7 shows the intensity of the peak for 3% and 6% disorder. In the $x < x_c$ case, the signal is lost at $T \lesssim T^0_N$ and it exhibits a clear suppression of weight at low T compared to the clean system. From Figs. 3.4(d,f) it is evident that most of this weight has been transferred to the $\mathbf{Q}_{Néel}$ wavevector. The $x > x_c$ case shows a smeared transition as opposed to the sharp transition of the clean system. The disorder induced $\mathbf{Q}_{stripe}$ signal persists to temperatures significantly

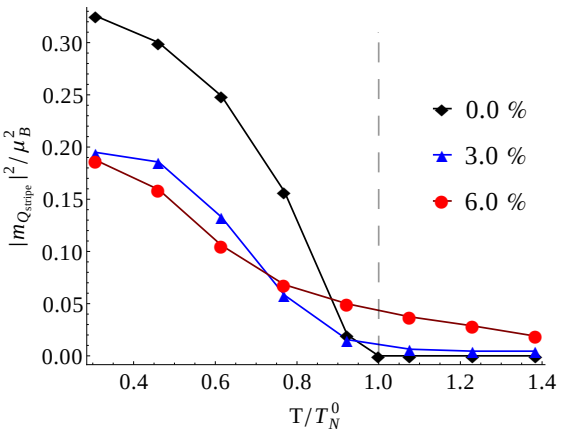

Figure 3.7: Temperature dependence of the magnetic $\mathbf{q} = \mathbf{Q}_{stripe}$ Bragg peak for the homogeneous system (black diamonds), $x = 3.0\%$ (blue triangles), and $x = 6.0\%$ (red dots) disorder. Vertical dashed line indicates $T = T_N^0$.

above the ordering temperature of the clean system, $T/T_N^0 \sim 1.4$, where the signal intensity has been suppressed by $\sim 90\%$ with respect to its low-T value consistent with elastic neutron measurements [Fig. 3.1].[12, 18]

Finally we comment on the reported absence of orthorhombic distortion in Mn-doped Ba-122.[12] Of course, since we do not explicitly include a coupling to the lattice in the model, we cannot make quantitative statements. However, in agreement with neutron experiments at low T, the $\mathbf{Q}_{stripe}$ peaks in Fig. 3.4(l) are sharp[12, 18], whereas the real-space magnetization clearly exhibits domains of predominantly $(\pi, 0)$, $(0, \pi)$, or both $(\pi, 0)$ and $(0, \pi)$ order as is evident from Fig. 3.4(k). Therefore, assuming that the structural transition is caused by a magneto-elastic coupling, we expect in the present case a resulting structural mixture of intertwined tetragonal and orthorhombic regions consistent with Ref. [18].

3.5 Conclusions

In summary, we have studied the cooperative effects of magnetic impurities within a realistic five-band model relevant for the iron pnictides. The resulting induced long-range magnetic stripe order of the conduction electrons constitute an example of an order-from-disorder phenomenon, which explains the main experimental observations of the magnetic properties of Mn doped $BaFe_2As_2$. This includes the presence of a high-T $\mathbf{Q}_{stripe}$ stripe magnetic phase beyond a critical Mn concentration, the presence of short-range checkerboard (π, π) spin fluctuations, and the absence of a clear tetragonal to orthorhombic structural transition.

Chapter 4

Local magnetization nucleated by non-magnetic impurities

Part of the material in this chapter has been published in J. Supercond. Novel Magn. 28, 1321 (2015).

4.1 Introduction

It is crucial to understand the role of disorder in high-temperature superconductors because the materials are obtained from chemical doping with substitutional impurity atoms. In this chapter we focus on the single-impurity problem in the normal paramagnetic state and study the local changes and emergent states induced by a non-magnetic potential. In particular, the concept of freezing of spin fluctuations around defects in multi-band paramagnetic systems is introduced. The theory of emergent defect states will be extended into the nematic, magnetic and superconducting phases in the following chapters. Some of the effects that will be discussed are:

- Nematogens, strongly anisotropic impurity states through the pinning of spin fluctuations, are proposed as a possible source of the reported transport anisotropy in the nematic paramagnetic state.
- Generation of dimer-like electronic structures deep inside the spin ordered phase are found around potentials, in agreement with STM local probes, and also relevant for the transport anisotropy in this phase.
- A short-ranged inhomogeneous magnetic order is found to coexist with superconductivity, consistent with the disordered magnetic phases detected by μSR around optimal doping in several compounds, which are not observable by neutrons.

- The remarkable enhancement of the superconducting transition temperature through impurity-induced local increased density of states.

Here, we present and describe the local properties of a single-impurity in detail, with the hope of making the disorder phenomena discussed in the upcoming chapters more comprehensible.

The existence of the local pinning of magnetic order is explained in terms of a strong impurity-enhancement of states near the Fermi level, and we map out the resulting phase diagram of the existence of magnetization as a function of impurity strength and Coulomb interactions. In particular, the presence of impurity-induced magnetism in only a certain range of potential scattering strengths can be understood from the specific behavior of the impurity resonant state. Finally, we discuss the important role played by the "gapped" e_g orbitals, making possible the existence of sharp resonant states in the paramagnetic phase.

The slowing down of magnetic fluctuations and subsequent induction of static short-range magnetic order near spatial inhomogeneities has been extensively discussed within one-band models relevant for cuprates.[54] This applies to nonmagnetic disorder[55, 51, 56], grain boundaries[57], and vortices[58]. Typically, in these cases a depletion of the density of states around the Fermi energy (ϵ_F) is necessary for the generation of local magnetic order due to the significant enhancement of the local density of states (LDOS) near the Fermi level only in the presence of a superconducting gap (or pseudogap) allowing for disorder-induced bound or resonant states [47]. This is not the case for the typical models applicable to iron pnictides as will be discussed below.

4.2 Model

Following the itinerant approach we used in the case of magnetic impurities, we model a single non-magnetic impurity in the paramagnetic state of the pnictides by the following Hamiltonian

$$\mathcal{H} = \mathcal{H}_0 + \mathcal{H}_{int} + \sum_{\mu\sigma} V_\mu c^\dagger_{\mathbf{i}^*\mu\sigma} c_{\mathbf{i}^*\mu\sigma}. \tag{4.1}$$

The first two terms, the five-orbital tight-binding model and the on-site Coulomb interactions, have been described in chapter 2. We remind the reader of the uneven orbital content of $\mathcal{H}_0$ around the Fermi level (see figure 2.2). While the three t_{2g} orbitals constitute the main contribution near the Fermi level, the weight of the two other d orbitals, the e_g orbitals, is minimal and are thus essentially 'gapped' for several hundreds of meV. This fact will be crucial in section 4.4. The last term adds a potential V_μ at the impurity site $\mathbf{i}^*$ and orbital μ. We include only intra-orbital terms consistent with first-principles studies of transition-metal atoms in

1111 materials. [59] In addition, we neglect the orbital dependence of the impurity potential for simplicity in most of this chapter. This assumption is not important for the results that will be presented below. After mean-field decoupling of $\mathcal{H}_{int}$, we solve the following eigenvalue problem $\sum_{\mathbf{j}\nu} H^{\mu\nu}_{\mathbf{ij}\sigma} u^n_{\mathbf{j}\nu\sigma} = E_{n\sigma} u^n_{\mathbf{i}\mu\sigma}$, where

$$H^{\mu\nu}_{\mathbf{ij}\sigma} = t^{\mu\nu}_{\mathbf{ij}} + \delta_{\mathbf{ij}}\delta_{\mu\nu}[-\mu_0 + \delta_{\mathbf{ii}^*} V_\mu + U\langle n_{\mathbf{i}\mu\bar{\sigma}}\rangle + \sum_{\mu'\neq\mu} (U'\langle n_{\mathbf{i}\mu'\bar{\sigma}}\rangle + (U'-J)\langle n_{\mathbf{i}\mu'\sigma}\rangle)], \tag{4.2}$$

on a 20×20 lattice with self-consistently obtained densities $\langle n_{\mathbf{i}\mu\sigma}\rangle = \sum_n |u^n_{\mathbf{i}\mu\sigma}|^2 f(E_{n\sigma})$ for each site and orbital. With these fields we can construct the spin polarization $m_{\mathbf{i}\mu} = \sum(n_{\mathbf{i}\mu\uparrow} - n_{\mathbf{i}\mu\downarrow})$ at each site and orbital. With the self-consistent eigenvalues $E_{n\sigma}$ and eigenvectors $u^n_{\mathbf{i}\mu\sigma}$ we can compute the LDOS at any site $\mathbf{i}$ in the presence of the impurity,

$$N(\mathbf{r},\omega) = -\frac{1}{\pi}\Im\left(\sum_{\mu,\sigma} \mathcal{G}^\mu_\sigma(\mathbf{r}_\mathbf{i},\omega)\right) = \sum_{n,\mu,\sigma} \frac{|u^n_{\mathbf{i}\mu\sigma}|^2}{\omega - E_{n\sigma} + i\eta}. \tag{4.3}$$

Here $\eta = 5$ meV is the artificial broadening of the Dirac delta functions arising from the imaginary part of the Greens functions, making them Lorentzian functions. The supercell method is used to acquire spectral resolution of the order of η.

4.3 Local magnetic order and impurity states

The mean field ground state of the Hamiltonian (4.1) without disorder ($V_\mu = 0$) can be controlled by the interaction parameter U. At $n = 6$ filling, for U lower than a critical value of $U_{c2} \sim 0.9$ eV, the homogeneous system remains non-magnetic. Above U_{c2} the system is unstable towards a spin density wave state $\mathbf{m}(\mathbf{r}) = \sum_{l=1,2} \mathbf{m}_l \exp(i\mathbf{Q}_l \cdot \mathbf{r})$, with the ordering vectors $\mathbf{Q}_1 = (\pi, 0)$ and $\mathbf{Q}_2 = (0, \pi)$. The preferred magnetic ground state, i.e. the designation of the $\mathbf{m}_1$ and $\mathbf{m}_2$ order parameters, was explored in chapter 2. In this chapter the system will always be kept below the long-range ordering critical interaction U_{c2}, and we only consider collinear polarization. Depending on parameters it can, however, be energetically favorable to spin polarize regions around the non-magnetic impurities even in the normal paramagnetic state. Figure 4.1(a) shows the real space magnetization in a case where impurity-induced order is present for low interactions, $U = 0.4$ eV $< U_{c2}/2$. In this particular case, the impurity site itself exhibits the largest induced moment in contrast to the similar one-band result where the nearest-neighbor sites contain the largest spin polarization[55, 51, 56]. The Fourier transform of the magnetization in Fig. 4.1(a) is shown in Fig. 4.1(b). It is dominated by broad peaks at $(0, 0)$ and (π, π), characteristic of short-range order.

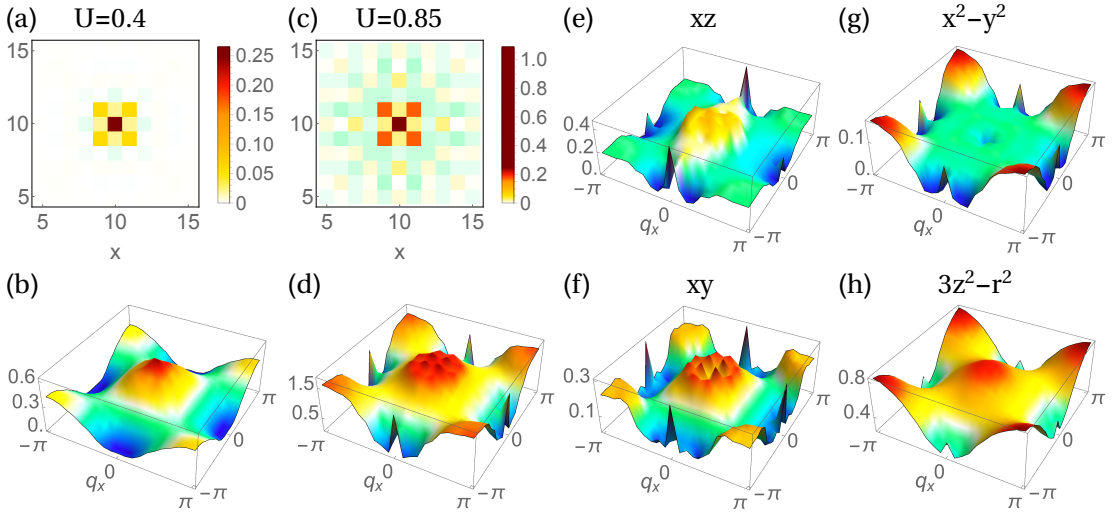

Figure 4.1: (a) Induced real-space magnetization in μ_B around a $V_\mu = 1.3$ eV impurity, and (b) corresponding momentum space representation for $U = 0.4$. (c) and (d) the same for $U = 0.85$ eV. Orbital content $m_\mu(\mathbf{q})$ of the polarization shown in (d) for the t_{2g} orbitals (e) xz and (f) xy, and the e_g orbitals (g) $x^2 - y^2$ and (h) $3z^2 - r^2$.

Surprisingly, the overall structure of $m(\mathbf{q})$ of this local order differs from the spin susceptibility of the clean system dominated by $\mathbf{Q}_1$ and $\mathbf{Q}_2$. Increasing the correlations, i.e. driving the system closer to the magnetic instability, the polarization amplitude around the defect, shown in figure 4.1(c), increases and becomes longer-ranged. The corresponding $m(\mathbf{q})$ thus develops additional substantial sharp peaks at $\mathbf{Q}_l = (0, \pi)/(\pi, 0)$, as can be seen in figure 4.1(d). These features are equivalent to the weak longer-range tails of the induced magnetization around magnetic impurities found in chapter 3. An analysis of the orbital content of the polarization in figures 4.1(e)-(f) reveals sharp dominating $\mathbf{Q}_l$ peaks in the $m(\mathbf{q})$ structure of the t_{2g} orbitals. The contribution from the d_{yz} orbital is not shown because the tetragonal symmetry of the system is preserved by the defect and hence it is the same as the one from d_{xz} with a $\pi/2$ rotation. The magnetization structure of the "gapped" e_g orbitals, shown in figures 4.1(g)-(h), differs slightly from that of the t_{2g} orbitals, with leading broad (π, π) peaks. It is remarkable that the orbital content of this local polarization is largely of $d_{3z^2-r^2}$ character, unlike the homogeneous long-range spin ordered state where the t_{2g} orbitals predominate. This will be explained in terms of impurity induced resonant states in the following section.

In order to map out when magnetization is locally nucleated, we explore the parameter space by varying the interaction U and impurity strength V_μ. For the band structure of Ref. [32], only repulsive potentials, $V_\mu > 0$, are capable of

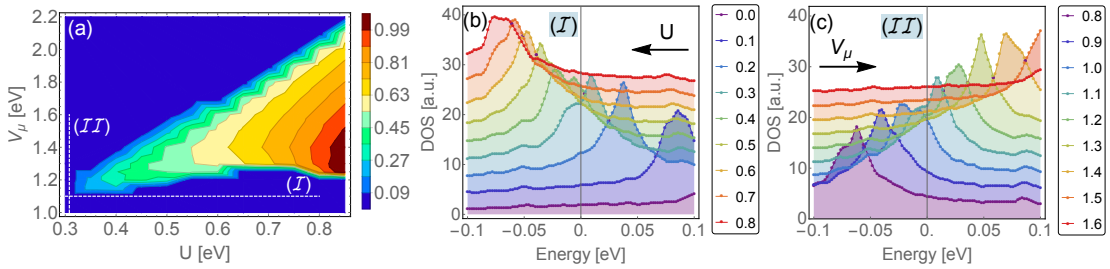

Figure 4.2: (a) Phase diagram of impurity-induced magnetization at the impurity site as a function of U and V_μ in the normal state. (b) LDOS versus energy at the impurity site for $V_\mu = 1.1$ eV varying U (path ($\mathcal{I}$) in (a)), and (c) for $U = 0.3$eV and a representative range of potential strengths V_μ (path ($\mathcal{II}$) in (a)). Curves in (b) and (c) have been offset vertically for clarity.

inducing magnetic order locally at zero temperature and $n = 6.0$ filling. The resulting moment at the potential site is shown in Fig. 4.2(a). The triangular-shaped region of finite impurity-induced magnetization exhibits a clear asymmetry by a linear (curved) phase boundary in the large (low) V_μ limit. It is noteworthy that due to the curved lower phase boundary, there exist values of the potential V_μ (around ~ 1.2 eV for the present band structure and doping level) where it is favorable to locally nucleate magnetism only for weak values of U, contrary to naive expectations from a standard spin density wave instability criterion in homogeneous systems.

The above results can be understood by studying the evolution of the LDOS in the presence of the impurity (see equation (4.3)). Specifically, by tracking the formation of impurity resonant states close to the Fermi energy as a function of U and V_μ at the impurity site. We focus initially on the effect of correlations U for a fixed potential $V_\mu = 1.1$ eV (horizontal dashed white line in Fig. 4.2(a)) with results shown in Fig. 4.2(b). Without correlations ($U = 0$), the resonant state exists at high positive energies (> 0.1 eV). For increasing U, however, as seen from Fig. 4.2(b) the resonant state is pushed to lower energies, crosses ϵ_F, and moves to negative energies. The largest density of states near ϵ_F is found around $U = 0.3$ eV which explains the curved lower edge of the magnetization region. Figure 4.2(c) shows the LDOS at the impurity site for $U \sim 0.3$ eV for different values of the impurity strength V_μ (vertical dashed white line in Fig. 4.2(a)). Evidently, the resonant state exhibits the opposite trend to Fig. 4.2(b) by moving to higher energies upon increasing the impurity strength. Thus, the enhanced LDOS at ϵ_F by the resonant state is maximal inside the triangular wedge-shaped region of Fig. 4.2(a), and the fact that impurity-induced magnetization exists in this same region is reminiscent of the Stoner instability criterion $N(\epsilon_F)U > 1$. When the LDOS enhancement and interaction U reach the Stoner threshold, the

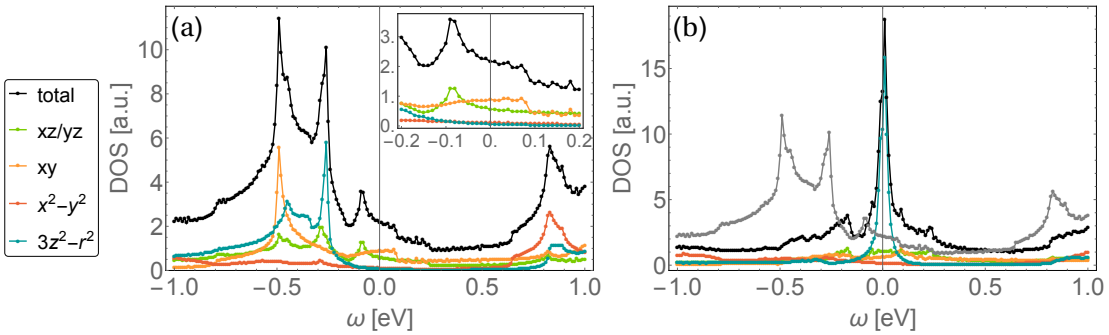

Figure 4.3: (a) Total DOS $N_0(\omega)$ in the unperturbed normal state (black) and the contributions from the different orbitals as specified in the legend. Inset shows a zoom of 400 meV around ϵ_F. (b) The same at the impurity site for the $V_\mu = 1.1$eV and $U = 0.3$eV case shown in figure 4.2. The unperturbed total DOS (gray) is shown for comparison.

system *locally* crosses a magnetic instability.

Even if in real systems the spin order around a single-impurity will in principle fluctuate, once a small coupling between neighboring impurities is included it will become static. The Mermin-Wagner theorem, which prohibits the development of long-range order in two dimensional system applies to infinite systems, which is not the case of the short range order studied here.

4.4 The "gapped" e_g orbitals

Let us now focus on the impurity induced state, a necessary ingredient for nucleation of local magnetic order. Extensive single-impurity studies in one-band two-dimensional metals in the context of cuprates have shown that a *depletion* of the density of states is needed to produce a resonant state near a non-magnetic impurity (see [47] and references therein). If there is no reduction in the DOS at low energies (the simplest model is a linear vanishing DOS around ϵ_F), the impurity state is broadened and merges with the continuum, i.e. the LDOS near the impurity does not exhibit any signature of a resonance state. Figure 4.3(a) shows the total DOS (black curve) in a 2 eV window around the Fermi energy of the homogeneous five-orbital model (4.1). It is essentially flat and finite (there are after all multiple bands crossing ϵ_F) within a 200 meV window around ϵ_F. Still, clear resonant states at the impurity sites were presented in figures 4.2(b)-(c) for a broad parameter range of V_μ and U. As will be shown below, this is an example of novel *multi-band* local phenomena.

Let us start with one of the standard ways of computing single-impurity states,

the T-matrix method. The expression for the full Green's function of a system in the presence of a delta-function potential $V(\mathbf{r}) = V\delta(\mathbf{r})$ is given by

$$\mathcal{G}(\mathbf{r}, \mathbf{r}'; \omega) = \mathcal{G}_0(\mathbf{r}, \mathbf{r}'; \omega) + \mathcal{G}_0(\mathbf{r}, 0; \omega)T(\omega)\mathcal{G}_0(0, \mathbf{r}'; \omega) \tag{4.4}$$

in terms of the T-matrix

$$T(\omega) = \frac{V}{1 - V\sum_{\mathbf{k}} \mathcal{G}_0(\mathbf{k}, \omega)}, \tag{4.5}$$

that accounts for multiple scattering off the impurity. Note that internal indexes in equation (4.4) have been omitted for clarity, and one should keep in mind that the Green's functions can be matrices. The poles of the total $\mathcal{G}$ which give the energy spectrum of single particle excitations, consist of the poles of the unperturbed $\mathcal{G}_0(\omega)$ and the poles of the T-matrix (4.5). The latter correspond to the appearance of new states induced by the impurity V. The usual strategy is thus to find the poles of the T-matrix, i.e. the solutions that satisfy the equation $\det[1 - V g_0(\omega)] = 0$, where $g_0(\omega) = \sum_{\mathbf{k}} \mathcal{G}_0(\mathbf{k}, \omega)$ is the unperturbed local Green's function. Splitting this function into real and imaginary parts, $g_0(\omega) = g_0'(\omega) + ig_0''(\omega) = g_0'(\omega) - i\pi N_0(\omega)$, the condition for poles in the T-matrix becomes

$$1/V = g_0'(\omega) - i\pi N_0(\omega) \tag{4.6}$$

In general the solutions to this equation (a set of two equations for the real and imaginary parts) are complex, $\Omega \equiv \Omega' + i\Omega''$, i.e. located at energy Ω' with a decay rate Ω''. From equation (4.6) it becomes clear why one needs a depletion in the unperturbed density of states $N_0(\omega)$. If the spectrum is fully gapped in some energy window, $N_0(\omega) = 0$, then any solution in that window is a 'genuine' bound state $\Omega = \Omega'$. The simplest example is an attractive potential $V(r) = -|V|\delta(\mathbf{r})$ in a system of non-interacting electrons, with a bound state outside (below) the band. [47] Another example is the state induced by a classical magnetic impurity in a fully-gapped s-wave superconductor first discussed by Yu, Shiba and Rusinov. [60, 46, 61] Increasing the density of states however, we start deviating from the condition (4.6), and the solution acquires a finite broadening Ω''. In other words, the overlap with the continuum only allows the formation of resonances or *virtual* bound states with a finite lifetime.

Having established the existence of impurity induced states in DOS-depleted energy ranges, let us turn to one of their physical implications: the modification of the LDOS. From equation (4.4) the DOS in the presence of the impurity is given by

$$N(\mathbf{r}, \omega) = N_0(\omega) - \frac{1}{\pi}\Im\left[\mathcal{G}_0(\mathbf{r}, 0; \omega)T(\omega)\mathcal{G}_0(0, \mathbf{r}; \omega)\right]. \tag{4.7}$$

The second term describes the local change in the DOS due to the defect $\delta N(\mathbf{r}, \omega)$. Focusing on the 'real' bound states we discussed earlier, where $N_0(\Omega) = 0$, the only

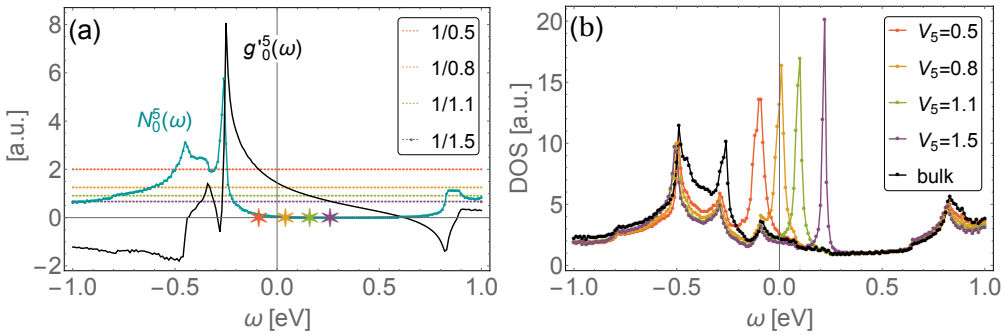

Figure 4.4: (a) Graphical solution of equation (4.6) for different $d_{3z^2-r^2}$-only impurity strengths V_5 as specified in the legend. (b) $N(\mathbf{r},\omega)$ at the impurity site for the V_5 cases used in (a). The total homogeneous DOS (black) is also shown as a reference.

contribution to the imaginary part is from the T-matrix, $\delta N(\mathbf{r},\Omega) = |\mathcal{G}'_0(\mathbf{r},\omega)|^2$ $\delta(\omega-\Omega)$. Hence one should expect strong modifications in the DOS around the impurity whenever equation (4.6) is fulfilled. When the new state is a virtual bound state, i.e. it has a finite lifetime, the Dirac delta function $\delta(\omega-\Omega)$ acquires a broadening and becomes a Lorentzian function.

After having revisited the conditions for impurity-induced states and their implications, let us go back to the case of a non-magnetic impurity in our multi-orbital metallic system (4.1). The unperturbed *local* Green's function $\hat{g}_0(\omega)$ and the impurity term $\hat{V}$ are 5×5 *diagonal* matrices in the $3d$ orbital basis, i.e $V_{\mu\nu} = g_0^{\mu\nu}(\omega) = 0$ if $\mu \neq \nu$. That leaves the denominator of the T-matrix (4.5) in a very simple form, and the new impurity states are solutions satisfying the following equation,

$$\det\left[\mathbb{I} - \hat{V}\hat{g}_0(\omega)\right] = \prod_{\mu}\left(1 - V_\mu g_0^\mu(\omega)\right) = 0. \tag{4.8}$$

That is, there are five *independent* conditions for poles in the T-matrix equivalent to equation (4.6), one for each orbital μ. The strategy to find sharp resonant states in a given energy window is then to look for orbitals with vanishing DOS in that energy range and find the potential strength that fulfills $1/V_\mu = g_0'^\mu(\omega)$. Since we are interested in impurity states around the Fermi level, the gapped e_g orbitals $d_{x^2-y^2}$ and $d_{3z^2-r^2}$ (see inset of figure 4.3(a)) are perfect candidates for sharp impurity resonant states. In fact, the orbital content of the resonant states that were presented in the previous section, shown in figure 4.3(b), are essentially of $d_{3z^2-r^2}$ character. Figure 4.4(a) shows a graphic solution of equation $1/V_5 = g_0'^5(\omega) - i\pi N_0^5(\omega)$ for several impurity strengths V_5, and the expected resonant state positions are shown with a star in each case. An LDOS calculation (4.3) at

the defect site in the presence of a $d_{3z^2-r^2}$-only impurity ($V_\mu = 0$ if $\mu = 1, ..., 4$) exhibits sharp impurity states in figure 4.4(b), in agreement with the graphic solution. We note that the ~ 100 meV shift position of the $V_5 = 1.1$ eV resonant state in figure 4.4(b) with respect to the $V_\mu = 1.1$ eV case in figure 4.3(b) is a consequence of self-consistency. Not allowing for readjustments of the densities and chemical potential in equation 4.2 in the presence of V_μ in the other orbitals (a non-selfconsistent calculation) results in the same resonant position in both cases. Resonant states for the other e_g orbital, $d_{x^2-y^2}$, were not found. Presumably, this has to do with the fact that very strong impurities ($V_3 > 5$ eV) are needed to fulfill equation (4.8) due to a very small $g_0'^3(\omega)$ around ϵ_F in this particular band $\mathcal{H}_0$.

Another important consequence of equation (4.8) is that the large unperturbed DOS $N_0^\mu(\omega)$ around the Fermi level in the three t_{2g} orbitals, a general property of all DFT-based models for Fe-based materials, prevents the formation of resonant states with t_{2g} character at low energies in the paramagnetic, non-superconducting phase. These orbitals, which rule the low energy physics of the homogeneous phases, share the spotlight with the e_g orbitals in the local phenomena of disordered systems.

The main result of this section is the crucial role played by the gapped e_g orbitals in the impurity resonant state formation. Their vanishingly small $N_0^\mu(\omega)$ near the Fermi level opens up the possibility of sharp resonant states at low energies, even if the total DOS of the metallic system is not depleted. For the present band, it is possible to generate reasonably sharp impurity-induced states of mainly $d_{3z^2-r^2}$ character in a wide range of parameters. Consequently, the local pinning of spin-fluctuations in the paramagnetic phase is possible, with a magnetization dominated by the $d_{3z^2-r^2}$ orbital (see figures 4.1(e)-(h)). These results highlight the importance of using realistic five-band models in studies of impurity-induced local order of the iron pnictides.

4.5 Strong potentials

In this last section we discuss an alternative way of locally pinning magnetic order: via a rearrangement of LDOS in the neighboring sites. This is the case of strong impurities, which as shown in figure 4.5(a) for a $V_\mu = 6$ eV potential, induce a spin polarization with largest amplitude at the nearest-neighbor sites. The structure in momentum space is very simple, with peaks at $\mathbf{Q}_1$ and $\mathbf{Q}_2$, as can be seen in figure 4.5(b). The orbital content analysis of the magnetic signal in figures 4.5(c)-(f) shows a dominating t_{2g} orbital character, in contrast to all the cases presented in section 4.3. In the presence of this strong impurity the LDOS at the impurity site is greatly suppressed and consequently some of the weight is transfered to the neighboring sites. This rearrangement is illustrated in figure 4.6(a), where the

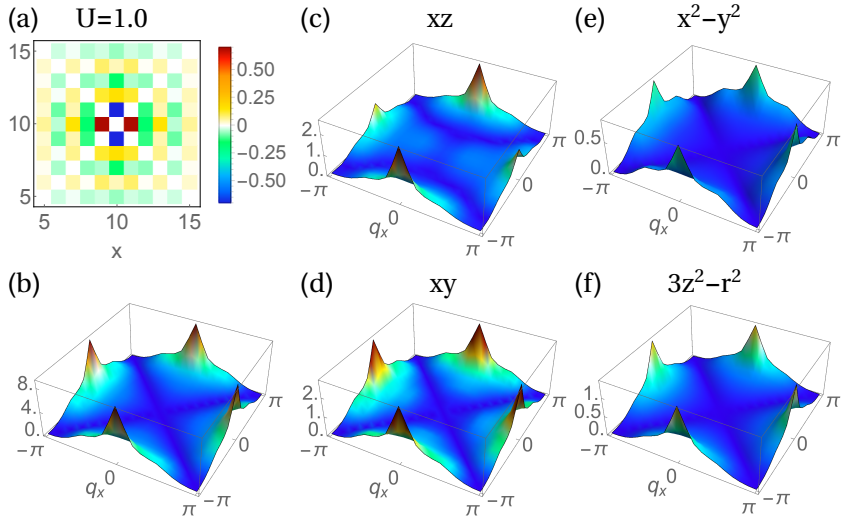

Figure 4.5: (a) Induced real-space magnetization in μ_B around a $V_\mu = 6$ eV impurity, and (b) corresponding momentum space representation for $U = 1.0$ and $T/T_N = 1.05$. Orbital content $m_\mu(\mathbf{q})$ for the t_{2g} orbitals (c) xz and (d) xy, and the e_g orbitals (e) $x^2 - y^2$ and (f) $3z^2 - r^2$.

total LDOS at the impurity site and at the two nearest neighboring sites (nn and nnn) is shown. The enhancement of the DOS at the nearest-neighboring site is enough to locally cross the magnetic instability in this case. This picture of piling up states that are being pushed away from a strong potential site is perhaps more intuitive than the sharp resonant state induced a weak impurity counterpart.

An important difference is the dominant role played by the t_{2g} orbitals in the case of strong potentials. The orbitally resolved LDOS at the nearest-neighbor site $\mathbf{r} = \mathbf{i}^* + \hat{\mathbf{x}}$ in figure 4.6(b) shows that the enhancement is mostly of yz and xy orbital character. The magnetic instability is thus crossed at these sites by the orbitals dominating the Fermi level, and the resulting local order is modulated at the ordering vectors $\mathbf{Q}_1$ and $\mathbf{Q}_2$ that govern the homogeneous spin susceptibility. Due to the relatively weak enhancement of the LDOS, the homogeneous system has to be close to the SDW instability (U close to U_{c2}) with high peaks in the spin susceptibility, for this type of local magnetic order to be induced.

4.6 Conclusions

In summary, we have discussed the generation of local magnetic order in the normal state of the Fe-based superconductors within a five-band model that includes on-site Coulomb interactions at the mean-field level. We have mapped out the phase

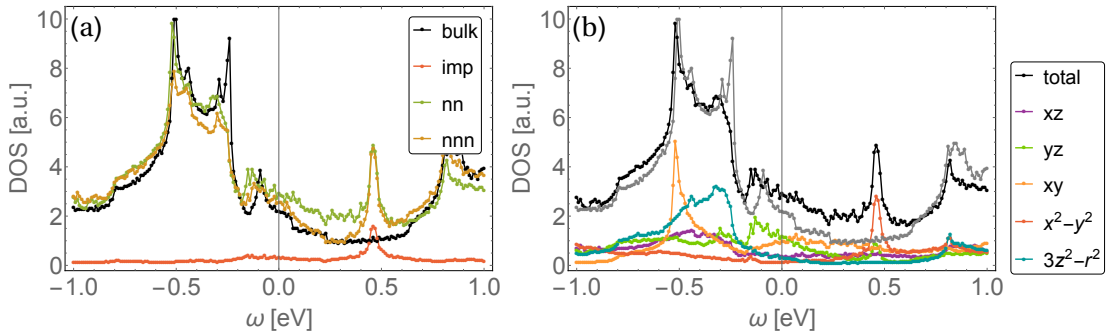

Figure 4.6: (a) Total LDOS at the impurity site $\mathbf{r} = \mathbf{i}^*$ (red), the nearest-neighbor site $\mathbf{r} = \mathbf{i}^* + \hat{\mathbf{x}}$ (green), the next nearest-neighbor site $\mathbf{r} = \mathbf{i}^* + \hat{\mathbf{x}} + \hat{\mathbf{y}}$ (orange) for the strong repulsive impurity $V_\mu = 6$ eV shown in figure 4.5. The homogeneous total DOS is also shown for comparison (black). (b) Total LDOS at the nearest-neighbor site (black) and the contributions from the different orbitals as specified in the legend. The unperturbed total DOS (gray) is shown for comparison.

diagram as a function of U and V_μ for the existence of local magnetic order, and explained the main topology of the phase diagram in terms of impurity-resonant states near the Fermi level. The gapped e_g orbitals, $d_{3z^2-r^2}$ for this particular band, play a primary role in generating sharp resonant states in the paramagnetic metallic state of these materials. Strong repulsive orbitals, can also induce local polarization, via an enhancement of DOS at the surrounding sites. The physical implications of these emergent impurity states when the system enters the superconducting, nematic or magnetic phases will be explored in the upcoming chapters.

Chapter 5

Emergent defect states as a source of resistivity anisotropy

Most of the material in this chapter has been published in
Phys. Rev. Lett. 113, 127001 (2014) and Phys. Rev. B 89, 100502(R) (2014).

5.1 Introduction

The origin of electronic nematic behavior, i.e. spontaneous breaking of discrete rotational symmetry preserving translational symmetry, is one of the most fascinating questions in the field of Fe-based superconductivity, involving the interplay of magnetic, orbital, and ionic fluctuations. Strong in-plane anisotropy has been reported in scanning tunneling spectroscopy (STM) [62], transport[63, 64, 65, 66, 67, 68, 80], angular resolved photoemission (ARPES)[69], neutron scattering[70], optical spectroscopy[71, 72, 73], shear modulus[74] and Raman[75] measurements. Since the various fluctuation channels in these multiband systems all couple to one another below the tetragonal to orthorhombic structural transition that occurs at T_s in many systems, all response functions become anisotropic and it is not easy to decide which fluctuations drive the ordering nematic phenomena observed. Theoretically, both spin nematic and orbital scenarios have been proposed[11].

In models with dominating orbital fluctuations, below T_s the occupation of the d_{xz} and d_{yz} orbitals becomes unequal, inducing an anisotropic the electronic structure. In the ferro-orbital ordered state, for example, the electron pockets at X and Y acquire different sizes and the hole pockets at Γ get elongated in opposite directions. If the dominating fluctuations are magnetic on the other hand, the spin response becomes anisotropic below T_s, with stronger fluctuations at one of the $\mathbf{Q}_l$ ordering vectors. Such anisotropies will certainly influence the measured properties that were mentioned above.

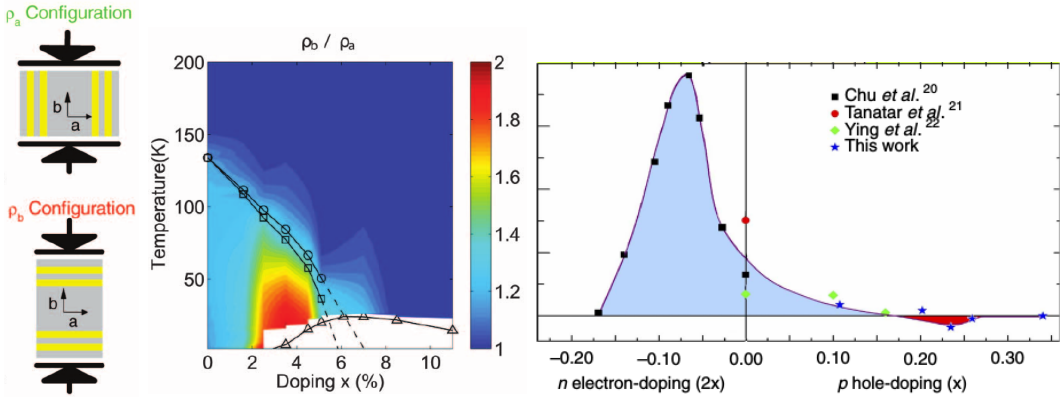

Figure 5.1: Transport anisotropy under uniaxial *stress*. (a) Diagram illustrating the transport measurements under stress (dark thick arrows). (b) Evolution of the in-plane resistivity anisotropy ρ_b/ρ_a on electron doped $Ba(Fe_{1-x}Co_x)_2As_2$ as a function of temperature and doping. $\rho_b/\rho_a > 1$ at higher temperatures than T_s, indicating substantial nematic fluctuations above the structural transition. The anisotropy grows with Co content, peaks in underdoped compositions, and is gone in overdoped crystals. From [64] (c) The maximum in-plane anisotropy ρ_{max} as a function of electron- and hole-doping. Note the significant asymmetry. From [67]

In this chapter we will mostly focus on the large in-plane anisotropy reported in transport measurements, one of the first experimental evidence for electronic nematicity. In order to motivate our work, we present below three experimental works on DC conductivity in both nematic and spin ordered phases, which contain several key aspects of the transport experiments in these systems.

Chu *et al* revealed that a large electronic anisotropy developed around the structural transition of $Ba(Fe_{1-x}Co_x)_2As_2$ via measurements of the in-plane resistivity, with the resistivity along the shorter b axis ρ_b being greater than ρ_a, $\rho_b > \rho_a$. [64] Free-standing crystals form structural twins to minimize the elastic energy in the orthorhombic state, and further cooling results in domains of spin stripe order. As a result, transport measurements (in fact, any bulk measurement) in these samples present only an *average* of any anisotropy in the system, which obscures the results. The in-plane anisotropy can nevertheless be probed using *uniaxial stress* along the orthorhombic a and b axes to detwin the crystals, as shown in figure 5.1(a). Resistivity data for several Co concentrations are presented in figure 5.1(b). The first counterintuitive result is the larger resistivity along b axis ($\rho_b > \rho_a$) for all samples, given that this lattice constant is shorter and the larger orbital overlap would naively imply lower resistivity. The degree of anisotropy reaches a maximum value of $\rho_b/\rho_a \sim 2$ in the underdoped regime

deep in the spin ordered phase, and vanishes ($\rho_b/\rho_a = 1$) in the overdoped samples. This non-monotonic doping behavior is in stark contrast with the very small lattice anisotropy $(a-b)/(a+b)$, which has a maximum value of 0.36% for the undoped compound and decreases with Co content. This was taken as an indirect evidence of the primary role played by itinerant electrons in driving the structural transition, and giving rise to the so-called electronic nematic phase. The second main result is the stress-induced anisotropy these materials exhibit well above T_s [figure 5.1(b)], which was taken as an indication of a substantial electronic nematic susceptibility. A remarkable transport property in this regime is the deviation of ρ_b from the initial metallic-like behavior well above T_s, and steep increase with decreasing temperature upon approaching the structural transition. In contrast, the current along the a axis keeps the metallic behavior over the entire T range. Both temperature dependences can be seen in figure 5.2.

Blomberg *et al* reported a very different behavior of the resistivity anisotropy on the hole-doped side [67]. Transport measurements were done on detwinned $(Ba_{1-x}K_x)Fe_2As_2$ crystals (also under uniaxial stress), and it was found that the $\rho_b - \rho_a$ anisotropy dramatically drops and changes sign for sufficiently large K-doping levels, as shown in figure 5.1(c). The reversal of the sign in hole-doped systems had been predicted in a model accounting for inelastic scattering of spin-fluctuations [83]. Still, these results raise the obvious question: why is there such a dramatic difference in the transport anisotropy with only a slight electron- or hole-doping? After all, nematic fluctuations were reported to be, from shear-modulus measurements, basically electron-hole symmetric. [74]

The last relevant experimental result came from Ishida *et al* [68]. They reported that, upon annealing, the resistivity anisotropy of the undoped $BaFe_2As_2$ nearly vanished, while significant anisotropy remained in Co-doped compounds. In general, the annealing process removes crystal defects and lattice dislocations, resulting in improved quality samples. Representative data is shown in figure 5.2 for as grown (top) and annealed (bottom) samples over a broad range of Co concentration. The results for the annealed crystals are particularly different from the as-grown ones in the low-doping regime ($x = 0$ and $x = 0.02$); both anisotropy and residual resistivity are remarkably decreased after annealing. For the under-doped samples ($x = 0.05$ and $x = 0.06$) on the contrary, the annealing effect is very weak. The magnitude of residual resistivity ($\rho(0K)$) both in a and b direction as well as their anisotropy remarkably increased in proportion to the doped Co content x in the spin ordered phase. With these results in hand, they concluded that the transport anisotropy is due to "nematogens" or anisotropic scattering potentials induced by Fe vacancies and Co defects. Such spatially extended defects aligned preferentially along the a axis have also been reported by local scanning probe studies [76, 77, 78], and are discussed in section 5.4.

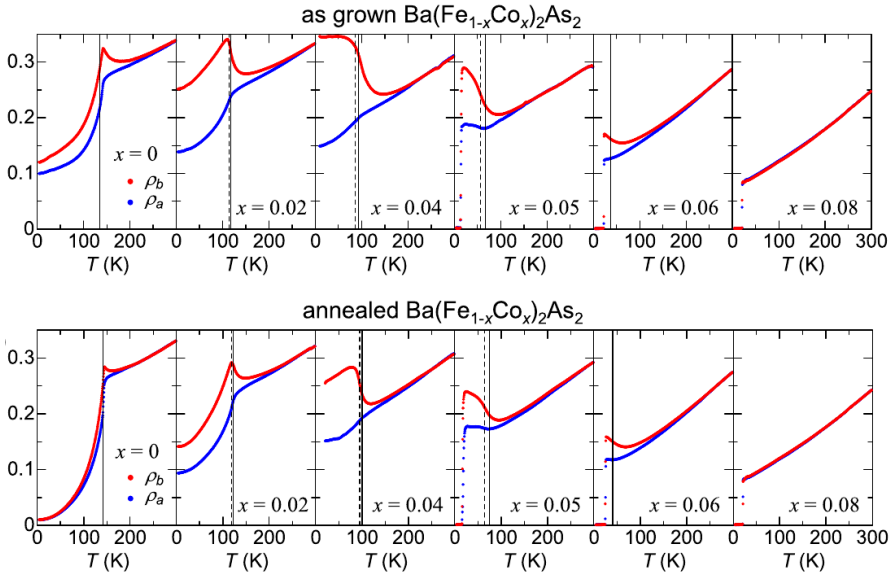

Figure 5.2: Temperature dependence of the in-plane resistivity (in mΩ cm units) ρ_a (blue) and ρ_b measured on *detwinned* (a) as-grown and (b) annealed $Ba(Fe_{1-x}Co_x)_2As_2$ crystals. Vertical lines indicate T_s (solid) and T_N (dashed) under unstressed conditions. From [68].

In general, resistivity is determined by both the electronic structure and the scattering. In these materials, the proposed orbital order more likely results in an anisotropy of *electronic structure*, whereas the spin-nematic ordering leads to an anisotropy of *electron scattering*. In the following section, we present a DC transport calculation via elastic scattering mechanism through the generation of strongly anisotropic impurity states. It should be noted that at the time we initiated our work, this was the available data and what mainly motivated and influenced our theoretical approach. Later on, a new technique developed by Chu *et al* made measurement of *elastoresistivity coefficients* possible, which provided new insights into the electronic anisotropy response and disorder effects in the paramagnetic phase. [79, 80, 81] We briefly discuss this data and the challenges it poses to the scattering scenario in section 5.3.

Our motivation to focus on impurity scattering can also be appreciated from figure 5.3, where we fit the resistivity data of the undoped 122 from Ref. [68] [figure 5.2] in the high temperature paramagnetic phase ($T > T_N \sim 141$K) to $\rho_{avg} = A + BT^2$. We find excellent agreement up to $T \sim 300$K, which argues in favor of conventional Fermi liquid and disorder scattering. More importantly, we find that $A \gg BT_N^2$ by an order of magnitude, implying that already at T_N

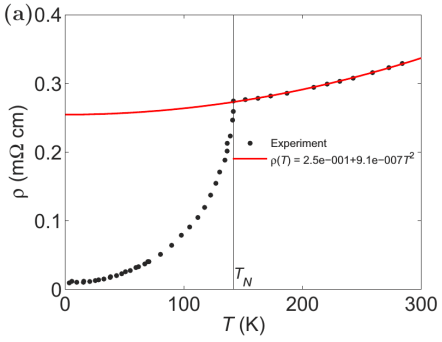

Figure 5.3: Dots: resistivity data extracted from Ref. [68]; line: fit to the data in the high temperature paramagnetic phase to $\rho_{avg} = 2.5 \times 10^{-1} + 9.1 \times 10^{-7} T^2$.

the *elastic scattering* from impurities dominates over inelastic processes. These observations suggest that elastic scattering might be significant in determining the resistivity anisotropy.

5.2 Transport in the nematic phase

In systems with large spin nematic susceptibility, strong anisotropy is expected in the spin fluctuations in the orthorhombic phase below T_s, even if the structural anisotropy is small. A cartoon of the spin susceptibility showing the onset of nematic order in the paramagnetic state is shown in figure 5.4. Such anisotropy will certainly influence transport properties; this is the basis of theories of transport by several groups[83, 84, 85], arguing that at T_s the magnetic correlation length becomes anisotropic and drives the anisotropy in the electronic inelastic scattering rate. Disorder is described entirely through a momentum-independent scattering rate and is required only to limit the contribution to the resistivity from "cold spots" on the Fermi surface. The transport anisotropy has also been studied within numerical Monte Carlo simulations of the spin-fermion model. [86]

In our work, the transport anisotropy of the nematic phase is also explained via spin fluctuation anisotropy, but through the generation of strongly anisotropic impurity states. This scenario is motivated by the observation by many STM experiments of C_4 symmetry breaking around point defects locally[62, 77, 76, 78, 87, 88]; these experiments can exhibit effects that are missed by average bulk probes. In fact, in some systems evidence for nematic symmetry breaking in the form of highly anisotropic C_2 defect states is seen in the nominally tetragonal phase above T_s[78]. These responses are generally attributed to residual local strains that break C_4 symmetry locally, together with a large residual nematic susceptibility.[89] In the

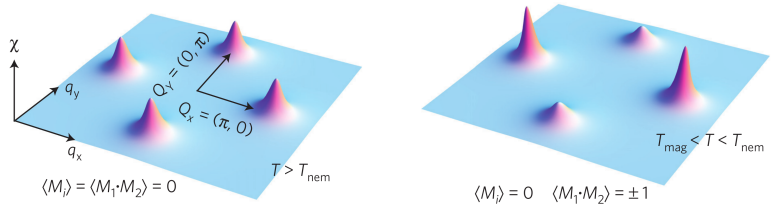

Figure 5.4: Onset of nematic order in the paramagnetic phase ($\langle \mathbf{M}_i = 0 \rangle$) in terms of the magnetic susceptibility $\chi(\mathbf{q})$. For $T > T_{nem}$ the two peaks at $(\pi, 0)$ and $(0, \pi)$ have equal amplitudes, and for $T_N < T < T_{nem}$ one of the peaks becomes stronger than the other, breaking the equivalence between the x and y directions. From [11].

ordered stripe $(\pi, 0)$ magnetic phase below the Néel temperature T_N in many of the parent and underdoped materials, the C_4 symmetry is broken by the magnetism itself. Nevertheless the symmetry breaking of the electronic structure around local Co defects in lightly doped Ca122 was observed to be so enhanced that this result was cited as the first evidence for a strong nematic tendency in these systems[62]. In addition, as suggested in Ref. [76], such "nematogen" defects could be responsible for the transport anisotropy.

There are several key aspects of the transport experiments [63, 64, 65, 66, 67, 68, 80] above T_N that any theory needs to account for:

1. The counterintuitive sign of the resistivity anisotropy on the electron-doped side, where $\rho_b > \rho_a$ although $b < a$.

2. The decrease of the anisotropy upon annealing [68].

3. The pronounced increase in ρ_b as T_N is approached, with continued metallic-like behavior in ρ_a.

4. The decrease in anisotropy both with increasing T and electron overdoping.

5. The possible sign change but also significant decrease of the anisotropy on the hole-doped side[67].

We consider the role of emergent defect states in these correlated systems and show they provide a natural explanation for the observations.

In this section, we discuss first the growth of anisotropic spin fluctuations in the nematic phase as T_N is approached from above. We extend the theory of impurity-induced emergent defects states into the nematic phase with an unbiased microscopic calculation of the local electronic structure near a point-like nonmagnetic impurity potential in a situation where the C_4 symmetry of the host bands

has been broken very slightly by e.g. applied uniaxial stress. This gives rise to the same anisotropic spin fluctuations considered as the source of transport anisotropy by the authors of refs. [83, 84, 85], but impurities play a very different and essential role. We find that the impurity state in the nematic phase is strongly anisotropic due to the enhanced background nematic response arising from electronic correlations.[90] Specifically, we calculate the momentum-dependent effective impurity potential, scattering rate, and conductivity in the nematic phase.

5.2.1 Model

The Hamiltonian is given by

$$\mathcal{H} = \mathcal{H}_0 + \mathcal{H}_{int} + \mathcal{H}_{oo} + \mathcal{H}_{imp}, \tag{5.1}$$

where $\mathcal{H}_0 + \mathcal{H}_{int}$ denotes the kinetic energy with tight-binding parameters adopted from Ref. [32] and on-site Coulomb interactions explained in detail in chapter 2. The chemical potential sets the doping level $x = 0$. We assume $U' = U - 2J$ and $J' = J$ and fix $U = 1.0$ eV and $J = U/4$. The term

$$\mathcal{H}_{oo} = \frac{\delta}{2} \sum_{\mathbf{i}} (n_{\mathbf{i}yz} - n_{\mathbf{i}xz}) \tag{5.2}$$

mimics the orthorhombicity of the band below T_s, for a non-zero δ orbital order parameter. We thus assume that an applied in-plane uniaxial stress to the crystal results in a small static ferro-orbital order, based on ARPES measurements of detwinned crystals. [69] We have also studied C_2 symmetric bands arising from hopping anisotropy and found similar results to those reported below. Finally, $\mathcal{H}_{imp} = \sum_{\mu\sigma} V_\mu c^\dagger_{\mathbf{i}^*\mu\sigma} c_{\mathbf{i}^*\mu\sigma}$ is the impurity potential, adding a potential $V_\mu = 1.5$ eV at the impurity site $\mathbf{i}^*$. We neglect the orbital dependence of the impurity potential for simplicity in this section ($V_\mu = V_{imp} = 1.5$ eV), and discuss the role of V_μ in section 5.3. The particular values for U and V_μ are not important except that both have to be in the range where magnetization is nucleated locally (see chapter 4). After mean-field decoupling of $\mathcal{H}_{int}$, we solve the following eigenvalue problem $\sum_{\mathbf{j}\nu} H^{\mu\nu}_{\mathbf{ij}\sigma} u^n_{\mathbf{j}\nu\sigma} = E_{n\sigma} u^n_{\mathbf{i}\mu\sigma}$, where

$$\begin{aligned} H^{\mu\nu}_{\mathbf{ij}\sigma} &= t^{\mu\nu}_{\mathbf{ij}} + \delta_{\mathbf{ij}}\delta_{\mu\nu}[-\mu_0 + \delta(\delta_{\mu,yz} - \delta_{\mu,xz}) + \delta_{\mathbf{ii}^*} V_{imp} \\ &+ U\langle n_{\mathbf{i}\mu\bar{\sigma}}\rangle + \sum_{\mu'\neq\mu} (U'\langle n_{\mathbf{i}\mu'\bar{\sigma}}\rangle + (U' - J)\langle n_{\mathbf{i}\mu'\sigma}\rangle)], \end{aligned} \tag{5.3}$$

on a 30×30 lattice with self-consistently obtained densities $\langle n_{\mathbf{i}\mu\sigma}\rangle = \sum_n |u^n_{\mathbf{i}\mu\sigma}|^2 f(E_{n\sigma})$ for each site and orbital.

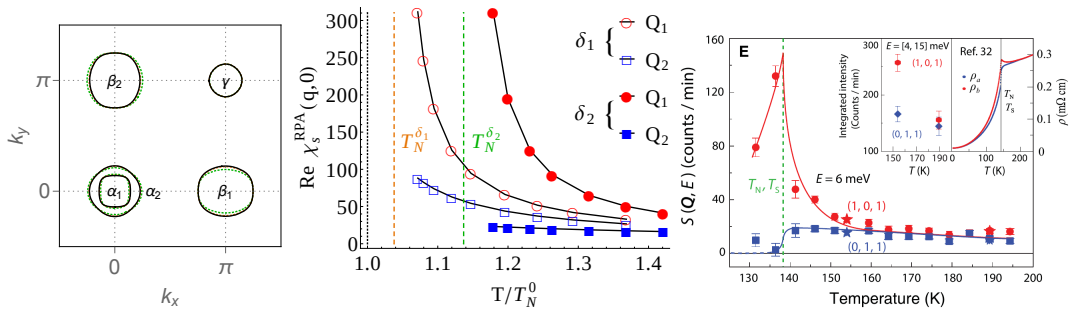

Figure 5.5: (a) Fermi surface in the tetragonal state (black line) and with a finite orbital order δ (dashed lines) (b) Real part of the homogeneous RPA spin susceptibility $\chi_s^{RPA}(\mathbf{q},0)$ at $\mathbf{Q}_1 \equiv (\pi,0)$ (red circles) and $\mathbf{Q}_2 \equiv (0,\pi)$ (blue squares) as a function of T normalized to the Néel temperature T_N^0 of the tetragonal band ($\delta = 0$). Open (solid) symbols refer to the degree of orbital order, $\delta_1 = 16$ meV ($\delta_2 = 80$ meV), and the dashed green (dashed orange) vertical lines indicate the corresponding relevant T_N^δ. (c) Temperature dependence of spin excitations for $BaFe_2As_2$ under uniaxial stress at $\mathbf{Q} = (1,0,1)$ and $(0,1,1)$, from [70].

5.2.2 Nematogens and anisotropic elastic scattering rate

In the homogeneous orthorhombic "nematic" phase above T_N, a non-zero δ breaks the tetragonal symmetry of the band dispersion as can be seen in the dashed Fermi surface in figure 5.5(a). This will already influence the transport properties and introduce a temperature independent anisotropy, as will be shown below. The important effect of the xz-yz orbital splitting is to enhance (diminish) the spin susceptibility at $\mathbf{Q}_1 \equiv (\pi,0)$ ($\mathbf{Q}_2 \equiv (0,\pi)$) as shown in Fig. 5.5(b) for two cases with $\delta_1 = 16$ meV ($T_N^{\delta_1}$) and $\delta_2 = 80$ meV ($T_N^{\delta_2}$). The enhanced susceptibility at $\mathbf{Q}_1 \equiv (\pi,0)$ pushes T_N up. As seen explicitly from Fig. 5.5, even a small orbital splitting δ leads eventually to an arbitrarily large spin anisotropy upon approaching the instability[90], in agreement with recent neutron scattering measurements, shown in figure 5.5(c). [70] This experiment demonstrated a direct link between transport anisotropy and spin excitation anisotropy, finding the same onset temperature for the measured in-plane difference of these two distinct properties.

How does the electronic structure near the impurities reflect the spin anisotropy of the nematic phase? The condensation of spin fluctuations around potentials in the paramagnetic phase was introduced in chapter 4. In Fig. 5.6 we show local magnetization $m(\mathbf{r})$ nucleated by an impurity in the nematic state as a function of T. As seen, the emergent defect object pins the order locally and therefore incorporates the growing spin fluctuation anisotropy in the host upon approaching the magnetic instability. The growing x-y anisotropy is clearly evident in the

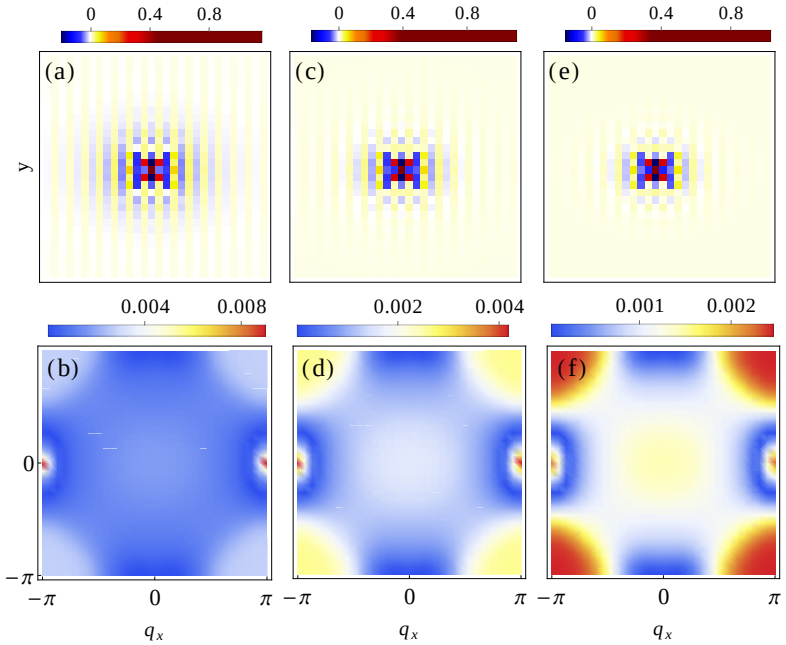

Figure 5.6: Real space magnetization $m(\mathbf{r})$ of a $V_{imp} = 1.5$ eV impurity for $\delta_2 = 80$ meV at temperatures $T/T_N^{\delta_2} = 1.23$ (a), 1.14 (c), and 1.06 (e). (b), (d) and (f) show the Fourier transform $|m(\mathbf{q})|$ of (a), (c) and (e), respectively.

Fourier images in the lower row of Fig. 5.6.

In order to determine the transport properties of the nematic defect states, we calculate first the scattering rate in the Born approximation

$$\frac{1}{\tau^l_{\mathbf{k}\alpha}} = n_{imp}\frac{2\pi}{\hbar}\frac{1}{V}\sum_{\mathbf{k}'\beta}\left|\mathrm{tr}\left(\hat{\sigma}_l\hat{\mathcal{V}}^{imp}_{\sigma\sigma'}(\mathbf{k}\alpha,\mathbf{k}'\beta)\right)\right|^2 \times \delta(\epsilon_{\mathbf{k}\alpha}-\epsilon_{\mathbf{k}'\beta})\left(1-\frac{\mathbf{v}^\alpha_F(\mathbf{k})\cdot\mathbf{v}^\beta_F(\mathbf{k}')}{|\mathbf{v}^\alpha_F(\mathbf{k})||\mathbf{v}^\beta_F(\mathbf{k}')|}\right), \tag{5.4}$$

where $l = 0$ ($l = 3$) corresponds to the charge (magnetic) scattering rate and $1/\tau_{\mathbf{k}\alpha} \equiv 1/\tau^0_{\mathbf{k}\alpha}+1/\tau^3_{\mathbf{k}\alpha}$ is the total scattering rate on band α. The term $\hat{\mathcal{V}}^{imp}_{\sigma\sigma'}(\mathbf{k}\alpha,\mathbf{k}'\beta)$ is the matrix element of the impurity Hamiltonian for the fully converged self-consistent eigenvalue problem,

$$\begin{aligned}\hat{\mathcal{V}}^{imp}_{\sigma\sigma'}(\mathbf{k}\alpha,\mathbf{k}'\beta) &\equiv \langle\mathbf{k}'\beta\sigma'|\mathcal{V}^{imp}|\mathbf{k}\alpha\sigma\rangle \equiv \langle\mathbf{k}'\beta\sigma'|\mathcal{H}-\mathcal{H}_{(V_{imp}=0)}|\mathbf{k}\alpha\sigma\rangle \\ &= \sum_{\mu\nu} a^{\alpha*}_{\mathbf{k}\mu}\omega^{\mu\nu}_{\mathbf{k}\sigma\mathbf{k}'\sigma'}a^{\beta}_{\mathbf{k}'\nu} - \epsilon_{\mathbf{k}\alpha}\delta_{\mathbf{k}\mathbf{k}'}\delta_{\alpha\beta}.\end{aligned} \tag{5.5}$$

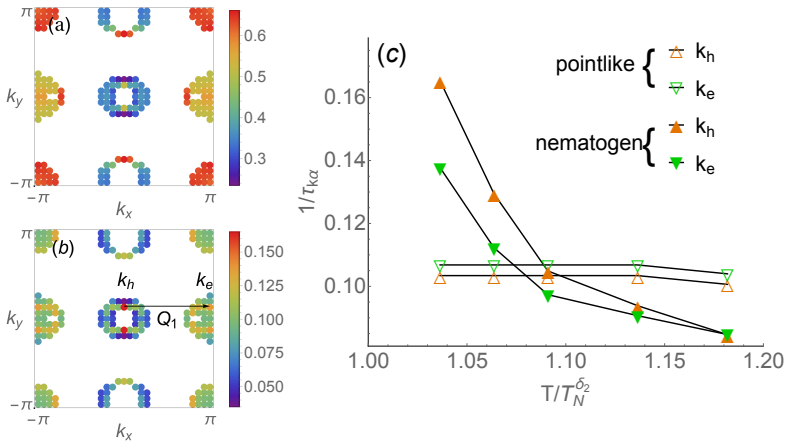

Figure 5.7: (a) Map of $1/\tau_{\mathbf{k}\alpha}$ vs. k_x, k_y for point-like $\hat{\mathcal{V}}^{imp}_{\sigma\sigma'}(\mathbf{k}\alpha, \mathbf{k}'\beta) = \hat{\sigma}_0 V_{imp} \sum_\mu a^{\alpha *}_{\mathbf{k}\mu} a^{\beta}_{\mathbf{k}'\mu}$ at $T/T_N^{\delta_2} = 1.036$. Values are shown for all $\mathbf{k}$ within a range $\sim 2k_BT$ of the Fermi surface. (b) Same map for nematogen with $\hat{\mathcal{V}}^{imp}_{\sigma\sigma'}(\mathbf{k}\alpha, \mathbf{k}'\beta)$ determined self-consistently. The arrow indicates the dominant $\mathbf{Q_1}$ scattering between the particle and hole pockets. (c) Scattering rates from (a) (scaled by 1/5) and (b) at $\mathbf{k}_h$, $\mathbf{k}_e$ plotted vs. T.

Here $\omega^{\mu\nu}_{\mathbf{k}\sigma\mathbf{k}'\sigma'} = \frac{1}{N} \sum_n \sum_{\mathbf{ij}} u^{n*}_{\mathbf{j}\nu\sigma'} u^{n}_{\mathbf{i}\mu\sigma} E_{n\sigma} e^{-i\mathbf{k}'\mathbf{r_j}} e^{i\mathbf{k}\mathbf{r_i}}$, and $a^{\alpha}_{\mathbf{k}\mu}$ are the matrix elements of the unitary transformation from orbitals to bands (see Appendix B). In order to decompose the total scattering rate into charge and magnetic channels in equation (5.4), we have used (in short hand notation) $|\mathcal{V}_\uparrow|^2 + |\mathcal{V}_\downarrow|^2 = (|\mathcal{V}_\uparrow + \mathcal{V}_\downarrow|^2 + |\mathcal{V}_\uparrow - \mathcal{V}_\downarrow|^2)/2$. Finally, $\mathbf{v}^{\alpha}_F(\mathbf{k})$ denotes the Fermi velocity of band α, and the last term in parentheses in Eq. (5.4) is an approximation to the vertex corrections in the full Kubo formula by Ziman [91] that has proven accurate for anisotropic scatterers [92].

In Fig. 5.7, we show the effect of local freezing of the spin fluctuations on the scattering rate anisotropy by plotting $1/\tau_{\mathbf{k}\alpha}$ explicitly, first for a point-like scatterer of potential V_{imp} with no self-consistency in 5.7(a). It is seen that the distribution of scattering weight reflects the small orbital ordering that has created a slightly orthorhombic Fermi surface (see also figure 5.5(a)). Since V_{imp} is momentum independent, the variation reflects primarily the band-orbital matrix elements for this model, i.e. $\hat{\mathcal{V}}^{imp}_{\sigma\sigma'}(\mathbf{k}\alpha, \mathbf{k}'\beta) = \hat{\sigma}_0 V_{imp} \sum_\mu a^{\alpha *}_{\mathbf{k}\mu} a^{\beta}_{\mathbf{k}'\mu}$. Figure 5.7(b) now shows how the nematogen scattering rate reflects the intrinsic spin fluctuations in the system. The localized object in real space couples fluctuations at all $\mathbf{q}$, but these include important contributions from those scattering processes that dominate the fluctuations in the homogeneous system, i.e. the scattering between like orbitals on hole and electron pockets as seen in 5.7(b). The point-like scatterer leads to a

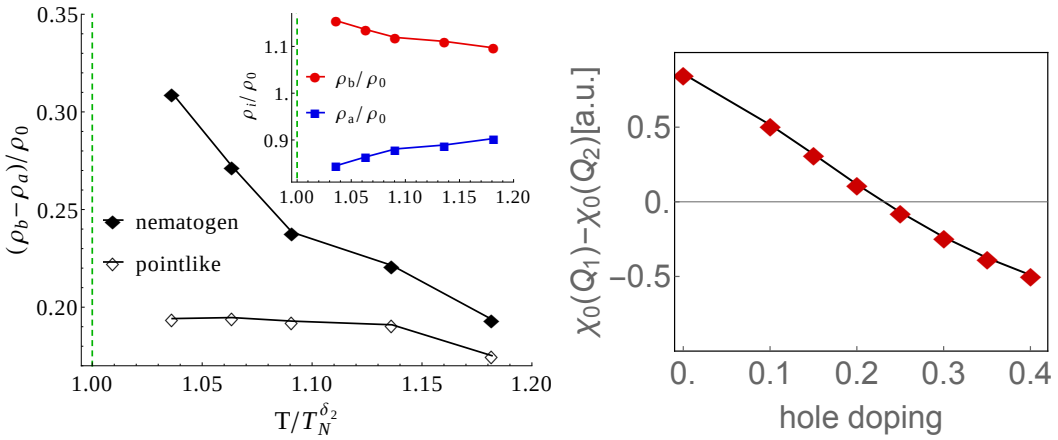

Figure 5.8: (a) Resistivity anisotropy $\Delta\rho$ versus T for non-self-consistent point-like (empty diamonds) and self-consistent nematogen (filled diamonds) impurity scatterers. Inset shows the T-dependence of ρ_a/ρ_0 (circles) and ρ_b/ρ_0 (squares) for the nematogen case. (b) Sign change of $\chi_0(\mathbf{Q}_1)-\chi_0(\mathbf{Q}_2)$ in the bare susceptibility at $n \sim 5.75$ as the system is hole-doped for a constant orbital order $\delta_1 = 16$ meV and $T/T_N^0 = 1.22$.

scattering rate that is nearly T-independent, while the nematogen scattering rate grows as the magnetic transition is approached, as shown in Fig. 5.7(c). For the nematogen scattering, the charge scattering rate is also nearly T-independent. It is the magnetic scattering rate that provides both the strong T-dependence and the enhanced anisotropy.

Turning finally to the conductivity obtained from

$$\sigma_{ij} = e^2 \frac{1}{V} \sum_{\mathbf{k}\alpha} \mathbf{v}_i^\alpha(\mathbf{k}) \mathbf{v}_j^\alpha(\mathbf{k}) \tau(\epsilon_{\mathbf{k}\alpha}) \left(-\frac{\partial f}{\partial \epsilon_{\mathbf{k}\alpha}} \right), \tag{5.6}$$

we show in Fig. 5.8 the resistivity anisotropy $\Delta\rho = (\rho_b - \rho_a)/\rho_0$ as a function of T with $\rho_0 = (\rho_a + \rho_b)/2$. As expected from Fig. 5.7, the anisotropy in the case of point-like scatterers is essentially T-independent and caused only by the band. On the other hand, for the nematogens $\Delta\rho$ rises rapidly upon approaching the magnetic instability, in agreement with experiments. As T_N is approached, the divergence of the spin fluctuation scattering rate is cut off eventually: in our simulation by the system size, in the real sample by the inter-nematogen distance.

5.2.3 Discussion

With the above results in hand, we can explain the key properties 1)-5) of the transport experiments discussed in the introduction. The impurity-based scenario with nematogens oriented along the longer a axis naturally explains points (1) ($\rho_b > \rho_a$) and (2) (annealing dependence). The temperature dependence of the nematogen scattering rate presented in figure 5.7 explains the upturn in ρ_b upon approaching T_N [point (3)]. Our picture assumes additionally that Ba122 system, in particular, contains significant amounts of disorder, which determines the large value of the resistivity near T_N. This is consistent with the large constant $\rho(T_N)$ and small T^2 coefficient in the parent and lightly doped materials [68]. These scatterers do not pin low-energy spin fluctuations, and hence cannot contribute to the resistivity anisotropy. In the parent compound even after annealing, a few vacancies in the FeAs plane creating stronger scatterers remain, and give rise to a small peak in the b-axis resistivity above T_N due to nematogen formation. Upon doping with Co, however, the concentration of nematogens rises quasi-linearly, enhances the resistivity anisotropy, and leads to peaks in ρ_b, as seen in experiment, until the critical doping where T_N goes to zero and the magnetic fluctuations driving the anisotropy weaken [point (4)]. The dramatic collapse of the transport anisotropy in the hole-doped system and sign change [point (5)], has two possible explanations in the elastic scattering scenario. The first one, doping with K introduces weaker out-of-plane scatterers that for the band structure in the underdoped regime cannot induce nematogens; the anisotropy is then essentially zero, with the exception of that driven by few residual in-plane vacancies. The second one is connected to the change in the spin response (through changes in the band structure) induced by the hole doping itself. We show in figure 5.8(b) the difference between the $\mathbf{Q}_1$ and $\mathbf{Q}_2$ bare susceptibility peaks of the system with a constant $\delta_1 = 16$ meV orbital order as a function of filling $n = 6 - x$ at high temperatures ($T/T_N^0 = 1.22$). The effect of the orbital splitting in enhancing the peak at $\mathbf{Q}_1$ and diminishing $\mathbf{Q}_2$ is weakened and eventually reversed, i.e. for sufficiently high hole-doping it enhances (diminishes) the spin susceptibility at $\mathbf{Q}_2$ ($\mathbf{Q}_1$). If a scatterer managed to pin the magnetic fluctuations in this region, they should rotate by $\pi/2$ with respect to the defects in the undoped system, and as the magnetic transition is approached contribute to the opposite transport anisotropy $\rho_b < \rho_a$.

We emphasize again that the physics of resistivity anisotropy in our view arises ultimately from the same anisotropy in the spin fluctuation spectrum invoked by the authors of Refs. [83, 84, 85]. Nevertheless, the importance of these fluctuations in the current picture is that they condense into an emergent defect state above T_N whose anisotropy grows in response to the small orthorhombic symmetry breaking below T_s, which then scatters electrons anisotropically. We have shown that a tiny Fermi surface asymmetry, reflected in a very weak anisotropy of the Drude weight,

is dramatically enhanced by spin fluctuations near T_N such that scattering rate anisotropies of order 100% are possible.

Strong evidence in favor of this picture comes from the annealing experiments of Ishida *et al.*[68], who show that when strong disorder is removed the anisotropy drops, and attribute the remaining anisotropy to Co atoms, as we do here. While a reduction in anisotropy with decreasing disorder is also possible in the inelastic scattering models, as pointed out e.g. by Breitkreitz *et al.*[85], it occurs in a parameter regime where spin fluctuation scattering dominates elastic scattering, in contrast to the situation in experiments.

In summary, we have discussed an impurity-driven scenario for the remarkable transport anisotropy in the nematic paramagnetic phase of Fe-based superconductors that explains the essential features of the measurements presented in section 5.1, and argues for an increased focus on the unusual role played by impurities in these systems with strong spin fluctuations near a magnetic transition. In the following section we present some of the new elastoresistivity measurements, the connection to nematogens, and the resulting challenges for theories based on anisotropic scattering mechanisms.

5.3 New developments and outlook

5.3.1 Elastoresistivity measurements

One of the most convincing evidences of an electronically driven nematic transition came from elastoresistivity measurements. [66] Applying tunable in-plane uniaxial *strain* (structural distortion) Chu *et al.* used the induced fractional change of the resistivity $(\rho_b - \rho_a)/\rho_0$ as a direct measure of the electronic nematic order parameter. Representative data showing the resistivity anisotropy (η) as a function of strain (ϵ) for different temperatures for the undoped $BaFe_2As_2$ are shown in figure 5.9(a). From a Ginzburg-Landau approach the response of the electronic nematic order parameter ψ in the limit of vanishing strain ϵ is obtained by minimizng the free energy [66],

$$\frac{d\psi}{d\epsilon} = \frac{\lambda}{a} = \frac{\lambda}{a_0(T - T^*)} \tag{5.7}$$

where a is the coefficient of the quadratic term of the nematic order parameter ψ (χ_{nem}^{-1}) and λ is the coupling between the strain and ψ. Now assuming that $\psi \propto \eta$, they fitted the linear part $d\eta/d\epsilon$ with a Curie-Weiss temperature dependence, and found a divergence upon approaching T_s from above, as shown in figure 5.9(b). The mean field nematic critical temperature T^* in equation (5.7) was extracted for several doping concentrations. It closely tracks the structural transition T_s, it is suppressed to zero at optimal doping and becomes negative at higher concentra-

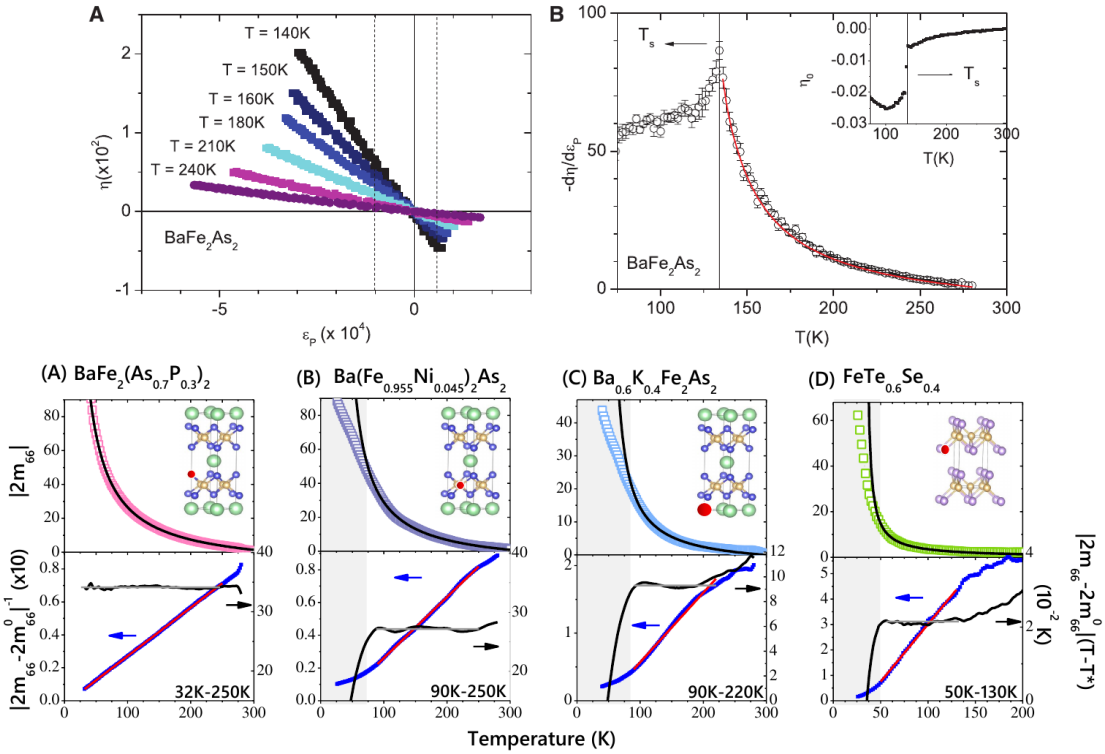

Figure 5.9: Elastoresistivity measurements. Top: (a) Relative change of resistivity $\eta = \Delta\rho/\rho_0$ as a function of strain $\epsilon = \Delta L/L$ at several temperatures above T_s. A linear fit of the data is shown in (b). The red line shows a fit to mean field model. From [66]. Bottom: Divergence of the elastoresistivy coefficient $m_{66} \propto \eta$ (in absolute value) of several families in optimally doped Fe-based SC. From [81].

tions. Recently, a systematic study of elastoresistivity coefficients on a wide range of Fe-based superconductors, reported the divergent anisotropic response to be a generic feature at optimal doping, illustrated in the lower row of figure 5.9. [81] This study included besides the electron doped Co and Ni doped $BaFe_2As_2$ compounds, the hole doped $(Ba_{1-x}K_x)Fe_2As_2$ system, which displays a sign change in η ($\rho_b < \rho_a$) and comparable absolute magnitude of the coefficient to the electron doped system. Similar results were obtained in isovalent substituted (it does not change the carrier concentration) $BaFe_2(As_{1-x}P_x)_2$ and chalcogenides $FeTe_{1-x}Se_x$.

The observed Curie-Weiss-like enhancement in these transport measurement is qualitatively consistent with shear modulus and Raman measurements, probes that have also studied nematic fluctuations in the paramagnetic state. [74, 75] The T^* values obtained from shear modulus measurements in Co–Ba122 agree remarkably well with the ones extracted from Raman measurements. The ones extracted from

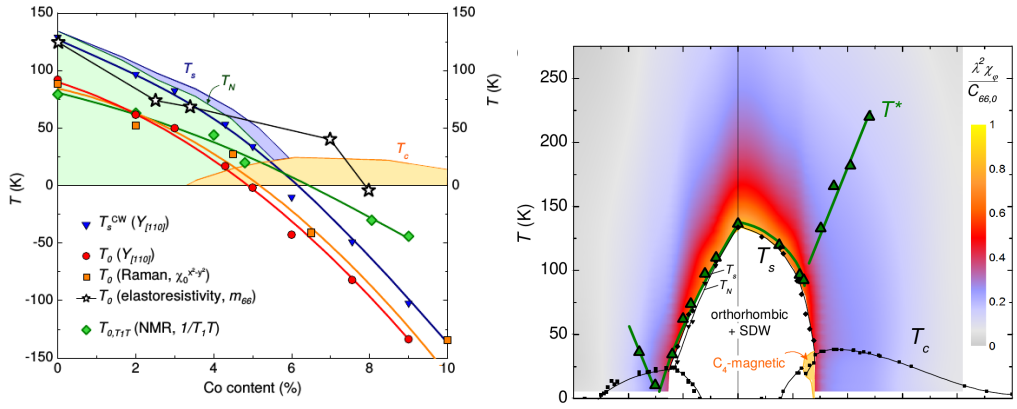

Figure 5.10: Right: Mean-field nematic critical temperature T^* by shear-modulus [21] (red circles), Raman scattering [75] (orange squares) and elastoresistivity [81] (black open stars). Left: Nematic susceptibility as a color-coded map in the composition-temperature phase diagram of Co-122 (left) and K-122 (right). From [21, 82].

transport measurements (figure 5.9) are however, significantly higher. The critical temperatures from the different probes can be seen in figure 5.10(a). Another relevant discrepancy between shear modulus and elastoresistance is the different doping dependence of T^* on the hole-doped side (K-122 samples). In the former, the nematic susceptibility is found to be largest for the undoped compound right above T_s and decrease smoothly with both electron and hole doping, as can be seen in figure 5.10(b). As we mentioned earlier, elastoresistivity places the maximum of the nematic susceptibility around optimal doping in both electron- and hole-doped sides. At the time of writing, the reason for this discrepancy is unclear.

The resistivity anisotropy of hole doped *detwinned* samples was introduced in section 5.1, and reported to be dramatically smaller than in the electron doped side [67] [figure 5.1(c)]. Despite the agreement in terms of the sign change $\rho_b - \rho_a$ for sufficiently hole doped compounds, the relative magnitude of the detwinned materials is quite different to the strain-induced elastoresistance. This last measurement finds a comparable anisotropy to the electron-doped systems (within a factor of two), as obvious from figure 5.9. Currently, the reason for this discrepancy is also unclear. There are, however, important differences between the "older" transport measurements presented in section 5.1 (uniaxial stress) and elastoresistance measurements (uniaxial strain), that one should keep in mind when doing comparisons:

- Under constant stress: applied to the system until the sample is fully detwinned, measure ρ at all T, also in the SDW state where one has FS recon-

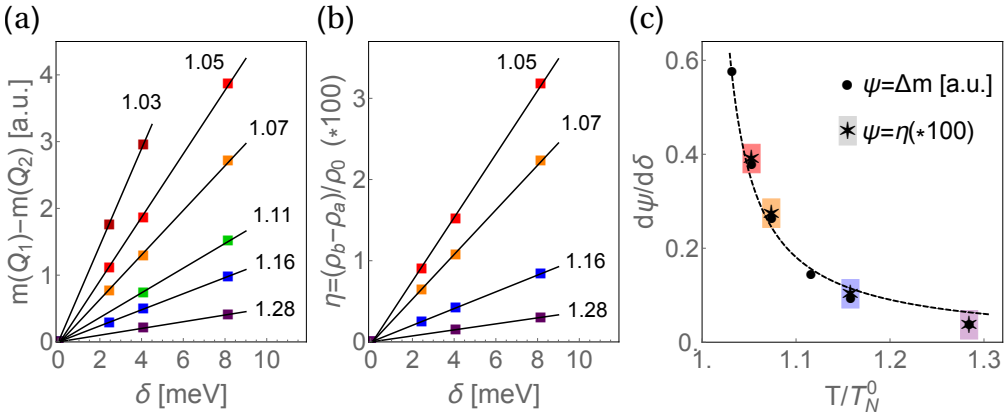

Figure 5.11: (a) Impurity-induced magnetic anisotropy $\Delta m \equiv |m(\mathbf{Q}_1)| - |m(\mathbf{Q}_2)|$ and (b) relative change of resistivity $\eta = \Delta\rho/\rho_0$ as a function of orbital order δ at several T above the tetragonal magnetic transition temperature $T/T_N^0 > 1$. A linear fit of both anisotropy responses $d\psi/d\delta$ in (a) and (b) is shown in (c) by black dots and stars, respectively. The dashed line shows a fit to Curie-Weiss temperature dependence with the critical temperature $T^* = T_N^0$.

struction.

- Under constant strain: orthorhombic distortion is controlled, measure the linear response of ρ at $T > T_s$.

Elastoresistivity is measurements stay always in the linear regime, whereas the constant stress experiments are most probably in the non-linear regime where other higher order terms may be important. In this respect, elastoresistivity measurements provide a more direct and controlled way of extracting information about the nematic order parameter.

We consider again the role of potential scatterers in the paramagnetic nematic phase and calculate transport properties under infinitesimal strain conditions. That is, what is the T dependence of the resistivity anisotropy *response* induced by a constant orbital order ($d\eta/d\delta$) arising from emergent defect states in the paramagnetic phase? We first show in figure 5.11(a) the anisotropy of the impurity-induced magnetic signal $\Delta m \equiv |m(\mathbf{Q}_1)|-|m(\mathbf{Q}_2)|$ (see $m(\mathbf{q})$ in figure 5.6) as a function of δ and several temperatures above the spin ordering temperature of the tetragonal system $T/T_N^0 > 1$. A linear fit of the data (black lines) is used to extract the T dependence of the magnetic anisotropy response $d\Delta m/d\delta$. As shown in figure 5.11(c), this local response (black dots) diverges upon approaching T_N^0, in a Curie-Weiss-like fashion (dashed line). The contribution to transport properties of the nematic defect states is calculated following the method of the

previous section, now as a function of δ and T. The resulting resistivity anisotropy for some of these defect states is shown in figure 5.11(b). A very similar response to the magnetic anisotropy shown in 5.11(a) is already apparent from this data. The resistivity anisotropy response $d(\Delta\rho/\rho_0)/d\delta$, plotted in figure 5.11(c) (stars), is almost identical to the magnetic anisotropy response (within a T independent constant), and diverges as T_N^0 is approached.

At higher ferro-orbital order strength $\delta > \delta_c \sim 10$ meV, the behavior of the resistivity anisotropy η can no longer be fitted to a linear function. The deviation becomes particularly pronounced at lower temperatures $T/T_N^0 \to 1$. This means that higher order terms become relevant in the resistivity calculation, and the system is no longer in the linear response regime. The $\delta > \delta_c$ non-linear regime is probably the relevant scenario for the uniaxial stress experiments presented in section 5.1, and what was used for the transport calculation in section 5.2.

These results show that the transport anisotropy response extracted from vanishingly small applied strain, i.e. the linear contribution to the anisotropy, can in principle be reproduced within the elastic scattering off nematogens scenario. The only requirement is having defects locally pinning spin fluctuations (details in chapter 4), and the scattering off such anisotropic states will induce a Curie-Weiss like T dependence in the resistivity anisotropy response [figure 5.11(c)]. The real challenge within the elastic scattering scenario is connected to the fact that the divergent anisotropy near optimal doping seems to be a generic feature [81]. This suggests some kind of substituent independence (Co, Ni, K, P, Te) and imposes constrains on theoretical models, which we discuss below.

5.3.2 Disorder independent transport anisotropy

Using this new technique, Kuo and Fisher[80] criticized the idea of an anisotropic scattering rate (both elastic and inelastic) as the source of transport anisotropy in the orthorhombic paramagnetic phase, since 1) as-grown and annealed samples have identical strain-induced resistivity anisotropies $d\eta/d\epsilon \propto m_{66}$, and 2) different chemical substituents (Co and Ni-substituted samples) corresponding to the same T_N exhibit very similar anisotropy responses as well, as shown in figure 5.12. This led (reasonably) to the conclusion that the measured transport anisotropy in the paramagnetic orthorhombic state cannot be due to elastic scattering from anisotropic defects, but can be understood in terms of Fermi surface anisotropy.

At first sight, the first observation [point (1)] seems to be in contradiction with what was reported by Ishida *et al* [68] [figure 5.2]. However, the older experiments were done under uniaxial *stress*, and the degree of detwinning and induced strain were not known. Like we mentioned earlier, it is safe to assume Ishida *et al* were not measuring the anisotropy of the system in the linear regime (where the induced strain is controlled), i.e. higher order terms were most probably relevant.

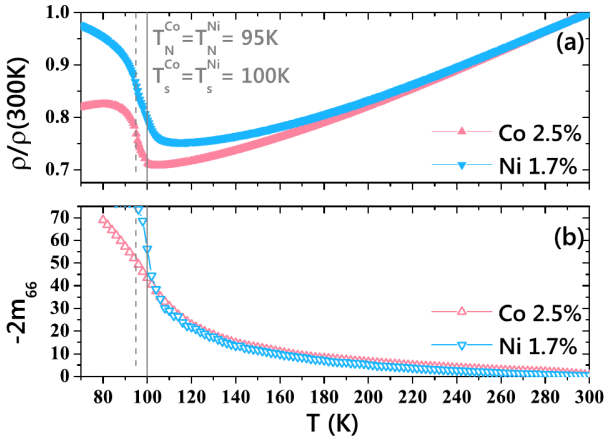

Figure 5.12: Comparison of elastoresistivity coefficients for Co and Ni doped samples with identical T_N values. T dependence of (a) the normalized resistance and (b) elastoresistivity coefficient $-2m_{66} \propto -d\eta/d\epsilon$. From [80].

It is not surprising then that both groups reached opposite conclusions, since their measurements were done under different experimental conditions.

The fact that the strain-induced anisotropies are identical [80] in as-grown (low RRR) and annealed (large RRR) samples [point (1)] does not directly rule out defect scattering effects. Large differences in sample quality and RRR (residual resistance ratio=R(300K)/R(0K)) are caused largely by out-of-plane disorder and lattice defects. If this kind of disorder does not create nematogens under infinitesimal strain, one should not expect a different resistivity anisotropy response. The main challenge for the elastic scattering mechanism is thus to prove that two different impurities like Co and Ni, with dissimilar scattering strengths, would give rise to the same resistivity anisotropy response $d\eta/d\delta$ [point (2)]. Moreover, that argument would have to hold for systems substituted with out-of-plane K and isovalent P, which, as mentioned earlier, exhibit comparable anisotropy responses.

From first principle calculations we know that the on-site potential differences between Co and Ni is about a factor of two ($V_{Ni} \sim 2V_{Co}$), i.e. Ni is twice as strong scatterer as Co is. [59] The next obvious question for the elastic scattering mechanism is then: how does the linear term of the resistivity anisotropy arising from emergent defect states presented on figure 5.11 depend on V_μ? We have shown that the anisotropy in the scattering rate arises from the spin fluctuations themselves, apparent in the diverging magnetic scattering rate; is there a regime where the charge part (τ^0) is negligible to the final anisotropy, and this is mostly determined by the magnetic part (τ^3)? A transport study using realistic impurity potentials relevant for Co and Ni could help establish the relevance of the bare

potential strength V_μ on transport anisotropy, which dressed by (the same) spin fluctuations give rise to a diverging magnetic scattering anisotropy. This will be the topic of future studies.

5.3.3 Nematogens in FeSe

We close this section with preliminary results of nematogens in FeSe, relevant for the transport anisotropy in these materials. FeSe undergoes structural and superconducting transitions at $T_s \sim 90$ K and $T_c \sim 8.5$, respectively, and does not develop long-range magnetic order down to the lowest temperatures. In principle, this makes FeSe a perfect candidate to disentangle contributions from magnetic and nematic orders in a wide T range. Resistivity measurements on strain-detwinned crystals of FeSe are shown in figure 5.13(d) for fixed strains ϵ_1 (blue) and ϵ_2 (purple) as a function of T. [93] Note the anisotropy has the opposite sign ($\rho_a > \rho_b$) to electron doped Ba-122. The measured anisotropy initially increases upon cooling, peaks slightly below T_s and decreases to small values on cooling down to the superconducting transition T_c . The strain-induced anisotropy response, $d\Delta\rho/d\epsilon$ (dashed orange line) displays a similar increase above T_s.

In order to explain these measurements by the elastic scattering mechanism, the first question to be addressed is: are nematogens developed in FeSe? If so, what kind of temperature dependence in the magnetic response and transport anisotropy should one expect in this system? ARPES measurements have reported data consistent with a more complex orbital type of order: a mixed s- and d-type ordering term. [94] We present below preliminary results that address some of these questions.

The first step involves finding a relevant band structure $\mathcal{H}_0$ for this system. Recently, Mukherjee *et al* presented a tight-binding band, which including a temperature dependent orbital order term, gave reasonable results for ARPES, quantum oscillations, Knight shift, spin-lattice relaxation and dynamical spin susceptibility compared to the experiments. [95, 96] The model assumes that below the structural transition at ~ 90 K the fourfold-symmetry broken phase is described by a mixed s- and d-type T-dependent orbital ordering term,

$$\mathcal{H}_{oo} = g(t)\left[\delta_s \sum_{\mathbf{k}} \left(n_{\mathbf{k}yz} - n_{\mathbf{k}xz}\right) + \delta_d \sum_{\mathbf{k}} \left(\cos k_x - \cos k_y\right)\left(n_{\mathbf{k}yz} + n_{\mathbf{k}xz}\right)\right]. \quad (5.8)$$

Here δ_s is the ferro-orbital order used throughout this chapter and δ_d is the bond-centered orbital order relevant for this material (for details see [95]). Both are assumed to have a mean-field T dependence $g(t)$ below T_s with $t = T/T_s$. Band splittings consistent with ARPES results [94] are reproduced by a $\delta_s = \delta_d = 50$ meV. At low temperatures, the spin susceptibility $\chi_s^{RPA}(\mathbf{q})$ of this model is

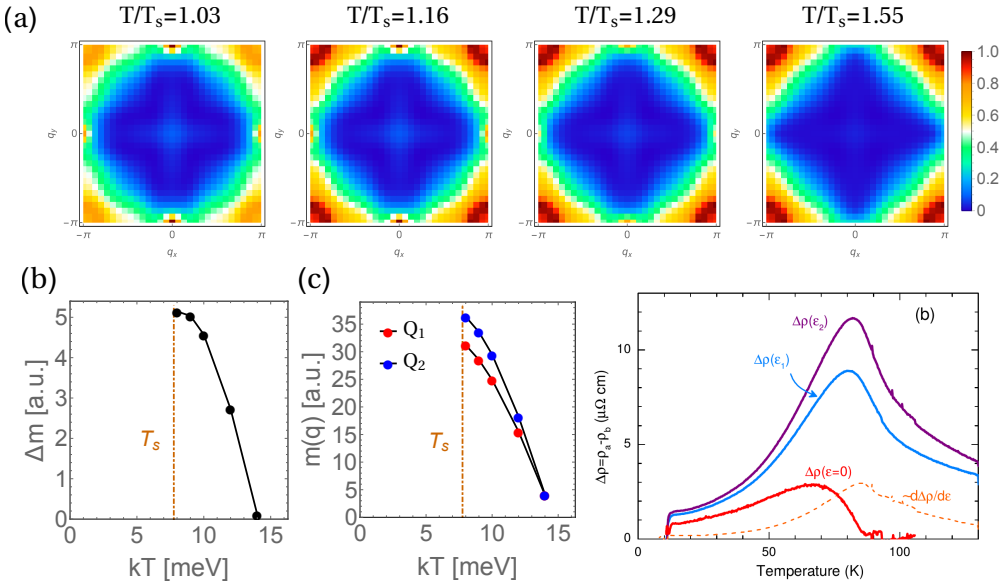

Figure 5.13: Transport anisotropy in FeSe. (a) $|m(q)|$ around a $V = 0.26$ eV defect for temperatures above T_s ($k_B T_s = 7.7$ meV $\rightarrow$ 90 K). The ferro-orbital order is set to $\delta_s = 5$ meV in the band structure from Ref. [96]. (b) Magnetic anisotropy pinned by the nematogen $\Delta m \equiv |m(\mathbf{Q}_2)| - |m(\mathbf{Q}_1)|$ and (c) the individual $|m(\mathbf{Q}_1)|$ and $|m(\mathbf{Q}_2)|$ components. Note $|m(\mathbf{Q}_1)| < |m(\mathbf{Q}_2)|$. (d) Resistivity measurements $\Delta\rho = \rho_a - \rho_b$ for two values of strain ϵ_1 and ϵ_2. The strain derivative $d\Delta\rho/d\epsilon$ was extracted from their difference $\Delta\rho(\epsilon_1) - \Delta\rho(\epsilon_2)$. The latter was used to extract the intrinsic part $\Delta\rho(\epsilon = 0)$. From [93].

very similar to the one presented in the previous section, i.e. $\chi_s(\mathbf{Q_1}) > \chi_s(\mathbf{Q_2})$. At temperatures above T_s, the strain is again assumed to induce a small ferro-orbital static order $\delta_s^* = \delta_s/10$. This results in a magnetic susceptibility with $\chi_s(\mathbf{Q_1}) < \chi_s(\mathbf{Q_2})$, opposite to the orbitally ordered state at low temperatures. Figure 5.13(a) shows the Fourier map of the magnetic structure around a weak potential $V_\mu = 0.26$ meV for different temperatures above the structural transition T/T_s in a system with $\delta_s^* = 5$ meV. The T dependence of the induced magnetic anisotropy $\Delta m \equiv |m(\mathbf{Q_2})| - |m(\mathbf{Q_1})|$ and the individual components are plotted in figures 5.13(b) and (c), respectively. These preliminary results look promising, because the transport anisotropy response arising from such nematogens should in principle give the right temperature diverging response with $\rho_a > \rho_b$. Resistivity calculations equivalent to those showed in figure 5.11 at $T/T_s > 1$ are thus the obvious next step.

Finally, at sufficiently low temperatures the orbital order ($g(t) \neq 0$) sets

in, and at sufficiently low temperatures reverses the magnetic anisotropy, i.e. $\chi_s(\mathbf{Q_1}) > \chi_s(\mathbf{Q_2})$. What happens to the nematogens in this T dependent environment? And how about the resulting T dependence of the resistivity anisotropy? The significant Fermi surface reconstruction in the orbital ordered state will certainly have an effect in the conductivity, through changes of both Drude weight and the scattering phase space. Model calculations of resistivity anisotropy in FeSe are essential to investigate whether the non-monotonic behavior reported in this material [figure 5.13(d)] is consistent with the anisotropic elastic scattering mechanism, and constitute another exciting future project.

5.4 Impurities in the spin-density wave phase

The relevance of impurity scattering to explain the resistivity anisotropy in Fe-based superconductors is currently under debate. In the beginning of this chapter, we presented transport measurements on detwinned samples (under uniaxial pressure) which suggested that elastic scattering might be significant in determining resistivity anisotropy, particularly in the antiferromagnetic state. [68] There are also indications of local defect states which break the C_4 symmetry. [77, 87, 88, 102, 103] Some clues are offered by STM experiments on defects in the underdoped, magnetically ordered phase, where the symmetry is already broken by the stripes spin-density wave order. Fourier transform scanning tunneling spectroscopy (STS) deduced the existence of electronic defects with C_2 symmetry[62] nucleated by the Co dopants in $Ca(Fe_{1-x}Co_x)_2As_2$, while a more detailed analysis reported a dimer structure.[76] A visualization of these anisotropic defects via current map at constant energy $I(\mathbf{r}, \omega)$ is shown in figure 5.14(a). The inset shows the environment of a Co atom, with a clear dimer shape. These dimers are approximately eight lattice constants (a) long and oriented along the AF a-axis (the Fe-Fe directions are along the diagonal direction). A Fourier transform of this map confirm a lack of periodicity, thus excluding periodic stripes as an explanation. It was further demonstrated that these states scatter quasiparticles in a very anisotropic manner, with the maximum scattering rate along the b-axis. This is consistent with the larger resistivity found along the ferromagnetic b-axis ($\rho_b > \rho_a$) in the low temperature antiferromagnetic phase in the electron-doped compounds.

As a first step in understanding the origin of local C_4 symmetry breaking observed in several experiments on various materials, it seems useful to study a situation where a known chemical impurity substitutes at a known position, and ask why such a dimer-like structure (with charge or local density of states peaks located such a great distance from the impurity site) should be induced by a Co atom. This problem should be accessible to weak-coupling theories of these systems, provided they account for the electronic states of the system to which

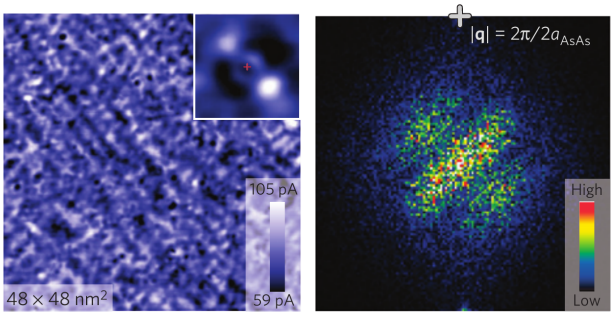

Figure 5.14: Visualizing the anisotropic impurity state structure in $Ca(Fe_{1-x}Co_x)_2As_2$. (a) Electronic structure as determined the current map $I(\mathbf{r}, \omega = -37meV)$. a and b axis are parallel to the diagonal directions. The inset shows characteristic non-dispersive electronic structure environment of a Co atom (red cross): a dimer-shaped impurity state $\sim 8a$ long. (b) Fourier transform of (a). No sharp peaks indicating a long-range periodic structure are seen in reciprocal space. From [76].

the impurity couples and treat interactions on the average. Hints that an unusual electronic state might be induced were found already in first principles calculations of a Co dopant in Ba-122, where the magnetic potential due to the Co was found to be oscillatory and exceed several unit cells[98]. Impurity-induced C_2 structures have been previously studied within a strong-coupling model[97] and a scenario based on a competing pocket density wave order which, however, has not been observed [99]. Finally, in Ref. [100], impurities were shown to pin fluctuating orbital order and create local states with broken C_4 symmetry but no dimerlike character.

Here, we study the origin of the electronic dimer states by an explicit, unbiased microscopic calculation of the local electronic densities near a point-like bare impurity potential within the SDW phase of the iron pnictides. We include a realistic account of the bands near the Fermi surface formed by the five Fe d-orbitals. The impurity causes a local (π, π) magnetic instability, which combined with the $(\pi, 0)$ order of the bulk SDW phase, results in unidirectional magnetic defects oriented along the AF a-axis, and associated electronic density dimers. This is a concrete example of a phenomenon which is largely unexplored, the local nucleation of a particular order in a bulk state with different order. We show how such emergent impurity states evolve from droplets at high temperatures T to nematogens in the low-T SDW phase. The final size of the low-T dimers is consistent with recent STM measurements[76], but depends within our theory on the "cooling rate", and we show how dimers of other lengths may also be obtained. Finally, we compute

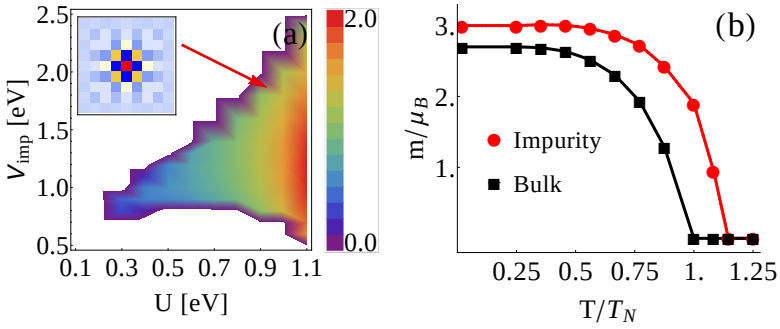

Figure 5.15: (a) Single impurity phase diagram displaying the impurity-induced magnetization at the impurity site at $T = 0$ vs. U and V_{imp}. Inset: spatial magnetization of the induced impurity state at $T = 0$ in the paramagnetic state. (b) Magnetization vs. T (normalized to the bulk Néel temperature T_N) at the impurity site (red curve) and in the bulk (black) with $U = 1.6$eV ($T_N = 0.3U$), and $V_{imp} = 0.1$eV.

the LDOS characteristics of the dimer states to compare with STM experiments, and discuss how our model can be used to perform realistic calculations of effective defect potentials for application to transport experiments.

5.4.1 Electronic dimers

One of the advantages of local probes like STM, is that they can directly access a single domain, and thus no detwinning technique is necessary. Measurements are done on free standing crystals. Here, we use the model introduced in the nematic phase, equation (5.1), and remove the ferro-orbital order term that described the external uniaxial pressure, i.e. we set $\delta = 0$. The kinetic part $\mathcal{H}_0$ is a tight-binding fit to the density functional theory (DFT) band-structure of Graser *et al.* [101] Similar results arise by using the band of Ikeda *et al* [32].

In Fig. 5.15(a) we show the single impurity phase diagram at low T for impurity-induced magnetic order vs. U and V_{imp} (below the bulk SDW phase transition at $U_{c2} \simeq 1.2$eV for $T = 0$). As seen, the potential generates local (π, π) magnetic order in a regime of intermediate strength repulsive V_{imp} (see chapter 4). When U exceeds U_{c2}, similar impurity-induced order takes place at high T above T_N as shown in Figs. 5.16(a,e). The local magnetic moment at the potential site is displayed in Fig. 5.15(b) where one clearly sees the extended magnetic impurity phase above T_N, and the enhanced impurity moments at low T over the bulk SDW magnetization. Upon lowering T, the C_4 symmetric high-T magnetic (π, π) droplets shown in Fig. 5.16(a,e) have to compete with the surrounding bulk $(\pi, 0)$

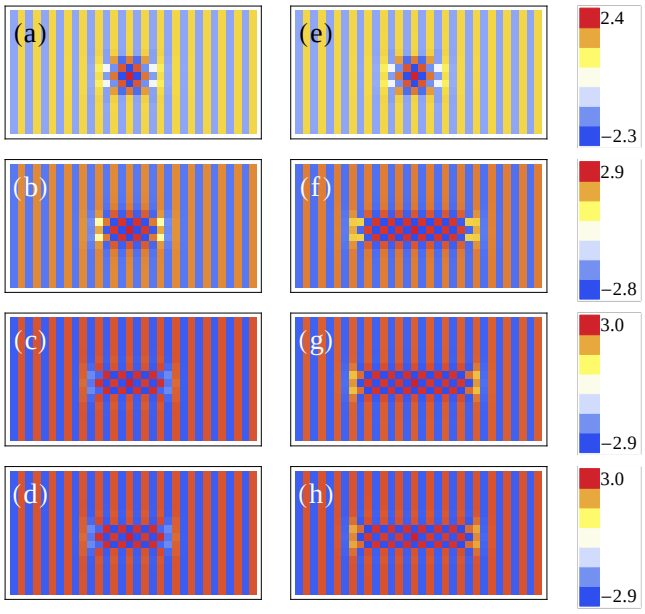

Figure 5.16: Magnetization in real-space upon lowering T with $U = 1.6$eV and $V_{imp} = 0.1$eV. From top to bottom: $T/T_N = 0.88, 0.67, 0.46, 0.25$. At each T, the system is iterated until the bulk magnetization has converged. The final low-T nematogen is stable and fully converged, but its length depends on the "cooling rate", as seen by comparison of the left and right columns distinguished by different cooling steps $\Delta T/T_N$=0.21 (left), 0.105 (right). Note that only half of the steps are shown for the slow cooling case.

SDW order. As shown in Fig. 5.16, the C_2 structure of the SDW phase leads to a magnetic cigarlike impurity structure, a nematogen aligned along the AF a-axis, which still exhibits the internal (π, π) magnetic structure of the high-T phase, but inherits an overall C_2 symmetry from the SDW background. While these low-T nematogens shown in Fig. 5.16 are stable and fully converged, their final length depends on the path of convergence, i.e. the number of steps taken in the cooling process, as seen explicitly by comparing the right and left columns in Fig. 5.16. The origin of this "cooling rate" dependence is simply a competition between the impurity-induced (π, π) moments and the SDW long-range order. We note that the existence of the nematogens is robust, and not dependent on the cooling rate, band-structure, or strength of the impurity potential V_{imp}.

Figure 5.17 summarizes the magnetic and electronic properties of the unidirectional low-T nematogens. As seen from Fig. 5.17(a,d), the impurity-induced magnetization nematogen consists of an odd number of sites (even number of lattice spacings) in length and width, and is always oriented along the AF a-axis.

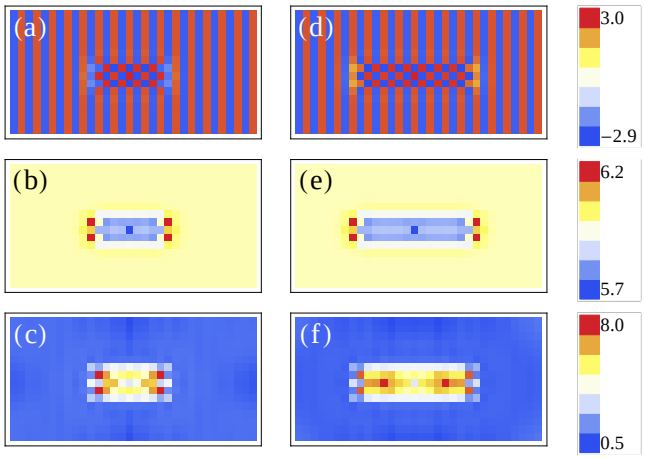

Figure 5.17: 2D real-space maps of (a,d) the magnetization, (b,e) the total electron charge density, and (c,f) the low-energy integrated LDOS for the same two low-T nematogens shown in Fig. 5.16(d,h).

This is because such a structure can lower its energy with a long unfrustrated boundary with the $(\pi, 0)$ order. In addition, in Fig. 5.17(b,e) we see that the nematogen exhibits peaks at both ends, resulting in an electronic dimerlike structure of the total charge density. This appears to be a general characteristic of these emergent impurity states, and also follows from the same energetic considerations, since the magnetic energy can be lowered by creating a charge state as homogeneous as possible; thus the excess charge from the impurity site is moved to the ends of the nematogen. Previous STM work has discovered the existence of electronic dimers in the LDOS,[88, 77, 102, 103] and recent partially integrated LDOS within the SDW phase found strong evidence for electronic dimers near Co dopants in $CaFe_2As_2$ [figure 5.14].[76] Within the present scenario, the existence of density dimers naturally explains the presence of LDOS dimers. However, as opposed to the robust existence of the nematogens, the detailed structure of the LDOS near the impurity sites is more sensitive to parameters. In Fig. 5.17 we show the integrated LDOS from -37meV to 0meV, which is identical to the range used in Ref.[76], indeed produces an LDOS dimer of $\sim 8a$ in both cases.

Figure 5.18 displays in greater detail the LDOS properties of the nematogens. The first point we wish to illustrate is that the size of the dimers deduced from the low-energy integrated LDOS is not necessarily the same as that in the (fully integrated) charge distribution. The low-energy integrated LDOS shown in Figs. 5.17(c,f) exhibits the dimer structure because of a peak in the LDOS at a particular site within the low-energy integration window. Figures 5.18(a,d) show the LDOS at an energy corresponding to the peak in the LDOS at this site, yield-

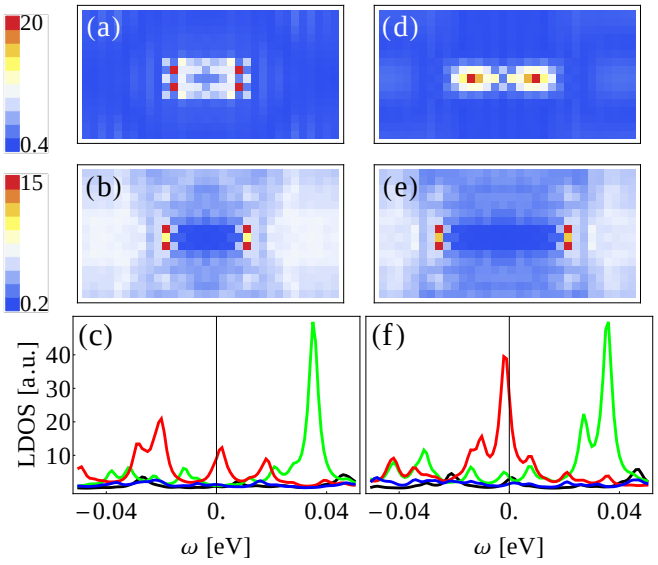

Figure 5.18: (a,b,d,e) 2D real-space maps of the LDOS at the characteristic low-energy dimer energy $\omega = -20$meV (a) and $\omega = -2$meV (d) and at the charge peak energy $\omega = -330$meV (b,e) for the nematogens in Fig. 2.6(b,e). Panels (c,f) display LDOS vs. ω for different sites in the system: bulk (black), impurity site (green), at the low-energy dimer peak (red), and at the charge density peak (blue).

ing essentially the same result as in Figs. 5.17(c,f). For the current parameters, the LDOS at the (distinct) sites where the charge distribution is maximal [Fig. 5.17 (b,e)] exhibits a peak at higher binding energy, as shown in Figs. 5.18(b,e). The structure of the low-energy LDOS can be more clearly inferred from Figs. 5.18(c,f) which show the energy dependence of the LDOS at several relevant sites in the nematogen. From the LDOS on the site corresponding to the low-energy dimer peak, for example, it is evident why the low-energy integrated LDOS exhibits a peak at roughly $4a$ from the impurity site in this case.

Local C_4 symmetry breaking defect signatures, including vortex states[77], have been observed in many different Fe based superconductors. We have not exhibited a mechanism for explaining all of them, but have begun the process of realistic modeling of those which can be expected to be driven by bulk magnetic order. The remarkable existence of large scale charge dimers induced around the impurities in our calculations is consistent with STM measurements on Ca-122[76], but it is intriguing that even larger electronic dimers have also been imaged by STM in FeSe samples which are not thought to be magnetic[77, 102]. While the simulations we have presented here are consistent with the sign and magnitude of the transport anisotropy in the ordered phase $T < T_N$, i.e. the stronger scattering along the

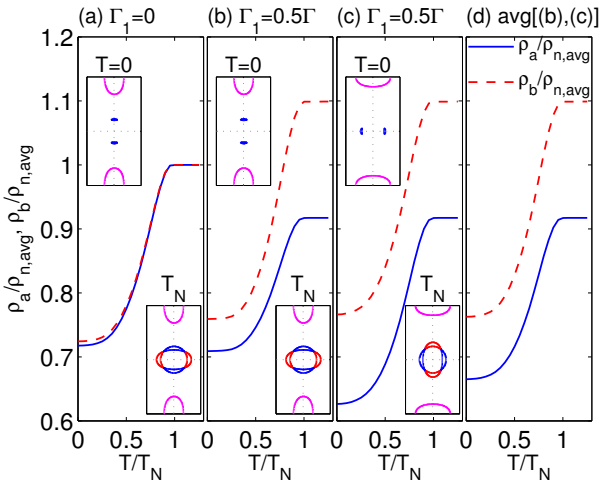

Figure 5.19: (a) Resistivity $\rho_{a,b}$ at $k_z = \pi$ for a 2-band model with isotropic scatterers ($\Gamma_1 = 0$). (b)–(c) Same at $k_z = \pi, 0$, respectively, for the anisotropic scatterers ($\Gamma_1 \neq 0$). (d) The average of (b) and (c). From [104].

b-axis induced by an object elongated along the a-axis, a conductivity calculation in the symmetry broken SDW phase including anisotropic scatterers is highly desirable.

We have been partly involved in a recent transport calculation in a two-band model, where current relaxation was assumed to be due to impurity scattering. [104] Figure 5.19 captures the main results, which are listed below:

1. The characteristic drop in the total resistivity below T_N is a consequence of a temperature driven Lifshitz transition, i.e. the collapse of the scattering rate due to the decrease in phase space upon partial gaping of the FS overcompensates the loss of carriers.

2. This result applies to a multiband system in a "dirty" limit, $\tau > W_0$, where W_0 is the SDW potential at $T = 0$.

3. Consistent with the results presented in section 5.2, extended anisotropic impurity states aligned along a give rise to $\rho_b > \rho_a$ in the paramagnetic state. More importantly, the anisotropy is independent of the ellipticity of the electron pockets provided the scattering is dominantly intra-band. Note that in 122 systems, the ellipticity of the electron pockets varies along k_z, with opposite signs in $k_z = 0$ and $k_z = \pi$. Consequently, in theories where the sign of the anisotropy is determined by the ellipticity of the electron pockets, at least a partial cancellation is expected after the k_z average.

4. In the SDW phase the above holds when the SDW potential is weak enough.

Resistivity results along the a- and b-axis for an anisotropic versus nematogen scatterers are shown in figures 5.19(a) and 5.19(b)-(d), respectively. The unusual temperature dependence of the resistivity and its anisotropy can thus be successfully described by considering the effect of anisotropic impurity scattering within a simple two-band model of a dirty SDW metal.

5.5 Conclusions

We have discussed an impurity-driven scenario for the transport anisotropy in Fe-based pnictides. In the paramagnetic nematic phase, the anisotropic spin fluctuations can be frozen by disorder, to create elongated magnetic droplets whose anisotropy grows as the magnetic transition is approached. Such states act as strong anisotropic defect potentials which scatter with much higher probability perpendicular to their length than parallel, although the actual crystal symmetry breaking is tiny. We have calculated the scattering potentials, relaxation rates, and conductivity in this region, and shown that such emergent defect states can explain all essential features of the transport anisotropy observed in experiments. New challenges to the elastic scattering mechanism from elastoresistivity measurements have been presented, and we have discussed pertinent calculations to help settle these issues. Finally, we have extended the impurity-induced emergent states theory to the the spin density wave phase. Stable unidirectional nematogens are formed locally, directed along the a-axis, and have typical length of ~ 10 lattice constants. Interestingly, these cigarlike impurity-states exhibit a dimer structure in the electronic density, in excellent agreement with STM experiments. The temperature dependence of the observed resistivity anisotropy in this phase was captured within a simple model of a dirty SDW metal with nematic defect structures.

Chapter 6

Unconventional disorder effects in correlated multi-band superconductors

Most of the material in this chapter has been published in
Phys. Rev. B 88, 220509(R) (2013). Part of it is in preparation to be submitted.

6.1 Introduction

The fundamental mechanism that causes the high-temperature superconductivity in FeSC is still a debated issue. The study of disorder leads to crucial information about the internal pairing symmetries of the condensate, and thereby the mechanism itself. For cuprates, heavy-fermions, and FeSC the study of disorder currently constitutes a very active line of research, motivated largely by the fact that these systems are made superconducting by "chemical disordering" (charge doping), but also boosted by controversies of the correct microscopic model, and a rapid development of local experimental probes over the past couple decades. [47, 112, 54] Focusing on multi-band FeSC, disorder studies have proven exceptionally rich and strongly material dependent. [110] Scanning tunneling spectroscopy has revealed a plethora of exotic atomic-sized impurity-generated states [88, 114, 115, 116], NMR and neutrons observe clear evidence of glassy behavior [117, 118], and μSR reveals magnetic phases generated by non-magnetic disorder. [136, 137] The resulting complex inhomogeneous phase and its properties in terms of thermodynamics and transport constitute an important open theoretical problem in the field.

In this chapter we study correlation-driven emergent impurity effects of both magnetic and nonmagnetic disorder relevant for Fe-based superconductors. We focus first on the spectral properties of the single-impurity problem in a multi-band

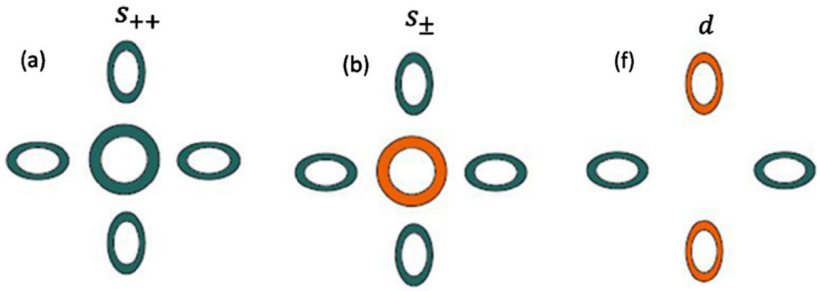

Figure 6.1: Schematic gaps $\Delta_\alpha(\mathbf{k})$ of FeSC. Color represents phase the order parameter. From [106]

superconductor in section 6.2 and move onto multi-impurity systems in section 6.3.

6.1.1 Gap symmetry and structure

The superconducting order parameter Δ or "gap function", is a complex function with both amplitude and phase that describes the macroscopic quantum state of Cooper pairs. The general BCS gap equation for multiband system with intra- and inter-band interactions $\Gamma_{\alpha\beta}(\mathbf{k}, \mathbf{k}')$ is given by

$$\Delta_\alpha(\mathbf{k}) = -\sum_{\mathbf{k}'\beta} \Gamma_{\alpha\beta}(\mathbf{k}, \mathbf{k}') \frac{\Delta_\beta(\mathbf{k}')}{2E_{\beta\mathbf{k}'}} \tanh \frac{E_{\beta\mathbf{k}'}}{2T}. \tag{6.1}$$

where α, β are band indices, and $E_{\beta\mathbf{k}'}$ is the quasiparticle energy. Details of the pairing interaction $\Gamma_{\alpha\beta}(\mathbf{k}, \mathbf{k}')$ can induce a variation in momentum space of the amplitude of the SC order parameter $\Delta_\alpha(\mathbf{k})$, or a variation of phase that could imply a change of sign. Understanding both the symmetry character of the superconducting ground states and the detailed structure should then provide clues to the microscopic pairing mechanism in the FeSC. Over the past years, a large number of experimental probes and theoretical works have focused on extracting information on the gap function in these materials [3, 105, 106].

The most relevant symmetry classes to the discussion of FeSC systems are the s-wave and d-wave symmetries. These tell you how the gap transforms under operations of the tetragonal symmetry of the crystal, for example whether it changes sign under a $\pi/2$ rotation. There are strong theoretical reasons supporting s-wave symmetry at optimal doping as will be shown below, but also possible exceptions to this in overdoped regions where d-wave symmetry becomes relevant. Within a given symmetry class, the order parameter $\Delta_\alpha(\mathbf{k})$ can also have a momentum dependent variation, i.e. a gap structure. This describes, for example, the internal

sign between the different FS, or the existence of nodes at a particular location. For the s-wave symmetry, the community has mostly focused on two possibilities: the so-called s_{++} and $s_{\pm}$ states. The former, shown in figure 6.1(a), has the same gap sign on both electron and hole pockets, whereas in the $s_{\pm}$ state, shown in figure 6.1(b), there is a sign change between those pockets. Both of these states have s-wave symmetry, and thus the OP maintains its sign under $\pi/2$ rotation. In d-wave states, on the contrary, there is a sign change of the OP under a $\pi/2$ rotation, as can be seen in figure 6.1(c).

The origin of pairing and details of the resulting gap structure are not topics we will focus on. Here, we present a brief description of the fluctuation exchange pairing mechanism. This is the mechanism that will be assumed to be responsible for superconducting pairing in our approach, in line with the itinerant scenario employed throughout our work. An overview of the different proposed pairing mechanisms in FeSC, including strong-coupling theories can be found in Refs.[105, 106] and references therein. Using a generalization of the 1-band spin fluctuation theory [107] to the multiorbital case, the effective pairing vertex is given by

$$\Gamma^{\beta\nu}_{\mu\alpha}(\mathbf{k},\mathbf{k}') = \left[\frac{3}{2}U^s\chi_s^{RPA}(\mathbf{k},\mathbf{k}')U^s + \frac{1}{2}U^s - \frac{1}{2}U^c\chi_c^{RPA}(\mathbf{k},\mathbf{k}')U^c + \frac{1}{2}U^c\right]^{\beta\nu}_{\mu\alpha}, \quad (6.2)$$

with the RPA spin- χ_s^{RPA} and charge susceptibilities χ_c^{RPA}, and where U^s and U^c are 5×5 matrices in orbital space with the Coulomb interaction parameters U, U', J and J' introduced in chapter 2. [35] Pairing from exchange of fluctuations thus contains contributions from *both* charge/orbital and spin fluctuations. For physical values of bare interactions, i.e. repulsive Coulomb U, U', J and J' interactions, the spin fluctuation terms χ_s^{RPA} dominate, since one is close to a magnetic instability. Pairing from repulsive Coulomb interactions, together with the structure of the Fermi surface, i.e. a repulsive interaction between hole and electron pockets, was used to predict the $s_{\pm}$ state early after the discovery of these materials. [108, 109] On the other hand, the importance of orbital degrees of freedom has motivated studies where the orbital fluctuations are found to play the leading role. An enhancement of the interorbital interaction parameter $U' > U$, for example, introduces a singularity in the charge channel. Some authors have sought the enhancement of the orbital channel by going beyond RPA and including Aslamasov-Larkin diagrams. [100] In that case, the resulting SC ground state is an s_{++} state. This shows the intimate relation between gap structure and the origin of SC, and has motivated a large number of experimental and theoretical works to extract information about the superconducting gap structure.

From the experimental point of view, even though many of the results appear as an ordinary consequence of the $s_{\pm}$ state, there are alternative explanations involving the s_{++} state as the ground state of the SC state. A recent review on

the SC state of FeSC regarding symmetry and structure aspects can be found in Ref. [106]

In our approach we will assume conventional bare interaction parameters, which lead to an enhancement of the spin fluctuation channel in equation (6.2) and results in an $s_{\pm}$ state. As mentioned earlier, we will not focus on the origin of the pairing, but rather on the role played by disorder in the multi-band $s_{\pm}$ state.

6.1.2 Impurity bound states

It is crucial to understand the role of disorder in high-temperature superconductors (SC) because the materials are obtained from chemical doping with substitutional impurity atoms. In addition, through the large advance of scanning tunneling microscopy (STM), local perturbations in the host material act as nano-probes of the underlying quantum state. For instance, the single-impurity problem has been applied with success to the study of cuprate SC [47, 112, 142].

The observation of a localized resonance near a nonmagnetic impurity in STM is one of the clearest indications of a sign-changing order parameter. This can be understood from quasi-particle scattering off a single-impurity. Nonmagnetic impurities are pair-breakers if they scatter electrons between portions of the Fermi surface with gaps of different sign. As a result, this kind of disorder does not induce in-gap bound states in the s_{++} state, and bound state formation was pointed out to be a useful tool to distinguish between s_{++} and $s_{\pm}$ states in early FeSC related theoretical works. If no bound state is seen, however, one may not conclude that the SC gap does not change sign. In two band models, it has been pointed out that the multiband aspect of these materials requires fine tuning of the potential for the bound state position and formation.[105, 128] We will show in the following section that within a realistic five-orbital model one always gets bound states if the potential is strong enough, and weaker potentials mainly cause spectral weight shifts between the SC coherence peaks. Magnetic impurities on the other hand, induce bound states in both s_{++} and $s_{\pm}$ states. Another possible complication arises then when establishing the magnetic nature of the impurities, since a nonmagnetic impurity can induce local magnetic order in the presence of correlations (see chapter 4).

From the experimental point of view, the LDOS measured by STM spectroscopy provides valuable information near defects. There are few cases where sub-gap quasiparticle excitations induced by (possibly in some cases) nonmagnetic impurities have been reported. Grothe *et al.* [88] systematically characterized five predominant defects in LiFeAs and observed multiple resonant states. In a similar study, Hanaguri *et al.* have located at least six different defect sites on the surface of LiFeAs, some of which induce genuine sub-gap bound states, as can be seen in figure 6.2.[119] The magnetic nature of the defects in the previous two experiments

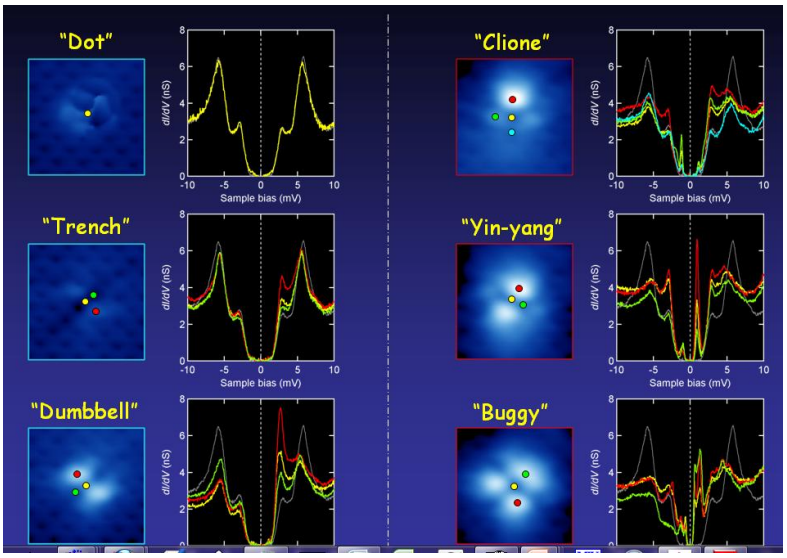

Figure 6.2: STM and STS measurements on native defects of LiFeAs. Some of the dI/dV spectra show clear in-gap bound states. From [119]

is unknown, but one may speculate that at least some of them are non-magnetic. Finally resonant-states around Cu atoms in NaFeAs were identified by Yang *et al.* [45] In this experiment, a careful study of DC magnetization suggested that Cu was non or very-weakly magnetic. As we will show in the next section, from a theoretical point of view, the difficulty of identifying these impurity-induced states is related to the broad features induced by weak non-magnetic impurities like Co or Ni. In these cases, the impurity pole occurs at energies between the SC coherence peaks, and the coupling to extended states larger that the gap minima broadens the impurity-state, effectively obscuring it. For an extended review on STM contributions to the understanding of the SC gap in FeSC the reader is referred to Ref. [111].

All these experimental findings have been claimed to be consistent with a single potential in the $s_{\pm}$ state. At the time of writing, there is however no theory which correctly captures the spectroscopic signatures of all these the complex states, nor the breaking of tetragonal symmetry in some of the cases shown in figure 6.2. The first part of the work presented in this chapter was motivated by the complex spectroscopic signatures in figure 6.2 and a first step towards realistic modeling of impurity states in multi-orbital superconductors is introduced in section 6.2.

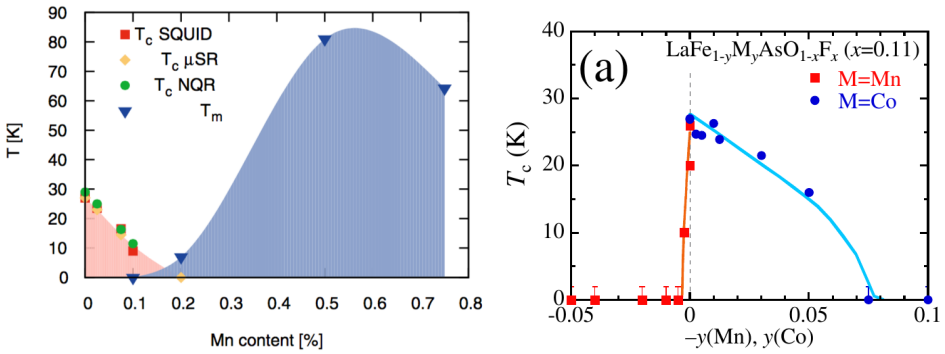

Figure 6.3: (a) Electronic phase diagram of $La(Fe_{1-x}Mn_x)AsO_{0.89}F_{0.11}$. The SC critical temperature T_c is determined from the techniques as specified in the inset. The magnetic transition temperature T_N was determined by μSR. Remarkably a $\sim$ 0.2% of Mn ($x = 0.002$, few per thousand!) destroys superconductivity. From [132]. (b) We show for comparison the Mn and Co T_c suppression from resistivity measurements, where the extreme effect of Mn is obvious. From [133]

6.1.3 T_c suppression

What are the consequences of including multiple impurities in the superconducting phase? The destruction of superconductivity by disorder is traditionally described by Abrikosov-Gorkov (AG) theory. This theory, however, ceases to be valid when interactions become important, impurities interfere and the SC order parameter is no longer homogeneous. In the second part of this chapter we study the effects of disorder, both magnetic and nonmagnetic, in the presence of correlations.

The study of magnetic impurities in the SC phase is motivated in part by the following remarkable experimental facts evident from Fig. 6.3(a): in optimally doped $LaFeAsO_{1-x}F_x$ a mere $\sim$ 0.2% magnetic Mn ions is enough to fully destroy the superconducting state. This extreme destruction of bulk superconductivity has been recently dubbed "the poisoning effect"[132]. Beyond $\sim$ 0.2% a new static magnetic phase is stabilized by this dilute concentration of Mn ions as seen from Fig. 6.3(a), with a 100% magnetic volume fraction (as seen by muons) at the lowest T. By contrast, for $NdFeAsO_{1-x}F_x$ and $SmFeAsO_{1-x}F_x$ near optimal doping, the corresponding T_c suppression rate is much lower with $\sim$ 4% ($NdFeAsO_{1-x}F_x$) and $\sim$ 8% ($SmFeAsO_{1-x}F_x$) being required to wipe out superconductivity[133, 134]. The severe T_c suppression found in Mn doped La-1111[132] agrees with transport measurements, shown in figure 6.3(b). The extreme effect of Mn (magnetic) as compared to that of Co (nonmagnetic) is obvious from this figure. In section 6.3, we extend the order-from-disorder theory developed in chapter 3 to the super-

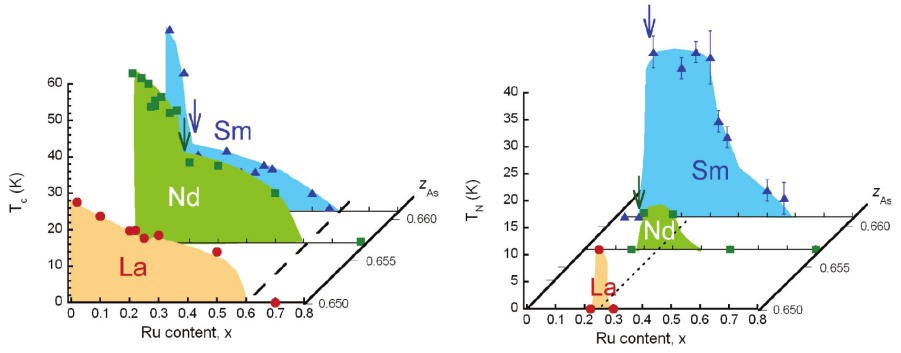

Figure 6.4: Transition temperatures in optimally doped $L(Fe_{1-x}Ru_x)AsO_{1-y}F_y$ for L = La, Sm and Nd as a function of Ru content. (a) SC critical temperatures T_c and (b) magnetic ordering temperatures T_N from μSR measurements. From [137].

conducting phase, and find that this model can naturally describe the poisoning effect.

Recent systematic experimental studies have focused on the properties of Ru ions substituting for Fe in optimally doped Sm-1111, Nd-1111, and La-1111[135, 136, 137]. In agreement with naive expectations of isovalent disorder, it takes a large amount (60%) of Ru to suppress T_c (an order of magnitude larger than Co for example). The T_c suppression as a function on Ru content in the three systems is shown in figure 6.4(a). Interestingly, however, a magnetic phase is induced at intermediate values of Ru content x, centered roughly around $x = 0.25$, and existing only at a finite span of Δx of Ru concentrations, as can be seen in figure 6.4(b). The magnetic phase is most pronounced with largest Δx and highest T_N in $SmFeAsO_{1-x}F_x$ and only marginally present in $LaFeAsO_{1-x}F_x$ where the poisoning effect upon Mn substitution was displayed. The appearance of static magnetism (arrows in figure 6.4) is concomitant with a marked change of the derivative $dT_c(x)/dx$. In the second part of section 6.3, we consider nonmagnetic disorder and explore the consequences of impurity-induced bound states around particular disorder structures. The appearance of a short-range magnetic phase at intermediate content x accompanying a change of $dT_c(x)/dx$ can be explained by considering local changes in clusters of impurities (dimers, trimers etc).

A final important development is the observation of a component of SDW order observed by e.g. muon spin rotation (μSR) experiments near optimally doped $Ba(Fe_{1-x}Co_x)_2As_2$[138, 139, 140] which "cooperates" with, rather than competes with SC as is commonly assumed. This component, which exists in an intermediate doping range around optimal doping, is evidently correlated with disorder and disappears above T_c.

6.2 Spectroscopic signatures of a single-impurity

For the Fe-based superconductors (FeSC), a recent series of experiments have measured the local density of states (LDOS) near various impurity sites.[110] In particular, STM measurements within the SC state have focused largely on FeSe, LiFeAs, and NaFeAs,[77, 103, 113, 114, 88, 119, 78] revealing a complex pattern of distinct impurity-induced LDOS modulations including unusual sub-gap bound states, local C_4 symmetry breaking, and generation of electronic dimers. At present no theoretical model exists which correctly captures the LDOS structure near these different impurity sites.

Theoretically, both potential and magnetic point-like scatterers can generate in-gap bound states in multi-band $s_{\pm}$-wave SC. The single-impurity problem has been addressed both within simplified two-band models,[120, 121, 122, 123, 124, 125, 126] and a five-band approach,[127] reaching, however, different conclusions about the presence and location of in-gap bound states. Recently, an important source of this discrepancy was shown to be the sensitivity of the low-energy states to the band structure and SC gap shape.[128, 105] For modeling disorder effects in FeSC, it is therefore crucial to include the correct band structure and minimize the sensitivity of the gap structure by self-consistently calculating the SC gaps arising from this band.

In this section, we present a first step towards realistic theoretical modeling of impurity states in LiFeAs, including magnetic correlations, by fixing both the band and the SC pairing constants from the DFT-acquired band structure of this material. The remaining degrees of freedom are associated with the impurity potential V_μ and the strength of the electronic correlations. Below, we focus first on the LDOS in the uncorrelated SC (U=J=0) and map out the LDOS around non-magnetic and magnetic impurities in LiFeAs. Second, when including correlations ($U, J \neq 0$) we show how impurities can locally induce magnetic order, and how STM measurements of the LDOS can be used to confirm our picture.

6.2.1 Homogeneous superconducting state

The starting point of the theoretical analysis is the following five-orbital Hamiltonian which describes the clean correlated superconducting system,

$$\mathcal{H} = \mathcal{H}_0 + \mathcal{H}_{int} + \mathcal{H}_{BCS}. \tag{6.3}$$

Here $\mathcal{H}_0$ constitutes the kinetic part obtained from a tight-binding fit to the DFT band-structure of LiFeAs. The explicit form of the tight-binding Hamiltonian is listed in Appendix C. The chemical potential is fixed so that the doping $x = \langle n \rangle - 6.0 = 0.0$, with the resulting structure and Fermi surface shown in figure 6.5.

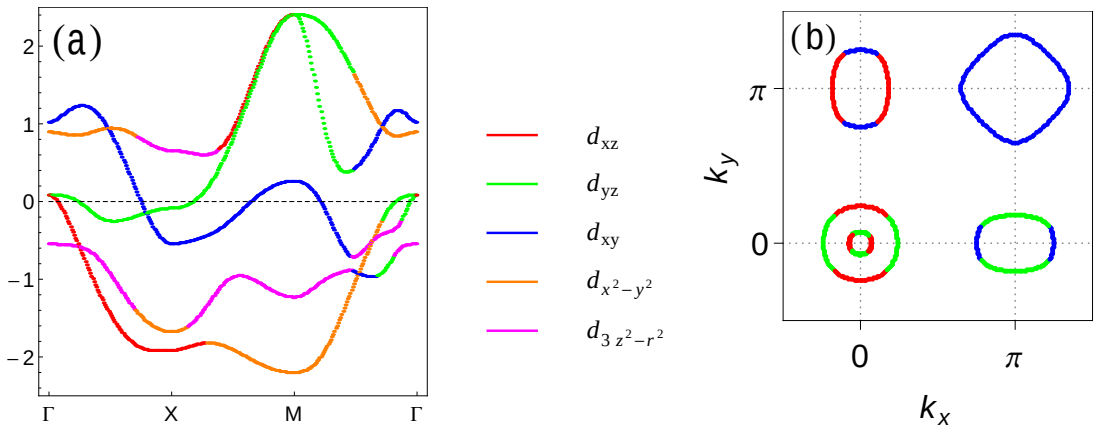

Figure 6.5: (a) Orbitally resolved band structure with $\Gamma = (0,0)$, $X = (\pi, 0)$ and $M = (\pi, \pi)$ denoting the symmetry points in the BZ corresponding to the one Fe unit cell. The main orbital contributions are shown by the colors as specified in the legend. (b) Fermi surface of the five orbital tight-binding Hamiltonian for the undoped system showing three hole pockets at Γ and M points and two electron pockets at X and Y points.

The second term in Eq.(6.3) describes the Coulomb interactions restricted to intrasite processes defined in chapter 2. It includes the intraorbital (interorbital) interaction U (U'), the Hund's rule coupling J and the pair hopping energy J'.

Superconductivity is described by the third term in Eq.(6.3), a BCS-like term

$$\mathcal{H}_{BCS} = -\sum_{\mathbf{i}\neq\mathbf{j},\mu\nu} [\Delta^{\mu\nu}_{\mathbf{ij}} c^{\dagger}_{\mathbf{i}\mu\uparrow} c^{\dagger}_{\mathbf{j}\nu\downarrow} + \text{H.c.}], \tag{6.4}$$

with a SC order parameter $\Delta^{\mu\nu}_{\mathbf{ij}} = \sum_{\alpha\beta} \Gamma^{\beta\nu}_{\mu\alpha}(\mathbf{r_{ij}}) \langle \hat{c}_{\mathbf{j}\beta\downarrow} \hat{c}_{\mathbf{i}\alpha\uparrow} \rangle$. Here $\Gamma^{\beta\nu}_{\mu\alpha}(\mathbf{r_{ij}})$ denotes the effective pairing strength between sites (orbitals) $\mathbf{i}$ and $\mathbf{j}$ (μ, ν, α and β) obtained from the RPA spin- χ_s^{RPA} and charge susceptibilities χ_c^{RPA} relevant for LiFeAs using equation (6.2). The real-space pairings are then obtained by $\Gamma^{\beta\nu}_{\mu\alpha}(\mathbf{r_{ij}}) = \sum_{\mathbf{q}} \Gamma^{\beta\nu}_{\mu\alpha}(\mathbf{q}) \exp(i\mathbf{q} \cdot (\mathbf{r_i} - \mathbf{r_j}))$ where we retain all possible orbital combinations up to next-nearest neighbors (NNN). For the present band, the RPA susceptibilities are strongly peaked near $(0, \pm\pi)$ and $(\pm\pi, 0)$ favoring an $s^{\pm}$ pairing state. In Fig. 6.6(a) we show the spatial dependence of the dominant intraorbital pairings $\Gamma^{\mu\mu}_{\mu\mu}(\mathbf{r_{ij}})$ obtained when $J = U/4$ and $U = 0.865$eV which yield a fully gapped $s^{\pm}$ phase with a two-gap peak-structure as seen from the total DOS in Fig. 5.5(b). It is striking that a very similar DOS has been recently measured in LiFeAs by several groups.[88, 103, 113] For comparison, the STM measurements on LiFeAs in figure 6.2 show the homogeneous spectra (white). As seen from Fig. 6.6(b) the inner coherence peaks (~ 7 meV) are dominated by the d_{xy} orbital, whereas the

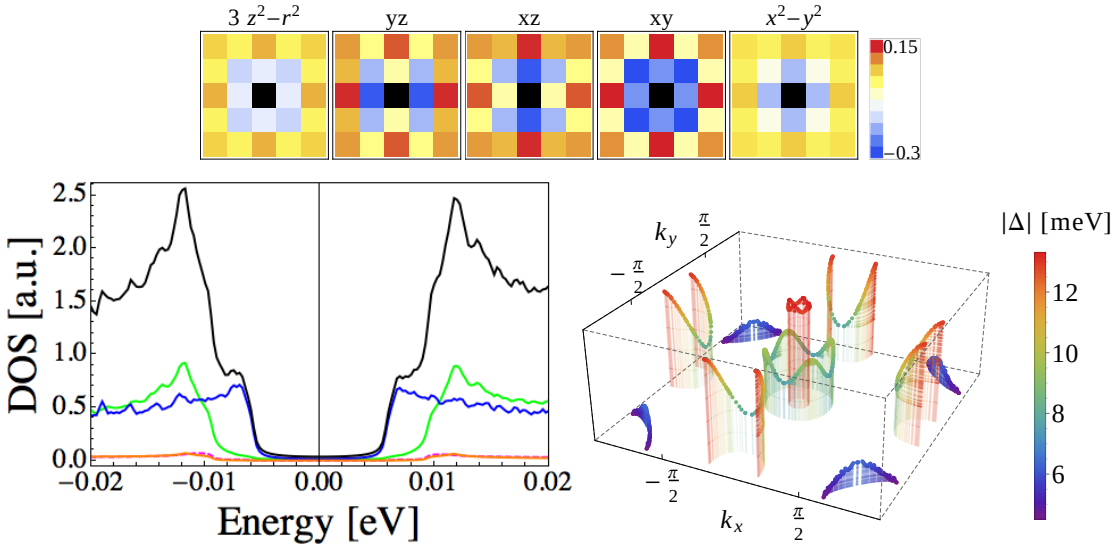

Figure 6.6: Top: spatial dependence of the intraorbital effective pairing constants $\Gamma^{\mu\mu}_{\mu\mu}(\mathbf{r_{ij}})$ in eV. The black center site is repulsive with ~ 2.5eV. Bottom: DOS for the homogeneous SC phase showing the total (black line) and orbitally resolved DOS (green: d_{yz}/d_{xz}; blue: d_{xy}; orange: $d_{x^2-y^2}$; magenta: d_{z^2}), and absolute value of the SC gap in momentum space $|\Delta(\mathbf{k})|$ showing a complex structure and different amplitudes in each pocket.

outer large-gap coherence peaks ($\sim$ 14 meV) consist of significant contributions from both the d_{xy} and d_{xz}/d_{yz} orbitals. In momentum space, the peaks at lower energy arise from a smaller gap on the outermost hole pocket around Γ, which is mainly d_{xy}, as opposed to a larger gap on the inner hole pockets around Γ and the electron pocket around M, which consist primarily of d_{xy} and d_{xz}/d_{yz} weight. These features are visible in the momentum structure of the SC gap, explicitly shown in figure 6.6(b). These results agree with recent ARPES measurements,[129, 130] STM quasi-particle interference (QPI),[113] and other theoretical studies.[131]

6.2.2 Single-impurity in the SC state

Having fixed both the band and the SC pairing, we proceed with the study of defect states in the correlated superconducting phase. The effect of a point-like impurity is described by adding the following term in the Hamiltonian (6.3)

$$\mathcal{H}_{imp} = \sum_{\mu\sigma} V^{\sigma}_{\mu} c^{\dagger}_{\mathbf{i}^*\mu\sigma} c_{\mathbf{i}^*\mu\sigma}, \tag{6.5}$$

which adds a local potential V_μ^σ at a site $\mathbf{i}^*$ on orbital μ with spin σ. The nonmagnetic defect is spin independent, $V_\mu^\uparrow = V_\mu^\downarrow$ (equivalent to the term in equation (4.1)), and for the magnetic impurity the itinerant electrons feel the opposite potentials, $V_\mu^\uparrow = -V_\mu^\downarrow$ (equivalent to equation (3.1)). We include only intraorbital terms in Eq.(6.5) consistent with first principles studies of transition metal atoms in LaFeAsO[59] and LiFeAs.[53]

In the absence of correlations, the dependence of the LDOS on V_μ^σ can be most easily obtained within the T-matrix approach (see section 4.4). Here, based on $\mathcal{H} = \mathcal{H}_0 + \mathcal{H}_{BCS}$ one obtains the free retarded 10×10 Nambu Greens function $G_0^R(k,\omega) = [(\omega + i\eta)I_{10\times 10} - \mathcal{H}_{Nambu}]^{-1}$ where

$$\mathcal{H}_{Nambu} = \begin{bmatrix} \mathcal{H}_0(k) & \mathcal{H}_{BCS}(k) \\ \mathcal{H}_{BCS}^\dagger(k) & -\mathcal{H}_0^T(-k) \end{bmatrix}. \tag{6.6}$$

The single impurity problem is solved exactly by the full Greens function given by $G^R(i,j,\omega) = G_0^R(0,\omega) + G_0^R(i,\omega)T(\omega)G_0^R(-j,\omega)$, where i,j denote sites in the lattice and $T(\omega)$ is the T-matrix.

Figure 6.7 shows the LDOS at the impurity and nearest neighbor (NN) sites for different nonmagnetic scattering strengths $V_\mu^\uparrow = V_\mu^\downarrow = V_{\rm imp}$ assumed to be orbitally independent for simplicity. As seen, in-gap bound states exist for all $|V_{\rm imp}| \gtrsim 1$eV, whereas weaker potentials ($|V_{\rm imp}| \lesssim 1$eV) mainly cause spectral weight shifts between the coherence peaks. Recent STM studies of Co and Cu impurities in superconducting $Na(Fe_{0.97-x}Co_{0.03}Cu_x)As$ found distinct LDOS modulations near these Fe substituents.[114, 45] Very weak spatial variation was reported around Co atoms. Using the effective impurity potential of Co obtained from *ab initio* calculations ($V_{\rm imp}^{Co} \sim -0.4$eV)[59, 53], we find that indeed the LDOS modulation are very weak as seen from Fig. 6.7(d). Near the Cu atoms, the STM study found weak in-gap quasiparticle excitations near the positive gap edge and a suppression of LDOS near the gap edge at negative bias.[45] Within our modeling, and in overall agreement with DFT, this implies that Cu behave as intermediate attractive scatterers, since the resulting LDOS shown in panels Fig. 6.7(b,c) agree with this finding.

Hanaguri *et al.* have located at least six different defect sites on the surface of LiFeAs, some of which induce genuine sub-gap bound states [Fig. 6.2].[119] As evident from Fig. 6.7 these may be caused by intermediate-strong scatterers. However, they can also arise from magnetic impurities. An STM study on NaFeAs found Curie-like free moment behavior in the case of Mn impurities indicating their magnetic nature.[45] For a single-site magnetic impurity, we show in Fig. 6.8 the evolution of the LDOS as a function of the strength of the magnetic scattering potential. In this case, at least four sub-gap bound states are present for all sizable impurity potentials. From the panels in Fig. 6.8, it is evident from comparison of

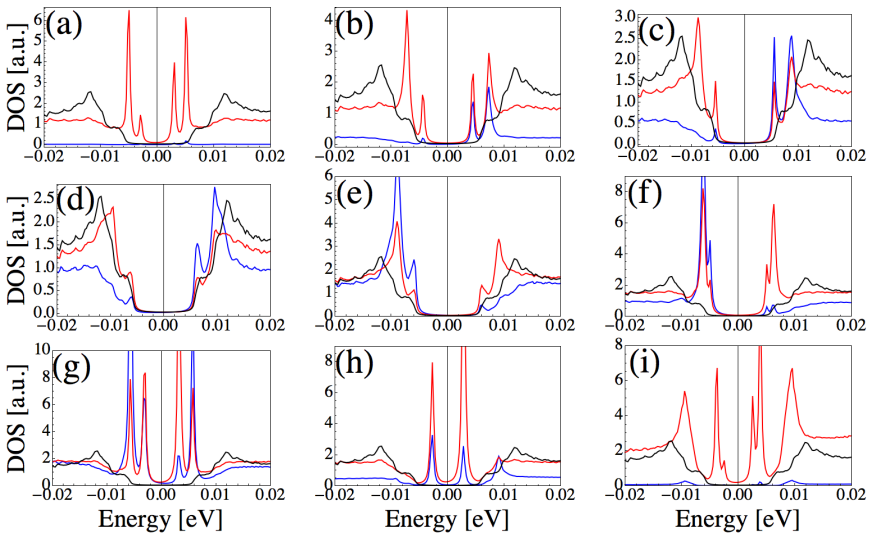

Figure 6.7: Total LDOS for nonmagnetic point-like scatterers at the impurity site (blue line) and at the NN site (red line). Panels (a-i) correspond to $V_{\text{imp}} = -8.0, -1.5, -0.75, -0.4, 0.4, 0.75, 1.5, 2.0, 8.0$eV. In all plots the solid black line is the DOS of the clean SC.

the red and green curves, that the LDOS exhibits a striking dependence on the spin polarization which may be utilized in future spin-tip polarized STM measurements to unambiguously determine the nature of the scatterers. For example, the absence of any qualitative difference between the measured sub-gap bound states with and without a spin-polarized tip would prove the nonmagnetic nature of the scatterer, and also provide a "smoking gun" for s±-wave pairing symmetry in FeSC.

We turn now to the study of disorder in the presence of electronic correlations. A mean-field decoupling of $\mathcal{H}_{int}$ leads to the following multi-band Bogoliubov de-Gennes (BdG) equations (Appendix D)

$$\sum_{\mathbf{j}\nu} \begin{pmatrix} H^{\mu\nu}_{\mathbf{ij}\sigma} & \Delta^{\mu\nu}_{\mathbf{ij}} \\ \Delta^{\mu\nu *}_{\mathbf{ij}} & -H^{\mu\nu *}_{\mathbf{ij}\bar{\sigma}} \end{pmatrix} \begin{pmatrix} u^n_{\mathbf{j}\nu} \\ v^n_{\mathbf{j}\nu} \end{pmatrix} = E_n \begin{pmatrix} u^n_{\mathbf{i}\mu} \\ v^n_{\mathbf{i}\mu} \end{pmatrix}, \tag{6.7}$$

where

$$\begin{aligned} H^{\mu\nu}_{\mathbf{ij}\sigma} = t^{\mu\nu}_{\mathbf{ij}} + \delta_{\mathbf{ij}}\delta_{\mu\nu}[-\mu_0 + \delta_{\mathbf{ii}^*}V_{\text{imp}} + U\langle n_{\mathbf{i}\mu\bar{\sigma}}\rangle \\ + \sum_{\mu'\neq\mu}(U'\langle n_{\mathbf{i}\mu'\bar{\sigma}}\rangle + (U'-J)\langle n_{\mathbf{i}\mu'\sigma}\rangle)]. \end{aligned} \tag{6.8}$$

The five-band BdG equations are solved on 28×28 lattices with stable solutions found through iterations of the following self-consistency equations

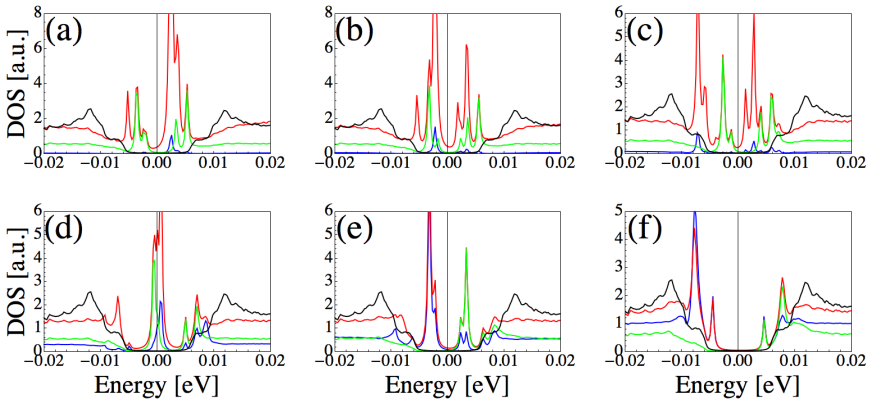

Figure 6.8: Total LDOS for magnetic point-like scatterers at the impurity site (blue lines) and at the NN site (red lines). The green lines show the spin-up LDOS at the NN site. Panels (a-f) correspond to $V_{\rm imp} = -8.0, -6.0, -4.0, -2.0, -1.0, -0.5$eV. Repulsive potentials lead to the same total LDOS (with interchanged spin polarization of the individual bound states).

$$\begin{aligned}
\langle n_{\mathbf{i}\mu\uparrow}\rangle &= \sum_n |u^n_{\mathbf{i}\mu}|^2 f(E_n) \\
\langle n_{\mathbf{i}\mu\downarrow}\rangle &= \sum_n |v^n_{\mathbf{i}\mu}|^2 (1-f(E_n)) \\
\Delta^{\mu\nu}_{\mathbf{ij}} &= \sum_{\alpha\beta} \Gamma^{\beta\nu}_{\mu\alpha}(\mathbf{r_{ij}}) \sum_n u^n_{\mathbf{i}\alpha} v^{n*}_{\mathbf{j}\beta} f(E_n),
\end{aligned} \tag{6.9}$$

where $\sum_n$ denotes summation over all eigenstates n. When calculating the LDOS,

$$N_i(\omega) = -\frac{1}{\pi}\Im \sum_{n\mu} \left[\frac{|u^n_{i\mu}|^2}{\omega - E_n + i\eta} + \frac{|v^n_{i\mu}|^2}{\omega + E_n + i\eta} \right] \tag{6.10}$$

we use 20×20 supercells to acquire spectral resolution of order ~ 0.5 meV.

In the paramagnetic non-superconducting state, when U is nonzero but still smaller than the critical value U_{c2} to enter a bulk SDW phase, magnetic order may be induced in the vicinity of the impurity as shown in Fig. 6.9(a). As seen from the single-impurity phase diagram in Fig. 6.9(b), the impurity-induced magnetization exists only in a finite wedge-shaped region in the $U - V_{\rm imp}$ phase space. The spin order is only induced around very strong repulsive impurities and the nearest-neighbor site exhibits the largest induced order. This kind of local order was introduced in chapter 4, and was related to a rearrangement of the LDOS around

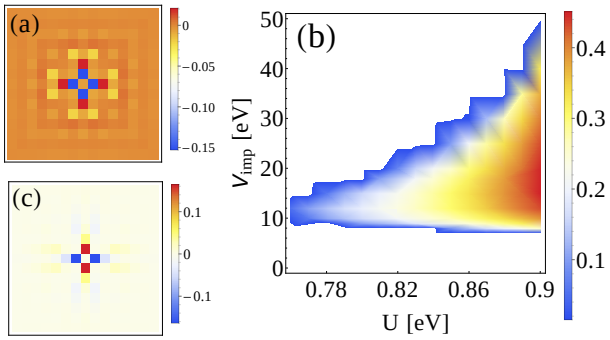

Figure 6.9: (a,c) Real-space resolved impurity-induced (a) magnetic order and (c) orbital order ($n_{xz} - n_{yz}$) near a repulsive point-like scatterer with $V_{\rm imp} = 8.0$eV and $U = 0.865$. (b) Single impurity phase diagram displaying the impurity induced magnetization at the NN site ($|m_{i^*+1}|$) versus U and $V_{\rm imp}$.

the impurity. The wedge-shaped region in Fig. 6.9(b) simply reflects the area where the LDOS enhancement at the NN sites is large enough to cross the magnetic instability. By contrast, attractive potentials are unable to support induced magnetization because the LDOS enhancements are too weak for this particular band structure. The induced short-ranged polarization is fully supported by superconductivity, which does not modify the wedge-shaped region in Fig. 6.9(b) and very weakly suppresses the amplitude of $m(\mathbf{r})$. A more extensive study of disorder-induced magnetic phases in superconducting systems will be presented in section 6.3. The formation of local moments near nonmagnetic scatterers in correlated hosts has been extensively discussed for cuprate SC.[51, 55]

Lastly we return to the topic of bound states and LDOS modulations near disorder sites. The self-consistency and possibility of induced order should alter the T-matrix results presented above. Specifically, the difference between the self-consistent BdG and the (non-selfconsistent) T-matrix approach is the correct spatial profile of $\Delta_{\mathbf{ij}}$ and the electron density $n_{\mathbf{i}}$ near the impurity within BdG. In addition, only BdG captures the impurity-induced local orbital order ($n_{xz} \neq n_{yz}$) at neighboring sites as shown in Fig. 6.9(c). In Fig. 6.10(a) we show the LDOS obtained within self-consistent BdG for the same parameters as in Fig. 6.7(i) and with a sub-critical $U = 0.84 < U_{c1}$. Compared to Fig. 6.7(i) we note a striking similarity to the non-selfconsistent T-matrix LDOS, which we find to be a general property for all impurity potentials. This ceases to be true, however, when $U > U_{c1}$ causing local magnetic order. As seen from Fig. 6.10(b), the LDOS in the case of induced order pushes essentially all the weight of the outer coherence peaks onto the impurity bound states. This effect is also reflected in the real-space LDOS maps of the bound state wave function shown in Fig. 6.10(c,d). Without induced

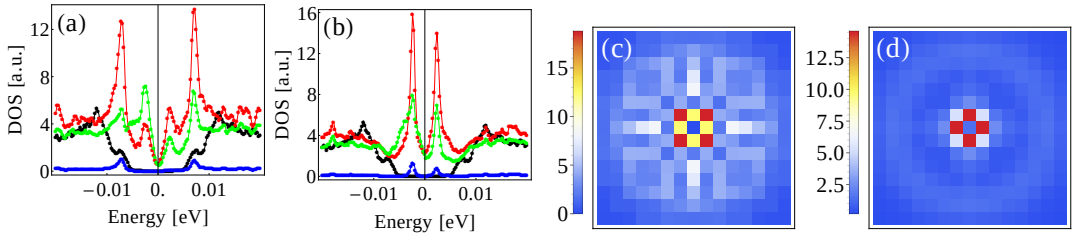

Figure 6.10: Comparison of the LDOS near a nonmagnetic scatterer with $V_{\text{imp}} = 8.0$eV in the absence [(a),(c)] and presence [(b),(d)] of induced magnetic order. (a) BdG LDOS versus energy on the impurity site (blue line), at the NN site (red line) and the NNN site (green line) for $U = 0.84\text{eV} < U_{c1}$. (b) Same as (a) for $U = 0.865\text{eV} > U_{c1}$. (c,d) Real-space LDOS maps at $\omega \sim -3$meV for the (a),(b) cases.

order its spectral weight undergoes a $\pi/4$ rotation (from NNN to NN or opposite) under $\omega \to -\omega$ (see Fig. 6.10(a)). In the presence of induced order however, most of the spectral weight remains at the magnetic NN sites for all bound states.

6.2.3 Conclusions

In summary, we have calculated the LDOS near magnetic and nonmagnetic impurities within a realistic five-band model which allows for disorder-induced order. Future studies which combines the DFT-obtained local Wannier states near impurity sites and the present BdG real-space approach constitute a natural next step in the realistic modeling of disorder in FeSC, to provide a quantitative description of the diverse real-space structures currently observed by STM. This method has been recently successfully applied to the problem of geometric dimers near defects in FeSe [141] and the Zn impurity problem on cuprate SC [142].

6.3 Correlation-driven disorder effects

The destruction of superconductivity by disorder is traditionally described by Abrikosov-Gorkov (AG) theory, which however ceases to be valid when impurities interfere and interactions become important. Here we study the effects of disorder on multi-band unconventional superconductors in the presence of correlations, and explore a completely different disorder paradigm dominated by strong deviations from standard AG theory due to the generation of local bound states and cooperative impurity behavior driven by interactions. Specifically we explain under which circumstances magnetic disorder acts as a strong poison destroying superconduc-

tivity at the sub-1% level, and when non-magnetic disorder, counter-intuitively, boosts the superconducting state while concomitantly inducing an inhomogeneous magnetic phase. Recent experimental studies of Fe-based superconductors (FeSC) have discovered that such unconventional disorder behavior is indeed present in those systems.

For the case of magnetic disorder, we find that correlations severely enhances the inter-impurity RKKY exchange interactions by inducing non-local long-range ordered magnetization that acts as an additional competitor to superconductivity. This results in an aggressive T_c suppression rate where superconductivity can be completely wiped out by sub-1% concentrations of magnetic impurity moments. This mechanism explains the "poisoning effect" discovered e.g. in Mn-doped 1111 pnictides where less than 0.3% Mn is enough to decrease T_c to zero, well beyond standard AG behavior. By contrast, for the case of non-magnetic disorder we find a highly robust superconducting state, in agreement with the earlier one-band studies, but in the current multi-orbital case additional locally impurity-generated bound states play an important role, and may even lead to an *enhancement* of T_c compared to clean (disorder-free) systems. This resilience to non-magnetic disorder is remarkable since, as we also show, clusters of impurities (dimers, trimers etc) locally pin magnetic order eventually causing a quasi-long-range ordered magnetic state with coexists with superconductivity. These latter results are in striking agreement with e.g. Ru-doped 1111 FeSC. In conclusion, our studies therefore reveal a highly segregated impurity response with very harmful (harmless) impact on superconductivity for magnetic (non-magnetic) disorder in correlated multi-band unconventional superconductors.

6.3.1 Model

The homogeneous superconducting system is modeled by the Hamiltonian (6.3), which describes short-range Coulomb repulsions in multi-band SC systems. For concreteness of the discussion below, we use a band structure $\mathcal{H}_0$ relevant to the 1111 compounds, with tight-binding parameters taken from [32]. This band structure was described in detail in section 2.2. The presence of the γ pocket at (π, π) was found to depend on the pnictogen height [143], which is controlled by the nearest-neighbor hopping parameter t_{xy}. Here, we use this result to model the difference between La-1111 (without the γ pocket) and Sm-1111 (with the γ pocket), as illustrated in figure 6.11. In agreement with a general $s_\pm$ state in FeSC, we include next-nearest neighbor intra-orbital pairing. Our results do not depend on this particular choice, and we keep only the dominant terms for simplicity. An extension to the full effective pairing $\Gamma^{\beta\nu}_{\mu\alpha}(\mathbf{q})$, described in the previous section, is straightforward. We take again a mean-field approach for the correlations and self-consistently solve the BdG equations (6.7)-(6.9) in 30×30 lattices. In this section

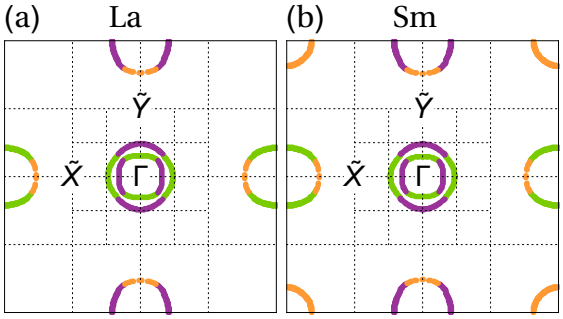

Figure 6.11: Fermi surface of (a) La-1111 and (b) Sm-1111. As the pnictogen height decreases (Sm → La) the d_{xy} (orange) γ pocket disappears from the Fermi surface. The presence of this pocket is controlled by the nearest-neighbor d_{xy} hopping parameter, $t_{xy}^{La} = 1.25 t_{xy}^{Sm}$.

the interaction parameters are referred to as $u \equiv U/U_c$, where U_c is the critical interaction parameter for the spin density wave instability. Additionally, we set $U' = U - 2J$, $J = U/4$ and $J' = J$ as elsewhere in this thesis.

6.3.2 Magnetic disorder

We start the discussion in the uncorrelated ($u = 0$) superconducting phase. A set of randomly distributed classical magnetic impurities is introduced in the La-1111 system [figure 6.11(a)] by the term

$$\mathcal{H}_{j_0 S_0} = \sum_{\{\mathbf{i}^*\}\mu\sigma} \sigma j_0 S_0 c^\dagger_{\mathbf{i}^*\mu\sigma} c_{\mathbf{i}^*\mu\sigma}. \tag{6.11}$$

This time-reversal breaking perturbation locally suppresses the superconducting order parameter $\Delta^\mu_{\mathbf{i}}$. The inclusion of several impurities leads to a spatially varying deteriorated order parameter $\Delta^\mu_{\mathbf{i}}$, and lowers the transition temperature T_c at which a non-zero solution of the gap equation exists. Eventually, for a sufficiently high critical concentration of impurities superconductivity is destroyed at all sites and $T_c = 0$. Fig. 6.12 shows the suppression of T_c as a function of magnetic impurity concentration. The main result of this section is the considerably faster T_c suppression when including short-range Coulomb interactions in the disordered system as seen in Fig. 2.5.

In order to understand this outcome, let us start with the local effects due to correlations around a single magnetic impurity. The exchange interaction term (6.11) induces a polarization in the spin of the surrounding itinerant electrons $m^\mu_{\mathbf{i}} = \sum_\sigma \sigma n_{\mathbf{i}\mu\sigma}$, which enters the mean-field Hamiltonian (6.7) in the following

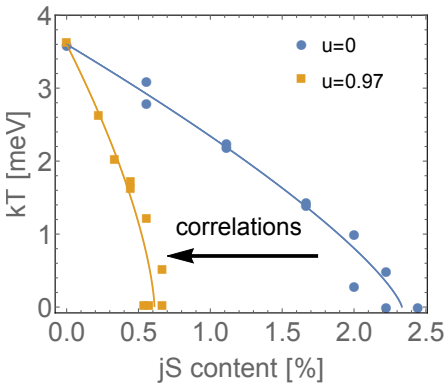

Figure 6.12: **Critical temperatures as a function of magnetic impurity concentration.** Point-like magnetic impurity moments are destructive for $s\pm$ superconductivity and the T_c suppression rate is strongly affected by electronic correlations as seen by the two T_c curves at $u = 0$ and $u = 0.97$ ($u \equiv U/U_c$). Correlations can strongly poison the superconducting state suppressing it entirely (at all sites) after only 0.5% disorder as seen by the orange curve. Concomitantly an inhomogeneous but volume-full magnetic phase appears similar to the experimental finding of Mn-doped La-1111 shown in Fig. 6.3(a). The impurity strength is $j_0 S_0 = 0.38$ eV.

form

$$\mathcal{H}_{js} = -\frac{1}{2}\sum_{\mathbf{i}\mu\sigma} \sigma \left(U m^{\mu}_{\mathbf{i}} + J \sum_{\nu\neq\mu} m^{\nu}_{\mathbf{i}} \right) c^{\dagger}_{\mathbf{i}\mu\sigma} c_{\mathbf{i}\mu\sigma}. \tag{6.12}$$

Note the Coulomb interaction is essential for this term to play any role. It is easy to see that equation (6.12) arising from correlations has the same form as the impurity term (6.11). We define an effective magnetic potential $\tilde{\mathcal{H}}_{j_0 S_0} \equiv \mathcal{H}_{j_0 S_0} + \mathcal{H}_{js} = \sum_{\mathbf{i}\mu\sigma} \sigma \mathfrak{S}_{\mathbf{i}\mu} c^{\dagger}_{\mathbf{i}\mu\sigma} c_{\mathbf{i}\mu\sigma}$, where

$$\mathfrak{S}_{\mathbf{i}\mu} = \left[j_0 S_0 \delta_{\mathbf{i}\mathbf{i}^*} - \frac{1}{2}\left(U m^{\mu}_{\mathbf{i}} + J \sum_{\nu\neq\mu} m^{\nu}_{\mathbf{i}} \right) \right] \equiv [j_0 S_0 \delta_{\mathbf{i}\mathbf{i}^*} + j s_{\mathbf{i}\mu}] \tag{6.13}$$

represents the effective extended magnetic impurity. Thus, interactions not only dress the bare magnetic impurity moment $j_0 S_0$ but additionally induce a spin polarization cloud of the itinerant electrons in the vicinity of the impurity $m^{\mu}_{\mathbf{i}}$. A cut of the induced magnetic potential $j s_{\mathbf{i}\mu}$ for a $j_0 S_0 = 0.38$ eV impurity as a function of the interaction parameter $u = U/U_c$ is shown in Fig 6.13(a). As seen, the size and amplitude of this magnetic puddle grows in a non-trivial way with u, as the system gets closer to the magnetic instability. Note the amplitude

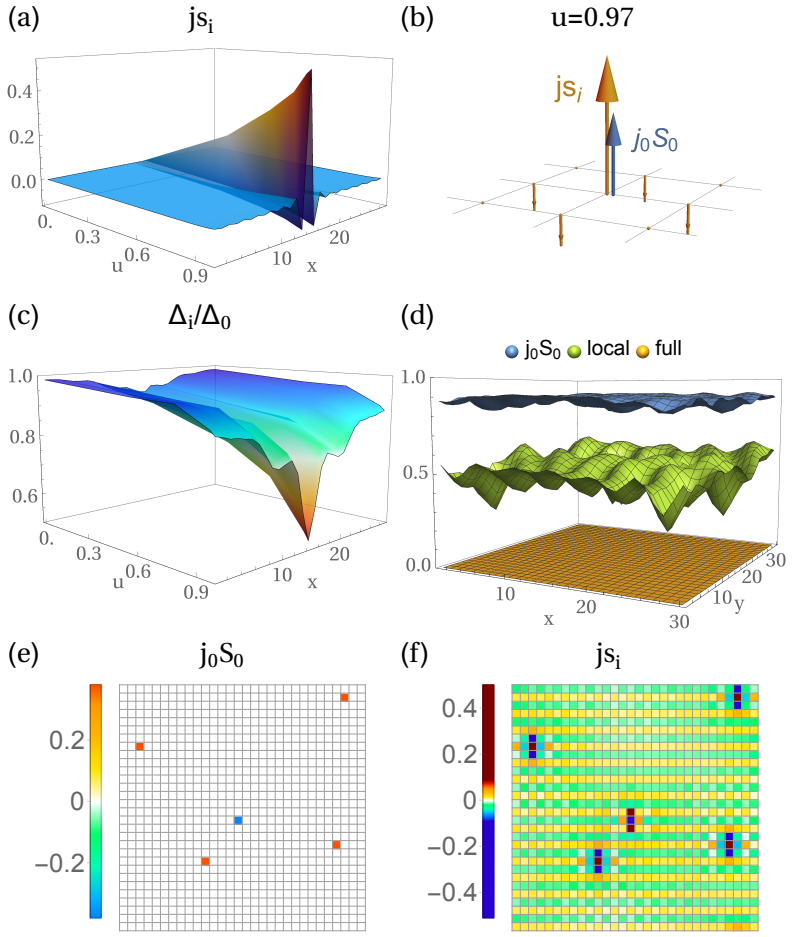

Figure 6.13: **Effect of correlations on the impurity response from magnetic disorder.** The magnetic impurity moments polarize locally the spin density leading to an extended magnetic puddle around each impurity site. As seen from (a) the size and amplitude of the puddle magnetization depends on u. The magnetic puddle at $u = 0.97$ is shown in (b). (c) Likewise the superconducting order parameter suppression locally also depends on u. The OP is plotted relative to its value in the homogeneous system. (d) Δ_i for $u = 0$ (blue), including only local polarization (green) and the full induced polarization (orange). (e) Bare magnetic potentials $j_0 S_0$ and (f) effective extended potential $js_\mathbf{i}$ for $u = 0.97$. The correlations strongly enhance the inter-puddle coupling by inducing a quasi-long-range ordered magnetic phase in-between the disorder sites. All the fields are plotted for the d_{xz} orbital.

is bounded by $U = U_c$ and $|m^{\mu}_{\mathbf{i}}| \leqslant 1$. Its real space structure can be seen in Fig. 6.13(b) for $u = 0.97$. It is largest at the impurity site, even exceeding the bare potential $j_0 S_0$, and changes sign on the nearest-neighbor sites. The amplitude decays two orders of magnitude within three lattice spacings. Superconductivity is affected by the additional competitor $js_{\mathbf{i}\mu}$, and as a result the local suppression of its order parameter $\Delta_{\mathbf{i}}$ increases with u as shown in Fig. 6.13(c). Getting close to a magnetic instability where correlations become important has therefore conspicuous local effects on superconductivity. This enhanced local pair breaking is not, however, the sole reason for the enhanced T_c suppression rate, which also requires understanding to the cooperative effect of multiple impurity moments.

When multiple impurities are included, the correlations among their spins become relevant, in particular as the system approaches the critical region $u \to u_c$. The spin polarized clouds around the impurities overlap, and the lowest free energy of the system is obtained by a constructive interference yielding quasi-long-range magnetic order. This effect was extensively studied in chapter 3. The inter-impurity regions are thus spin polarized due to this enhanced RKKY-like interaction between the impurities. Figs. 6.13(e) and 6.13(f) illustrate a case with uncorrelated 0.55% bare $j_0 S_0 = 0.38$ eV impurities and the induced $js_{\mathbf{i}}$ from the cooperative effect due to interactions, respectively. In addition to the local effect discussed above, the system clearly prefers to develop a finite magnetization $js_{\mathbf{i}}$ at *all* sites from this cooperative multi-impurity RKKY effect. This quasi-long range magnetic order is yet another competitor for superconductivity.

We show in Fig. 6.13(d) a disentangled plot of these two separate (local vs. long-range) effects on the superconducting order parameter suppression. The blue surface is the self-consistent solution of the gap equation $\Delta_{\mathbf{i}}$ of the $u = 0$ system shown in Fig. 6.13(e). The superconducting order parameter is hardly affected by the bare magnetic potentials, and this is reflected in the correspondingly low T_c suppression of Fig. 6.12. When the system is driven towards the critical region with $u \neq 0$, the bare potentials get locally dressed [Fig. 6.13(b)], and quasi-long-range magnetic order sets in in between the disorder sites [Fig. 6.13(f)]. We consider first the former effect by including only the on-site and nearest-neighbor effective magnetic potentials. This is done by setting the induced polarization of the system to zero at all sites $m(\mathbf{r}) = 0$, except those close to the impurities ($\mathbf{i}^*$ and nearest neighbors). The green surface of Fig. 6.13(d) is the resulting substantially reduced inhomogeneous $\Delta_{\mathbf{i}}$ solution of the gap equation due to the modified *local* potentials by $js_{\mathbf{i}}$. Now when the second effect, quasi-long-range magnetic order, is also allowed by including the $js_{\mathbf{i}}$ induced by interactions at all sites, superconductivity is completely wiped put, as illustrated by the $\Delta_{\mathbf{i}} = 0$ orange surface in the same figure. Hence, both the strong short range and the weaker long range induced magnetic orders exhibit comparable strength in suppressing superconductivity. Only

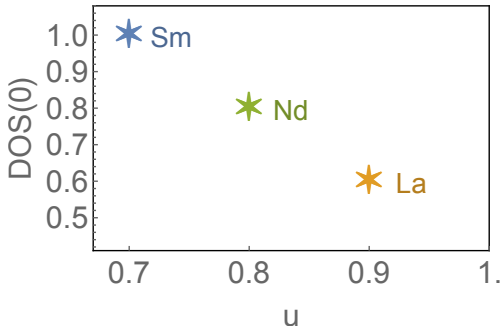

Figure 6.14: Phase diagram of the optimally doped L-1111 compounds we hypothesize from the Mn substituted experiments. [133, 134, 132] Here L =La, Nd and Sm.

by incorporating both these two distinct correlation effects is it possible to understand the aggressive sub-1 % T_c suppression rate shown in Fig. 6.12.

Kuroki *et al.* found that a reduction in the pnictogen height generally suppresses superconductivity by solving the Eliashberg equation using band structures based on virtual lattice structures. [143] In agreement with their results, we find that for the same pairing constants, the homogeneous (disorder-free) critical temperature T_c is a factor of two larger in the Sm-1111 system than in La-1111 system shown in figures 6.11(b) and 6.11(a), respectively. In our case, this is directly related to an increased DOS at the Fermi level due to the presence of the γ pocket. Within our model we can thus locate the optimally doped L-1111 compounds in a DOS versus correlation phase diagram illustrated in Fig 6.14. The higher DOS results in a higher T_c and as $u \to 1$ the system exhibits a more severe poisoning. We use this picture together with figure 6.12 to answer the initial question: why does it require an order of magnitude more magnetic Mn moments to suppress T_c to zero in optimally doped Sm-1111?

6.3.3 Non-magnetic disorder

We now turn to the discussion of non-magnetic disorder, and remind the reader about the set of puzzling experimental findings in Ru substituted L-1111 (L =La, Nd, Sm) summarized in Fig. 6.4. In agreement with naive expectations of isovalent (does not introduce carriers) disorder, it takes a large amount (60%) of Ru to suppress T_c. Interestingly, however, a magnetic phase is induced at intermediate values of Ru content x, centered roughly around $x = 0.25$, and existing only at a finite span of Δx of Ru concentrations. The magnetic phase is most pronounced with largest Δx and highest T_N in $SmFeAsO_{1-x}F_x$ and only marginally present

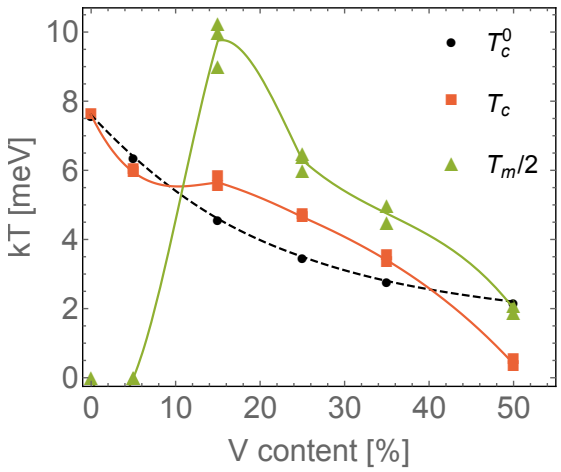

Figure 6.15: **Critical temperatures as a function of non-magnetic impurity concentration.** The superconducting critical temperature T_c (red squares) depends only weakly on the disorder concentration. The black dashed curve shows the critical T for the clean system T_c^0 where only the band-widening effect has been included. As seen there are regions of x where the bound state effect (see main text) has even enhanced T_c for the disordered case as compared to the clean system. This results in a change of dT_c/dx. A bulk magnetic phase (green triangles) is induced around the same x by the the non-magnetic disorder, and is largely seeded by dimer-like structures as explained in Fig. 6.16.

in $LaFeAsO_{1-x}F_x$ even though the latter system displays the poisoning effect and therefore is more correlated as shown above. The appearance of magnetic order is concomitant with a marked change of the derivative dT_c/dx.

We model the random distribution of non-magnetic impurities as

$$\mathcal{H}_V = \sum_{\{\mathbf{i}^*\}\mu\sigma} V_\mu c^\dagger_{\mathbf{i}^*\mu\sigma} c_{\mathbf{i}^*\mu\sigma}. \tag{6.14}$$

with a V_μ potential strength in orbital μ. Following first-principles calculations of Ru, a weak potential $V_\mu = 0.03$ eV is set on all orbitals [59]. Since a finite content of Ru induces short-range spin order, we incorporate here some of the ideas that were introduced in chapter 4 in the context of freezing of spin fluctuations. In particular, the generation of sharp-resonant states around defects was shown to be crucial. The weak single-potential from first-principles calculations does not include these states, and thus we allow ourselves to tune the screening potential of the gapped $3z^2 - r^2$ orbital (V_5). For $V_5 = 0.7$ eV, the single-impurity does not induce a resonant state at ϵ_F, but clusters of impurities (e.g. dimers and the like) develop structures of sharp resonant states which have important consequences,

as will be shown below. Besides the potential scattering part V_μ, first-principles calculations show that the bandwidth of the electronic structure increases about a factor of two with Ru content going from $x = 0$ to $x = 1$ (see Appendix E.1 for band structure details). The band-widening effect is accounted for in our model by introducing a renormalization of the hopping amplitudes $t_{\mathbf{ij}}^{\mu\nu} \rightarrow (1 + x)t_{\mathbf{ij}}^{\mu\nu}$, where x is the concentration of impurities. We include impurity concentrations in the range $x \in (0, ..., 0.5)$ in the Sm-1111 system [figure 6.11(b)] with intermediate correlations $u = 0.7$.

Our main results are summarized in figure 6.15, which includes an emerging magnetic dome (T_m) centered at $\sim 20\%$ impurity content, and a weakening superconducting state (T_c) with a recovery region concomitant with the appearance of the magnetic phase at around 10%.

The key effect of non-magnetic impurities is illustrated in figure 6.16. The positions of a random ensemble of 15% defects is shown in figure 6.16(a) (black and red sites); the corresponding LDOS of the $3z^2 - r^2$ orbital at the Fermi level $N_5(r, \omega = 0)$ in the normal state in figure 6.16(b). As seen, inhomogeneous structures of sharp resonant states have developed around the scatterers, where the brightest sites in 6.16(b) can be linked to 'dimer-like' structures highlighted in red in 6.16(a). The red colored sites represent structures where a particular impurity site has an occupied next-nearest neighbor site (nnn) and not more than one occupied nearest neighbor site (nn). The most simple structure fulfilling this condition is a pair of nnn impurities (dimer), and that is why we call these structures dimer-like. The increased LDOS at the Fermi level has remarkable consequences as will be discussed below:

1. A short-ranged magnetic dome T_m forms above a critical content $x > x_c$.

2. T_c is enhanced by disorder around the same concentration.

We start with the magnetic response of the system and explicitly show in figure 6.16(d) the self-consistent real space structure of the spin density of the $3z^2-r^2$ orbital $m_{\mathbf{i}}^5 = n_{\mathbf{i}5\uparrow} - n_{\mathbf{i}5\downarrow}$. The rest of the orbitals are polarized in a similar way, but with a much lower amplitude. The spin of the itinerant electrons appears polarized in areas with the brightest dimer-like structures in figure 6.16(b). This agrees with the local Stoner criteria presented in chapter 4. Namely, when the LDOS enhancement and interaction u reach a threshold, the system is *locally* pushed through the magnetic instability and develops a spontaneous magnetization. In order to characterize this short-range magnetic phase we define a critical temperature T_m, determined from the magnetic volume fraction v of a field $B(\mathbf{r})$ felt by muons through dipolar interaction (Appendix E.2):

$$B(\mathbf{r}) = \sum_i \frac{m_i}{|\mathbf{r}_i|^3} \tag{6.15}$$

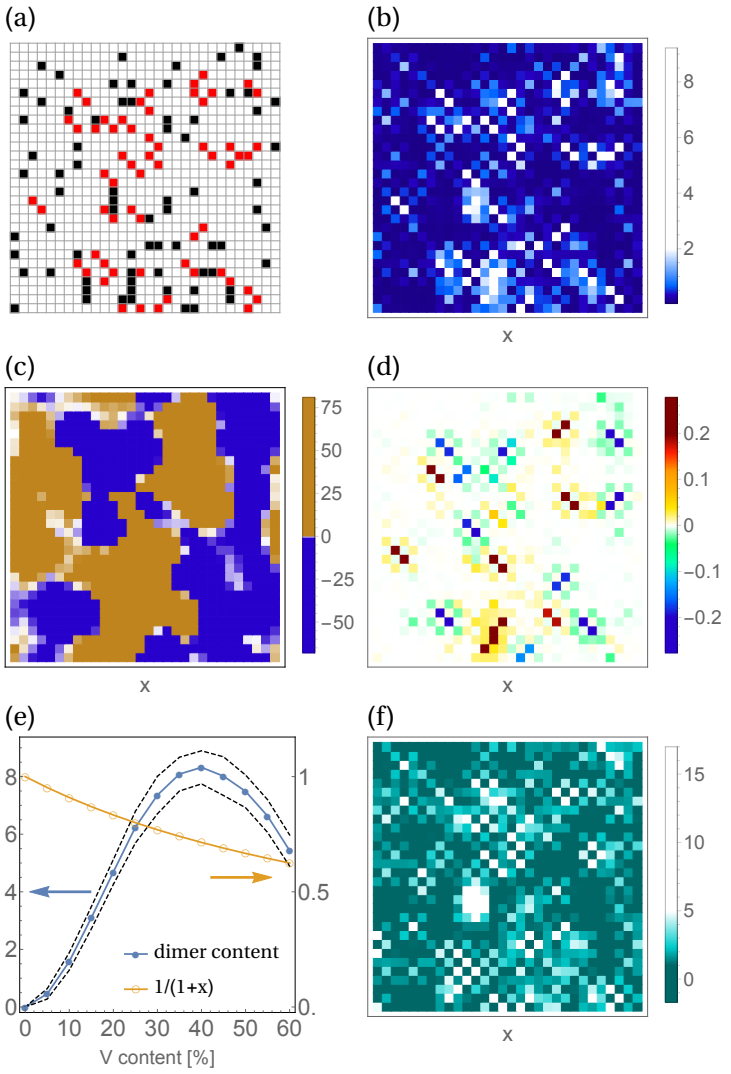

Figure 6.16: **Dimer-like structures and enhanced LDOS.** 15% configuration (a) V_μ positions, highlighted in red 'dimer-like' arrangements, (b) LDOS of the gapped orbital $N_5(r, \omega = 0)$, (c) $B(r)$ (6.15) felt by muons with orange (blue) larger (smaller) than 5mT, and (d) spin polarization $\mathbf{m}_5(r)$. (e) Dimer density (blue dots) as a function of disorder concentration x and the bandwidth effect $1/(1+x)$ (orange circles) relevant for renormalization of interactions and pairing. (f) Superconducting order parameter relative to its value in the clean system with wider band $\Delta_5(r)/\Delta_5^0(r)$

where $\mathbf{r}_i$ is the distance between the muon site $\mathbf{r}$ and the moment position m_i of the itinerant electrons. The magnetic ordering temperature T_m in μSR experiments is

extracted from the temperature evolution of the fraction of muons which detect a local moment. Conventionally, this is called magnetic volume fraction. T_m is taken as the temperature where the volume fraction is 50%, i.e. $\upsilon = 0.5$. We characterize our magnetic phase using the same criteria, which enables us to perform a more direct comparison with the available experimental μSR data (figure 6.4). As an example we show in figure 6.16(c) the field $B(\mathbf{r})$ felt by muons from the magnetic structure in figure 6.16(d). The color scale is set so that an amplitude bigger (smaller) than 5mT is orange (blue). In this case, the 15% concentration exhibits a nearly full volume fraction ($\upsilon \sim 1$), in agreement with experiments [136, 137]. The evolution of the magnetic critical temperature T_m as a function of impurity concentration x for different configurations is shown in figure 6.15, existing only for intermediate values of x, in agreement with experiments (figure 6.4(b)).

The dimer induced LDOS enhancement mechanism naturally explains the increase of T_m starting at intermediate values of impurity concentration $x_c \sim 10\%$. As the concentration of disorder in the system increases, more dimer-like structures with high LDOS and subsequent local polarized areas develop, and at a critical concentration x_c the system acquires $\upsilon > 0.5$ (as seen by muons) and a non-zero T_m. The density of dimer-like structures in the system (as defined by the red sites in figure 6.16(a)) as a function of disorder concentration x is plotted in figure 6.16(e) (blue). It actually peaks at a larger concentration ($\sim 40\%$) than the magnetic dome does [fig 6.15]. This earlier decrease in T_m of the short-range spin ordered phase is a consequence of the band-widening effect $W \to (1+x)W$ introduced by Ru disorder (Appendix E.1). Specifically, the interactions in the system get renormalized, $\tilde{u} \equiv u/(1+x)$, which results in effectively lower correlations, and makes it harder to locally cross the magnetic instability as x increases. The renormalization factor $1/(1+x)$ is plotted in the same figure (orange circles). Where exactly the magnetic dome peaks is then a compromise between the two effects introduced by the impurities: the enhanced LDOS around dimer-like structures and the effective weakening of correlations via band widening.

The superconducting state is also affected by the impurities: i) the band widening, ii) the pair-breaking scattering effect in the sign changing $s_\pm$ state, and iii) the LDOS enhancement are important effects to be considered. First of all, we find a monotonic decrease in the critical temperature of the clean system (disorder-free) due to the widening of the band. Just like it happens with interactions, the superconducting pairing is renormalized to lower values, $\tilde{\Gamma} \equiv \Gamma/(1+x)$, which leads to a smooth decrease of the critical temperature of the clean system (T_c^0 in figure 6.15). Including a random ensemble of potentials V_μ results in a new critical temperature evolution T_c as a function of x, consisting of three regions with deviations from the T_c^0 curve apparent in figure 6.15: 1) an initial sharper drop ($T_c < T_c^0$) in the $0 < x < 10\%$ range, 2) a subsequent recovery and enhancement ($T_c > T_c^0$) in the

$10 < x < 40\%$ initiated with a change of $dT_c(x)/dx$, and finally 3) a complete destruction ($T_c = 0$) beyond $x \sim 50\%$ concentration.

The first region with the more severe drop is dominated by the (weak) pair-breaking effect of non-magnetic impurities in the sign-changing $s_\pm$ state ($V_\mu = 0.03$ eV). On the other hand, superconductivity can also benefit from the resonant state structure around dimer-like arrangements [figure 6.16(b)]. In figure 6.16(f) the self-consistent SC order parameter is shown relative to its value in the clean system $\Delta_{\mathbf{i}5}/\Delta^0_{\mathbf{i}5}$. Remarkably, its amplitude is enhanced by an order of magnitude in resonant-state regions. The increased LDOS in these regions turn into a larger effective local pairing $\tilde{\Gamma}_5(r) \sim N_5(r, \omega = 0)\Gamma_5$. At some critical concentration, the local enhanced pairing overcompensates the pair-breaking effect of the other orbitals, the derivative $dT_c(x)/dx$ is changed, and the system enters the second region, with an enhanced critical temperature $T_c/T_c^0 = 1.25$. This enhancement is somehow surprising, since, as we discussed earlier, these regions have locally pinned magnetic order [figure 6.16(d)]. A careful analysis of the distribution of resonant states in figure 6.16(b), and the profile of the magnetic and SC order parameters in figures 6.16(d) and 6.16(f), shows that the system minimizes its free energy by spin polarizing regions with the highest LDOS while simultaneously enhancing the superconducting order parameter in the remaining areas with weaker amplitudes of the resonant states. Finally, for higher disorder content [region (3)], the pair-breaking effect of the other orbitals and the competition with magnetic order overrule the $\Delta_5(r)$ enhancement and superconductivity is completely destroyed.

In summary, we find that particular clusters of potentials generate sharp resonant state structures that lead to a short range magnetic order at intermediate concentrations. The generation of this order, which coexists with superconductivity, is accompanied by a change in dT_c/dx resulting from enormous enhancement of the LDOS and SC order parameter of a particular e_g orbital. This behavior is in excellent agreement with the experimental results shown in figure 6.4. An inspection of this figure shows that the induced magnetic phase is more (less) extended in the materials exhibiting the less (more) poisoning effect by Mn substitution. We argued earlier that from the poisoning scenario, La-1111 is the most correlated material [figure 6.14]; so why would it have a less extended short-range magnetic phase? In principle, a higher u could facilitate to locally cross the magnetic instability. Within the theory of impurity-induced order presented in chapter 4, a possible explanation is a different screening of the $d_{3z^2-r^2}$ orbital in Ru substituents in systems with different pnictogen heights, i.e. a slightly different V_5. This would shift the bound-state structure away from the Fermi level, locally weakening the Stoner condition. We have checked that potentials with $V_5 = 0.5$ eV in the La-1111 system [figure 6.11(a)] with $u = 0.97$ results in a diminished magnetic dome.

The impurity-induced order found here provides also a candidate for the dis-

tinct magnetic phases found recently in SC Co-doped $BaFe_2As_2$[138, 139] and NaFeAs[140]. For example near optimally doped $Ba(Fe_{1-x}Co_x)_2As_2$, μSR discovered a disordered inhomogeneous magnetic phase which was not observable by neutrons.[139] Within the present theoretical scenario, such a phase could be stabilized by a multiple-Co dopant effect similar to the result shown in Fig. 6.16(d) where local dopant clusters induce magnetic order but are, however, too weakly coupled to neighboring clusters to be seen by neutron scattering.

6.3.4 Conclusion

In summary, we have developed a model of disorder in correlated multi-orbital systems that naturally describe a large set of puzzling experimental data including:

1. The nearly immediate suppression of superconductivity (poisoning effect) in La-1111 by Mn substitution and subsequent generation of a long-range ordered magnetic phase.

2. A less severe poisoning effect (T_c suppression rate) by introduction of Mn for other known 1111 materials.

3. The much slower T_c suppression rate and the creation of an impurity-induced magnetic phase in 1111 materials upon substitution of Fe by Ru, but existing only for intermediate values of Ru concentrations.

4. The fact that the Ru-induced magnetic phase is more (less) extended in the materials exhibiting the less (more) significant poisoning effect by Mn substitution.

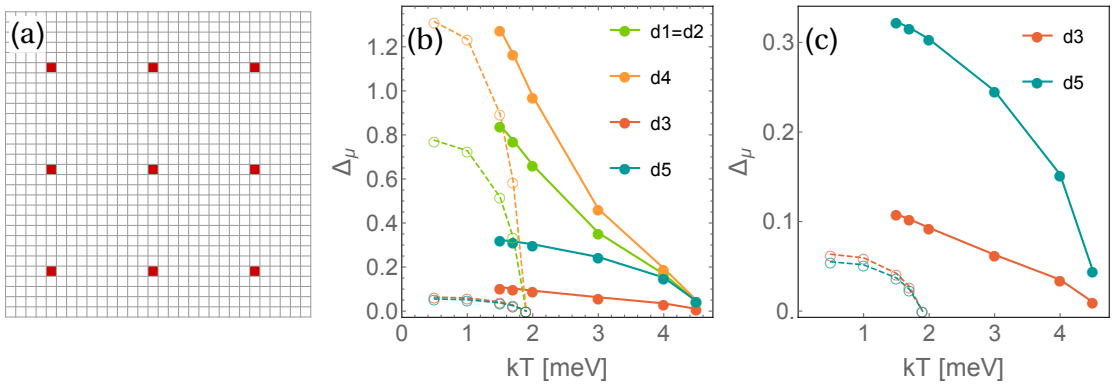

Figure 6.17: **T_c enhancement by disorder in a super-lattice.** (a) Super-lattice of 9 impurities in a 30×30 system. (b) Superconducting order parameter $\Delta_\mu(r)$ for $\{1 = xz, 2 = yz, 3 = x^2 - y^2, 4 = xy, 5 = 3z^2 - r^2\}$. The full (empty) circles represent the super-lattice (clean) system. An average of the order parameter is shown as a representative value. (c) Same in a smaller scale for the e_g orbitals where the resonant state and correspondingly the enhancement of $\Delta_\mu(r)$ is most pronounced. The potential strength are $V_5 = 0.7$ eV and zero for the rest of the orbitals.

6.4 Outlook

The remarkable T_c enhancement found as a result of resonant state structures around particular clusters of impurities deserves further study. These include for example, the extent of the T_c/T_c^0 rates one can get using different super-lattices of impurities. Figure 6.17 shows the SC order parameters of the individual orbitals in the homogeneous case (dashed lines) and a super-lattice of evenly spaced nine impurities of V_5-only character (full lines). As can be seen in the figure, for this particular choice of parameters, the superconducting critical temperature T_c is increased by a factor of 2.5. This is a consequence of the enormous increase of the superconducting order parameter in the $d_{3z^2-r^2}$ orbital, explicitly shown in figure 6.17(c), arising from sharp resonant state formation in this orbital.

This poses the interesting open question of how to use 'appropriate disorder' to engineer new systems with optimized superconducting properties, including an enhanced T_c.

Appendix A

Mean-field model for competing magnetic phases

A.1 Real space

The starting Hamiltonian consists of a five-orbital tight-binding band relevant to the pnictides,

$$\mathcal{H}_0 = \sum_{ij,\mu\nu,\sigma} t_{ij}^{\mu\nu} \hat{c}_{i\mu\sigma}^{\dagger} \hat{c}_{j\nu\sigma} - \mu_0 \sum_{i\mu\sigma} \hat{c}_{i\mu\sigma}^{\dagger} \hat{c}_{i\mu\sigma}. \tag{A.1}$$

The operators $c_{\mathbf{i}\mu\sigma}^{\dagger}$ ($c_{\mathbf{i}\mu\sigma}$) create (annihilate) an electron at site i in orbital state μ with spin σ, and μ_0 is the chemical potential which adjusts the filling. The indices μ and ν denote the five iron orbitals d_{xz}, d_{yz}, d_{xy}, $d_{x^2-y^2}$, and d_{z^2}. Here, x refers to a filling of $\langle n \rangle = n_{opt} - x$ where $n_{opt} = 5.91$ is the optimal doping for magnetism for this band. Thus $x = -0.09$ corresponds to the undoped case with $\langle n \rangle = 6.0$.

The interacting part of the Hamiltonian is described by the multi-orbital onsite Hubbard model

$$\begin{aligned} \mathcal{H}_{int} = U \sum_{i\mu} \hat{n}_{i\mu\uparrow} \hat{n}_{i\mu\downarrow} + U' \sum_{i,\mu<\nu,\sigma} \hat{n}_{i\mu\sigma} \hat{n}_{i\nu\bar{\sigma}} + (U' - J) \sum_{i,\mu<\nu,\sigma} \hat{n}_{i\mu\sigma} \hat{n}_{i\nu\sigma} \\ + J \sum_{i,\mu<\nu,\sigma} \hat{c}_{i\mu\sigma}^{\dagger} \hat{c}_{i\nu\bar{\sigma}}^{\dagger} \hat{c}_{i\mu\bar{\sigma}} \hat{c}_{i\nu\sigma} + J' \sum_{i,\mu<\nu,\sigma} \hat{c}_{i\mu\sigma}^{\dagger} \hat{c}_{i\mu\bar{\sigma}}^{\dagger} \hat{c}_{i\nu\bar{\sigma}} \hat{c}_{i\nu\sigma}, \end{aligned} \tag{A.2}$$

with $U' = U - 2J$, $J' = J$, and $J = U/4$.

We mean-field decouple Eq. (A.2) for all fields $\langle \hat{c}_{i\mu\sigma}^{\dagger} \hat{c}_{j\nu\sigma'} \rangle$ which leads to the following mean-field Hamiltonian

$$\mathcal{H}^{MF} = \sum_{ij\mu\nu} \begin{pmatrix} \hat{c}_{i\mu\uparrow}^{\dagger} & \hat{c}_{i\mu\downarrow}^{\dagger} \end{pmatrix} \begin{pmatrix} \varphi_{ij\uparrow}^{\mu\nu} & \omega_{ii\uparrow}^{\mu\nu} \\ \omega_{ii\downarrow}^{\mu\nu} & \varphi_{ij\downarrow}^{\mu\nu} \end{pmatrix} \begin{pmatrix} \hat{c}_{j\nu\uparrow} \\ \hat{c}_{j\nu\downarrow} \end{pmatrix}, \tag{A.3}$$

where

$$\varphi^{\mu\nu}_{ij\sigma} = t^{\mu\nu}_{ij} + \delta_{\mu\nu}[-\mu_0 + U\langle\hat{n}_{i\mu\bar{\sigma}}\rangle + U'\langle\hat{n}_{i\nu\bar{\sigma}}\rangle + (U'-J)\langle\hat{n}_{i\nu\sigma}\rangle] \\ - \bar{\delta}_{\mu\nu}[(U'-J)\langle\hat{c}^{\dagger}_{i\nu\sigma}\hat{c}_{i\mu\sigma}\rangle + J\langle\hat{c}^{\dagger}_{i\nu\bar{\sigma}}\hat{c}_{i\mu\bar{\sigma}}\rangle + J'\langle\hat{c}^{\dagger}_{i\mu\bar{\sigma}}\hat{c}_{i\nu\bar{\sigma}}\rangle], \tag{A.4}$$

$$\omega^{\mu\nu}_{ii\sigma} = \delta_{\mu\nu}[-U\langle\hat{c}^{\dagger}_{i\mu\bar{\sigma}}\hat{c}_{i\mu\sigma}\rangle - J\langle\hat{c}^{\dagger}_{i\nu\bar{\sigma}}\hat{c}_{i\nu\sigma}\rangle] - \bar{\delta}_{\mu\nu}[U'\langle\hat{c}^{\dagger}_{i\nu\bar{\sigma}}\hat{c}_{i\mu\sigma}\rangle + J'\langle\hat{c}^{\dagger}_{i\mu\bar{\sigma}}\hat{c}_{i\nu\sigma}\rangle]. \tag{A.5}$$

with $\bar{\delta}_{\mu\nu} = 1 - \delta_{\mu\nu}$. Eq. (A.3) is diagonalized by a unitary transformation $\hat{c}_{i\mu\uparrow} = \sum_n u^n_{i\mu}\hat{\gamma}_n$ and $\hat{c}_{i\mu\downarrow} = \sum_n \bar{u}^n_{i\mu}\hat{\gamma}_n$ and the following unrestricted fields are obtained self-consistently

$$\langle\hat{c}^{\dagger}_{i\mu\uparrow}\hat{c}_{j\nu\uparrow}\rangle = \sum_n u^{n*}_{i\mu}u^n_{j\nu}f(E_n), \tag{A.6}$$

$$\langle\hat{c}^{\dagger}_{i\mu\downarrow}\hat{c}_{j\nu\downarrow}\rangle = \sum_n \bar{u}^{n*}_{i\mu}\bar{u}^n_{j\nu}f(E_n), \tag{A.7}$$

$$\langle\hat{c}^{\dagger}_{i\mu\uparrow}\hat{c}_{i\nu\downarrow}\rangle = \sum_n u^{n*}_{i\mu}\bar{u}^n_{i\nu}f(E_n), \tag{A.8}$$

$$\langle\hat{c}^{\dagger}_{i\mu\downarrow}\hat{c}_{i\nu\uparrow}\rangle = \sum_n \bar{u}^{n*}_{i\mu}u^n_{i\nu}f(E_n), \tag{A.9}$$

for all sites i, j and orbital combinations μ, ν. Here E_n denote the eigenvalues, and f is the Fermi function. From these fields we obtain the spin and charge configurations of the final solution in real space

$$M^x(\mathbf{r}) = \sum_\mu \left(\langle\hat{c}^{\dagger}_{i\mu\uparrow}\hat{c}_{i\mu\downarrow}\rangle + \langle\hat{c}^{\dagger}_{i\mu\downarrow}\hat{c}_{i\mu\uparrow}\rangle\right), \tag{A.10}$$

$$M^z(\mathbf{r}) = \sum_\mu \left(\langle\hat{c}^{\dagger}_{i\mu\uparrow}\hat{c}_{i\mu\uparrow}\rangle - \langle\hat{c}^{\dagger}_{i\mu\downarrow}\hat{c}_{i\mu\downarrow}\rangle\right), \tag{A.11}$$

$$n(\mathbf{r}) = \sum_\mu \left(\langle\hat{c}^{\dagger}_{i\mu\uparrow}\hat{c}_{i\mu\uparrow}\rangle + \langle\hat{c}^{\dagger}_{i\mu\downarrow}\hat{c}_{i\mu\downarrow}\rangle\right). \tag{A.12}$$

A.2 Momentum space

In order to readily study the electronic properties we also solve the above model in momentum space with the mean-fields $\langle\hat{c}^{\dagger}_{\mu\sigma}(k)\hat{c}_{\nu\sigma'}(k+q_l)\rangle$, where $q_l = \{0, Q_1, Q_2, Q_1+Q_2\} \equiv \{q_0, q_1, q_2, q_3\}$. The mean-field Hamiltonian in momentum space takes the following form

$$\sum_{k\mu\neq\nu\sigma}{}' \Psi^\dagger \begin{pmatrix} \xi^{\mu\nu}(k)+N_0^{\mu\nu} & W_1^{\mu\nu} & W_2^{\mu\nu} & N_3^{\mu\nu} & \tilde{N}_0^{\mu\nu} & \tilde{W}_1^{\mu\nu} & \tilde{W}_2^{\mu\nu} & \tilde{N}_3^{\mu\nu} \\ & \xi^{\mu\nu}(k+q_1)+N_0^{\mu\nu} & N_3^{\mu\nu} & W_2^{\mu\nu} & \tilde{W}_1^{\mu\nu} & \tilde{N}_0^{\mu\nu} & \tilde{N}_3^{\mu\nu} & \tilde{W}_2^{\mu\nu} \\ & & \xi^{\mu\nu}(k+q_2)+N_0^{\mu\nu} & W_1^{\mu\nu} & \tilde{W}_2^{\mu\nu} & \tilde{N}_3^{\mu\nu} & \tilde{N}_0^{\mu\nu} & \tilde{W}_1^{\mu\nu} \\ & & & \xi^{\mu\nu}(k+q_3)+N_0^{\mu\nu} & \tilde{N}_3^{\mu\nu} & \tilde{W}_2^{\mu\nu} & \tilde{W}_1^{\mu\nu} & \tilde{N}_0^{\mu\nu} \\ & & & & \xi^{\mu\nu}(k)+N_0^{\mu\nu} & -W_1^{\mu\nu} & -W_2^{\mu\nu} & N_3^{\mu\nu} \\ & & & & & \xi^{\mu\nu}(k+q_1)+N_0^{\mu\nu} & N_3^{\mu\nu} & -W_2^{\mu\nu} \\ & & H.c. & & & & \xi^{\mu\nu}(k+q_2)+N_0^{\mu\nu} & -W_1^{\mu\nu} \\ & & & & & & & \xi^{\mu\nu}(k+q_3)+N_0^{\mu\nu} \end{pmatrix} \Psi,$$

where

$$\Psi^\dagger = \left(\hat{c}^\dagger_{\mu\uparrow}(k)\ \hat{c}^\dagger_{\mu\uparrow}(k+q_1)\ \hat{c}^\dagger_{\mu\uparrow}(k+q_2)\ \hat{c}^\dagger_{\mu\uparrow}(k+q_3)\ \hat{c}^\dagger_{\mu\downarrow}(k)\ \hat{c}^\dagger_{\mu\downarrow}(k+q_1)\ \hat{c}^\dagger_{\mu\downarrow}(k+q_2)\ \hat{c}^\dagger_{\mu\downarrow}(k+q_3) \right), \quad \text{(A.13)}$$

and the summation $\sum_k'$ is done in the reduced Brillouin zone $-\pi/2 < k_x, k_y < \pi/2$. The entries below the main diagonal were not included for clarity but are obtained by the transpose conjugate of the upper triangular matrix. All entries of the mean-field Hamiltonian are defined below

$$\xi^{\mu\nu}(k+q_l) = \epsilon^{\mu\nu}(k+q_l) - \mu_0\delta_{\mu\nu}, \quad \text{(A.14)}$$

$$N_0^{\mu\nu} = \delta_{\mu\nu}\left[Un_0^\mu + (2U'-J)n_0^\nu\right] + \bar{\delta}_{\mu\nu}\left[(-U'+2J)n_0^{\nu\mu} + J'n_0^{\mu\nu}\right], \quad \text{(A.15)}$$

$$W_l^{\mu\nu} = \delta_{\mu\nu}\left[-UM_l^\mu - JM_l^\nu\right] - \bar{\delta}_{\mu\nu}\left[U'M_l^{\nu\mu} + J'M_l^{\mu\nu}\right], \quad \text{(A.16)}$$

$$N_3^{\mu\nu} = \delta_{\mu\nu}\left[Un_3^\mu + (2U'-J)n_3^\nu\right] + \bar{\delta}_{\mu\nu}\left[(-U'+2J)n_3^{\nu\mu} + J'n_3^{\mu\nu}\right], \quad \text{(A.17)}$$

$$\tilde{N}_0^{\mu\nu} = \delta_{\mu\nu}\left[-U\tilde{n}_0^\mu - J\tilde{n}_0^\nu\right] - \bar{\delta}_{\mu\nu}[U'\tilde{n}_0^{\nu\mu} + J'\tilde{n}_0^{\mu\nu}], \quad \text{(A.18)}$$

$$\tilde{W}_l^{\mu\nu} = \delta_{\mu\nu}\left[-U\tilde{M}_l^\mu - J\tilde{M}_l^\nu\right] - \bar{\delta}_{\mu\nu}[U'\tilde{M}_l^{\nu\mu} + J'\tilde{M}_l^{\mu\nu}], \quad \text{(A.19)}$$

$$\tilde{N}_3^{\mu\nu} = \delta_{\mu\nu}\left[-U\tilde{n}_3^\mu - J\tilde{n}_3^\nu\right] - \bar{\delta}_{\mu\nu}[U'\tilde{n}_3^{\nu\mu} + J'\tilde{n}_3^{\mu\nu}]. \quad \text{(A.20)}$$

Using the unitary transformation $\hat{c}_{\mu\uparrow}(k+q_l) = \sum_n u_{l\mu}^n(k)\gamma_n$ and $\hat{c}_{\mu\downarrow}(k+q_l) = \sum_n \bar{u}_{l\mu}^n(k)\gamma_n$ (where $l = 0,1,2,3$) the mean-fields are then self-consistently obtained from the relations

$$n_0^{\mu\nu} = \sum_{k\sigma}\langle\hat{c}^\dagger_{\mu\sigma}(k)\hat{c}_{\nu\sigma}(k)\rangle = \sum_{kn}{}'\sum_{l=0}^{3}\left[u_{l\mu}^{n*}(k)u_{l\nu}^n(k) + \bar{u}_{l\mu}^{n*}(k)\bar{u}_{l\nu}^n(k)\right]f_n,$$

$$n_3^{\mu\nu} = \sum_{k\sigma}\langle\hat{c}^\dagger_{\mu\sigma}(k)\hat{c}_{\nu\sigma}(k+q_3)\rangle = \sum_{kn}{}'\left\{\sum_{l=1,4}\left[u_{l\mu}^{n*}(k)u_{\bar{l}\nu}^n(k) + \bar{u}_{l\mu}^{n*}(k)\bar{u}_{\bar{l}\nu}^n(k)\right]\right.$$

$$+\sum_{l=2,3}\left[u_{l\mu}^{n*}(k)u_{\bar{l}\nu}^{n}(k)+\bar{u}_{l\mu}^{n*}(k)\bar{u}_{\bar{l}\nu}^{n}(k)\right]\Bigg\}f_n,$$

$$M_1^{\mu\nu}=\sum_{k\sigma}\sigma\langle\hat{c}_{\mu\sigma}^{\dagger}(k)\hat{c}_{\nu\sigma}(k+q_1)\rangle=\sum_{kn}{}'\Bigg\{\sum_{l=1,2}\left[u_{l\mu}^{n*}(k)u_{\bar{l}\nu}^{n}(k)-\bar{u}_{l\mu}^{n*}(k)\bar{u}_{\bar{l}\nu}^{n}(k)\right]$$

$$+\sum_{l=3,4}\left[u_{l\mu}^{n*}(k)u_{\bar{l}\nu}^{n}(k)-\bar{u}_{l\mu}^{n*}(k)\bar{u}_{\bar{l}\nu}^{n}(k)\right]\Bigg\}f_n,$$

$$M_2^{\mu\nu}=\sum_{k\sigma}\sigma\langle\hat{c}_{\mu\sigma}^{\dagger}(k)\hat{c}_{\nu\sigma}(k+q_2)\rangle=\sum_{kn}{}'\Bigg\{\sum_{l=1,3}\left[u_{l\mu}^{n*}(k)u_{\bar{l}\nu}^{n}(k)-\bar{u}_{l\mu}^{n*}(k)\bar{u}_{\bar{l}\nu}^{n}(k)\right]$$

$$+\sum_{l=2,4}\left[u_{l\mu}^{n*}(k)u_{\bar{l}\nu}^{n}(k)-\bar{u}_{l\mu}^{n*}(k)\bar{u}_{\bar{l}\nu}^{n}(k)\right]\Bigg\}f_n,$$

$$\tilde{n}_0^{\mu\nu}=\sum_{k\sigma}\sigma\langle\hat{c}_{\mu\bar{\sigma}}^{\dagger}(k)\hat{c}_{\nu\sigma}(k)\rangle=\sum_{kn}{}'\sum_{l=0}^{3}\left[\bar{u}_{l\mu}^{n*}(k)u_{l\nu}^{n}(k)-u_{l\mu}^{n*}(k)\bar{u}_{l\nu}^{n}(k)\right]f_n,$$

$$\tilde{n}_3^{\mu\nu}=\sum_{k\sigma}\sigma\langle\hat{c}_{\mu\bar{\sigma}}^{\dagger}(k)\hat{c}_{\nu\sigma}(k+q_3)\rangle=\sum_{kn}{}'\Bigg\{\sum_{l=1,4}\left[\bar{u}_{l\mu}^{n*}(k)u_{\bar{l}\nu}^{n}(k)-\bar{u}_{l\mu}^{n*}(k)u_{\bar{l}\nu}^{n}(k)\right]$$

$$+\sum_{l=2,3}\left[\bar{u}_{l\mu}^{n*}(k)u_{\bar{l}\nu}^{n}(k)+u_{l\mu}^{n*}(k)\bar{u}_{\bar{l}\nu}^{n}(k)\right]\Bigg\}f_n,$$

$$\tilde{M}_1^{\mu\nu}=\sum_{k\sigma}\langle\hat{c}_{\mu\bar{\sigma}}^{\dagger}(k)\hat{c}_{\nu\sigma}(k+q_1)\rangle=\sum_{kn}{}'\Bigg\{\sum_{l=1,2}\left[\bar{u}_{l\mu}^{n*}(k)u_{\bar{l}\nu}^{n}(k)+u_{l\mu}^{n*}(k)\bar{u}_{\bar{l}\nu}^{n}(k)\right]$$

$$+\sum_{l=3,4}\left[\bar{u}_{l\mu}^{n*}(k)u_{\bar{l}\nu}^{n}(k)+u_{l\mu}^{n*}(k)\bar{u}_{\bar{l}\nu}^{n}(k)\right]\Bigg\}f_n,$$

$$\tilde{M}_2^{\mu\nu}=\sum_{k\sigma}\langle\hat{c}_{\mu\bar{\sigma}}^{\dagger}(k)\hat{c}_{\nu\sigma}(k+q_2)\rangle=\sum_{kn}{}'\Bigg\{\sum_{l=1,3}\left[\bar{u}_{l\mu}^{n*}(k)u_{\bar{l}\nu}^{n}(k)+u_{l\mu}^{n*}(k)\bar{u}_{\bar{l}\nu}^{n}(k)\right]$$

$$+\sum_{l=2,4}\left[\bar{u}_{l\mu}^{n*}(k)u_{\bar{l}\nu}^{n}(k)+u_{l\mu}^{n*}(k)\bar{u}_{\bar{l}\nu}^{n}(k)\right]\Bigg\}f_n,$$

where the abbreviation $f_n \equiv f(E_n(k))$ has been used.

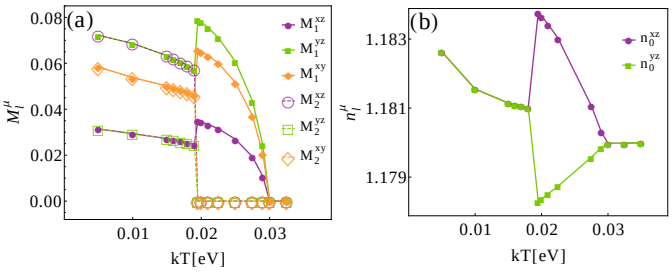

Figure A.1: Orbitally resolved (a) magnetic OPs for d_{xz}, d_{yz} and d_{xy}, and (b) charge OPs for d_{xz} and d_{yz} as a function of temperature for $x = -0.09$.

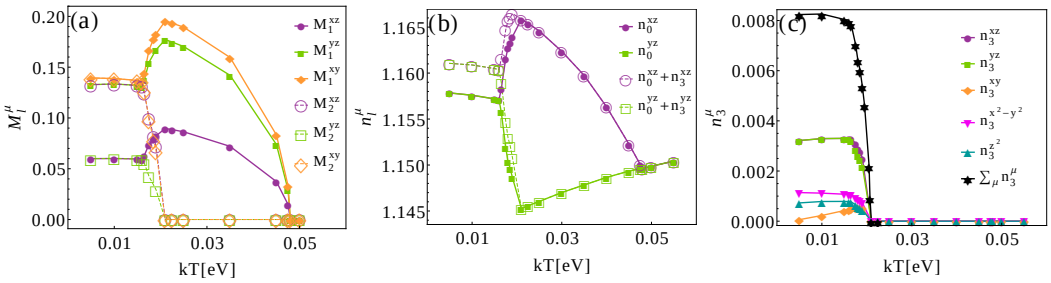

Figure A.2: Orbitally resolved (a) magnetic OPs for d_{xz}, d_{yz} and d_{xy}, (b) charge OPs for d_{xz} and d_{yz}, and (c) (π, π) charge OPs for all orbitals as a function of temperature for $x = 0.02$.

A.3 Orbitally resolved order parameters

The Figs. A.1 and A.2 show the orbital content of the magnetic and charge order parameters versus T corresponding to the results presented in Fig. 2 of the main text. The largest magnetic order parameter (OP) components M_l^μ correspond to the best nested orbitals, d_{xz}/d_{yz} for $x = -0.09$ in Fig. A.1(a), and d_{xy} for the higher filling of $x = 0.02$ in Fig. A.2(a) where the $\gamma - \beta_i$ nesting has improved. The remaining orbital components are not shown for presentational simplicity. The ferro-orbital order ($n_0^{xz} > n_0^{yz}$) can be seen across the PM-MS transition in Figs. A.1(b) and A.2(b), and it collapses upon formation of both SVC and CSDW order. In addition, a small $q_3 \equiv \mathbf{Q_1} + \mathbf{Q_2} = (\pi, \pi)$ charge order develops as soon as $M_2 > 0$ in the CSDW phase. Figure A.2(c) shows the orbital character of this charge order, and the dominant contributions arise from the d_{xz} and d_{yz} orbitals.

Appendix B

Elastic scattering rate

We give a detailed derivation of the momentum dependent effective impurity potential $\hat{\mathcal{V}}^{imp}_{\sigma\sigma'}(\mathbf{k}\alpha, \mathbf{k}'\beta) \equiv \langle \mathbf{k}'\beta\sigma'|\mathcal{V}^{imp}|\mathbf{k}\alpha\sigma\rangle$ which is part of the scattering rate (5.4). Here α and β are the band index and from now we only consider non-spin flip processes $\sigma' = \sigma$. The full Hamiltonian can be written as

$$\mathcal{H} = \tilde{\mathcal{H}}_0 + \mathcal{H}_{imp} \tag{B.1}$$

where $\tilde{\mathcal{H}}_0 = \mathcal{H}_0 + \mathcal{H}_{int} + \mathcal{H}_{oo}$ is the tight-binding band with the static ferro-orbital order and the Hartree-Fock mean-fields, i.e. the impurity free system under uniaxial stress. The matrix elements we are after are then

$$\langle \mathbf{k}'\beta\sigma|\mathcal{V}^{imp}|\mathbf{k}\alpha\sigma\rangle = \langle \mathbf{k}'\beta\sigma|\mathcal{H} - \tilde{\mathcal{H}}_0|\mathbf{k}\alpha\sigma\rangle = \langle \mathbf{k}'\beta\sigma|\mathcal{H}|\mathbf{k}\alpha\sigma\rangle - \epsilon_{\mathbf{k}\alpha}\delta_{\mathbf{k}\mathbf{k}'}\delta_{\alpha\beta}. \tag{B.2}$$

Here the last term contains the band energies $\epsilon_{\mathbf{k}\alpha}$ of the unperturbed system $\tilde{\mathcal{H}}_0$. The first term is calculated as

$$\begin{aligned}
\langle \mathbf{k}'\beta\sigma|\mathcal{H}|\mathbf{k}\alpha\sigma\rangle &= \sum_{mn}\langle \mathbf{k}'\beta\sigma|m\sigma\rangle\langle m\sigma|\mathcal{H}|n\sigma\rangle\langle n\sigma|\mathbf{k}\alpha\sigma\rangle \\
&= \sum_{n}\langle \mathbf{k}'\beta\sigma|n\sigma\rangle\langle n\sigma|\mathbf{k}\sigma\rangle E_{n\sigma} \\
&= \sum_{n}\sum_{\mathbf{ij}\mu\nu}\langle \mathbf{k}'\beta\sigma|\mathbf{r_j}\nu\sigma\rangle\langle \mathbf{r_j}\nu\sigma|n\sigma\rangle\langle n\sigma|\mathbf{r_i}\mu\sigma\rangle\langle \mathbf{r_i}\mu\sigma|\mathbf{k}\alpha\sigma\rangle E_{n\sigma} \\
&= \frac{1}{N}\sum_{n}\sum_{\mathbf{ij}\mu\nu} a^{\beta}_{\mathbf{k}'\nu}e^{-i\mathbf{k}'\mathbf{r_j}}u^{n*}_{\mathbf{j}\nu\sigma}u^{n}_{\mathbf{i}\mu\sigma}a^{\alpha*}_{\mathbf{k}\mu}e^{i\mathbf{k}\mathbf{r_i}}E_{n\sigma}
\end{aligned} \tag{B.3}$$

Here $|n\sigma\rangle$ are the eigenstates of the full Hamiltonian $\mathcal{H}$ associated to the eigenenergy $E_{n\sigma}$, which in real space representation become $u^n_{\mathbf{i}\mu\sigma}$ (so $\mathcal{H}u^n_{\mathbf{i}\mu\sigma} = E_{n\sigma}u^n_{\mathbf{i}\mu\sigma}$). Note we have used twice the complete set $|\mathbf{r_i}\mu\sigma\rangle$ which includes both site and orbital information. We also used in the last step $\langle \mathbf{r_i}\mu\sigma|\mathbf{k}\alpha\sigma\rangle = \frac{1}{\sqrt{N}}a^{\alpha*}_{\mathbf{k}\mu}e^{i\mathbf{k}\mathbf{r_i}}$, where

$a^{\alpha}_{\mathbf{k}\mu}$ are the band to orbital transformation elements in $\mathbf{k}$ space ($\tilde{\mathcal{H}}_0 a^{\alpha}_{\mathbf{k}\mu} = \epsilon_{\mathbf{k}\alpha} a^{\alpha}_{\mathbf{k}\mu}$). By doing the real space and n sums the expression becomes

$$\langle \mathbf{k}'\beta\sigma|\mathcal{H}|\mathbf{k}\alpha\sigma\rangle = \sum_{\mu\nu} a^{\alpha *}_{\mathbf{k}\mu} \omega^{\mu\nu}_{\mathbf{k}\mathbf{k}'} a^{\beta}_{\mathbf{k}'\nu} \tag{B.4}$$

where $\omega^{\alpha\beta}_{\mathbf{k}\mathbf{k}'} = \frac{1}{N} \sum_n \sum_{\mathbf{ij}} u^{n*}_{\mathbf{j}\nu\sigma} u^{n}_{\mathbf{i}\mu\sigma} E_{n\sigma} e^{-i\mathbf{k}'\mathbf{r_j}} e^{i\mathbf{k}\mathbf{r_i}}$.

Appendix C

Band structure for LiFeAs

The explicit form of the tight-binding Hamiltonian

$$H_0 = \sum_{\mathbf{k},\mu\nu,\sigma} \xi_{\mu\nu}(\mathbf{k}) c^\dagger_{\mathbf{k}\mu\sigma} c_{\mathbf{k}\nu\sigma} \tag{C.1}$$

is listed in equation (C.2). The indices μ and ν run through 1 to 5 corresponding to the Fe orbitals $d_{3z^2-r^2}$, d_{yz}, d_{xz}, d_{xy}, and $d_{x^2-y^2}$. The hopping parameters and on-site energies are given in tables C.1 and C.2. For our 2D real space lattice we the take the $k_z = 0$ cut, and the resulting band structure and Fermi surface are shown in figure 6.5.

$$\begin{aligned}
\xi_{11}(\mathbf{k}) = &-2t^{11}_x \cos k_x - 2t^{11}_y \cos k_y + 2t^{11}_{xx} \cos 2k_x + 2t^{11}_{yy} \cos 2k_y \\
&+ 4t^{11}_{xy} \cos k_x \cos k_y - 4t^{11}_{xz} \cos k_x \cos k_z - 4t^{11}_{yz} \cos k_y \cos k_z \\
&+ 8t^{11}_{xyz} \cos k_x \cos k_y \cos k_z + 2t^{11}_z \cos k_z + 2t^{11}_{zz} \cos 2k_z \\
&+ 4t^{11}_{xxyy} \cos 2k_x \cos 2k_y + \epsilon_1 \\
\xi_{22}(\mathbf{k}) = &-2t^{22}_x \cos k_x - 2t^{22}_y \cos k_y + 2t^{22}_z \cos k_z + 4t^{22}_{xy} \cos k_x \cos k_y \\
&+ 2t^{22}_{xx} \cos 2k_x + 2t^{22}_{yy} \cos 2k_y - 4t^{22}_{xxy} \cos 2k_x \cos k_y - 4t^{22}_{xyy} \cos k_x \cos 2k_y \\
&+ 4t^{22}_{xxyy} \cos 2k_x \cos 2k_y - 4t^{22}_{xz} \cos k_x \cos k_z \\
&+ 4t^{22}_{yyz} \cos 2k_y \cos k_z - 8t^{22}_{xxyz} \cos 2k_x \cos k_y \cos k_z + 4t^{22}_{xxz} \cos 2k_x \cos k_z \\
&- 8t^{22}_{xyyz} \cos k_x \cos 2k_y \cos k_z + 8t^{22}_{xyz} \cos k_x \cos k_y \cos k_z + \epsilon_2 \\
\xi_{33}(\mathbf{k}) = &-2t^{33}_x \cos k_x - 2t^{33}_y \cos k_y + 2t^{33}_z \cos k_z + 4t^{33}_{xy} \cos k_x \cos k_y + 2t^{33}_{xx} \cos 2k_x \\
&+ 2t^{33}_{yy} \cos 2k_y - 4t^{33}_{xxy} \cos 2k_x \cos k_y - 4t^{33}_{xyy} \cos k_x \cos 2k_y \\
&+ 4t^{33}_{xxyy} \cos 2k_x \cos 2k_y + 4t^{33}_{yyz} \cos 2k_y \cos k_z - 8t^{33}_{xxyz} \cos 2k_x \cos k_y \cos k_z \\
&+ 4t^{33}_{xxz} \cos 2k_x \cos k_z - 4t^{33}_{xz} \cos k_x \cos k_z - 8t^{33}_{xyyz} \cos k_x \cos 2k_y \cos k_z
\end{aligned} \tag{C.2}$$

$$
\begin{aligned}
&+ 8t^{33}_{xyz}\cos k_x \cos k_y \cos k_z + \epsilon_3 \\
\xi_{44}(\mathbf{k}) = {} & 2t^{44}_{z}\cos k_z + 4t^{44}_{xy}\cos k_x \cos k_y - 4t^{44}_{xz}\cos k_x \cos k_z - 4t^{44}_{yz}\cos k_y \cos k_z \\
&- 4t^{44}_{xxy}\cos 2k_x \cos k_y - 4t^{44}_{xyy}\cos k_x \cos 2k_y + 4t^{44}_{xxz}\cos 2k_x \cos k_z \\
&+ 4t^{44}_{yyz}\cos k_z \cos 2k_y + 8t^{44}_{xyz}\cos k_x \cos k_y \cos k_z + 4t^{44}_{xxyy}\cos 2k_x \cos 2k_y \\
&- 8t^{44}_{xxyz}\cos 2k_x \cos k_y \cos k_z - 8t^{44}_{xyyz}\cos k_x \cos 2k_y \cos k_z \\
&+ 8t^{44}_{xxyyz}\cos 2k_x \cos 2k_y \cos k_z + \epsilon_4 \\
\xi_{55}(\mathbf{k}) = {} & -2t^{55}_{x}\cos k_x - 2t^{55}_{y}\cos k_y + 2t^{55}_{z}\cos k_z + 2t^{55}_{xx}\cos 2k_x + 2t^{55}_{yy}\cos 2k_y \\
&+ 4t^{55}_{xy}\cos k_x \cos k_y + 4t^{55}_{xxyy}\cos 2k_x \cos 2k_y + 4t^{55}_{xxz}\cos 2k_x \cos k_z \\
&+ 4t^{55}_{yyz}\cos 2k_y \cos k_z + 8t^{55}_{xyz}\cos k_x \cos k_y \cos k_z - 4t^{55}_{xz}\cos k_x \cos k_z \\
&- 4t^{55}_{yz}\cos k_y \cos k_z + \epsilon_5 \\
\xi_{12}(\mathbf{k}) = {} & -2it^{12}_{x}\sin k_x + 2it^{12}_{xx}\sin 2k_x + 4it^{12}_{xy}\sin k_x \cos k_y - 4it^{12}_{xyy}\sin k_x \cos 2k_y \\
&- 4it^{12}_{xxy}\sin 2k_x \cos k_y - 4it^{12}_{xz}\sin k_x \cos k_z + 4it^{12}_{xxyy}\sin 2k_x \cos 2k_y \\
&+ 8it^{12}_{xyz}\sin k_x \cos k_y \cos k_z + 4it^{12}_{xxz}\sin 2k_x \cos k_z \\
\xi_{13}(\mathbf{k}) = {} & -2it^{13}_{y}\sin k_y + 2it^{13}_{yy}\sin 2k_y + 4it^{13}_{xy}\sin k_y \cos k_x - 4it^{13}_{yz}\sin k_y \cos k_z \\
&- 4it^{13}_{xxy}\cos 2k_x \sin k_y - 4it^{13}_{xyy}\cos k_x \sin 2k_y + 4it^{13}_{xxyy}\sin 2k_y \cos 2k_x \\
&+ 8it^{13}_{xyz}\cos k_x \sin k_y \cos k_z + 4it^{13}_{yyz}\sin 2k_y \cos k_z \\
\xi_{14}(\mathbf{k}) = {} & -4t^{14}_{xy}\sin k_x \sin k_y - 4t^{14}_{xxyy}\sin 2k_x \sin 2k_y - 8t^{14}_{xyz}\sin k_x \sin k_y \cos k_z \\
&+ 8t^{14}_{xxyz}\sin 2k_x \sin k_y \cos k_z + 8t^{14}_{xyyz}\sin k_x \sin 2k_y \cos k_z \\
\xi_{15}(\mathbf{k}) = {} & -2t^{15}_{x}\cos k_x - 2t^{15}_{y}\cos k_y + 2t^{15}_{xx}\cos 2k_x + 2t^{15}_{yy}\cos 2k_y \\
&- 4t^{15}_{xxy}\cos 2k_x \cos k_y - 4t^{15}_{xyy}\cos k_x \cos 2k_y - 4t^{15}_{xz}\cos k_x \cos k_z \\
&- 4t^{15}_{yz}\cos k_y \cos k_z + 4t^{15}_{xxz}\cos 2k_x \cos k_z + 4t^{15}_{yyz}\cos 2k_y \cos k_z \\
\xi_{23}(\mathbf{k}) = {} & -4t^{23}_{xy}\sin k_x \sin k_y - 4t^{23}_{xxyy}\sin 2k_x \sin 2k_y + 4t^{23}_{xxy}\sin 2k_x \sin k_y \\
&+ 4t^{23}_{xyy}\sin k_x \sin 2k_y \\
\xi_{24}(\mathbf{k}) = {} & -2it^{24}_{y}\sin k_y + 2it^{24}_{yy}\sin 2k_y + 4it^{24}_{xy}\sin k_y \cos k_x \\
&- 8it^{24}_{xxyz}\cos 2k_x \sin k_y \cos k_z - 4it^{24}_{xxy}\cos 2k_x \sin k_y - 4it^{24}_{xyy}\cos k_x \sin 2k_y \\
&+ 4it^{24}_{xxyy}\sin 2k_y \cos 2k_x + 8it^{24}_{xyz}\cos k_x \sin k_y \cos k_z - 4it^{24}_{yz}\sin k_y \cos k_z \\
\xi_{25}(\mathbf{k}) = {} & -2it^{25}_{x}\sin k_x + 2it^{25}_{xx}\sin 2k_x + 4it^{25}_{xy}\sin k_x \cos k_y - 4it^{25}_{xyy}\sin k_x \cos 2k_y \\
&- 4it^{25}_{xxy}\cos k_y \sin 2k_x + 4it^{25}_{xxz}\cos k_z \sin 2k_x - 4it^{25}_{xz}\cos k_z \sin k_x \\
\xi_{34}(\mathbf{k}) = {} & -2it^{34}_{x}\sin k_x + 2it^{34}_{xx}\sin 2k_x + 4it^{34}_{xy}\sin k_x \cos k_y \\
&- 8it^{34}_{xyyz}\sin k_x \cos 2k_y \cos k_z - 4it^{34}_{xxy}\sin 2k_x \cos k_y - 4it^{34}_{xyy}\sin k_x \cos 2k_y \\
&+ 4it^{34}_{xxyy}\sin 2k_x \cos 2k_y + 8it^{34}_{xyz}\sin k_x \cos k_y \cos k_z - 4it^{34}_{xz}\sin k_x \cos k_z \\
\xi_{35}(\mathbf{k}) = {} & -2it^{35}_{y}\sin k_y + 2it^{35}_{yy}\sin 2k_y + 4it^{35}_{xy}\sin k_y \cos k_x - 4it^{35}_{xxy}\cos 2k_x \sin k_y
\end{aligned}
$$

$$
\begin{aligned}
&- 4it^{35}_{xyy}\sin 2k_y\cos k_x + 4it^{35}_{yyz}\sin 2k_y\cos k_z - 4it^{35}_{yz}\sin k_y\cos k_z \\
\xi_{45}(\mathbf{k}) &= 4t^{45}_{xxy}\sin 2k_x\sin k_y + 4t^{45}_{xyy}\sin k_x\sin 2k_y \\
&+ 8t^{45}_{xxyz}\sin 2k_x\sin k_y\cos k_z + 8t^{45}_{xyyz}\sin k_x\sin 2k_y\cos k_z
\end{aligned}
$$

Table C.1: Hopping parameters on the XY plane

$t_i^{\mu\nu}$	$i=x$	$i=y$	$i=xy$	$i=xx$	$i=yy$	$i=xxy$	$i=xyy$	$i=xxyy$	ϵ_μ
$\mu\nu=11$	-0.024	-0.024	-0.040	-0.010	-0.010			-0.015	-0.43
$\mu\nu=22$	0.38	0.051	0.26	-0.075	0.0137	-0.022	0.045	0.038	0.0088
$\mu\nu=33$	0.051	0.38	0.26	0.014	-0.075	0.045	-0.022	0.038	0.0088
$\mu\nu=44$			0.076			0.029	0.029	-0.034	-0.13
$\mu\nu=55$	-0.40	-0.40	-0.032	-0.049	-0.049			0.021	-0.40
$\mu\nu=12$	-0.17		-0.13	0.013		0.012	0.013	-0.020	
$\mu\nu=13$		-0.17	-0.13		0.013	0.013	0.012	-0.020	
$\mu\nu=14$			0.078					-0.015	
$\mu\nu=15$	-0.34	0.34		0.032	-0.032	-0.010	0.010		
$\mu\nu=23$			0.11			0.030	0.030	0.048	
$\mu\nu=24$		-0.28	0.087		0.011	-0.015	-0.015	-0.0090	
$\mu\nu=25$	0.40		0.10	-0.0061		0.016	-0.032		
$\mu\nu=34$	-0.28		0.087	0.011		-0.015	-0.015	-0.0090	
$\mu\nu=35$		-0.40	-0.10		0.0061	0.032	-0.016		
$\mu\nu=45$						0.018	-0.018		

Table C.2: Hopping parameters out of the XY plane

$t_i^{\mu\nu}$	$i=z$	$i=xz$	$i=yz$	$i=zz$	$i=xyz$	$i=xxz$	$i=yyz$	$i=xxyz$	$i=xyyz$
$\mu\nu=11$	-0.056	-0.0306	-0.0306	0.0041	-0.013				
$\mu\nu=22$	0.0078	0.035			0.0096	0.025	-0.010	0.014	-0.0058
$\mu\nu=33$	0.0078		0.035		0.0096	-0.010	0.025	-0.0058	0.014
$\mu\nu=44$	0.055	-0.049	-0.049		0.036	0.031	0.031	-0.014	-0.014
$\mu\nu=55$	-0.037	0.0079	0.0078		0.016	-0.010	-0.010		
$\mu\nu=12$		0.030			0.015	0.0066			
$\mu\nu=13$			0.030		0.015		0.0066		
$\mu\nu=14$					-0.013			-0.0081	-0.0081
$\mu\nu=15$		0.016	-0.016			0.0080	-0.0080		
$\mu\nu=23$									
$\mu\nu=24$			0.0077		-0.0075			-0.012	
$\mu\nu=25$		-0.010				0.016			
$\mu\nu=34$		0.0077			-0.0075				-0.012
$\mu\nu=35$			0.010				-0.016		
$\mu\nu=45$								0.0094	-0.0094

Appendix D

Self-consistent BdG equations with superconductivity

D.1 BdG equations

Let us start with the Hamiltonian

$$\mathcal{H} = \mathcal{H}_0 + \mathcal{H}_{int} + \mathcal{H}_{BCS} + \mathcal{H}_{imp}, \tag{D.1}$$

which describes a SC system with interactions and disorder. We first mean-field decouple the interactions in the density channel,

$$\mathcal{H}_{int}^{MF} = \sum_{i,\mu\neq\nu,\sigma} [U\langle\hat{n}_{i\mu\bar{\sigma}}\rangle + U'\langle\hat{n}_{i\nu\bar{\sigma}}\rangle + (U'-J)\langle\hat{n}_{i\nu\sigma}\rangle]\hat{c}^{\dagger}_{i\mu\sigma}\hat{c}_{i\mu\sigma} \tag{D.2}$$

and bring the Hamiltonian to a quadratic form.

The first step to get the BdG equations is to compute the commutators $[H^{MF}, \hat{c}_{i\mu\sigma}]$. We will do this in two differing ways. In the first way, we split the mean field Hamiltonian up and find the commutator of each piece. The kinetic energy term,

$$\begin{aligned}
[H_0, \hat{c}_{i\mu\sigma}] &= \sum_{klab\sigma'} t^{ab}_{kl}[\hat{c}^{\dagger}_{ka\sigma'}\hat{c}_{lb\sigma'}, \hat{c}_{i\mu\sigma}] \\
&= -\sum_{klab\sigma'} t^{ab}_{kl}\{\hat{c}^{\dagger}_{ka\sigma'}, \hat{c}_{i\mu\sigma}\}\hat{c}_{lb\sigma'} \\
&= -\sum_{j\nu} t^{\mu\nu}_{ij}\hat{c}_{j\nu\sigma}.
\end{aligned} \tag{D.3}$$

The Hartree-Fock interacting term,

$$[H_{int}^{MF}, \hat{c}_{i\mu\sigma}] = \sum_{ka\neq b\sigma'} (Un_{ka\bar{\sigma}'} + U'n_{kb\bar{\sigma}'} + (U'-J)n_{kb\sigma'})[\hat{c}^{\dagger}_{ka\sigma'}\hat{c}_{ka\sigma'}, \hat{c}_{i\mu\sigma}] \tag{D.4}$$

$$
\begin{aligned}
&= -\sum_{ka\neq b\sigma'} (U n_{ka\bar{\sigma}'} + U' n_{kb\bar{\sigma}'} + (U'-J) n_{kb\sigma'}) \{\hat{c}^\dagger_{ka\sigma'}, \hat{c}_{i\mu\sigma}\} \hat{c}_{ka\sigma'} \\
&= -\sum_{\mu\neq\nu} (U n_{i\mu\bar{\sigma}} + U' n_{i\nu\bar{\sigma}} + (U'-J) n_{i\nu\sigma}) \hat{c}_{i\mu\sigma}.
\end{aligned}
$$

The superconducting term,

$$
\begin{aligned}
[H_{BCS}, \hat{c}_{i\mu\sigma}] &= -\sum_{kl}\sum_{pt} \Delta^{pt}_{kl} [\hat{c}^\dagger_{kp\uparrow}\hat{c}^\dagger_{lt\downarrow}, \hat{c}_{i\mu\sigma}] \\
&= -\sum_{kl}\sum_{pt} \Delta^{pt}_{kl} (\{\hat{c}^\dagger_{lt\downarrow}, \hat{c}_{i\mu\sigma}\}\hat{c}^\dagger_{kp\uparrow} - \{\hat{c}^\dagger_{kp\uparrow}, \hat{c}_{i\mu\sigma}\}\hat{c}^\dagger_{lt\downarrow}) \\
&= -\sum_{kp} \Delta^{p\mu}_{ki} \hat{c}^\dagger_{kp\uparrow}\delta_{\sigma\downarrow} + \sum_{lt} \Delta^{\mu t}_{il} \hat{c}^\dagger_{lt\downarrow}\delta_{\sigma\uparrow} \\
&= -\sum_{j\nu} \Delta^{\nu\mu}_{ji} \hat{c}^\dagger_{j\nu\uparrow}\delta_{\sigma\downarrow} + \sum_{j\nu} \Delta^{\mu\nu}_{ij} \hat{c}^\dagger_{j\nu\downarrow}\delta_{\sigma\uparrow}.
\end{aligned} \tag{D.5}
$$

where $\Delta^{\mu\nu}_{ij} = \sum_{qs} \Gamma_{\mu qs\nu}(r) \langle \hat{c}_{js\downarrow}\hat{c}_{iq\uparrow}\rangle$. Finally the impurity term,

$$
\begin{aligned}
[H_{imp}, \hat{c}_{i\mu\sigma}] &= \sum_{i*a\sigma'} V_{imp} [\hat{c}^\dagger_{i*a\sigma'}\hat{c}_{i*a\sigma'}, \hat{c}_{i\mu\sigma}] \\
&= V_{imp}\hat{c}_{i\mu\sigma}\delta_{ii*}.
\end{aligned} \tag{D.6}
$$

We turn now to the second method, were we use the spin-generalized Bogoliubov transformation,

$$
\begin{aligned}
\hat{c}_{i\mu\sigma} &= \sum_n (u^n_{i\mu\sigma}\hat{\gamma}_{n\sigma} + v^{n*}_{i\mu\sigma}\hat{\gamma}^\dagger_{n\bar{\sigma}}), \\
\hat{c}^\dagger_{i\mu\sigma} &= \sum_n (u^{*n}_{i\mu\sigma}\hat{\gamma}^\dagger_{n\sigma} + v^{n}_{i\mu\sigma}\hat{\gamma}_{n\bar{\sigma}}).
\end{aligned} \tag{D.7}
$$

Here, n is the index of the new eigenstates and eigenvalues. The diagonalized Hamiltonian is $H = GS + \sum_{n\sigma} E_{n\sigma}\hat{\gamma}^\dagger_{n\sigma}\hat{\gamma}_{n\sigma}$ and hence it runs only for those n states with the associated eigenvalue $E_{n\sigma} > 0$. With this transformation we use the commutators

$$
\begin{aligned}
[H^{MF}, \hat{\gamma}_{n\sigma}] &= -E_{n\sigma}\hat{\gamma}_{n\sigma}, \\
[H^{MF}, \hat{\gamma}^\dagger_{n\sigma}] &= E_{n\sigma}\hat{\gamma}^\dagger_{n\sigma},
\end{aligned} \tag{D.8}
$$

to compute the commutators using the second method:

$$
[H^{MF}, \hat{c}_{i\mu\uparrow}] = \sum_n (-E_{n\uparrow} u^n_{i\mu\uparrow}\hat{\gamma}_{n\uparrow} + E_{n\downarrow} v^{n*}_{i\mu\uparrow}\hat{\gamma}^\dagger_{n\downarrow}), \tag{D.9}
$$

$$[H^{MF}, \hat{c}_{i\mu\downarrow}] = \sum_n (E_{n\uparrow} v^{n*}_{i\mu\downarrow} \hat{\gamma}^\dagger_{n\uparrow} - E_{n\downarrow} u^n_{i\mu\downarrow} \hat{\gamma}_{n\downarrow}).$$

We now have two equivalent ways of expressing the commutators. By equating the coefficients of the $\hat{\gamma}$ operators, we arrive to the Bogoliubov-de Gennes equations:

$$\begin{aligned} -E_{n\uparrow} u_{i\mu\uparrow} = &- \sum_{j\nu} t^{\mu\nu}_{ij} u^n_{j\nu\uparrow} - \sum_{\mu\neq\nu} [-\mu_0 + \delta_{ii*} V_{imp} + U n_{i\mu\downarrow} + U' n_{i\nu\downarrow} + \\ &+ (U' - J) n_{i\nu\uparrow}] u^n_{i\mu\uparrow} + \sum_{j\nu} \Delta^{\mu\nu}_{ij} v^n_{j\nu\downarrow}, \end{aligned} \tag{D.10}$$

$$\begin{aligned} E_{n\uparrow} v^{n*}_{i\mu\downarrow} = &- \sum_{j\nu} t^{\mu\nu}_{ij} v^{n*}_{j\nu\downarrow} - \sum_{\mu\neq\nu} (-\mu_0 + \delta_{ii*} V_{imp} + U n_{i\mu\uparrow} + U' n_{i\nu\uparrow} + \\ &+ (U' - J) n_{i\nu\downarrow}) v^{n*}_{i\mu\downarrow} - \sum_{j\nu} \Delta^{\nu\mu}_{ji} u^{n*}_{j\nu\uparrow}, \end{aligned} \tag{D.11}$$

$$\begin{aligned} E_{n\downarrow} v^{n*}_{i\mu\uparrow} = &- \sum_{j\nu} t^{\mu\nu}_{ij} v^{n*}_{j\nu\uparrow} - \sum_{\mu\neq\nu} (-\mu_0 + \delta_{ii*} V_{imp} + U n_{i\mu\downarrow} + U' n_{i\nu\downarrow} + \\ &+ (U' - J) n_{i\nu\uparrow}) v^{n*}_{i\mu\uparrow} + \sum_{j\nu} \Delta^{\mu\nu}_{ij} u^{n*}_{j\nu\downarrow}, \end{aligned} \tag{D.12}$$

$$\begin{aligned} -E_{n\downarrow} u_{i\mu\downarrow} = &- \sum_{j\nu} t^{\mu\nu}_{ij} u^n_{j\nu\downarrow} - \sum_{\mu\neq\nu} (-\mu_0 + \delta_{ii*} V_{imp} + U n_{i\mu\uparrow} + U' n_{i\nu\uparrow} + \\ &+ (U' - J) n_{i\nu\downarrow}) u^n_{i\mu\downarrow} - \sum_{j\nu} \Delta^{\nu\mu}_{ji} v^n_{j\nu\uparrow}, \end{aligned} \tag{D.13}$$

Upon a little manipulation we can write these equations in matrix form:

$$\begin{pmatrix} \hat{\xi}_\uparrow & \hat{\Delta}^{\mu\nu}_{ij} \\ \hat{\Delta}^{\nu\mu*}_{ji} & -\hat{\xi}^*_\downarrow \end{pmatrix} \begin{pmatrix} u^n_\uparrow \\ v^n_\downarrow \end{pmatrix} = E_{n\uparrow} \begin{pmatrix} u^n_\uparrow \\ v^n_\downarrow \end{pmatrix}, \tag{D.14}$$

and

$$\begin{pmatrix} \hat{\xi}_\downarrow & -\hat{\Delta}^{\nu\mu}_{ji} \\ -\hat{\Delta}^{\mu\nu*}_{ij} & -\hat{\xi}^*_\uparrow \end{pmatrix} \begin{pmatrix} u^n_\downarrow \\ v^n_\uparrow \end{pmatrix} = E_{n\downarrow} \begin{pmatrix} u^n_\downarrow \\ v^n_\uparrow \end{pmatrix}. \tag{D.15}$$

Here the matrix operators are defined as:

$$\hat{\xi}_\sigma u_{i\mu} = \sum_{j\nu} t^{\mu\nu}_{ij} u_{j\nu} + \sum_{\mu\neq\nu} (-\mu_0 + V_{imp}\delta_{ii*} + U n_{i\mu\bar{\sigma}} + U' n_{i\nu\bar{\sigma}} + (U' - J) n_{i\nu\sigma}) u_{i\mu}, \tag{D.16}$$

$$\hat{\Delta}_{ij}^{\mu\nu} u_{i\mu} = -\sum_{j\nu} \Delta_{ij}^{\mu\nu} u_{j\nu}.$$

By applying to equations (D.14) the transformation

$$\begin{pmatrix} u_{\uparrow}^{n} \\ v_{\downarrow}^{n} \\ E_{n\uparrow} \end{pmatrix} \rightarrow \begin{pmatrix} v_{\uparrow}^{n*} \\ u_{\downarrow}^{n*} \\ -E_{n\downarrow} \end{pmatrix} \tag{D.17}$$

one obtains equations (D.15). Since we are only concerned with eigenvectors corresponding to positive eigenvalues and the previous symmetry holds, the diagonalization of a single Hermitian matrix is necessary:

$$\begin{pmatrix} \hat{\xi}_{\uparrow} & \hat{\Delta}_{ij} \\ \hat{\Delta}_{ji}^{*} & -\hat{\xi}_{\downarrow}^{*} \end{pmatrix} \begin{pmatrix} u^{n} \\ v^{n} \end{pmatrix} = E_n \begin{pmatrix} u^{n} \\ v^{n} \end{pmatrix} \tag{D.18}$$

and account for *all* states.

D.2 Self-consistent fields

We can now express the self-consistent parameters of our mean field Hamiltonian in terms of the eigenvectors and eigenvalues:

$$\begin{aligned} n_{i\mu\uparrow} = \langle \hat{c}_{i\mu\uparrow}^{\dagger} \hat{c}_{i\mu\uparrow} \rangle &= \sum_{n} |u_{i\mu\uparrow}^{n}|^2 \langle \hat{\gamma}_{n\uparrow}^{\dagger} \hat{\gamma}_{n\uparrow} \rangle + \sum_{n} |v_{i\mu\uparrow}^{n}|^2 \langle \hat{\gamma}_{n\downarrow} \hat{\gamma}_{n\downarrow}^{\dagger} \rangle \\ &= \sum_{n} |u_{i\mu\uparrow}^{n}|^2 f(E_{n\uparrow}) + \sum_{n} |v_{i\mu\uparrow}^{n}|^2 f(-E_{n\downarrow}) \\ &= \sum_{n, E_{n\uparrow}>0} |u_{i\mu\uparrow}^{n}|^2 f(E_{n\uparrow}) + \sum_{n, E_{n\uparrow}<0} |u_{i\mu\uparrow}^{n}|^2 f(E_{n\uparrow}) \\ &= \sum_{l} |u_{i\mu}^{l}|^2 f(E_l) \end{aligned} \tag{D.19}$$

where $\sum_n$ sums only for those n values which have positive (or negative when specified) eigenvalues, $E_{n\sigma} > 0$, and $\sum_l$ sums for *all* states with positive and negative eigenvalues. The symmetry (D.17) has been used. A very similar calculation gives for the spin down density,

$$\begin{aligned} n_{i\mu\downarrow} = \langle \hat{c}_{i\mu\downarrow}^{\dagger} \hat{c}_{i\mu\downarrow} \rangle &= \sum_{n} |u_{i\mu\downarrow}^{n}|^2 \langle \hat{\gamma}_{n\downarrow}^{\dagger} \hat{\gamma}_{n\downarrow} \rangle + \sum_{n} |v_{i\mu\downarrow}^{n}|^2 \langle \hat{\gamma}_{n\uparrow} \hat{\gamma}_{n\uparrow}^{\dagger} \rangle \\ &= \sum_{n} |u_{i\mu\downarrow}^{n}|^2 f(E_{n\downarrow}) + \sum_{n} |v_{i\mu\downarrow}^{n}|^2 f(-E_{n\uparrow}) \end{aligned} \tag{D.20}$$

$$= \sum_{n,E_{n\uparrow}<0} |v^n_{i\mu\downarrow}|^2 f(-E_{n\uparrow}) + \sum_{n,E_{n\uparrow}>0} |v^n_{i\mu\downarrow}|^2 f(-E_{n\uparrow})$$
$$= \sum_l |v^l_{i\mu}|^2 (1 - f(E_l))$$

The superconducting field:

$$\Delta^{\mu\nu}_{ij} = \sum_{qs} \Gamma_{\mu qs\nu}(r) \langle \hat{c}_{js\downarrow} \hat{c}_{iq\uparrow} \rangle \tag{D.21}$$
$$= \sum_{qs} \Gamma_{\mu qs\nu}(r) [\sum_n u^n_{js\downarrow} v^{n*}_{iq\uparrow} \langle \hat{\gamma}_{n\downarrow} \hat{\gamma}^\dagger_{n\downarrow} \rangle + \sum_n v^{n*}_{js\downarrow} u^n_{iq\uparrow} \langle \hat{\gamma}^\dagger_{n\uparrow} \hat{\gamma}_{n\uparrow} \rangle]$$
$$= \sum_{qs} \Gamma_{\mu qs\nu}(r) [\sum_{n,E_{n\uparrow}<0} v^{n*}_{js\downarrow} u^n_{iq\uparrow} f(E_{n\uparrow}) + \sum_{n,E_{n\uparrow}>0} v^{n*}_{js\downarrow} u^n_{iq\uparrow} f(E_{n\uparrow})]$$
$$= \sum_{qs} \Gamma_{\mu qs\nu}(r) \sum_l v^{l*}_{js} u^l_{iq} f(E_l).$$

D.3 Local density of states

The spin resolved LDOS in the superconducting system:

$$N_{i\sigma}(\omega) = -\frac{1}{\pi} \Im \sum_{n\mu} [\frac{|u^n_{i\mu\sigma}|^2}{\omega - E_{n\sigma} + i\eta} + \frac{|v^n_{i\mu\sigma}|^2}{\omega + E_{n\bar{\sigma}} + i\eta}] \tag{D.22}$$

So that the spin-up part is given by,

$$N_{i\uparrow}(\omega) = -\frac{1}{\pi} \Im \sum_{n\mu} [\frac{|u^n_{i\mu\uparrow}|^2}{\omega - E_{n\uparrow} + i\eta} + \frac{|v^n_{i\mu\uparrow}|^2}{\omega + E_{n\downarrow} + i\eta}] \tag{D.23}$$
$$= -\frac{1}{\pi} \Im \sum_{n\mu} [\frac{|u^n_{i\mu\uparrow}|^2}{\omega - E_{n\uparrow} + i\eta} + \frac{|u^n_{i\mu\uparrow}|^2}{\omega - E_{n\uparrow} + i\eta}]$$
$$= -\frac{1}{\pi} \Im \sum_{l\mu} [\frac{|u^l_{i\mu}|^2}{\omega - E_l + i\eta}]$$

and in a similar way the spin-down,

$$N_{i\downarrow}(\omega) = -\frac{1}{\pi} \Im \sum_{n\mu} [\frac{|u^n_{i\mu\downarrow}|^2}{\omega - E_{n\downarrow} + i\eta} + \frac{|v^n_{i\mu\downarrow}|^2}{\omega + E_{n\uparrow} + i\eta}] \tag{D.24}$$
$$= -\frac{1}{\pi} \Im \sum_{l\mu} [\frac{|v^l_{i\mu}|^2}{\omega + E_l + i\eta}]$$

and the total LDOS is computed by summation of both spin components,

$$N_i(\omega) = -\frac{1}{\pi}\Im \sum_{n\mu} \left[\frac{|u_{i\mu}^n|^2}{\omega - E_n + i\eta} + \frac{|v_{i\mu}^n|^2}{\omega + E_n + i\eta} \right] \tag{D.25}$$

Appendix E

Ru substitution

E.1 Bandwidth increase

In Fig. E.1, we compare the band structures of LaFeAsO and LaRuAsO to understand the effect of Ru substitution. The first-principles calculations of the electronic structure were performed within the density functional theory by F. Bernardini. To help the comparison of the results, we rescaled the abscissas in Fig. E.1 to fit the band structure of LaRuAsO with the Brillouin zone for the LaFeAsO system. The band structure of LaFeAsO (solid lines) is characterized by a valence band originating from Fe-3d orbitals. We see that the band ranges from 0.15 to -2.15 eV and is separated from the As-4p band by a small pseudo gap. The width of the Fe-3d band is 2.3 eV. The arrow (black) in Fig. E.1 shows the estimated width of the band from its topmost d_{xz+yz} state to the lowermost $d_{x^2-y^2}$ one. The LaRuAsO and LaFeAsO band structures clearly differ in the dispersion of the Ru-4d orbitals related band. To help the readability of the band structure in Fig. E.1, we used the so-called fat-bands representation, where the size of the dots is proportional to the weight of the Ru-4d orbitals. We see that Ru-4d states span over a range of $\sim$ 4 eV. In Fig. E.1, it is still possible to identify the states with the d_{xz+yz} and $d_{x^2-y^2}$ characters at Γ to define the width of the valence band in LaRuFeAs. The long (red) arrow shows the estimated width of the Ru-4d band. we resorted to a criterion based on the density of states projected onto the Fe and Ru d-orbitals to define the d band width. We define the function $P(E)$ as:

$$P(E) = \int_{-\infty}^{E} [(1-x)D_{\mathrm{Fe}}(\varepsilon) + xD_{\mathrm{Ru}}(\varepsilon)]d\varepsilon. \tag{E.1}$$

where $D_{\mathrm{Fe}}(\varepsilon)$ and $D_{\mathrm{Ru}}(\varepsilon)$ are the values of the projected density of states (PDOS) onto the Fe-3d and Ru-4d orbitals, respectively. The physical meaning of $P(E)$ is the amount of electron density for energies below E coming from d states of Fe

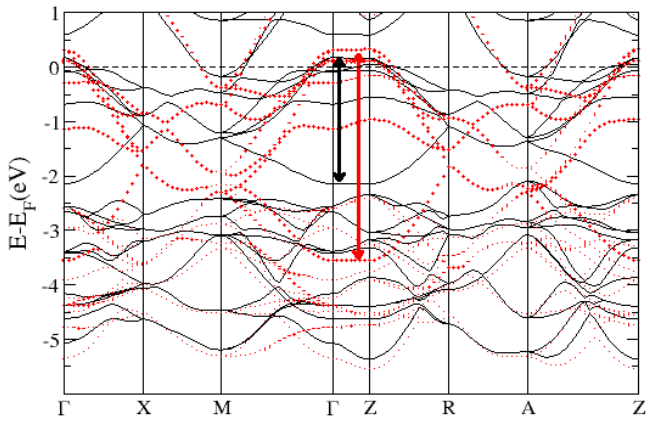

Figure E.1: Band structures for LaFeAsO (lines) and LaRuAsO (dots). The size of the dots is proportional to the weight of the Ru-4*d* orbitals. The LaRuAsO band structure is rescaled to fit the first Brillouin zone of LaFeAsO (see text).

and Ru. By using $P(E)$, we can define in an unambiguous way the band width in $R\mathrm{Fe}_{1-x}\mathrm{Ru}_x\mathrm{AsO}$. We find that $P(E)$ in LaFeAsO is 1.515 for $E = -2.15$ eV and 6.3 for $E = 0.15$ eV. We define the minimum of the band, E_L, as the value that fulfills the relation $P(E_\mathrm{L}) = 1.515$, and the maximum, E_U, as the value for which $P(E_\mathrm{U}) = 6.3$. With this criterion, we computed the lower and upper limits of the d related band in $R\mathrm{Fe}_{1-x}\mathrm{Ru}_x\mathrm{AsO}$.

In Fig. E.2, we show the energies of the upper and lower edges of the TM-related band; the band center defined as the average $E_\mathrm{av} = \frac{1}{2}(E_\mathrm{U} + E_\mathrm{L})$; the bandwidth $E_W = E_\mathrm{U} - E_\mathrm{L}$. Fig. E.2 shows that the La vs. Sm substitution does not influence the position and the width of the transition metal d band. The band center energy E_av is weakly dependent of Ru concentration. The bandwidth increases from 2.3 to 4.8 with Ru content. This is the most relevant effect of Ru substitution on the band structure of $R\mathrm{Fe}_{1-x}\mathrm{Ru}_x\mathrm{AsO}$. The change in the bandwidth is due, in equal amount, to an increase of the band maximum and a decrease of the band minimum. The band minimum goes from -2.15 to -3.2 eV, increasing the hybridization of Ru-4*d* orbitals with the As-4*p*. The band maximum increases from 0.15 to 1.6 eV, showing that Ru related bands extend far beyond the Fermi level into the unoccupied states.

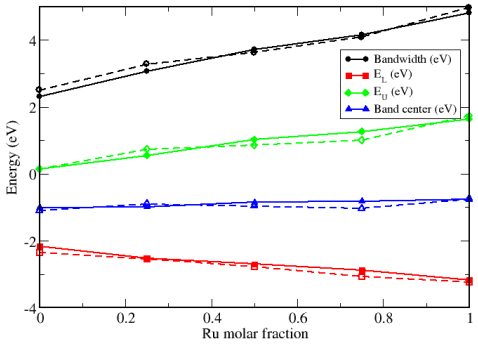

Figure E.2: Band parameters for TM related d-bands. Solid lines and filled symbols refer to $LaFe_{1-x}Ru_xAsO$, while dashed lines and open symbols refer to $SmFe_{1-x}Ru_xAsO$.

E.2 Comparison with μSR

The magnetic ordering temperature T_m in μSR experiments is extracted from the temperature evolution of the fraction of muons which detect a local moment. Conventionally, this is called magnetic volume fraction. T_m is taken as the temperature where the volume fraction is 50%. Therefore, it does not necessarily mean that half of the sample has gone magnetic. Using this probe one can roughly estimate the width of the local field distribution at the muon site, which in case of over-damped oscillations, is of the same order of the mean value of the local field. The local field is proportional to the staggered moment mainly through the dipolar coupling. Here we implement the map from a given staggered magnetization field at the muon sites $\mathbf{r}$:

$$B(\mathbf{r}) = \sum_{i\mu} \frac{m_{i\mu}}{|\mathbf{r}_i|^3} \tag{E.2}$$

where the relative distance between the muon site $\mathbf{r}$ and the moment position $m_{i\mu}$ is $\mathbf{r}_i = (ax_i - (a/2 + ax), ay_i - (a/2 + ay), c_0)$. Here we have used the symmetric position of the main muon site $(a/2, a/2, c_0)$, with $a = 2.83$Å and $c_0 = 0.78$Å, illustrated in figure E.3. We show examples of three magnetic states and their corresponding $B(\mathbf{r})$ in figure E.4.

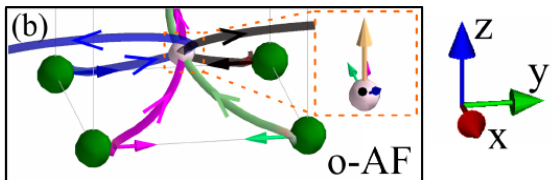

Figure E.3: Illustration of main muon site (white sphere) with respect to Fe sites (green spheres). From [25]

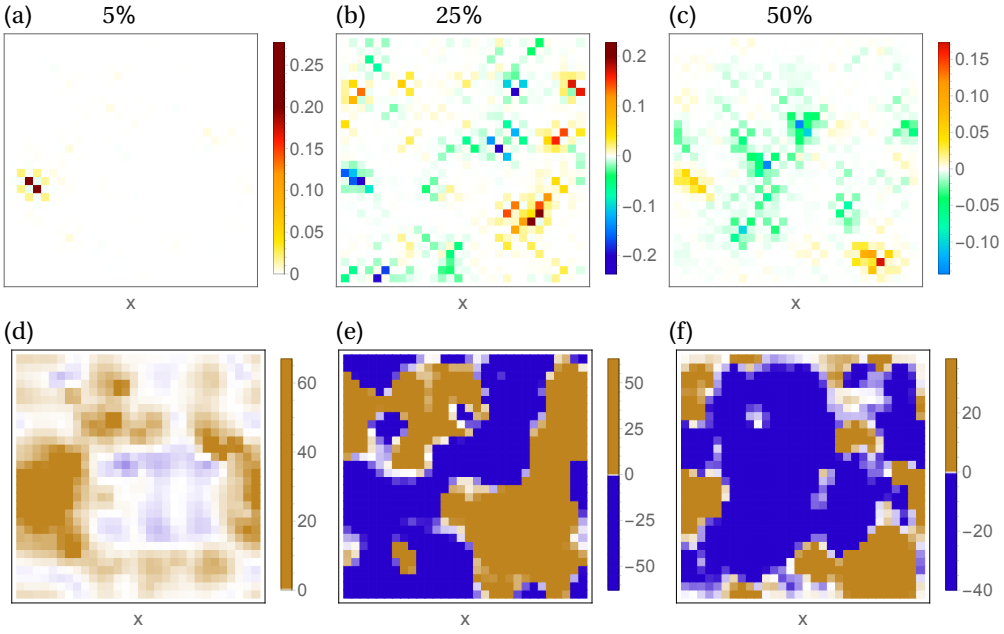

Figure E.4: Spin polarization $\mathbf{m}_5(r)$ (a) 5%, (b) 25% and (c) 50% non-magnetic disorder content. (d), (e), (f) The fields $B(\mathbf{r})$ of the previous configurations, respectively.

Bibliography

[1] Y. Kamihara, T. Watanabe, M. Hirano, and H. Hosono, J. Am. Chem. Soc. **130**, 3296 (2008).

[2] Johnpierre Paglione, Richard L. Greene, Nature Physics **6**, 645-658 (2010)

[3] A. V. Chubukov, Ann. Rev. Mod. Cond. Mat. Phys. **3**, 57 (2012).

[4] D. J. Scalapino, Rev. Mod. Phys. **84**, 1383 (2012).

[5] A. T. Rømer, A. Kreisel, I. Eremin, M. A. Malakhov, T. A. Maier, P. J. Hirschfeld, and B. M. Andersen, ArXiv:1506.03593.

[6] Frank Krüger, Sanjeev Kumar, Jan Zaanen, and Jeroen van den Brink, Phys. Rev. B **79**, 054504 (2009)

[7] J. Lorenzana, G. Seibold, C. Ortiz, and M. Grilli, Phys. Rev. Lett. **101**, 186402 (2008).

[8] I. Eremin and A. V. Chubukov, Phys. Rev. B **81**, 024511 (2010).

[9] P. M. R. Brydon, J. Schmiedt, and C. Timm, Phys. Rev. B **84**, 214510 (2011).

[10] G. Giovannetti, C. Ortix, M. Marsman, M. Capone, J. van den Brink, and J. Lorenzana, Nat. Commun. **2**, 398 (2011).

[11] R. M. Fernandes, A. V. Chubukov, and J. Schmalian, Nature Phys. **10**, 97 (2014).

[12] M. G. Kim, A. Kreyssig, A. Thaler, D. K. Pratt, W. Tian, J. L. Zarestky, M. A. Green, S. L. BudÕko, P. C. Canfield, R. J. McQueeney, and A. I. Goldman, Phys. Rev. B **82**, 220503(R) (2010).

[13] S. Avci, O. Chmaissem, S. Rosenkranz, J. M. Allred, I. Eremin, A. V. Chubukov, D. Y. Chung, M. G. Kanatzidis, J.-P. Castellan, J. A. Schlueter, H. Claus, D. D. Khalyavin, P. Manuel, A. Daoud-Aladine, and R. Osborn, Nat. Commun. **5**, 3845 (2014).

[14] X. Wang, J. Kang, and R. M. Fernandes, Phys. Rev. B **91**, 024401 (2015).

[15] G. S. Tucker, D. K. Pratt, M. G. Kim, S. Ran, A. Thaler, G. E. Granroth, K. Marty, W. Tian, J. L. Zarestky, M. D. Lumsden, S. L. Bud'ko, P. C. Canfield, A. Kreyssig, A. I. Goldman, and R. J. McQueeney, Phys. Rev. B **86**, 020503(R) (2012).

[16] Y. Texier, Y. Laplace, P. Mendels, J. T. Park, G. Friemel, D. L. Sun, D. S. Inosov, C. T. Lin, and J. Bobroff, Europhys. Lett. **99**, 17002 (2012).

[17] D. LeBoeuf, Y. Texier, M. Boselli, A. Forget, D. Colson, and J. Bobroff, Phys. Rev. B **89**, 035114 (2014).

[18] D. S. Inosov, G. Friemel, J. T. Park, A. C. Walters, Y. Texier, Y. Laplace, J. Bobroff, V. Hinkov, D. L. Sun, Y. Liu, R. Khasanov, K. Sedlak, Ph. Bourges, Y. Sidis, A. Ivanov, C. T. Lin, T. Keller, and B. Keimer, Phys. Rev. B **87**, 224425 (2013).

[19] E. Hassinger, G. Gredat, F. Valade, S. René de Cotret, A. Juneau-Fecteau, J.-Ph. Reid, H. Kim, M. A. Tanatar, R. Prozorov, B. Shen, H.-H. Wen, N. Doiron-Leyraud, and L. Taillefer, Phys. Rev. B **86**, 140502(R) (2012).

[20] F. Waßer, A. Schneidewind, Y. Sidis, S. Wurmehl, S. Aswartham, B. Büchner, and M. Braden, Phys. Rev. B **91**, 060505(R) (2015).

[21] A. E. Böhmer, F. Hardy, L. Wang, T. Wolf, P. Schweiss, and C. Meingast, Nat. Commun. **6**, 7911 (2015).

[22] J. M. Allred, S. Avci, D. Y. Chung, H. Claus, D. D. Khalyavin, P. Manuel, K. M. Taddei, M. G. Kanatzidis, S. Rosenkranz, R. Osborn, and O. Chmaissem, arXiv:1505.01433.

[23] B. P. P. Mallett, P. Marsik, M. Yazdi-Rizi, T. Wolf, A. Böhmer, F. Hardy, C. Meingast, D. Munzar, and C. Bernhard, Phys. Rev. Lett. **115**, 027003 (2015).

[24] J. M. Allred, K. M. Taddei, D. E. Bugaris, M. J. Krogstad, S. H. Lapidus, D. Y. Chung, H. Claus, M. G. Kanatzidis, D. E. Brown, J. Kang, R. M. Fernandes, I. Eremin, S. Rosenkranz, O. Chmaissem, and R. Osborn, doi:10.1038/nphys3629 (2016).

[25] B. P. P. Mallett, Yu. G. Pashkevic, A. Gusev, Th. Wolf, C. Bernhard, Europhys. Lett. **111**, 57001 (2015).

[26] Liran Wang, F. Hardy, A. Böhmer, T. Wolf, P. Schweiss, C. Meingast, Phys. Rev. B **93**, 014514 (2016).

[27] E. Hassinger, G. Gredat, F. Valade, S. Rene de Cotret, O. Cyr-Choiniere, A. Juneau-Fecteau, J.-Ph. Reid, H. Kim, M. A. Tanatar, R. Prozorov, B. Shen, H.-H. Wen, N. Doiron-Leyraud, Louis Taillefer, arXiv:1512.05912 (2015).

[28] K.M. Taddei, J.M. Allred, D.E. Bugaris, S.H. Lapidus, M.J. Krogstad, R. Stadel, H. Claus, D.Y. Chung, M.G. Kanatzidis, S. Rosenkranz, R. Osborn, O. Chmaissem, arXiv:1601.05693 (2016).

[29] M. H. Christensen, Jian Kang, B. M. Andersen, I. Eremin, R. M. Fernandes, Phys. Rev. B **92**, 214509 (2015)

[30] J. Kang, X. Wang, A. V. Chubukov, and R. M. Fernandes, Phys. Rev. B **91**, 121104(R) (2015).

[31] D. D. Khalyavin, S. W. Lovesey, P. Manuel, F. Kruger, S. Rosenkranz, J. M. Allred, O. Chmaissem, R. Osborn, Phys. Rev. B **90**, 174511 (2014)

[32] H. Ikeda, R. Arita, and J. Kunes, Phys. Rev. B **81**, 054502 (2010).

[33] Eric Fawcett, Rev. Mod. Phys. **60**, 209 (1988).

[34] J. Schmiedt, P. M. R. Brydon, and C. Timm, Phys. Rev. B **85**, 214522 (2012).

[35] S. Graser, T. A. Maier, P. J. Hirschfeld, and D. J. Scalapino, New J. Phys. **11**, 025016 (2009).

[36] R. Wiesendanger, Rev. Mod. Phys. **81**, 1495 (2009).

[37] M Enayat eta al, Science **345**, 6197 (2014).

[38] Y. Singh, M. A. Green, Q. Huang, A. Kreyssig, R. J. McQueeney, D. C. Johnston, and A. I. Goldman, Phys. Rev. B **80**, 100403 (2009).

[39] X. Wang and R. M. Fernandes, Phys. Rev. B **89**, 144502 (2014).

[40] D. N. Aristov and S. V. Maleyev, Phys. Rev. B **56**, 8841 (1997).

[41] A. Akbari, I. Eremin, and P. Thalmeier, Phys. Rev. B **84**, 134513 (2011).

[42] T. Vojta, J. Low. Temp. Phys. **161**, 299 (2010).

[43] K. Binder and A. P. Young, Rev. Mod. Phys. **58**, 801 (1986).

[44] K. H. Fischer and J. A. Hertz, *Spin Glasses* (Cambridge University Press, Cambridge 1999).

[45] H. Yang, Z. Wang, D. Fang, Q. Deng, Q.-H. Wang, Y.-Y. Xiang, Y. Yang, and H.-H. Wen, Nature Comm. **4**, 2173 (2013).

[46] H. Shiba, Prog. Theor. Phys. **40**, 435 (1968).

[47] A. V. Balatsky, I. Vekhter, and J.-X. Zhu, Rev. Mod. Phys. **78**, 373 (2006).

[48] H. Suzuki, T. Yoshida, S. Ideta, G. Shibata, K. Ishigami, T. Kadono, A. Fujimori, M. Hashimoto, D. H. Lu, Z.-X. Shen, K. Ono, E. Sakai, H. Kumigashira, M. Matsuo, and T. Sasagawa, Phys. Rev. B **88**, 100501(R) (2013).

[49] V. Thampy, J. Kang, J. A. Rodriguez-Rivera, W. Bao, A. T. Savici, J. Hu, T. J. Liu, B. Qian, D. Fobes, Z. Q. Mao, C. B. Fu, W. C. Chen, Q. Ye, R. W. Erwin, T. R. Gentile, Z. Tesanovic, and C. Broholm, Phys. Rev. Lett. **108**, 107002 (2012).

[50] E. F. Shender and S. A. Kivelson, Phys. Rev. Lett. **66**, 2384 (1991).

[51] B. M. Andersen, P. J. Hirschfeld, A. P. Kampf, and M. Schmid, Phys. Rev. Lett. **99**, 147002 (2007).

[52] Norman Y. Yao, Leonid I. Glazman, Eugene A. Demler, Mikhail D. Lukin, Jay D. Sau, Phys. Rev. Lett. **113**, 087202 (2014).

[53] T. Berlijn, *private communication.*

[54] H. Alloul, J. Bobroff, M. Gabay, and P. J. Hirschfeld, Rev. Mod. Phys **81**, 45 (2009).

[55] J. W. Harter, B. M. Andersen, J. Bobroff, M. Gabay, and P. J. Hirschfeld, Phys. Rev. B **75**, 054520 (2007).

[56] B. M. Andersen, S. Graser, and P. J. Hirschfeld, Phys. Rev. Lett. **105**, 147002 (2010).

[57] U. Tricoli and B. M. Andersen, J. Supercond. Novel Magn. **25**, 1329 (2012).

[58] B. M. Andersen, O. F. Syljuaasen, and P. Hedegård, Phys. Rev. B **80**, 052509 (2009).

[59] K. Nakamura, R. Arita, and H. Ikeda, Phys. Rev. B **83**, 144512 (2011).

[60] L. Yu, Acta Phys. Sin. **21**, 75 (1965).

[61] A. I. Rusinov,Sov. Phys. JETP **9** 85 (1969).

[62] T.-M. Chuang, M. P. Allan, J. Lee, Y. Xie, N. Ni, S. L. Bud'ko, G. S. Boebinger, P. C. Canfield, and J. C. Davis, Science **327**, 181 (2010).

[63] M. A. Tanatar, E. C. Blomberg, A. Kreyssig, M. G. Kim, N. Ni, A. Thaler, S. L. Budko, P. C. Canfield, A. I. Goldman, I. I. Mazin, and R. Prozorov, Phys. Rev. B **81**, 184508 (2010).

[64] J.-H. Chu, J. G. Analytis, K. De Greve, P. L. McMahon, Z. Islam, Y. Yamamoto, and I. R. Fisher, Science **329**, 824 (2010).

[65] J. J. Ying, X. F. Wang, T. Wu, Z. J. Xiang, R. H. Liu, Y. J. Yan, A. F. Wang, M. Zhang, G. J. Ye, P. Cheng, J. P. Hu, and X. H. Chen, Phys. Rev. Lett. **107**, 067001 (2011).

[66] J.-H. Chu, H.-H. Kuo, J. G. Analytis, and I. R. Fisher, Science **337**, 710 (2012).

[67] E. C. Blomberg, M. A. Tanatar, R. M. Fernandes, I. I. Mazin, B. Shen, H.-H. Wen, M. D. Johannes, J. Schmalian, and R. Prozorov, Nature Comm. **4**, 1914 (2013).

[68] S. Ishida, M. Nakajima, T. Liang, K. Kihou, C. H. Lee, A. Iyo, H. Eisaki, T. Kakeshita, Y. Tomioka, T. Ito, and S. Uchida, Phys. Rev. Lett. **110**, 207001 (2013); J. Am. Chem. Soc. **135**, 3158, (2013).

[69] M. Yi, D. Lu, J.-H. Chu, J. G. Analytis, A. P. Sorini, A. F. Kemper, B. Moritz, S.-K. Mo, R. G. Moore, M. Hashimoto, W.-S. Lee, Z. Hussain, T. P. Devereaux, I. R. Fisher, and Z.-X, Shen, Proc. Natl. Acad. Sci. USA **108**, 6878 (2011).

[70] Xingye Lu, J. T. Park, Rui Zhang, Huiqian Luo, Andriy H. Nevidomskyy, Qimiao Si, Pengcheng Dai, Science **345**, 657 (2014).

[71] M. Nakajima, T. Liang, S. Ishida, Y. Tomioka, K. Kihou, C. H. Lee, A. Iyo, H. Eisaki, T. Kakeshita, T. Ito, and S. Uchida, Proc. Natl. Acad. Sci. USA **108**, 12238 (2011).

[72] A. Dusza, A. Lucarelli, F. Pfuner, J. H. Chu, I. R. Fisher, and L. Degiorgi, Europhys. Lett. **93**, 37002 (2001).

[73] C. Mirri, A. Dusza, S. Bastelberger, M. Chinotti, J.-H. Chu, H.-H. Kuo, I.R. Fisher, L. Degiorgi, Phys. Rev. Lett. **115**, 107001 (2015).

[74] A. E. Böhmer, P. Burger, F. Hardy, T. Wolf, P. Schweiss, R. Fromknecht, M. Reinecker, W. Schranz, and C. Meingast, Phys. Rev. Lett. **112**, 047001 (2014).

[75] Y. Gallais, R. M. Fernandes, I. Paul, L. Chauviere, Y.-X. Yang, M.-A. Measson, M. Cazayous, A. Sacuto, D. Colson, A. Forget, Phys. Rev. Lett. **111**, 267001 (2013).

[76] M. P. Allan, T.-M. Chuang, F. Massee, Y. Xie, N. Ni, S. L. Bud'ko, G. S. Boebinger, Q. Wang, D. S. Dessau, P. C. Canfield, M. S. Golden, and J. C. Davis, Nat. Phys. **9**, 220 (2013).

[77] C.-L. Song, Y.-L. Wang, P. Cheng, Y.-P. Jiang, W. Li, T. Zhang, Z. Li, K. He, L. Wang, J.-F. Jia, H.-H. Hung, C. Wu, X. Ma, X. Chen, and Q.-K. Xue, Science **332**, 1410 (2011).

[78] E. P. Rosenthal, E. F. Andrade, C. J. Arguello, R. M. Fernandes, L. Y. Xing, X. C. Wang, C. Q. Jin, A. J. Millis, A. N. Pasupathy, Nature Phys. **10**, 225 (2014).

[79] Hsueh-Hui Kuo, Maxwell C. Shapiro, Scott C. Riggs, Ian R. Fisher, Phys. Rev. B **88**, 085113 (2013).

[80] H.-H. Kuo and I. R. Fisher, Phys. Rev. Lett. **112**, 227001 (2014).

[81] Hsueh-Hui Kuo, Jiun-Haw Chu, Steven A. Kivelson, Ian R. Fisher, arXiv:1503.00402 (2015).

[82] Anna E. Böhmer, Christoph Meingast, C. R. Physique **17**, 90-112 (2016).

[83] R. M. Fernandes, E. Abrahams, and J. Schmalian, Phys. Rev. Lett. **107**, 217002 (2011).

[84] K. Sugimoto, P. Prelovsek, E. Kaneshita, T. Tohyama, Phys. Rev. B **90**, 125157 (2014).

[85] M. Breitkreiz, P. M. R. Brydon, C. Timm, Phys. Rev. B **90**, 121104(R) (2014).

[86] Shuhua Liang, Gonzalo Alvarez, Cengiz Şen, Adriana Moreo, Elbio Dagotto, Phys. Rev. Lett. **109**, 047001 (2012).

[87] X. Zhou, C. Ye, P. Cai, X. Wang, X. Chen, and Y. Wang, Phys. Rev. Lett. **106**, 087001 (2011).

[88] S. Grothe, S. Chi, P. Dosanjh, R. Liang, W. N. Hardy, S. A. Burke, D. A. Bonn, and Y. Pennec, Phys. Rev. B **86**, 174503 (2012).

[89] J.C. Davis and P.J. Hirschfeld, Nature Phys. **10**, 1 (2014).

[90] B. M. Andersen, S. Graser, and P. J. Hirschfeld, Europhys. Lett. **97**, 47002 (2012).

[91] J. M. Ziman, Adv. Phys. **10**, 1 (1961).

[92] W. E. Lawrence and L. A. Cole, J. Phys. F: Met. Phys. **15**, 833 (1985).

[93] M. A. Tanatar, A. E. Böhmer, E. I. Timmons, M. Schütt, G. Drachuck, V. Taufour, S. L. Bud'ko, P. C. Canfield, R. M. Fernandes, R. Prozorov, arXiv:1511.04757 (2015).

[94] Y. Suzuki, T. Shimojima, T. Sonobe, A. Nakamura, M. Sakano, H. Tsuji, J. Omachi, K. Yoshioka, M. Kuwata-Gonokami, T. Watashige, R. Kobayashi, S. Kasahara, T. Shibauchi, Y. Matsuda, Y. Yamakawa, H. Kontani, K. Ishizaka,Phys. Rev. B **92**, 205117 (2015).

[95] Shantanu Mukherjee, A. Kreisel, P. J. Hirschfeld, Brian M. Andersen, Phys. Rev. Lett. **115**, 026402 (2015).

[96] A. Kreisel, Shantanu Mukherjee, P. J. Hirschfeld, Brian M. Andersen, Phys. Rev. B **92**, 224515 (2015).

[97] C.-C. Chen, R. Applegate, B. Moritz, T. P. Devereaux, R. R. P. Singh, New Journal of Physics **13**, 043025 (2011).

[98] A. F. Kemper, C. Cao, P. J. Hirschfeld, and H.-P. Cheng, Phys. Rev. B **80**, 104511 (2009).

[99] J. Kang and Z. Tesanovic, Phys. Rev. B **83**, 020505 (2011).

[100] Y. Inoue, Y. Yamakawa, and H. Kontani, Phys. Rev. B **85**, 224506 (2012).

[101] S. Graser, T. A. Maier, P. J. Hirschfeld, and D. J. Scalapino, New J. Phys. **11**, 025016 (2009).

[102] C.-L. Song, Y.-L. Wang, Y.-P. Jiang, L. Wang, K. He, X. Chen, J. E. Hoffman, X.-C. Ma, and Q.-K. Xue, Phys. Rev. Lett. **109**, 137004 (2012).

[103] T. Hanaguri, *private communication*.

[104] Y. Wang, Maria N. Gastiasoro, Brian M. Andersen, M. Tomić, Harald O. Jeschke, Roser Valentí, Indranil Paul, P. J. Hirschfeld, Phys. Rev. Lett. **114**, 097003 (2015).

[105] P. J. Hirschfeld, M. M. Korshunov, and I. I. Mazin, Rep. Prog. Phys. **74**, 124508 (2011).

[106] P.J. Hirschfeld, Comptes Rendus Physique **17**, 197 (2016).

[107] N. F. Berk and J. R. Schrieffer, Phys. Rev. Lett. **17**, 433 (1966).

[108] I.I. Mazin, D.J. Singh, M.D. Johannes, M.H. Du, Phys. Rev. Lett. **101**, 057003 (2008).

[109] Kazuhiko Kuroki, Seiichiro Onari, Ryotaro Arita, Hidetomo Usui, Yukio Tanaka, Hiroshi Kontani, Hideo Aoki, Phys. Rev. Lett. **101**, 087004 (2008).

[110] J. E. Hoffman, Rep. Prog. Phys. **74**, 124513 (2011).

[111] Can-Li Song and Jennifer E. Hoffman, Current Opinion in Solid State and Materials Science **17**, 39-48 (2013).

[112] Oystein Fischer, Martin Kugler, Ivan Maggio-Aprile, Christophe Berthod, Christoph Renner, Rev. Mod. Phys. **79**, 353 (2007).

[113] M. P. Allan, A. W. Rost, A. P. Mackenzie, Y. Xie, J. C. Davis, K. Kihou, C. H. Lee, A. Iyo, H. Eisaki, and T.-M. Chuang, Science **336**, 563 (2012).

[114] H. Yang, Z. Wang, D. Fang, T. Kariyado, G. Chen, M. Ogata, T. Das, A. V. Balatsky, and H.-H. Wen, Phys. Rev. B **86**, 214512 (2012).

[115] S. Chi, S. Johnston, G. Levy, S. Grothe, R. Szedlak, B. Ludbrook, R. Liang, P. Dosanjh, S. A. Burke, A. Damascelli, D. A. Bonn, W. N. Hardy, and Y. Pennec, Phys. Rev. B **89**, 104522 (2014).

[116] J.-X. Yin, Z. Wu, J.-H. Wang, Z.-Y. Ye, J. Gong, X.-Y. Hou, L. Shan, A. Li, X.-J. Liang, X.-X. Wu, J. Li, C.-S. Ting, Z.-Q. Wang, J.-P. Hu, P.-H. Hor, H. Ding, S. H. Pan, Nat. Phys. **11**, 543 (2015).

[117] A. P. Dioguardi, J. Crocker, A. C. Shockley, C. H. Lin, K. R. Shirer, D. M. Nisson, M. M. Lawson, N. apRoberts-Warren, P. C. Canfield, S. L. BudÕko, S. Ran, and N. J. Curro, Phys. Rev. Lett. **111**, 207201 (2013).

[118] X. Lu, D. W. Tam, C. Zhang, H. Luo, M. Wang, R. Zhang, L. W. Harriger, T. Keller, B. Keimer, L.-P. Regnault, T. A. Maier, and P. Dai, Phys. Rev. B **90**, 024509 (2014).

[119] T. Hanaguri, *private communication*.

[120] T. K. Ng and Y. Avishai, Phys. Rev. B **80**, 104504 (2009).

[121] M. Matsumoto, M. Koga, and H. Kusunose, J. Phys. Soc. Jpn. **78**, 084718 (2009).

[122] Y. Bang, H.-Y. Choi, and H. Won, Phys. Rev. B **79**, 054529 (2009).

[123] W.-F. Tsai, Y.-Y. Zhang, C. Fang, and J. P. Hu, Phys. Rev. B **80**, 064513 (2009).

[124] D. Zhang, Phys. Rev. Lett. **103**, 186402 (2009).

[125] J. Li and Y. Wang, Europhys. Lett. **88**, 17009 (2009).

[126] A. Akbari, I. Eremin, and P. Thalmeier, Phys. Rev. B **81**, 014524 (2010).

[127] T. Kariyado and M. Ogata, J. Phys. Soc. Jpn. **79**, 083704 (2010).

[128] R. Beaird, I. Vekhter, and J.-X. Zhu, Phys. Rev. B **86**, 140507(R) (2012).

[129] S. V. Borisenko, V. Zabolotnyy, A. Kordynuk, D. Evtushinsky, T. Kim, I. Morozov, R. Follath, and B. Büchner, Symmetry **4**, 251 (2012).

[130] K. Umezawa, Y. Li, H. Miao, K. Nakayama, Z.-H. Liu, P. Richard, T. Sato, J. B. He, D.-M. Wang, G. F. Chen, H. Ding, T. Takahashi, and S.-C. Wang, Phys. Rev. Lett. **108**, 037002 (2012).

[131] Y. Wang, A. Kreisel, P. J. Hirschfeld, T. A. Maier, D. J. Scalapino, S. V. Borisenko, and V. B. Zabolotnyy, Phys. Rev. B **88**, 174516 (2013).

[132] F. Hammerath, P. Bonfá, S. Sanna, G. Prando, R. De Renzi, Y. Kobayashi, M. Sato, and P. Carretta, Phys. Rev. B **89**, 134503 (2014).

[133] M. Sato, Y. Kobayashi, S. C. Lee, H. Takahashi, E. Satomi, and Y. Miura, J. Phys. Soc. Jpn. **79**, 014710 (2010).

[134] S. J. Singh, J. Shimoyama, A. Yamamoto, H. Ogino, and K. Kishio, Physica C (Amsterdam) **494**, 57 (2011).

[135] E. Satomi, S. C. Lee, Y. Kobayashi, and M. Sato, J. Phys. Soc. Jpn. **79**, 014710 (2010).

[136] S. Sanna, P. Carretta, P. Bonfá, G. Prando, G. Allodi, R. De Renzi, T. Shiroka, G. Lamura, A. Martinelli, and M. Putti, Phys. Rev. Lett. **107**, 227003 (2011).

[137] S. Sanna, P. Carretta, R. De Renzi, G. Prando, P. Bonfá,, M. Mazzani, G. Lamura, T. Shiroka, Y. Kobayashi, and M. Sato, Phys. Rev. B **87**, 134518 (2013).

[138] C. Bernhard, A. J. Drew, L. Schulz, V. K. Malik, M. Rössle, Ch. Niedermayer, T. Wolf, G. D. Varma, G. Mu, H.-H. Wen, H. Liu, G. Wu, and X. H. Chen, New J. Phys. **11**, 055050 (2009).

[139] C. Bernhard, C. N. Wang, L. Nuccio, L. Schulz, O. Zaharko, J. Larsen, C. Aristizabal, M. Willis, A. J. Drew, G. D. Varma, T. Wolf, and Ch. Niedermayer, Phys. Rev. B **86**, 184509 (2012).

[140] J. D. Wright, T. Lancaster, I. Franke, A. J. Steele, J. S. Möller, M. J. Pitcher, A. J. Corkett, D. R. Parker, D. G. Free, F. L. Pratt, P. J. Baker, S. J. Clarke, and S. J. Blundell, Phys. Rev. B **85**, 054503 (2012).

[141] Peayush Choubey, T. Berlijn, A. Kreisel, C. Cao, P. J. Hirschfeld, Phys. Rev. B **90**, 134520 (2014).

[142] A. Kreisel, Peayush Choubey, T. Berlijn, B. M. Andersen, P. J. Hirschfeld, Phys. Rev. Lett. **114**, 217002 (2015).

[143] Kazuhiko Kuroki, Hidetomo Usui, Seiichiro Onari, Ryotaro Arita, Hideo Aoki, Phys. Rev. B **79**, 224511 (2009).